This electronic thesis or dissertation has been downloaded from the King's Research Portal at https://kclpure.kcl.ac.uk/portal/

Image guided liposomal nanoparticles for drug delivery

Amrahli, Maral

Awarding institution:
King's College London

The copyright of this thesis rests with the author and no quotation from it or information derived from it may be published without proper acknowledgement.

END USER LICENCE AGREEMENT

Unless another licence is stated on the immediately following page this work is licensed

under a Creative Commons Attribution-NonCommercial-NoDerivatives 4.0 International

licence. https://creativecommons.org/licenses/by-nc-nd/4.0/

You are free to copy, distribute and transmit the work

Under the following conditions:

- Attribution: You must attribute the work in the manner specified by the author (but not in any way that suggests that they endorse you or your use of the work).
- Non Commercial: You may not use this work for commercial purposes.
- No Derivative Works - You may not alter, transform, or build upon this work.

Any of these conditions can be waived if you receive permission from the author. Your fair dealings and other rights are in no way affected by the above.

Take down policy

If you believe that this document breaches copyright please contact librarypure@kcl.ac.uk providing details, and we will remove access to the work immediately and investigate your claim.

Download date: 06. Oct. 2023

IMAGE GUIDED LIPOSOMAL NANOPARTICLES FOR DRUG DELIVERY

Maral AMRAHLI

A thesis submitted to King's College London in partial fulfilment for the degree of

Doctor of Philosophy

Supervisors:

Dr. Maya THANOU

Dr. Po-Wah SO

Faculty of Life Sciences & Medicine School of Cancer and Pharmaceutical Sciences

2020

This thesis shows research conducted at King's College London between July 2015 and March 2020 under the supervision of Dr Maya Thanou and Dr. Po-Wah So. I certify that this research is original and any parts of the work that have been conducted by collaboration have been clearly indicated. I also certify that the text was written by me. Also, I have clearly indicated suitable citation any part of this thesis that has already been published in the literature.

Signature  Date: 09.03.2020

Abstract:

Clinical imaging including as PET, CT and MRI have revolutionised the detection and management of diseases such as cancer. When imaging agents are coupled onto nanosized carriers they provide information on the tumour location as well as provide an insight into their biodistribution. Therefore, these nanocarriers can be involved in integration of diagnosis and therapy in a single platform, which is called theranostics. Image Guided Focused Ultrasound drug delivery is a promising strategy for enabling both cancer diagnosis and treatment using the same nanocarrier delivery/diagnostic system. The aim of this project is to develop near infrared fluorescence (NIRF) and magnetic resonance imaging (MRI) labelled liposomes for targeted image guided drug delivery when combined with focused ultrasound (FUS). FUS can be applied for regional increase in temperature (hyperthermia) whereas MR guided FUS (MRgFUS) is a clinically used instrument that can provide this controlled hyperthermia.

Previous studies have shown that incorporation of chelated Gd^{3+} lipids into liposomal formulations empowered these nanoparticles with MRI contrast enhancement. Here, various spacers between the chelating ligand (head group) and the lipid tail were introduced, to investigate their effects on liposomes' T_1 relaxivities, a parameter used for measuring the contrast efficiency. Image guided thermosensitive PEGylated liposomes (iTSLs) were prepared with various Gd^{3+} chelated lipids that were made for the purpose of this study. In addition, a second, near infrared fluorescence (NIRF) label was also included in the liposomes for optical imaging. The

prepared iTSLs were characterised by T_1 relaxivities using a 400 MHz NMR and 9.4 T MRI. Gd^{3+} concentrations of liposome formulation were determined by Inductively Coupled Plasma Optical Emission Spectrometry (ICP-OES) and Total Reflection X-Ray Fluorescence (TXRF). In addition, these two analytical methods were compared for reproducibility and accuracy for assessment of Gd^{3+} concentrations in liposomes. Moreover, the liposomal formulations incorporating with MRI and NIRF lipids were loaded with a chemotherapeutic agent (doxorubicin). *In vivo*, the tumours were monitored with doxorubicin when released via heat activation by FUS, which showed intrinsic drug fluorescence change. iTSLs accumulation in tumours at defined time points (post injection) *in vivo* were investigated with both imaging techniques (NIRF and MRI).

Both NMR and MRI relaxometries studies showed potential for MR contrast enhancement. T_1-weighted images showed positive enhancement for all iTSLs, with longer spacers apparently having a stronger effect. In mice, administration of iTSLs have shown a time-dependent tumour contrast enhancement and the change in T_1 was quantified over time. The studies on xenograft mice models provided evidence that mild FUS-induced hyperthermia greatly improves the iTSLs uptake in tumours and trigger rapid drug release which improves the overall therapeutic index.

Publications:

Centelles MNMN, Wright M, So P-W, et al. Image guided thermosensitive liposomes for focused ultrasound drug delivery: Using NIRF labelled lipids and topotecan to visualise the effects of hyperthermia in tumours. J Control Release. 2018; 280: 87–98

Zaaroor M, Sinai A, Goldsher D, et al. 5th International Symposium on Focused Ultrasound: North Bethesda, MD, USA. 28 August- 1 September 2016. In: Journal of Therapeutic Ultrasound. 2016.

Study presented in Chapter 4 is under review for publication.
MR-labelled thermosensitive liposomes and focused ultrasound for precise drug release in triple negative breast cancers
Maral Amrahli, Miguel Centelles, Paul Cressey, Martynas Prusevicius, Wladyslaw Gedroyc, Xiao Yun Xu, Po-Wah So, Michael Wright, and Maya Thanou

Acknowledgments

I would like to thank the Ministry of Education in the Republic of Azerbaijan for funding me over the years. I would also like to thank King's College, London for the opportunity to pursue this research. I am grateful to my supervisors, firstly Dr. Maya Thanou for her guidance and support during my PhD and secondly Dr. Po-Wah So for her knowledge about MRI and introducing me to TXRF. Special mention for Dr. Michael Wright for being so incredibly intelligent and making himself available around the clock to assist. Thanks to all you for sharing your knowledge and making this project possible.

I would like to also acknowledge my colleagues for their help and assistance over the years, namely Zi Hong Mok, Jasmin Wilson, Muhammed Rahman and Jana Javorovic. Special thanks to Paul Cressey for going through the shared struggles in the many long, big, large and endless experiments which included my crazy moods. I hope you will have a great academic career.

On a personal note, I would like to thank my Mum for hitting my head with the car boot (by mistake) when she was convincing me to apply to KCL. Thank you for giving your life to me so that I may have a great future, if it was not you, I would not be here my angel mama. Also, I would like to acknowledge my first and only Azeri friend who has a heart of gold and always has my back, supporting me like an angel keeping her wings around me. Thank you so much Konul Mustafayeva. One of the best things that

happened to me during this PhD was I became part of a new family here, dearest Ber and Jim thank you so much for making London feel like home and welcoming me into your family. I can never convey my full gratitude for your love, support and help. I would like to thank all my relatives in Azerbaijan that supported me over the far distances and never doubted me.

The most special thanks go to my other half, kocacim benim Joseph Walsh. I cannot thank you enough for all your support and help. Day and night, you were there for me, listening to everything about this project, proofreading ever single page again and again and going through the hurdle with me without complaint. No words genuinely can express how grateful I am for being married to you and all the things you do for me. I am very lucky to have you. Iyi ki varsin!

Uncle Vagif, we lost you to cancer years ago, but we have never forgotten you! I wish I could save you; I wish you could see my graduation. I wish you I could thank you more for being such a wonderful person… This is for you.

Table of Contents

Table of Figures, Schemes, Tables and Equations

Figures:

Schemes:

Tables:

Equations:

Abbreviations

%ID – % Injected Dose
^{13}C – Carbon-13
^{1}H – Proton-1
ANOVA – Analysis of Variance
CA – Contrast Agent
CT – Computed Tomography
DAD –Diode Array Detector
DCM – Dichloromethane
DLS – Dynamic Light Scattering
DMSO – Dimethyl sulphide
DOTA – 1,4,7,10-Tetraazacyclododecane-1,4,7,10-Tetraacetic Acid
DOX – Doxorubicin
DPPC – 1,2-sn-glycero-3-phosphatidylcholin
DSC – Differential Scanning Calorimetry
DTPA – Diethylenetriaminepentaacetic Acid
ECF – Extracellular fluid
EDXRF – Energy Dispersive X-Ray Fluorescence
EMA – European Medicines Agency
EPR – Enhanced Permeability Retention
ESI-MS – Electrospray mass spectroscopy
FBS – Fetal Bovine Serum
FDA – United States Food and Drug Administration
FFC – Fast Field Cycling
FLD – Fluorescence Detector
FOV – Field of View
FSE – Fast Spin Echo
FUS – Focused Ultrasound
GBCA – Gadolinium Based Contrast Agents
Gd – Gadolinium
Gd1 – Gadovist
GHz – Gigahertz
GL – Gadovist Encapsulated Liposomes
HAT – Heat Activated Cytotoxic
HIFU – High Intensity Focused Ultrasound
HPLC – High Performance Liquid Chromatography
HSA – Human Serum Albumin
i.v. – Intravenous injection
ICP-MS – Inductively Coupled Plasma-Mass Spectrometry
ICP-OES – Inductively Coupled Plasma Optical Emission Spectrometry
iTSL – Image Guided Thermosensitive Liposomes
iTSL – Image Guided Thermosensitive Liposomes with Doxorubicin
K – Kelvin
LD_{50} – Lethal dose that kills 50% of test animals
LTSL – Lysolipid Thermosensitive Liposome

MeOH – Methanol
MHz – Megahertz
MION – Micron Iron Oxide Nanoparticles
MRgFUS – Magnetic Resonance guided Focused Ultrasound
MRI – Magnetic Resonance Imaging
NIR – Near Infrared
NIRF – Near Infrared Fluorescence
NMR – Nuclear Magnetic Resonance
NMRD – Nuclear Magnetic Resonance Dispersion
NSF – Nephrogenic Systemic Fibrosis
^{o}C – Degree Celsius
PBS – Phosphate Buffered Saline
PDI – Polydispersity Index
PEG – Polyethylene Glycol
PET – Positron Emission Tomography
ppb – Parts per billion
ppm – Parts per million
PRF – Proton Resonance Frequency
q – Hydration number
r.t. – Room temperature
R_1 – Longitudinal relaxation rate ($1/T_1$)
R_2 – Transverse relaxation rate ($1/T_2$)
$R_{1(0)}$ – Buffer Relaxation Rate ($1/T_{1(o)}$)
r_1 – T_1 molar relaxivity (Relaxation rate ($R_1=1/T_1$) per concentration in mM (R_1/[Gd]))
R^2 – Coefficient of Determination
r_2 – T_2 molar relaxivity (Relaxation rate ($R_2=1/T_2$) per concentration in mM (R_2/[Gd]))
RES – Reticuloendothelial System
RF – Radiofrequency
RO – Reverse Osmosis
ROIs – Regions of Interest
s.c. –subcutaneous
SD – Standard Deviation
SD – standard deviation
SE – Standard Error
SHO – SCID Hairless Outbred
SPIO – Superparamagnetic Iron Oxide
SPION – Superparamagnetic Iron Oxide Nanoparticles
STL – Short-chain elastin-like polypeptide incorporating thermosensitive liposome
T – Tesla
T_1 – Longitudinal relaxation time
T_2 – Transverse relaxation time
TE – Echo Time
TFA – Trifluoroacetic acid
TLC – Thin Layer Chromatography
T_m – Phase Transition Temperature
TR – Repetition Time
TSL – Thermosensitive Liposome

TTSL – Traditional Thermosensitive Liposome
TXRF – Total Reflection X-Ray Fluorescence
US – Ultrasound
USPIO – Ultra Small Superparamagnetic Iron Oxide
UV/VIS – Ultra-violet/visible
v/v – Volume per volume
w% – Weight per weight percent
XRF – X-Ray Fluorescence
$\Delta\delta$ – Change in chemical shift
λ ex – Excitation wavelength
τ_D – Translational diffusion
τ_M – Water residency time
τ_R – Rotational correlation time

1. Introduction

1.1 Magnetic Resonance Imaging

1.1.1 Principles of MRI

Magnetic Resonance Imaging (MRI) uses magnetic properties of the body to obtain detailed images from any part of the body. The hydrogen nucleus which has a single proton is used for imaging purposes due to its abundance in water and fat [1]. With sufficient computational support, the aggregates of these MRI signals can become a three-dimensional molecular image that displays tissues, and organs. MRI requires magnetic field and radiofrequency rather than ionizing radiation, unlike X-ray or CT (computed tomography) imaging, thus it has a great clinical safety profile with high spatial resolution [2,3].

MRI has four main components: the primary magnet, gradient coils, radiofrequency (RF) system and the supporting computer system. Magnetic field strength (B_0) of MRI is measured in Tesla (T) [4]. Currently, most of the clinically available MRI scanners are with magnetic field strengths of 1.5 T or 3 T. Although recently, human sized MRI systems with 7 T field strength have become available for clinical applications [5]. The strength of the magnetic field (B_0) can be manipulated along x, y and z directions by using gradient coils, which allows the localisation of image slices (does not change the direction of the magnetic field) [1,4].

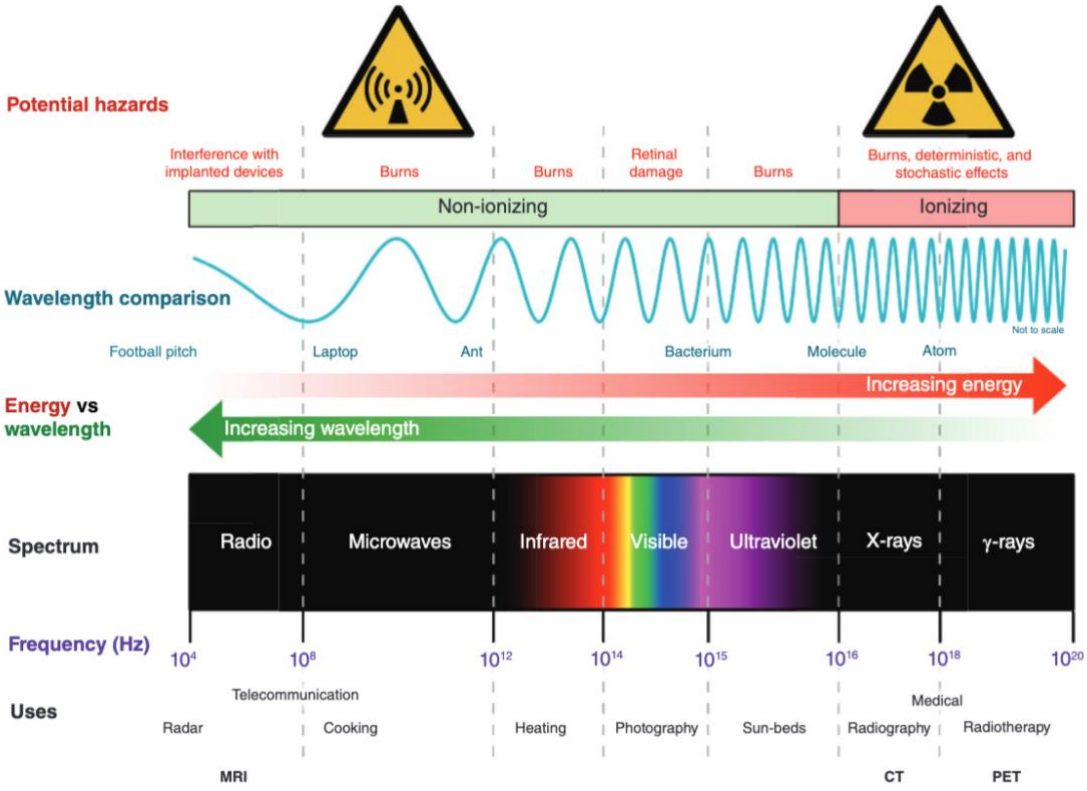

Figure 1.1:The electromagnetic spectrum showing the frequencies and energies of the imaging modalities and their potential hazards. The image was adopted from Westbrook *et al.* [6]

MRI is based on the principles of Nuclear Magnetic Resonance (NMR). It can measure the interaction between the external magnetic field (B_0) and the magnetic atomic nuclei. The nuclei with non-zero quantum spin such as ^{1}H (I: ± 1/2), ^{13}C (I: ± 1/2), ^{19}F (I: ± 1/2), ^{23}Na (I: ± 3/2), and ^{17}O (I: ± 5/2) can absorb and emit electromagnetic radiation at a characteristic radio frequency (RF) under a strong external magnetic field [7]. In general, nuclei with an odd mass number or atomic weight, are observable under MRI [6,8].

^{1}H is the most abundant isotope of hydrogen in nature, which is commonly present in the human body (water and fat tissues) [9]. Positively charged protons of the hydrogen spins (angular momentum) induce a local magnetic field and act as a small magnet with a magnetic moment (μ). In the absence of a strong external magnetic field (B_0), the individual magnetic moments of hydrogen nuclei are disoriented. However, under the external magnetic field (B_0), the magnetic moments of hydrogen nuclei align parallel (spin-up) or antiparallel (spin-down) to the magnetic field. Quantum theory explains this alignment of the magnetic moments with the energy states (number of energy states: $2I + 1$), whereas hydrogen protons will have two possible; lower (spin-up) and higher (spin-down) energy states (Zeeman effect) [6]. The alignment number of the spin in the low or high energy populations can be predicted by the Boltzmann equation **(Equation 1.1)** which depends on the temperature and the energy difference. Energy difference between states depends on the magnetic field (B_0). Another outcome of the magnetic field on a hydrogen nucleus is that the magnetic moments of hydrogen start to wobble around the B_0 which is called precession [3,8,9] **(Figure 1.2)**. The frequency of the precession is directly proportional to the applied magnetic field strength and gyromagnetic ratio constant of the nuclei which is expressed by Larmor's equation **(Equation 1.2).**

$$\frac{N^+}{N^-} = e^{-\Delta E/kT} \quad with \quad \Delta E = h\omega_0$$

Equation 1.1: Boltzmann distribution of spins in the lower and higher energy states where the number of spins in the lower state (N^-) and in the higher state (N^+) are shown accordingly. The energy difference between the states (ΔE) measured in Joules (J), Boltzmann constant (k) is 1.381×10^{-23} J/K. Temperature (T) is in Kelvin and *h* is Planck's constant (6.629×10^{34} J/s).

$$\omega_0 = \gamma B_0$$

Equation 1.2: Larmor's equation. Larmor frequency is ω_0, gyromagnetic ratio is γ and large magnetic field of the MRI scanner is B_0.

The gyromagnetic ratio is a nuclei specific constant and it shows the relationship between the spin angular momentum and the magnetic moment of the nuclei. In particular, the gyromagnetic ratio of hydrogen nuclei is 42.58 MHz/T, whereas other MR visible nuclei will possess different gyromagnetic constants. Hence, under the same magnetic field strength, magnetic moments of each nuclei will precess at different frequencies. [6].

At thermal equilibrium, a large proportion of the magnetic moments of the spins align with B_0 since it corresponds to a lower energy state, which results in the net magnetization (M_0) which is referred to as longitudinal magnetization **(Figure 1.2)**. Moreover, as the strength of the magnetic field increases, the energy differential between low and high energy states increases. Hence, the number of low energy spins also increases (higher energy is required for the high energy spin), thus, the net magnetization increases [6,8].

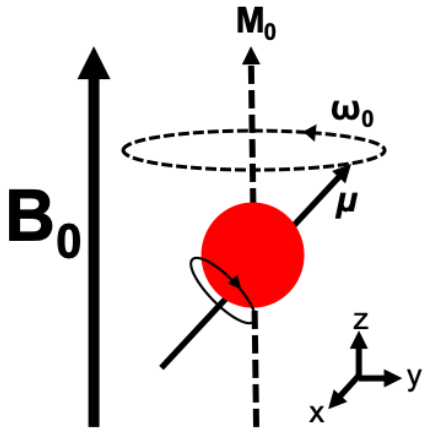

Figure 1.2**:** Precession of the magnetic moment (μ) of spinning ^{1}H nucleus at the Larmor frequency (ω_0). At thermal equilibrium under the magnetic field (B_0) a static net magnetization (M_0) is produced oriented in the longitudinal direction (z-oriented).

The radiofrequency (RF) coils produce pulses that generates an oscillating magnetic field, B_1. This field B_1, is applied perpendicular to the B_0 magnetic field, causing disturbance of the net magnetization. When applied at the frequency equal to the Larmor frequency, hydrogen nuclei in a "low energy state" gain energy and enter an

"excited state". On the other hand, hydrogen nuclei with "high energy state" release energy and return to the low energy state. Since there is a greater number of low energy spins, the net impact of the RF pulse is energy absorption. This effect of the RF pulse is known as the 'resonance effect' [6,9]. The application of RF pulse at the Larmor frequency for a defined time (sufficient that energy will be absorbed) tilts the net magnetization vector 90° (depends on the magnitude of the B_1 field and the duration) from where it lies in the x-y plane (transverse plane). The resulting magnetisation induces an electrical signal, which when emitted is detectable by a conductive receiver coil placed in close proximity [6,9,10].

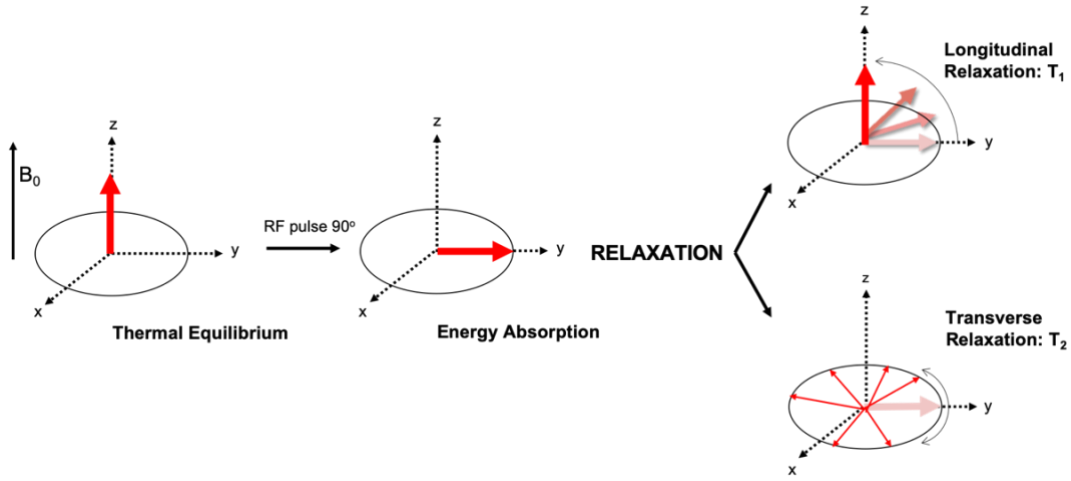

Figure 1.3: Longitudinal (T_1) and transverse (T_2) relaxation process. A 90° RF pulse along the x-axis, moves the net magnetization vector on the zy-plane towards the y-axis. Once the RF pulse is off, magnetic moments lose their coherence (out-phase; multiple vectors on the transverse plane), transverse magnetisation decreases (T_2 relaxation) and longitudinal magnetisation starts to recover (T_1 relaxation).

When the RF pulse is turned off, the net magnetization begins to relax back to the thermal equilibrium state and the magnetic moments of hydrogen nuclei start to precess out-phase, which is known as relaxation [4]. As a result, two forms of relaxation occur. The decay of the transverse component of magnetization is called transverse or spin-spin relaxation (T_2 relaxation). Secondly, the recovery of the longitudinal component of magnetization is known as longitudinal relaxation (T_1 relaxation) **(Figure 1.3)** [4,10,11]**.**

1.1.2 Longitudinal (T_1) and Transverse (T_2) Relaxation Mechanism

The T_1 relaxation is a process of energy exchange between the spins and their surroundings, whereas spins return to their low energy state with a loss of energy to the surroundings. As a result, the net magnetization (after a RF pulse) returns to the thermal equilibrium as an exponential function with a time constant T_1 **(Figure 1.4)**. T_1, is the time taken for the recovery of the net magnetisation to 63% of its equilibrium. This relaxation time is dependent on the tumbling rate of the molecule that contains the hydrogen nuclei. Tumbling of the molecules produces a fluctuating magnetic field where proton of nearby molecules are exposed to this field. If the tumbling rate is close to the Larmor frequency, energy exchange is more favourable. For example, a free water molecule has a fast tumbling rate, therefore, it has a long T_1 relaxation time [4,8,10,11].

In contrast to T_1 relaxation, T_2 relaxation depends on the energy transfer between the spins. Worthy of note, with the absence of the B_1 field, the magnetic moments

of hydrogen nuclei precess out-phase (incoherent), however, following a RF excitation pulse, the spins gain coherence, in other words, they precess in-phase in the transverse plane. Over time, they lose their coherence and precess out-phase due to the interaction of the neighbouring magnetic moments (T_2 relaxation) and the inhomogeneities in the B_0 magnetic field (T_2^* relaxation involves both causes). As a result, the transverse component of the net magnetisation decreases exponentially and eventually disappears **(Figure 1.4)**. The time constant, T_2, describes the time taken for the decay of the transverse component of the magnetisation to reach 37% of its initial value [4,10]. Given that spin-spin interactions affect the T_2 relaxation time, in the presence of the free water molecules spins move rapidly and far away from each other, thus there is less interaction between spins, which leads to long T_2 relaxation. On the other hand, water-based tissues that have solid and large molecular content (e.g.: muscle, grey matter) have shorter T_2 relaxation times, because movement of bound water molecules are slower thus spins tend to interact with each other [4,10,12].

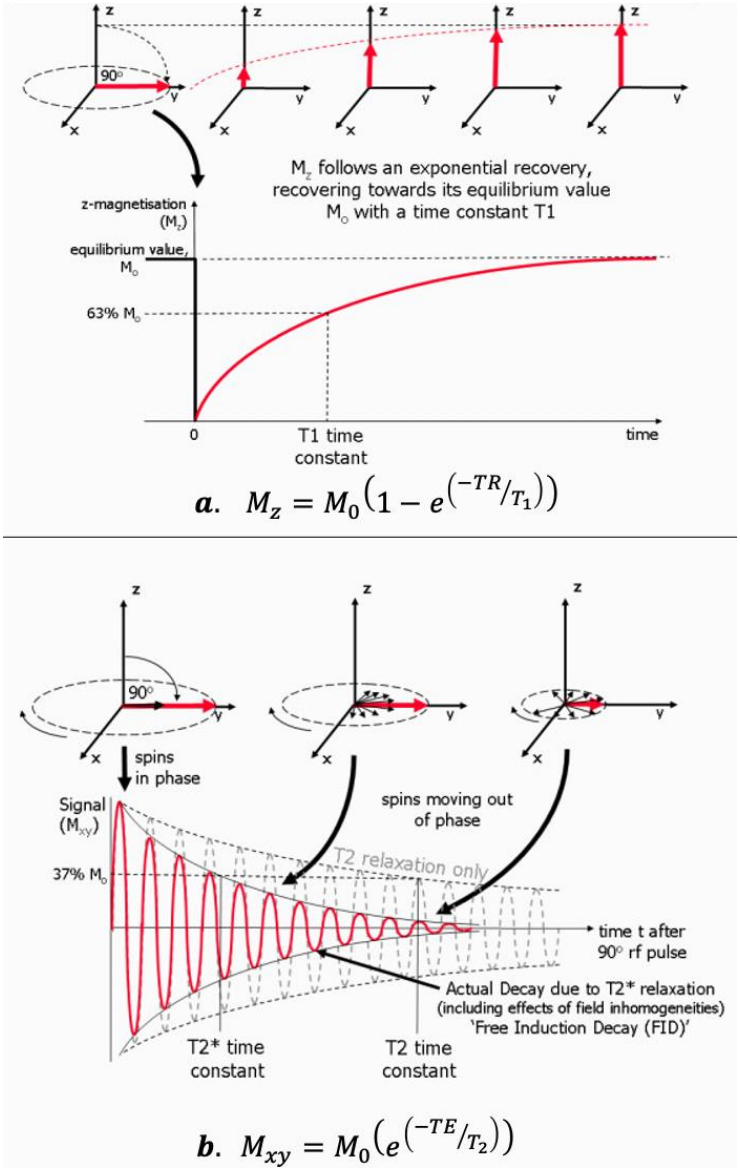

Figure 1.4: Exponential processes of longitudinal (M_z) and transverse (M_{xy}) magnetization with time constants T_1 and T_2 respectively. Indicated T_2^* relaxation is combining the effects of the T_2 relaxation and the de-phasing that occurs due the inhomogeneities (local variations) in the magnetic field. TR is repetition time, time between two RF pulses; TE is echo time, time interval from RF pulse to the reached maximum signal amplitude; T_1 is longitudinal relaxation time, T_2 is transverse relaxation time; M_0 is net magnetization at thermal equilibrium. Adopted from Ridgway *et al.* [10]

1.2 MRI Contrast Agents

One issue with MRI is lack of sensitivity, therefore a wide variety of contrast agents (CA) have been developed in order to enhance the signal to provide a substantial diagnostic sensitivity for various neoplastic, inflammatory and functional abnormalities [13]. These contrast agents can improve both the sensitivity and specificity of MRI signals, and consequently expand non-invasive diagnosis [14,15].

The MRI contrast agents are not directly visible in MRI *per se*, but they change the MRI signal of tissues by altering their intrinsic parameters such as T_1 and T_2 relaxation times. Moreover, some extrinsic parameters such as strength of the magnetic field, choice of pulse sequence and length of the parameters like TR (repetition time) and TE (echo time) are also important to consider during the MR imaging [13,16].

Contrast agents that contain paramagnetic metal ions such as Gd^{3+}, reduce the longitudinal relaxation time (T_1) of surrounding water protons. As a result, short T_1 relaxation time appears to show bright contrast in T_1-weighted images [7]. On the contrary, transverse contrast agents are providing negative contrast in T_2-weighted images and commonly superparamagnetic materials such as large iron oxide particles are used. Pertinently, the vast majority of clinical MRI studies use gadolinium (Gd) based contrast agents (GBCAs) [7,14,16,17].

1.2.1 Relaxivity

The efficiency of the T_1 or T_2 CAs are quantified by their longitudinal (r_1) and/or transverse (r_2) molar relaxivities. Relaxivity measures the change in relaxation rate (R_1 and R_2; equivalent to $1/T_1$ and $1/T_2$) in the presence of the CA. This relaxivity is expressed in units of $mM^{-1}s^{-1}$ [16–19]. Therefore, relaxivity, r_1 or r_2, is a constant that shows the ability of a CA to shorten the T_1 and/or T_2 relaxation times of the water protons. Additionally, r_1 and r_2 values of CAs are dependent on the external magnetic field, temperature, size and chemical structure of the CA and the water accessibility into the magnetic centre [16,20–22]

In the human body, water generally demonstrates 5-20 times longer T_1 relaxation than T_2 [14]. Accordingly, contrast agents can affect both T_1 and T_2 relaxation times of the surrounding water protons, thus, the r_2/r_1 ratio is used to define whether the contrast agent is a potential longitudinal (T_1) or transverse (T_2) contrast agent [23]. For instance, low molecular weight paramagnetic complexes have low r_2/r_1 ratio which is close to 1 and are classified as longitudinal contrast agents. On the other hand, iron oxide nanoparticles have very high r_2/r_1 ratio and therefore they are referred to as transverse or T_2 contrast agents [14,23].

1.2.2 Paramagnetic Contrast Agents

The gadolinium ion (Gd^{3+}) is the most commonly selected lanthanide ion used in MRI as a paramagnetic contrast agent. This is because Gd^{3+} has 7 unpaired electrons in its *f* subshell and hence a high spin quantum number (S=7/2). It possesses high magnetic

moments and a long electronic relaxation time [24]. Gadolinium (Gd) is not the only element that can serve as a paramagnetic contrast agent. For example, transition metals such as manganese ion (Mn^{2+}) are important paramagnetic agents. Mn^{2+} has 5 unpaired electrons in its *d* subshell and exhibits a high magnetic moment. To date, there are only two Mn^{+2} based contrast agents that have been previously approved for clinical use: a liver-specific [Mn]DPDP (Teslascan®) and $MnCl_2$ based oral contrast agent (LumenHance®). However, both of these contrast agents have been withdrawn [25]. In general, Mn complexes have demonstrated poor stability and kinetic inertness compared to Gd complexes [14,26]. This is one of the key reasons that the development of Mn-based contrast agents has been unable to substitute GBCAs.

The ionic radii of the trivalent Gd^{3+} is 1.05 Å which is close to the ionic radii of the divalent Ca^{2+} (1.12 Å) [27]. Consequently, free Gd^{+3} ions can outcompete Ca^{2+} ions in biological systems that use Ca^{2+} such as voltage gated calcium channels [28]. Moreover, free forms of Gd^{3+} can replace endogenous metals like zinc and accumulate Gd^{3+} in the liver, lymph nodes and bones [13,29]. Hence, free Gd^{+3} ions are toxic in the body and in order to reduce this toxicity it is important to strongly chelate Gd^{3+} ions with biocompatible ligands. Typically, ligands that are used for chelation are composed of multidentate ligands that have eight donor atoms such as amines or carboxylates [14,28,30–32].

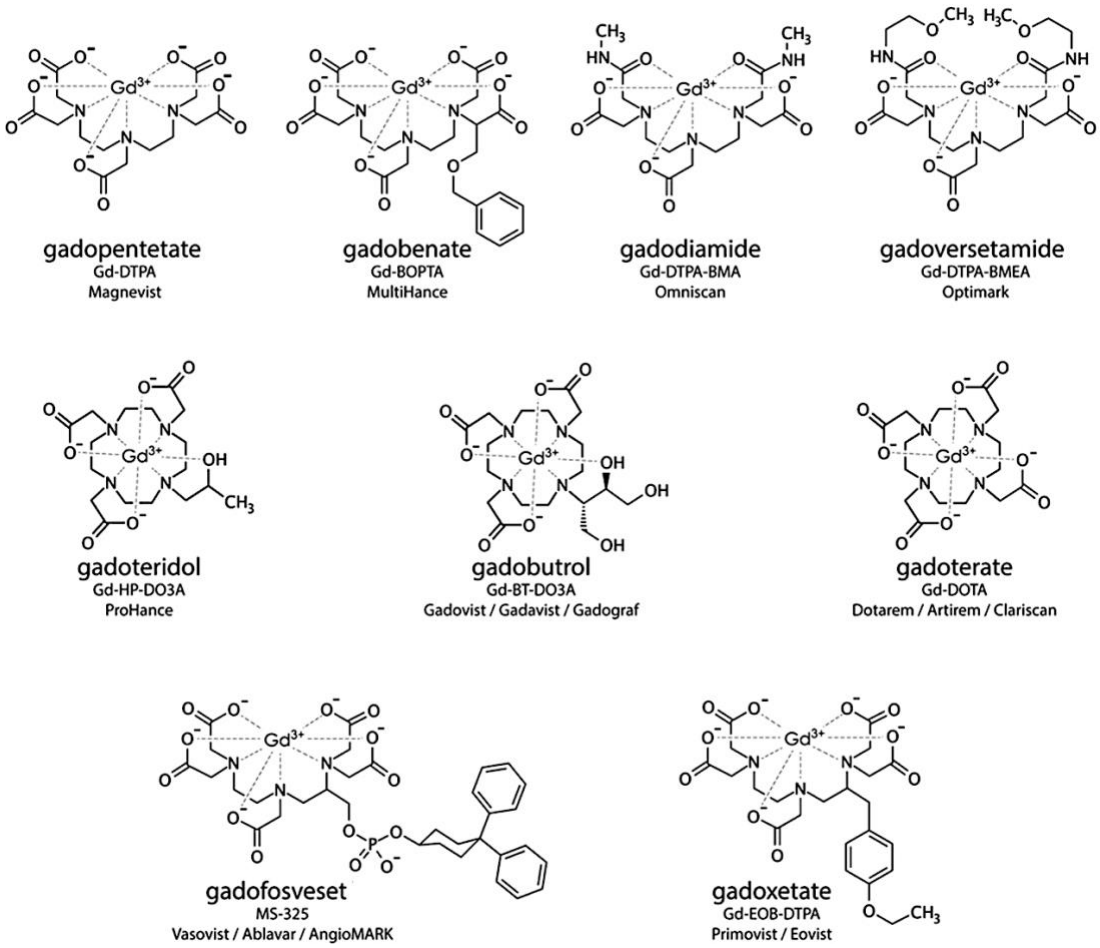

Figure 1.5: Structures of commercial gadolinium-based contrast agents including linear, macrocyclic and protein binding (primarily albumin) paramagnetic contrast agents. Adopted from McDonald *et al.* [33]

The unpaired electron spins of the Gd^{3+} ions induce longitudinal relaxation in nearby water protons by generating a fluctuating magnetic field [27]. The T_1 relaxation of GBCAs is explained by the two main mechanisms: inner-sphere relaxation which is the relaxation of the water molecules directly coordinated in the paramagnetic centre and; outer-sphere relaxation which is the relaxation of the water molecules in the second coordination sphere and beyond, i.e. bulk water [16]. There are several

parameters that govern relaxation, such as: **1.** the number of the water molecules in the inner coordination sphere (q); **2.** the mean of the residency time of the inner sphere coordinated water molecules (τ_M), which is the inverse of the water exchange rate (k_{ex}) and **3.** the rotational correlation time (τ_R) **(Figure 1.6)** [16,34,35]. Increasing the number of the water molecules coordinated to the inner sphere of the Gd^{3+} chelate, in other words a higher hydration number (q), would increase the T_1 relaxivity. However, coordinating more than one water molecule results in reduced kinetic and thermodynamic stability that can cause toxicity [31,36]. Accordingly, Gd^{3+} ions are commonly chelated with octadentate ligands to form GBCAs with either linear structures such as DTPA (diethylenetriamine pentaacetic acid) or macrocyclic structure such as DOTA (tetraaza-cyclododecane tetraacetic acid) as demonstrated in **Figure 1.5** [14,28,30–32]. This allows to retain one water molecule in the inner coordination sphere of the Gd^{3+} ion (q=1) which is crucial for enhancement of the T_1 relaxivity [28,31]. As a consequence of chelating Gd^{3+} with ligands of DOTA and DTPA, the water exchange rate slows down by more than 200-fold the rate of the free Gd^{3+} ions ($Gd(H_2O)_8^{3+}$), which was determined by ^{17}O NMR by Micksei *et al*. [28,37]. The τ_R parameter describes the tumbling of the Gd-complex that creates the fluctuating magnetic field which results in the relaxation of the water molecules [16,34,36] **(Figure 1.6)**. A tumbling rate close to the Larmor frequency improves the relaxation however, low molecular weight GBCAs tumble in the gigahertz (GHz) range whereas Larmor frequency of the clinical scanners are in the megahertz (MHz) range (i.e. at 3 T proton Larmor frequency is 127.74 MHz) [34]. Therefore, one of the important strategies to improve the T_1 relaxivity is to increase the rotational correlation time by increasing the size of the contrast agents. One of the approaches was the

development of the MS-325 (gadofosveset trisodium) **(Figure 1.5)**. This is a Gd-based blood pool contrast agent that prolongs plasma half-life by binding to human serum albumin (HAS) and increases the T_1 relaxivity of the water protons in plasma [22]. The rotational correlation time of MS-325 increases 60 to 100 fold after binding to the HAS which corresponds to the high T_1 relaxivity **(Table 1.1)** [38,39].

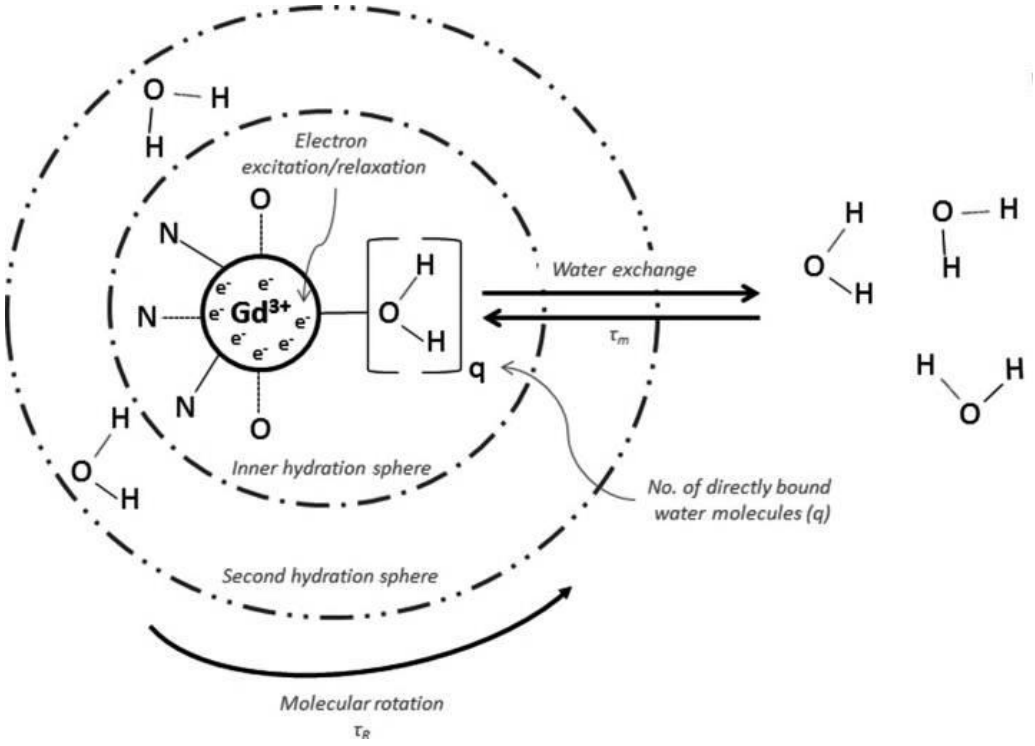

Figure 1.6: Schematic representation of inner and second hydration sphere water interactions with gadolinium including associated parameters; τ_M: water residency time, τ_R: rotational correlation time and q: hydration number. Adopted from Lohrke *et al*. [30]

Trade Name	Name of the Chemical	Generic Name	Applications	Class/ Charge	r_1 (3 T in plasma, 37°C)	Approval	Market Availability
Dotarem®	[Gd]DOTA	gadoterate meglumine	ECF	Macrocyclic/Ionic	3.5 $mM^{-1}s^{-1}$	1989 (EU) 2013 (US)	available
Prohance®	[Gd]HPDO3A	gadoteridol	ECF	Macrocyclic/ Non-ionic	3.7 $mM^{-1}s^{-1}$	1992	available
Gadovist® (EU) Gadavist® (US)	[Gd]DO3A-butrol	gadobutrol	ECF	Macrocyclic/ Non-ionic	5.0 $mM^{-1}s^{-1}$	1998 (EU) 2011 (US)	available
Magnevist®	[Gd]DTPA	gadopentetate dimeglumine	ECF	Linear/Ionic	3.7 $mM^{-1}s^{-1}$	1988	suspended
Omniscan®	[Gd]DTPA-BMA	gadodiamide	ECF	Linear/Non-ionic	4.0 $mM^{-1}s^{-1}$	1992	suspended
Optimark™	[Gd]DTPA-BMEA	gadoversetamide	ECF	Linear/Non-ionic	4.5 $mM^{-1}s^{-1}$	1999	suspended
Multihance®	[Gd]BOPTA	gadobenate dimeglumine	primarily ECF, liver	Linear/Ionic	5.5 $mM^{-1}s^{-1}$	2004	limited to use for liver
Ablavar® Vasovist®	MS-325	gadofosveset trisodium	blood pool	Linear/Ionic	9.9 $mM^{-1}s^{-1}$	2005 (EU) 2008 (US)	no longer available
Primovist® (EU) Eovist® (US)	[Gd]EOB-DTPA	disodium gadoxetic acid	liver	Linear/Ionic	6.2 $mM^{-1}s^{-1}$	2005 (EU) 2008 (US)	limited to use for liver

Table 1.1: Properties of marketed Gadolinium based contrast agents (GBCAs). Market availability of GBCAs determined from The European Medicines Agency (EMA) decision EMA/457616/2017; r_1 is the T_1 (longitudinal) molar relaxivity that was measured by Rohrer *et al.* at 37 °C in plasma using 3 T MRI. ECF = Extracellular fluid [14,22,30].

Although chelation is a limiting factor in enhancing the T_1 relaxation due to the lower hydration number and slower water exchange rate, it remains an important design requirement to avoid the toxicity of free Gd^{3+} in the body [28,35]. Ligands that form Gd-complexes must be thermodynamically and kinetically stable especially for *in vivo* use. Macrocyclic ligands like DOTA and HPDO3A have been used to chelate

gadolinium and display high kinetic and thermodynamic stabilities where the Gd^{3+} is caged in the preorganised cavity of the ligand. On the other hand, some linear complexes have shown thermodynamic stability (e.g [Gd]DTPA) similar to macrocyclic complexes. The kinetic stability of such complexes is very low, particularly bis-amide derivatives of DTPA (e.g. [Gd]DTPA.BMA). [Gd]DTPA.BMA can easily lead to transmetallation by endogenous ions [29,40]. Transmetallation is the exchange of a metal of an organometallic compound with another metal species [41]. Accordingly, Laurent *et al.* have assessed the transmetallation of the macrocyclic and linear GBCA *in vitro* by measuring the longitudinal relaxation rates of solutions containing GBCAs and 2.5 mM $ZnCl_2$ in a phosphate buffer at 37°C, pH=7. Thus, as transmetallation takes place, the released Gd^{3+} precipitates as $GdPO_4$. The results of that transmetallation study show that macrocyclic ligands are highly stable (no reaction for 4 days) whilst the linear Gd-complexes are highly sensitive to transmetallation by Zn^{2+} [42].

In 1988, world's first contrast agent, Magnevist® ([Gd]DTPA) was launched and since then, more GBCAs have been developed and become available for clinical use **(Table 1.1)** [30]. Initially, thermodynamic stability was one of the most important factors for the development of the new contrast agents. Hence, kinetic inertness was not fully appreciated and studied until the emergence of the safety concerns [43]. In 2006, Grobner *et al.* have shown the link between the nephrogenic systemic fibrosis (NSF) and GBCA. NSF is a systemic fibrotic disorder that was observed in patients with renal impairment after administering linear GBCA, in particular [Gd]DTPA.BMA [44]. The

majority of the GBCAs are excreted renally, but patients with renal impairment have low glomerular filtration rate so GBCA retain for a longer period of time, which raises the occurrence of transmetallation taking place [29,45]. Furthermore, Kanda *et al.* has demonstrated the detection of the residual of gadolinium in the brain of patients with normal renal function who had previously administered GBCA repeatedly [46]. The tendency of the linear contrast agents to leach Gd^{3+} under biological conditions and the associated potential toxicity due to transmetallation (i.e. gadolinium deposition in the skin, bone and liver in long-term studies) has resulted in the limitation of their use or withdrawal from the European market due to safety concerns [47,48]. In the USA, the Food and Drug Administration (FDA) has requested new class warnings and patient medication guides to be produced for GBCAs, informing patients of the potential toxicity of these products [48–50]. As a result, due to the recent concern over the link between nephrogenic systemic fibrosis and retention of released Gd^{3+} in tissues has meant that stronger chelation with closed ring or cage ligands are now preferred [29] Therefore, since regulatory bodies such as EMA have restricted the use of linear GBCAs, macrocyclic GBCAs are commonly used to enhance tissue visibility and differentiation in clinical MRI (e.g. Gadovist® or ProHance®, see **Figure 1.5, Table 1.1**). In conclusion, the macrocyclic GBCAs' T_1 molar relaxivity is comparable to the linear GBCAs. Their superior safety performance due to their stability decreases the transmetallation concerns but does not eliminate them, necessitating further studies to improve the contrast enhanced MRI imaging modality.

1.2.3 Superparamagnetic Contrast Agents

Superparamagnetic iron oxide nanoparticles (SPION) contrast agents are colloidal materials consisting of iron oxide particles which exhibit high magnetic susceptibility. The iron oxide core is usually made of magnetite (Fe_3O_4) or maghemite (γFe_2O_3) and surface is coated with bio-compatible materials such as dextran, carboxymethylated dextran or polyethylene glycol (PEG) to form colloidal suspension in order to avoid toxicity caused by aggregation [51–53]. Surface coating is not only to stabilise the particles but can be engineered further to provide various or multiple functional groups [54].

According to their sizes superparamagnetic contrast agents can be categorised into three groups: first, ultra-small superparamagnetic iron oxide (USPIO) particles with a diameter of less than 50 nm; second, superparamagnetic iron oxide (SPIO) nanoparticles with a diameter in the range of 50 nm to 1 µm; last, micron sized iron oxide particles with diameter larger than a micron (MION) [14,53]. T_2 molar relaxivity of the superparamagnetic agents are affected by the particle size, generally T_2 relaxivity improves as the particle size increases. However, the iron oxide crystalline core loses its superparamagnetic property as size diameter reaches beyond 15 nm [55].

SPIONs can enhance both T_1 and T_2 relaxations of the tissues but the effect on T_2 is more pertinent due to the high r_2/r_1 ratio [14]. Therefore, as SPIONs shorten the transverse (T_2) relaxation of water protons, they provide negative signal intensity

(darkened) in T_2 weighted images. SPION-enhanced MR imaging is able to visualise macrophage rich tissues such as liver, spleen, lymph nodes or bone marrow due to the preferential uptake of the CA by the reticuloendothelial system (RES) [52,53].

Superparamagnetic nanoparticles possess very large magnetic moment compared to individual coordination complexes (gadolinium chelates) under the external magnetic field. This large magnetic moment (magnetic susceptibility) contributes to the local changes in the magnetic field that leads to inhomogeneity of the local magnetic field. Consequently, the spins of the surrounding protons of the water molecules de-phase and create a shorter T_2 relaxation [14,16]. Furthermore, if the magnetic susceptibility is severe, this can cause geometric distortion or obliteration of organ boundaries on MR images [16,53].

Trade Name	Name of the Compound	Generic Name	Applications	Hydrodynamic Size (nm)/ Coating agent	Half-life in humans (hours)/ Dosage (µmol Fe/kg)	Approval
Feraheme®	Code 7228	Ferumoxytol (USPIO)	Blood pool agent, brain lesions, liver, lymph nodes, blood vessels	30/ Carboxylmethyl-dextran T10	10-14/18-74	Aprroved for iron replacement only, but off-label use
Clariscan®	NC-100150	PEG-feron (USPIO)	Blood pool agent	20/ Pegylatedstarch	6/36 (oral)	Used in clinical trials but has been discontinued
Endorem® (EU); Feridex® (US)	AMI-25	Ferumoxides (SPIO)	Liver	120–180/ Dextran T10	2/30	Approved but withdrawn from major markets
Resovist®	SH U 555 A	Ferucarbotran (SPIO)	Liver	60/ Carboxydextran	2.4-3.6/8/12	Approved but withdrawn from major markets
Sinerem® Combidex®	AMI-227	Ferumoxtran-10 (USPIO)	Metastatic lymph nodes, macrophage imaging.	15–30/Dextran T10, T1	24-36/45	Used in clinical trials but has been discontinued

Table 1.2: Properties of the superparamagnetic nanoparticles (SPIONs) that have been in the market or clinical investigations [14,16,56]

Since mid 90s several SPIONs have been developed and approved for MR imaging, as are listed in **Table 1.2**. However, most of these contrast agents have either been withdrawn from the major markets or had clinical developments discontinued after clinical trials such as Ferumoxides (Endorem® (EU), Feridex® (US and Japan)) and Ferucarbotran (Resovist® (EU and Japan)) [14,54]. By extension, Ferumoxytol (Ferahem®) is an USPIO which is an approved therapy for iron deficiency anaemia. However, the off-label use of Ferumoxytol for MRI was investigated and reported by clinicians and researchers as a potential MRI contrast agent throughout the body including the CNS, liver, lymph nodes and the cardiovascular system. The size of nanoparticles is around 30.0 ± 2 nm and the T_1 relaxivity (r_1) and T_2 relaxivity (r_2) were 15 $mM^{-1}s^{-1}$ and 89 $mM^{-1}s^{-1}$ respectively at 37 ^oC in water at 1.5 T MRI [57]. As a result, SPIONs have received great attention over the years due to their MRI sensitivity and their malleability with respect to surface modification, caveated by the need for further studies to assess the contrast agent efficiency as well as the potential toxicities, to allow for optimal clinical applications.

1.2.4 New Generation Paramagnetic Contrast Agents

MRI is a very valuable imaging modality that provides great spatial and temporal resolution with deep tissue penetration. As mentioned earlier, one of the drawbacks is low sensitivity. Therefore, several gadolinium-based contrast agents (GBCAs) have been introduced to the clinical practice and extensively used worldwide since 1988. GBCAs that were approved for clinical use were considered extremely safe when used in patients with normal kidney function at recommended dose until the point that great concerns started when Kanda *et al.* (2004) reported the gadolinium

deposition in patients with normal kidney functions [58]. The current concerns about GBCAs have moved the research towards the design and development of novel contrast agents with an improved safety profile and sensitivity.

One of the important approaches in developing novel GBCAs is to optimise them for high relaxivity enabling administration at a lower dose than the conventional clinical GBCAs. The approved dose for conventional extracellular fluid (ECF) GBCAs is in the range of 0.1 to 0.3 mmol/kg and the T_1 molar relaxivity values vary from 3.5 to 6.6 $mM^{-1}s^{-1}$ in blood plasma at 3 T [22]. Recently, a new low molecular weight (0.97 kDa) macrocyclic GBCA, gadopiclenol (P03277) has been developed with improved water accessibility (q=1.7) and reduced tumbling rate [59]. It has been reported that T_1 relaxivity of gadopiclenol is high in comparison to commercial contrast agent gadobutrol (Gadovist®) 11.6 vs 5.0 $mM^{-1}s^{-1}$ respectively at 3.0 T in human plasma. Moreover, an *in vivo* study in rats with hepatic colorectal cancer metastases also demonstrated that tumour contrast enhancement with gadopiclenol is significantly better than the Gadovist® at 9.4 T. Published studies show that gadopiclenol exhibit high kinetic stability and similar pharmacokinetic profile as conventional ECF GBCAs and it is currently undergoing human clinical trials [59,60].

Another approach for potential GBCAs is to design biochemically targeted agents to increase specificity to a molecular target and enhance local contrast. Developing targeted contrast agents is challenging but has a large impact on detection, staging, prognosis and treatment of various diseases, such as cancer, Alzheimer's or

cardiovascular disease. These targeted contrast agents help in understanding the complex biology behind each [14]. GBCAs can be conjugated with targeting moieties such as antibodies, proteins, peptides and small molecules in order to detect the desired biomarker [61]. There are a number of important factors that need to be considered for designing targeted GBCAs; in particular, affinity and specificity towards the targeted biomarker are major considerations [61]. It is important to note that sensitivity of the MRI is within the range of μM, thus biomarkers that are in the pM-nM range are not suitable for imaging with targeted GBCAs [62].

As discussed in one of the previous sections, human serum albumin (HAS) is a protein that presents in the blood at high concentration. Among the clinically approved contrast agents, MS-325 (gadofosveset trisodium) is a blood pool agent that noncovalently binds to the albumin with high affinity (bound fraction up to 90%) and enhances the relaxivity [63,64]. However, production of this contrast agent has been discontinued since 2017 due to the poor sales [61].

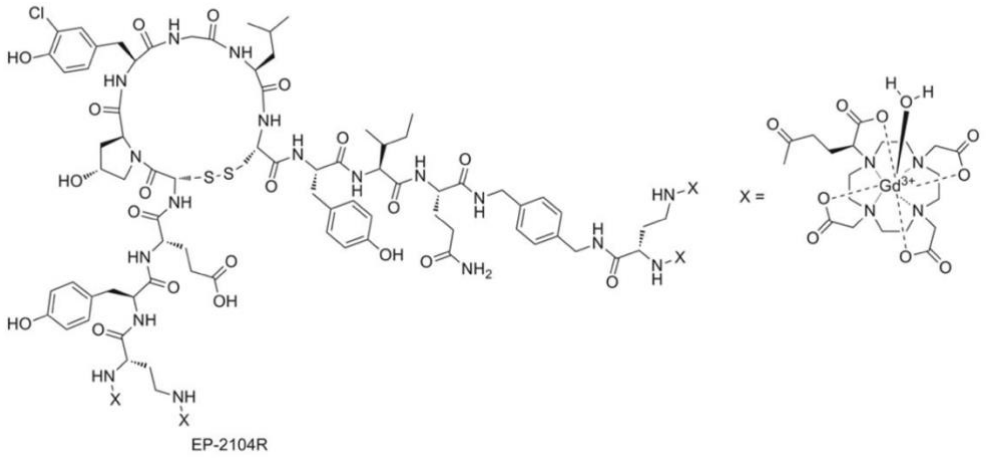

Scheme 1.1: Structure of EP-2104R, a fibrin-targeting GBCA. Adopted from De Leõn-Rodríguez *et al.* [43]

MRI imaging of fibrin is an example of the potential impact of targeted GBCAs. Fibrin is an important biomarker to detect thrombus and has been studied comprehensively in the literature [14,32,43]. It is the most highly abundant protein of thrombus (blood clot) that presents at high concentrations (20–100 µM) and it is not found in plasma or healthy tissues [43]. EP-2104R (Scheme 1.1) is a promising fibrin targeted GBCA that can detect thrombus by binding to fibrin, and consists of a small peptide carrying 4 chelators of [Gd]DOTA [65]. According to findings of Overoye-Chan et al. EP-2104R has great specificity for fibrin over fibrinogen (over 100-fold) and serum albumin (over 1000-fold) both *in vitro* and *in vivo*. The T1 relaxivity of EP-2104R is 71.4 $mM^{-1}s^{-1}$ (17.4 $mM^{-1}s^{-1}$ per $Gd^{3+)}$ when it binds to the fibrin at 37 ^{o}C at 1.4 T [65]. This T1 relaxivity enhancement can be also attributed to slow rotational tumbling when the contrast agent is bound to fibrin. EP-2014R was progressed to clinical trials based on its potential in preclinical studies [43,61,66].

Another strategy to increase the utility of imaging contrast agents is to slow down the rotational motion of the complex by increasing the molecular weight. This approach has led to design and synthesis of macromolecular GBCAs that can have a high payload of Gd^{3+} ions within the same unit. These contrast agents are typically based on the incorporation of multiple derivatives of [Gd]DOTA/[Gd]DTPA complexes onto macromolecules or nanoparticles. Examples include polymers, dendrimers, micelles and liposomes and they have been explored in the literature extensively [67–69]. Such Gd-based macromolecules/nanoparticles have promising potential as next generation MRI agents due to their ability to carry large payload of Gd^{3+} ions; to tune the physicochemical properties that can affect the pharmacokinetics, tissue distribution and to functionalise the surface with specific targeting agents [69]. Besides the versatile composition, their increased size compared to low molecular contrast agents can lead to an enhancement of the T_1 relaxation due to a slower rotational correlation time (τ_R) [68,69].

1.2.5 Paramagnetic Liposomes

The scope of this report is based on paramagnetic liposomal MRI contrast agents. Liposomes are spherical unilameller nanoparticles that are composed of a lipid bilayer and an aqueous inner core. Typically, the size of such self-assembled vesicles can vary from 50 to 250 nm [70,71]. Liposomes provide an offset to the sensitivity issue of MRI due to their high payload of Gd^{3+} that can influence relaxivity. As highlighted in previous sections, there are several parameters that can affect the relaxivity, including water accessibility (hydration number), water exchange rate and rotation correlation time which is strongly driven by the composition and the size of

the paramagnetic liposomes [20]. However, optimal relaxivity properties do not necessarily mean that paramagnetic liposomal composition is optimal in terms of pharmacokinetic and biodistribution profiles. Therefore, it is important to keep the appropriate balance between the parameters in order to minimize the potential toxic side effects. Although, liposomes generally exhibit longer circulation times in the body compared to small molecule contrast agents, tuning such properties is feasible with liposomal formulations to develop effective and safe MRI contrast agents [69,70]. There are two approaches to develop paramagnetic liposomes as MRI contrast agents; either encapsulation of the hydrophilic paramagnetic agents inside the aqueous core of the liposome or incorporation of the paramagnetic functionalized lipid into the lipid membrane [70,71].

1.2.5.1 Paramagnetic Liposomes Encapsulating Contrast Agents

The high versatility of liposomes enables them to carry MRI contrast agents. Hydrophilic small molecules (like clinically approved GBCAs) can be easily encapsulated within the aqueous core of the liposomes. Although the encapsulation of hydrophilic gadolinium complexes increases the Gd^{3+} payload in the aqueous core, this approach affects the interaction of gadolinium complexes with the surrounding bulk water protons. The water permeability of the lipid membrane potentially restricts water access to the intraliposomal compartment that contains the contrast agents. This results in reduction of the longitudinal relaxivity (r_1) [70–72]. The permeability of the lipid membrane is dependent on the lipid composition. An increase in the permeability of the membrane may affect the water flux across the membrane which can consequently increase r_1 [71]. These liposomes have been used

beneficially for monitoring the drug release in response to temperature due to the membrane transition properties that alter the T_1 relaxivity [68,73,74]. In particular, Wang *et al.* have designed [Gd]DTPA.BMA (Omniscan®) encapsulated thermosensitive liposomes to understand the liposome's viability as a carrier of a contrast agent. This acted as a proxy for drug release during tumour treatment comprising chemotherapy combined with hyperthermia. The study takes advantage of the increased permeability of the liposome near the phase transition temperature (T_m) that results in increased T_1 relaxivity triggered by the release of encapsulated paramagnetic contrast agent [75]. The change in the relaxation time was observed *in vitro* within a specified temperature range (30-50 ^oC) at multiple time points over 1 h interval at 0.47 T. The outcomes of the study imply that temperature sensitive liposomes are stable below 37 ^oC for 1 h since T_1 relaxation time slightly decreased, however T_1 began rapidly decreasing from 38 - 44 ^oC, which aligned with 44 ^oC being the T_m point according to the differential scanning calorimetry (DSC) findings [75].

Similarly, de Smet *et al*. have reported a thermosensitive liposomal formulation encapsulating both doxorubicin and 250 mM of a paramagnetic contrast agent [Gd]HPDO3A (ProHance®). In this system, the change in the molar relaxivity as a function of temperature allows monitoring of the drug release. According to the *in vitro* study, the rapid release of the doxorubicin and paramagnetic contrast agent from the liposomes was observed near the melting phase transition temperature at 42 ^oC (T_m defined as the offset of the DSC peak) which was also confirmed with a sharp increase in r_1 at 7 T (30-50 ^oC heating interval) [76,77]. A proof of concept study

was also carried out in 9L gliosarcoma tumour bearing rats using clinical 3 T MRgFUS system **(see Chapter 3.1.10).** The temperature-triggered release of the paramagnetic contrast agent was monitored with T_1 mapping of the tumour. A linear correlation between the change in longitudinal relaxation time (ΔR_1), doxorubicin and gadolinium concentration was observed in the tumour tissues [77].

1.2.5.2 Paramagnetic Liposomes Incorporating Contrast Agents

The incorporation of lipidic paramagnetic contrast agents (mainly Gd-functionalised lipids) into the liposomal bilayer is another approach to enhance the r_1. This approach demonstrates an improved T_1 molar relaxivity compared to the aforementioned encapsulating approach due to paramagnetic metal complexes on the outer surface having easy access to the bulk water [19,70,78]. However, Gd-complexes in the inner leaflet (facing the aqueous cavity) will have less contribution to the overall T_1 relaxivity due to the limited water exchange over the lipid membrane [79]. Nevertheless, Gd-chelates located in the outer sphere are exposed to the slow rotational motion of the liposomes which contribute to the overall T_1 relaxivity [70]. Accordingly, over 20 years ago Kabalka *et al.* first demonstrated the incorporation of [Gd]DTPA derivatives (DTPA-phosphatidyl ethanolamine, DTPA.PE, or DTPA-stearylamine, DTPA.SA) into the liposome surface to enhance the T_1 relaxivity [80,81]. The [Gd]DTPA.bis(stearylamide) ([Gd]DTPA.BSA) was used in their studies and became a commercially available MRI lipid [79,82–84].

In light of this, Kamaly *et al.* have synthesized a macrocyclic Gd based lipid, designed for liposomal MRI contrast agent, [Gd]DOTA.DSA. MRI studies of [GdDOTA.DSA lipid in aqueous solution (micellar structure) were performed and T_1 relaxation time did

not significantly differ from the commercial contrast agent, Magnevist®, at the clinically relevant dose of 0.5 mM at 4.7 T. Furthermore, liposomes were formulated with the same lipid [Gd]DOTA.DSA and the T_1 relaxivity was found to be 4.10 ± 0.34 $mM^{-1}s^{-1}$ at 4.7 T [83]. Another study by Erdogan *et al.* has also shown that gadolinium loaded polychelating amphiphilic polymers (multiple gadolinium chelating groups [Gd]DTPA on the main chain as side chains; [Gd]-loaded PAP) incorporated to the membrane of the polyethylene glycol (PEG) coated liposome significantly increase the T_1 relaxivity in comparison with monomeric [Gd].DTPA-phosphatidyl ethanolamine ([Gd]DTPA.PE) incorporated to liposomes. A cancer-specific monoclonal anti-nucleosome 2C5 antibody (mAb 2C5) was also attached to the liposome surface for the specific and efficient tumour MRI [85,86].

Hak *et al*. have synthesized [Gd]DOTA.DSPE and incorporated this in a liposomal formulation with the following lipids DSPC, PEG^{2000}-DSPE and cholesterol. The contrast agent efficiency and structural properties were characterised *in vitro* including the transmetallation with Zn^{2+} [79]. Nuclear magnetic relaxation dispersion (NMRD) studies showed that T_1 relaxivity was increasing with increased temperature due to the increased water exchange across the membrane. Accordingly, the T_1 relaxivity of the liposome (per Gd^{3+}) was 11.8 $mM^{-1}\,s^{-1}$ at 25 ^{o}C, 1.41 T whereas at 37 ^{o}C an increased T_1 relaxivity was observed, 12.8 $mM^{-1}s^{-1}$ at 1.41 T [79]. They have established that T_1 relaxivities of [Gd]DOTA and [Gd]DTPA (both around 4 $mM^{-1}s^{-1}$) are significantly lower than [Gd]DOTA.DSPE incorporated liposomes. Moreover, it

was reported that [Gd]DOTA.DSPE does not exhibit transmetallation with Zn^{2+} which is important from the safety point of view [79].

Another study by Silva *et al.* has designed gadolinium complexes with aliphatic chain ligands of *N-alkyl-N- methylglucamine*: with alkyl = octanoyl (L8) or decanoyl (L10) shown in **Scheme 1.2**. The Gd-complexes were synthesized with a stoichiometric ratio of 1:2; metal:ligands. The two aliphatic chains on adjacent coordinating arms were incorporated in the liposomal bilayer in order to reduce the local rotational motion of the Gd-complexes [87]. First, T_1 relaxivities of Gd-complexes (GdL8 and GdL10) in aqueous solution were compared with gadopentetate dimeglumine, [Gd]DTPA (Magnevist®). Results show that GdL8 and GdL10 have significantly higher r_1 than [Gd]DTPA; r_1 values are 11.90 ± 0.02 $mM^{-1} s^{-1}$, 12.30 ± 0.01 $mM^{-1} s^{-1}$ and 4.98 ± 0.03 $mM^{-1} s^{-1}$ respectively at 25 °C and 0.47 T [87]. Then, liposomes were prepared with soybean phosphatidylcholine and aforementioned Gd-complexes. T_1 relaxivity of GdL8 in liposome form 11.92 ± 0.03 $mM^{-1} s^{-1}$ was found to be similar to free GdL8, but an increased T_1 relaxivity was observed for GdL10 in liposome form; 15.5 ± 0.12 $mM^{-1} s^{-1}$ at 25 °C and 0.47 T [87]. Overall, the results show that both GdL8 and GdL10 complexes incorporated to liposomes have higher T_1 relaxivity compared to conventional contrast agents.

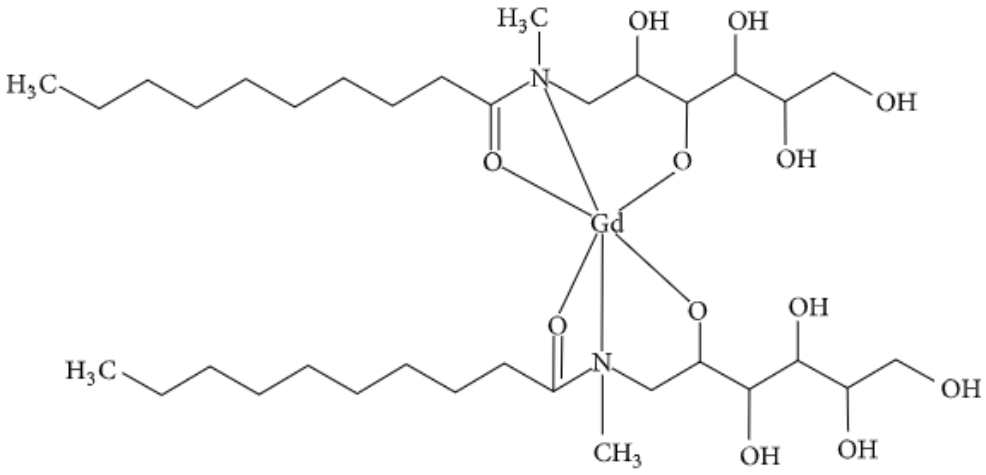

Scheme 1.2: Structure of the gadolinium complex with N-alkyl-N-methylglucamine ligand (used for GdL8 and GdL10). Adopted from Silva *et al.* [87]

Laurent *et al.* have studied the effect of the type and the length of the amphiphilic complexes on T_1 relaxivities of paramagnetic 1,2-*sn*-glycero-3-phosphatidylcholine (DPPC) based liposomes. They have observed that the best efficiency as an MRI contrast agent was obtained when the liposomal membrane was less structured due to the increased permeability [78].

1.2.6 Measuring the Concentration of Gadolinium

Magnetic Resonance Imaging (MRI) is a non-invasive imaging modality, which can be augmented/visualised by the administration of contrast agents (CAs), many of which contain chelates of gadolinium, e.g., Gadovist® [3]. Novel gadolinium based CAs take a variety of forms such as polymers, liposomes, dendrimers, and nanoparticles, and are being developed with improved efficacy for MRI. Given the variety of CAs with Gd-complexes, it is important to be able to differentiate their effectiveness.

Therefore, the molar relaxivities (r_1, r_2) are used to compare novel CAs. Since molar relaxivities are proportional to gadolinium concentrations, this necessitates gadolinium quantification. Furthermore, it is also important to quantify the kinetic liability of the gadolinium concentration *in vitro* and *in vivo* to determine the toxicity profile due to the increased awareness of the safety profile of the commercial GBCAs.

In this section, the most common methods for determining the gadolinium concentration of the liposomal contrast agents will be described based on the instrumental techniques that are used in the field.

Inductively Coupled Plasma-Mass Spectrometry (ICP-MS) and Inductively Coupled Plasma-Optical Emission Spectrometry (ICP-OES) are commonly used analytical techniques to detect gadolinium concentration [88]. Both ICP-hyphenated techniques are similar, and quantification is based upon use of calibration standards measured in matching a sample matrix for accuracy and precision [89]. In both techniques, samples are delivered into a nebuliser that produces aerosol and then the fine aerosol is introduced to argon plasma which has an extremely high temperature of 10000 K [90]. Both ICP-OES and ICP-MS can measure a variety of metals including Gd. ICP-OES detects the optical emission of the characteristic wavelength for individual elements, and ICP-MS the characteristic atomic mass of an element via mass spectrometry. In ICP-OES, interfering elements should be considered while selecting the wavelengths for the analysis [90]. Additionally, with ICP-MS analysis of metals like Gd, two types of interference needs to be considered:

1. isobaric interferences, Gd have several isotopes with varying natural abundance and different elements have identical mass can interfere with gadolinium ions such as $^{156/158/160}Gd$ and $^{156/158/160}Dy$; 2. polyatomic interferences, this occurs due to the polyatomic ions with the same ratio of mass/charge such as ^{155}Gd versus $^{138}Ba^{16}O^{1}H^{+}$ or $^{137}Ba^{18}O^{+}$ or $^{139}La^{16}O^{+}$ or $^{138}Ce^{16}O^{1}H^{+}$ [90].

Detection limits are in the parts per million (ppm) or parts per billion (ppb) range for ICP-OES, whereas ICP-MS can detect down to parts per trillion (ppt) depending on the metal [91]. However, ICP-MS is a more expensive and complex technique than ICP-OES [92]. For ICP-MS and ICP-OES, samples need to be more diluted and/or digested with strong acids/oxidants such as nitric acid (HNO_3), hydrochloric acid (HCl) and/or hydrogen peroxide (H_2O_2) to release metals from nanoparticles into aqueous media [89,92,93]. However, sample digestion may be incomplete and/or there is progressive sample loss with each step, resulting in measurement errors. Also, as these techniques are capable of measuring trace amounts, contamination at each step is a potential issue, and may originate from reagents, equipment and/or the environment [94,95]. Further, such sample preparation steps can be time-consuming and costly, and disadvantageous in quality assurance [96].

In this report I have proposed the use of Total Reflection X-Ray Fluorescence Spectrometry (TXRF) for detection of gadolinium content in nanoparticles for the development of liposomal MRI contrast agents. TXRF is another analytical technique which is a variation of the classical XRF (X-ray Fluorescence) spectroscopy that allows

analysis of trace elements in liquids, suspensions, powders or other solid samples [97–99]. TXRF can quantify the metal composition of multi-metal samples with negligible matrix effect if applied as an appropriately thin layer and particularly pertinent to contrast agents that are liposome-based. Samples are deposited in a thin layer of 0.1 – 10 µm to minimise matrix absorption and secondary excitation to satisfy the infinitely thin film model, such that a simple linear relationship exists between net intensity and concentration [100]. TXRF can simultaneously measure a wide range of elements and detection limits can be as low as a few parts per billion (ppb) in assorted samples including plasma [101]. One of the illuminating advantages of using TXRF is that the technique is relatively matrix-independent compared to ICP-hyphenated techniques. Quantification of gadolinium, whether conjugated to lipids (gadolinium lipids) that comprise the lipid bilayer or encapsulated in liposomes, require digestion to solubilise the gadolinium into aqueous solution for ICP-OES and ICP-MS analyses [97–99]. TXRF can obviate the need for solubilisation of gadolinium into aqueous solution and so sample preparation can be relatively straightforward. Thus, TXRF is a relatively easy and fast technique for gadolinium detection in liposomal contrast agents that only requires drying and homogenization of the samples after addition of an internal standard for accurate quantifications.

Commonly, ICP methods are used in the literature to determine Gd concentration of liposomal nanoparticles. As an illustration, Tilborg *et al.* have prepared dual labelled poly(ethylene glycol) (PEG) coated liposomes carrying both paramagnetic and fluorescent imaging agents. They have determined the time dependent

concentrations of Gd in blood and organ tissues of mice using ICP-OES and ICP-MS in order to study blood clearance kinetics and the biodistribution of their liposomal formulation. Samples were digested with acids under the heat and diluted further with ultrapure water [102]. In another study, Ray *et al.* have developed PEGylated thermosensitive liposomes encapsulating superparamagnetic iron oxide nanoparticles, [Gd]DTPA and drug mimetic molecule (fluorescein) to simultaneously monitor the drug release with real-time MRI imaging. They have quantified the iron and gadolinium concentrations of digested and diluted liposome samples by using ICP-OES [103]. There is a shortage of good examples of the usage of TXRF methods for Gd based liposomes. However, Telgmann *et al*. have proposed to use TXRF for the quantification of gadolinium in urine and blood samples. They have analysed urine and blood samples of patients that have administered Gd-based MRI contrast agents. They have validated their TXRF measurements with ICP-MS. Sample preparation for TXRF was straightforward and minimal for analysis of blood (only centrifuged), and urine samples without any excessive pre-treatments (such as digestion or dilution). However, sample preparation for ICP-MS was demanding for blood samples, where microwave digestion was employed [93]. They have concluded that TXRF is a simple and rapid alternative for gadolinium analysis in human body fluids that can be used in clinical laboratories.

1.3 Liposomes for Drug Delivery

Bangham *et al.* introduced liposomes as a part of the drug delivery system in the 1960s [104]. Since then the whole concept of the liposomal drug delivery has become essential for research and clinical applications [105]. Liposomes are carriers that are composed by lipids and vary in size from 0.025 μm to 2.5 μm in diameter and can incorporate a number of functional groups **(Figure 1.7)** [106]. A lipid self-assembly mechanism leads to the formation of spheres when one or more lipids are hydrated in aqueous media. Thus, liposomes have an aqueous core and a lipid bilayer which allows both hydrophobic and lipophilic molecules to be used as drug payload. There are several methods to prepare liposomes including thin film hydration, ethanol injections, sonication, membrane extrusion and freeze-thaw [106]. The properties of the liposomes alter with the lipid composition, surface charge and size, and the method that has been employed for preparation, which can provide unique therapeutic features for physical properties of tumours [106].

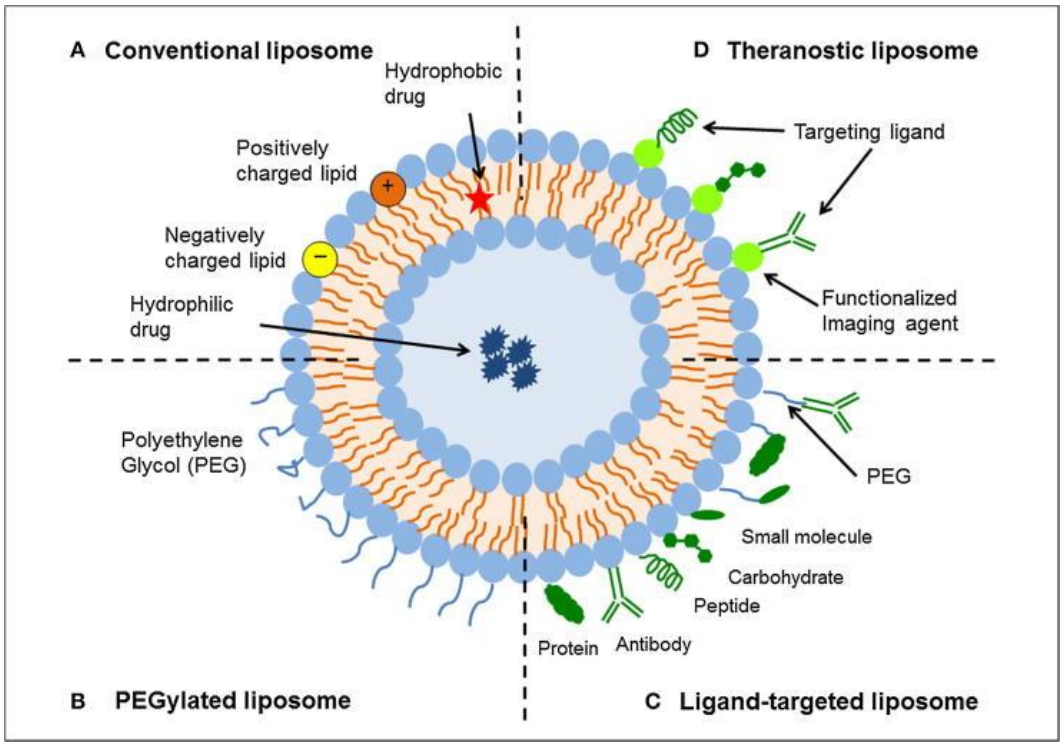

Figure 1.7: Schematic representation of the different types of liposomes used in drug delivery systems. Adopted from Sercombe *et al.* [107]

According to Pattni *et al.* liposomes have several advantages as a drug delivery carrier, such as high stability to hinder biological and chemical degradation throughout storage and clinical applications. Also, liposomes can change the pharmacodynamics of a drug by improving the body circulation and reducing toxicity related side effects [105]. Another important advantage is their flexibility regarding their chemical modification which allows various attachments on their surface for several purposes (ligands for targeting, probes for imaging etc.) [105]. Accordingly, these features of liposomes come with important clinical applications of liposomal drug formulations. In particular, Doxil® was a pioneer liposomal drug delivery system

which was approved by the Food and Drug Administration (FDA) in 1995 [108]. Several indications, AIDS-related Kaposi`s sarcoma, ovarian cancer, metastatic breast cancer and multiple myeloma, were approved by the FDA and EMA (European Medicine Agency). Doxil® shows superiority compared to free doxorubicin in pharmacokinetics, bio-distribution and reduced side effects; most particularly cardiotoxicity [108–110]. This doxorubicin loaded liposomal formulation benefits from the enhanced permeability retention (EPR) effect [111]. The EPR effect provides a passive targeted drug delivery by exploiting relatively leaky vasculature meaning enhanced permeability and sparse lymphatic drainage causing increased retention of nanoparticles in typical solid tumours [112]. **Table 1.3** shows some examples of liposomal drug combinations.

Trade Name	Drug	Indication	Ref.
Ambisome®	Liposomal amphotericin B	Presumed fungal infection	[113]
DaunoXome®	Liposomal daunorubicin	AIDS related Kaposi's sarcoma	[114,115]
DepoCyt®	Liposomal cytarabine	Neoplastic and lymphomatous meningitis	[116,117]
DepoDur®	Liposomal morphine sulphate	Pain management	[118]
Doxil®	PEGylated liposomal doxorubicin	Kaposi's sarcoma, ovarian and breast cancer	[108–110]
Epaxal®	Liposomal inactivated hepatitis A virus	Hepatitis A	[119]
Lipodox®	PEGylated liposomal doxorubicin	Kaposi's sarcoma, ovarian and breast cancer	[120]
Lipoplatin®	Liposomal cisplatin	Pancreatic, head and neck, breast cancer	[121]
Myocet®	Liposomal doxorubicin	Metastatic breast cancer	[117]
Marqibo®	Liposomal vincristine	Acute lymphoblastic leukaemia	[122]
Onco-TCS®	Liposomal vincristine	Non-Hodgkin lymphoma	[123]
Onivyde®	PEGylated liposomal irinotecan	Pancreatic cancer	[124]
ThermoDox®	Thermosensitive liposomal doxorubicin	Hepatocellular carcinoma	[125,126]

Table 1.3: Examples of liposomal drug combinations that are undergoing clinical trials or FDA approved.

In general, there are four main types of liposomes that are used for the drug delivery systems as demonstrated in **Figure 1.7** [107]. First generation liposomes are conventional liposomes that consist of a lipid bilayer that can be composed of charged or neutral phospholipids and cholesterol thus forming an aqueous core. Therefore, it is possible to incorporate hydrophobic compounds into the lipid bilayer and the hydrophilic compounds into the aqueous space. Such liposomes were used

for encapsulation of drugs like doxorubicin [107]. Although, they have demonstrated reduced toxicity, and improved pharmacokinetic and biodistribution in comparison to free drug *in vivo*; rapid elimination from the bloodstream was the limiting factor for its therapeutic efficacy [107]. This was due to the opsonization by plasma components and uptake by the macrophages of the RES, particularly in the spleen and liver [127]. To address the liposome circulation time in the blood, sterically stabilized liposomes were introduced by incorporation of hydrophilic polymer coating [107,128,129]. Thus, polyethylene glycol (PEG) coating was incorporated to the liposome surface [130]. A good examples of a PEGylated liposomes is Doxil® [110,117,128].

Targeted liposomes were developed to provide a targeted drug delivery at the requisite site by functionalization of liposomes with a suitable ligand such as antibodies, small molecules, peptides, proteins, or carbohydrates [131]. Doxorubicin-loaded folic acid (5-fluorouracil) labelled liposomes were prepared by Moghimipour *et al.* for targeting of folate receptor. Folate targeted liposomes have shown higher cellular uptake than free drug [132]. The newest generation of liposomes utilizes the combination of functionalities and modifications in order to overcome the challenges of liposomes with a single functionality [131]. Therefore, liposomes with two ligands or two anticancer drugs or theranostic liposomes (have both therapeutic and imaging modality) have been developed and reported in the literature [107,131,133].

1.3.1 Thermosensitive Liposomes

Liposomes with controlled release properties have a potential for delivery of chemotherapeutic drug to solid tumours. In principle, the drug-loaded liposomes should accumulate in the tumour site (via EPR; enhanced permeability retention), and subsequently release their cargo upon exposure to stimuli such as temperature elevation or pH change [73,131,134,135]. When the release stimulus is properly timed, drug-loaded liposomes can retain their drug for hours, allowing for high tumour uptake and accumulation of liposomes, before then releasing the drug at high local concentration [136]. Thus, numerous studies have been undertaken to develop stimuli sensitive liposomes. In this report I will be focusing on temperature sensitive (thermosensitive) liposomes (TSLs) for drug delivery.

In 1978, Yatvin *et al.* have introduced the first thermosensitive liposomal formulation consisted of 1,2-dipalmitoyl-*sn*-glycero-3-phosphocholine (DPPC) and 1,2-distearoyl-sn-glycero-3-phosphocholine (DSPC) in the molar ratio of 3:1. This formulation was able to release an encapsulated hydrophilic drug in response to the increased temperature (hyperthermia). They have used slightly higher temperatures (44 ^{o}C) than the physiological temperature (37 ^{o}C) to target drug delivery [137]. From this point of view, the concept of the hyperthermia (ideally mild hyperthermia in range of 39-42 ^{o}C [138,139]) combined with TSL became advantageous for drug delivery in two ways: first, it can induce controlled release of the encapsulated drug on the targeted area; second, mild hyperthermia can enhance the vascular permeability that can increase the particle diffusion and accumulation [135,140]. Nevertheless,

the phase transition temperature (T_m) of the lipid membrane where structural changes occur, is crucial for thermosensitive liposomes to be able to release the drug on the targeted areas with mild hyperthermia. This avoids drug release in healthy tissue at body temperature. The lipid membranes have a characteristic T_m that varies according to the lipid composition and molecular structure(s) of the relevant lipids. When temperature approaches the T_m the transition occurs from the solid gel (L_β) to liquid-crystalline (L_α) phase where lipid head groups gain mobility [141,142]. In the gel phase, lipids are tightly packed where hydrocarbon chains are fully extended and the headgroups are restricted on the membrane. Furthermore, the membrane is less permeable to water and hydrophilic drugs. At T_m point permeability is the highest due to the coexistence of membranes in both gel and liquid-crystalline phase forming grain boundaries [136]. Above the T_m the bilayer transitions into the liquid phase. In the liquid-crystalline phase the lipids are still confined to the membrane, however, they can now move freely and rapidly. This enables the membrane to become permeable facilitating release of the encapsulated drug, as shown in **Figure 1.8** [136,139,143].

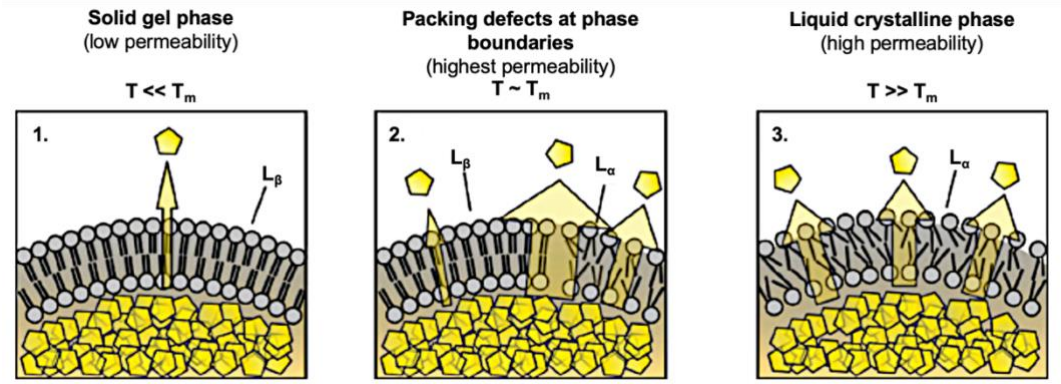

Figure 1.8: Schematic representation of lipid bilayer before and after the phase transition temperature (T_m). The structure changes from solid gel phase to liquid-crystalline phase that is associated with drug release. Adopted from Kneidl *et al.*[136]

The traditional tool to determine the lipid phase transition temperature is differential scanning calorimetry (DSC). When the liposomes undergo phase transition from a gel phase to liquid-crystalline phase heat absorption occurs. This absorption is recorded in DSC as a heat flow and is a function of the temperature. T_m of the lipid is defined as the temperature recorded at maximum heat flow [142,144]. According to **Figure 1.9**, measuring the changes of the calorimetric enthalpy (ΔH_{cal}) during the phase transitions of the lipid bilayers provides important information for designing the optimal liposomal drug carriers based on their thermal behaviour. These enthalpy changes correspond to changes of the heat capacity (C_{pmax}) of lipids during the transition from solid gel to the liquid-crystalline phase [142].

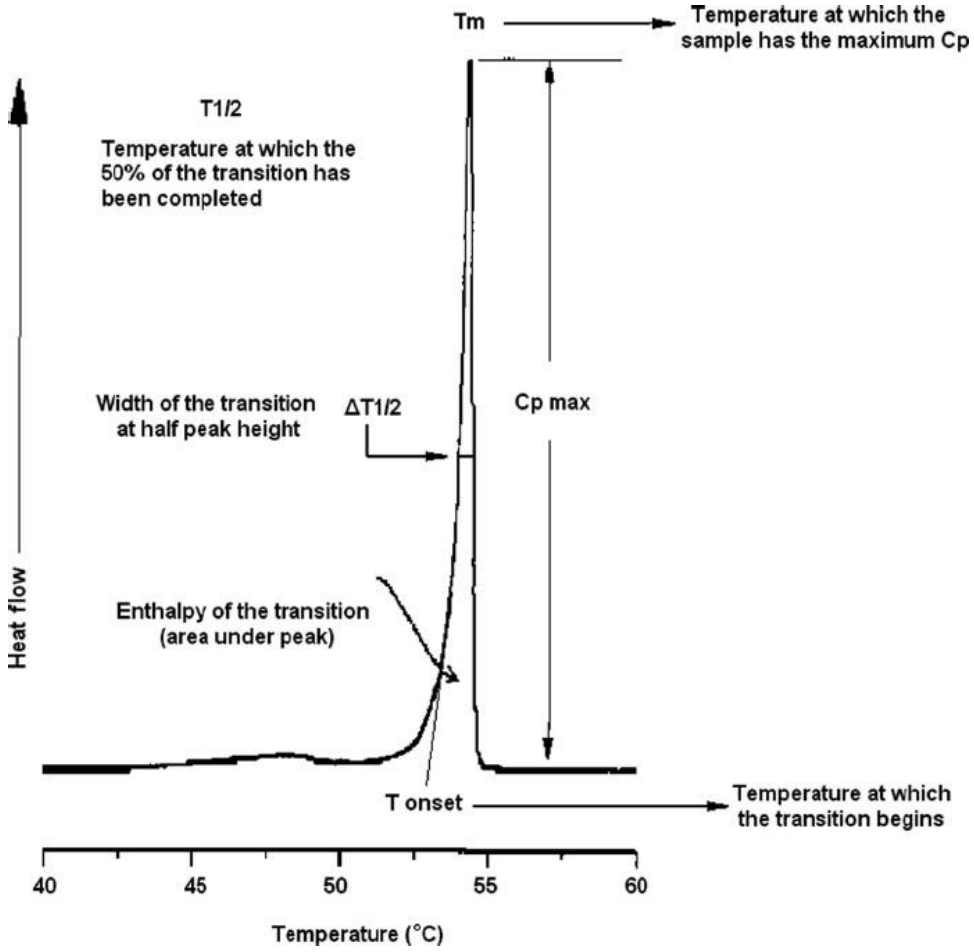

Figure 1.9: Characteristic parameters of a differential scanning calorimetry (DSC). Adopted from Demetzos *et al.* [142]

The major component in most TSLs is DPPC due to its T_m (41 ^oC) being above the body temperature, however it has been reported that DPPC is limiting drug release [135–137]. To address this issue, DPPC was combined with other lipids such as DSPC (T_m = 55 ^oC) and hydrogenated soy phosphocholine (HSPC) (T_m = 52 ^oC) and they were referred to traditional thermosensitive liposomes (TTSLs) [143,145]. Building on the work of Yatvin *et al*., several traditional TSL formulations were designed and studied in order to improve *in vitro* liposome stability; to increase the drug release rate and

to demonstrate that combining TSL with hyperthermia provides an increase in the accumulation of the cytotoxic drugs at the tumour site. This enhances their therapeutic effect [135,136,139]. Gabrer *et al.* have studied the incorporation of cholesterol and PEG-phosphatidylethanolamine in order to stabilise TSL formulations *in vitro*. It was showed that using cholesterol in TSL eliminates the T_m as the lipids are in a liquid-crystalline ordered phase. However, the TSLs composed in DPPC:HSPC:cholesterol:DPPE-PEG molar ratio of 50:25:15:3 have demonstrated a delay in the complete release of the encapsulated doxorubicin, where 60% of release was observed during 30 minutes of incubation at 42 ^{o}C in human plasma [146]. It is possible to have onset of necrosis in healthy tissues with the long heating required for TTSL formulations [143]. Prevention of the aforementioned issue is feasible under mild hyperthermia (39-42 ^{o}C) whilst achieving simultaneous drug release and/or using focal hyperthermia.

In 1999 Needham *et al.* have proposed to incorporate lysolipids into PEGylated thermosensitive liposomes such that they can lower the phase transition temperature and stimulate rapid release of encapsulated drug, also referred to as lysolipid containing thermosensitive liposomes (LTSLs) [143,147]. Lysolipids contain only one hydrocarbon chain and have a proportionately large headgroup relative to their tail which makes them more hydrophilic. Moreover, lysolipids have a tendency to form micelles (positive intrinsic curvature). Upon heating lysolipid-containing TSLs, as temperature approaches the T_m, grain boundaries form and melting begins at these boundaries (drug release occurs). Lysolipids accumulate at the boundaries and

form stabilized defects in the bilayer which enhances the release as shown in **Figure 1.10** [143]. The commonly used lysolipids are 1-palmitoyl-2-hydroxy-*sn*-glycero-3-phosphocholine (MPPC) and 1-stearoyl-2-hydroxy-*sn*-glycero-3-phosphocholine (MSPC) **Scheme 1.3** [139].

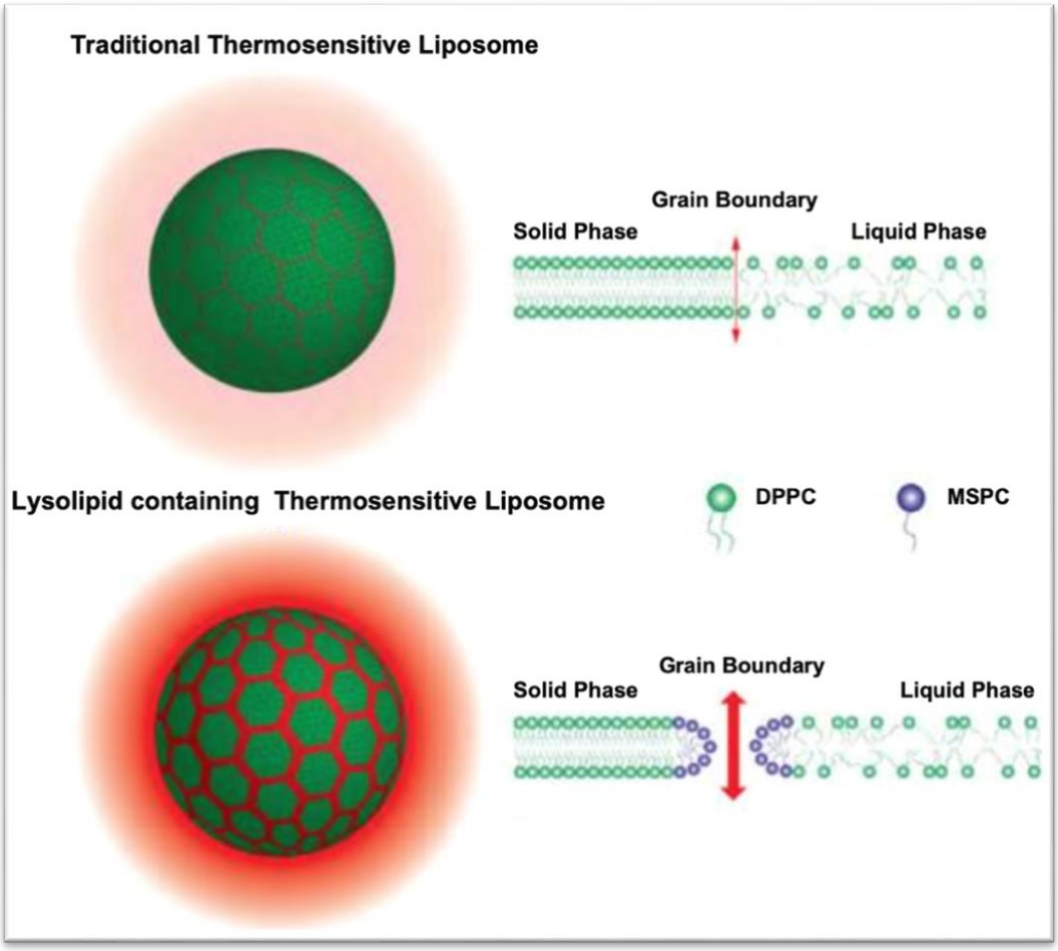

Figure 1.10: Proposed mechanisms of drug release from traditional thermosensitive liposomes and lysolipid containing thermosensitive liposomes during heating. Adopted from Ta *et al.* [143].

Needham *et al.* have demonstrated that incorporating a small amount of MPPC or MSPC (10 mol%) into the liposomes composed of DPPC significantly enhances the release payload and shifts the phase transition from ~41.9 to 40.5 ^{o}C and 41.3 ^{o}C respectively [147–149]. The LTSL formulation made of DPPC:MPPC:PEG^{2000}-DSPE (90:10:4) had released ~45% of entrapped doxorubicin in the first 20 seconds at 42 ^{o}C compared to pure DPPC where it has only released 20% over 1 hour [148]. They have shown that LTSLs are able to release the entrapped drug rapidly in the mild hyperthermia range (39–42 ^{o}C) which is clinically attainable [147–149].

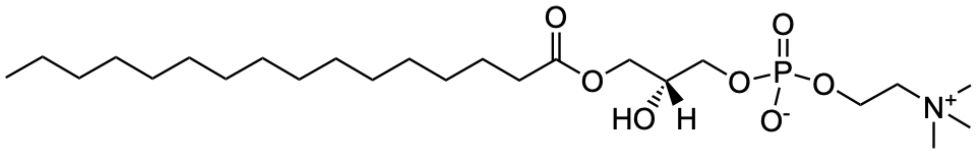

1-palmitoyl-2-hydroxy-*sn*-glycero-3-phosphocholine (MPPC; 16:0 lyso-PC)

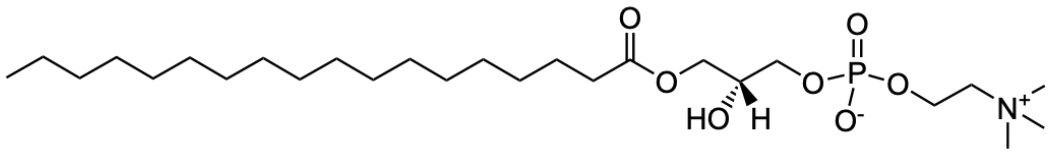

1-stearoyl-*sn*-glycero-3-phosphocholine (MSPC; 18:0 lyso-PC)

Scheme 1.3: Chemical structures of common lysolipids MPPC and MSPC.

Furthermore, Thermodox®, a LTLs (lysolipid-containing thermosensitive liposome), was developed by Celsion (Lawrenceville, NJ) which was built on the earlier research of Needham *et al*. [147,148]. Thermodox® is composed of DPPC:MSPC:PEG^{2000}-DSPE (86.5:9.7:3.8 mol%) with encapsulation of doxorubicin (T_m at 41.5 ^{o}C) and it is the

first thermosensitive liposomal formulation to reach clinical trials. The inclusion of 9.7 mol% MSPC to the formulation of Thermodox® gives 60% release of drug in the first 20 s at 41.3 ^{o}C [150]. In preclinical studies, Thermodox® yielded accumulated levels of doxorubicin that were approximately 4 and 36 times higher at the tumour site for non-thermosensitive doxorubicin loaded liposomes and free doxorubicin respectively, resulting in better treatment efficacy (heated at 42 ^{o}C for 1h) [151,152]. Thermodox® is in clinical trials investigating treatments for primary liver cancer (hepatocellular carcinoma) and recurring chest-wall breast cancer and made it as far as phase III clinical trials. These clinical trials were designed to combine chemotherapy with mild local hyperthermia by using radiofrequency ablation (RFA), microwave or high intensity focused ultrasound (HIFU) [125,152,153].

Even though Thermodox® is a PEGylated LTSL formulation, it is actually not as stable as other conventional liposomes (non-thermosensitive). In comparison to Doxil®, Thermodox® does not retain the encapsulated drug for that long and while the plasma half-life of the lysolipid of LTSL is 8 h, the encapsulated doxorubicin plasma half-life is 1.3 hours [154]. Accordingly, Banno *et al*. have confirmed a significant loss of lysolipid (70%) from the Thermodox® formulation at 37 ^{o}C within a 1 h post injection period during an *in vivo* study with mice. It has been suggested the dissociation of lysolipid content could be due to the interaction of LTSLs with plasma proteins and cellular membrane pools [155]. In the light of this, Lindner *et al.* have developed a novel synthetic phospholipid 1.2-dipalmitoyl-*sn*-glycero-3-phosphoglyceroglycerol (DPPGOG or $DPPG_2$). The novel lipid was incorporated into

thermosensitive liposomal formulation composed of DPPC:DSPC:DPPGOG (50:20:30 mol%) and provided significantly prolonged circulation in plasma whilst maintaining the rapid release profile of Thermodox® like LTSLs at 42 ^{o}C for 1 h [140,156]. Initial *in vitro* studies of TSLs with $DPPG_2$ encapsulated drug showed plasma half-life of 9.6 h in hamsters and 5.0 h in rats [140].

In another study, Tagami *et al*. have developed a novel heat activated cytotoxic (HaT) thermosensitive liposomal formulation with Brij78 surfactant and DPPC lipid at molar ratio of 96:4. The Brij78 is a non-ionic surfactant consists of acyl chain that can replace the functions of lysolipid and PEG^{2000}-DSPE. The HaT nanoparticles were loaded with doxorubicin and proposed for drug delivery under mild hyperthermia that can release loaded drug at 40-41 ^{o}C in 2-3 minutes (100% release) [157,158].. *In vivo* they have treated BALB/c mice bearing mammary carcinoma tumours (EMT-6) with HaT, Thermodox® like LTSL and free doxorubicin. Doxorubicin uptake in heated tumours was 5.6 times larger than free doxorubicin and 1.5 times larger than LTSL. This was also substantiated by the enhanced antitumor effect of HaT in comparison to LTSL [157].

Formulations with great drug release profiles can be designed, however the next generation requires improvement over the base lipids for its development. Today's formulations have increased drug release profile. However, they are lacking stability at body temperature causing short blood clearance times.

1.3.2 Focused Ultrasound for Drug Delivery

1.3.2.1 Fundamentals of Ultrasound

Ultrasound (US) is produced by ultrasound transducers, devices that convert electrical energy into ultrasound waves (electrical energy transformed into mechanical energy). Ultrasound waves are sound vibrations which can be defined as longitudinal mechanical waves propagated through a medium at a frequency greater than 20 kHz, making it higher than the upper audible limit of human hearing [159].

Ultrasound is used commonly in diagnosis (imaging) because ultrasound-based technologies are cheap, safe and portable in size. In a therapeutic context, ultrasound can be used for ablation or hyperthermia induced drug release, and the effect of ultrasound on tissues can be modulated by changing multiple parameters including acoustic pressure, frequency, duty cycle, intensity and wave shape [160].

During propagation through a medium, an ultrasound wave causes a change in pressure through a sequence of compression and rarefaction (decompression) events which is referred to as acoustic pressure. The frequency is the number of the compression and decompression cycles in a unit of time, which is measured in Hertz. In medical applications, frequency of ultrasound is typically divided into three categories: low frequency (20-200 kHz), medium frequency (0.3-3 MHz) and high frequency (>3MHz) [159,161]. The frequency determines the level of penetration and spatial resolution of the image, lower frequencies provide higher penetration of

tissues however give poor spatial resolution and vice versa **Figure 1.11** [162]. However, frequencies higher than 10 MHz are not used clinically due to their superficial tissue penetration (<1 cm) [163]. Frequencies around 1 MHz have considered to be the most useful for heat deposition [164]. Moreover, the duty cycle (pulse ratio) determines the ratio of pulse duration against pulse period e.g. 10 % DC, 10 Hz PRF implies – 100ms on; 900ms off repeated. A low ratio enables the maintenance of set temperatures in tissues, this is crucial for controlling hyperthermia below ablative temperatures [165]. The ultrasound intensity (also known as acoustic intensity or power) is the rate of energy carried through a unit area by the ultrasound wave (e.g. watts per square centimetre) [166]. The acoustic intensity decreases as the ultrasound wave penetrates tissue [167] with US energy being converted to heat.

Attenuation is the decrease in acoustic energy per unit distance travelled. Absorption is the major source of attenuation. This is where energy is absorbed by the tissue from the tissue's resistance to the movement from pressure being caused by the US. The work being done by the US wave forcing the tissue to move against its resistance is energy converted to heat within the tissue, which is then lost from the US wave and the wave attenuates. [168]. The focused ultrasound beams attenuate in the bone tissues 10-20 times higher than the soft tissues, which cause rapid absorption of the transmitted ultrasound beam which degrades to heat [168].

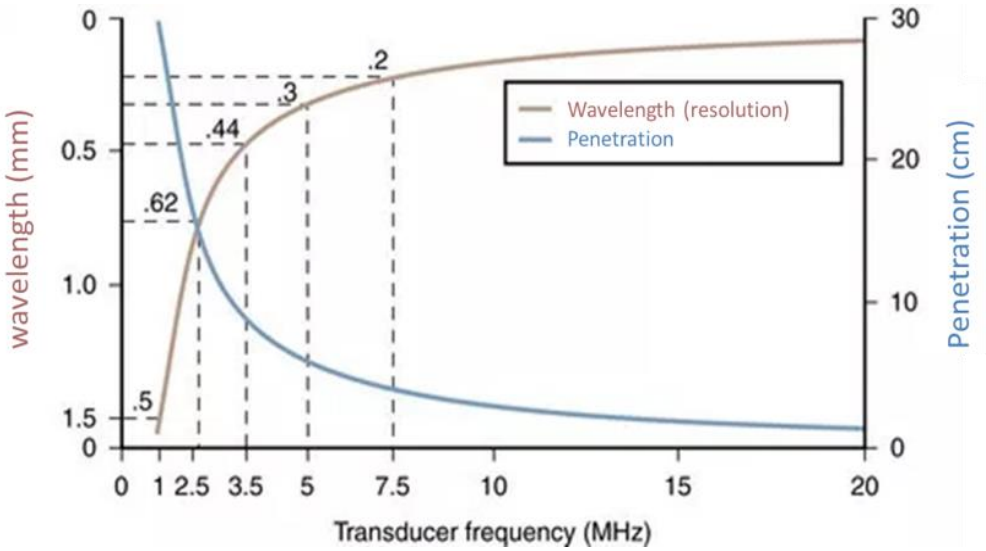

Figure 1.11: Relationship between frequency against tissue penetration and spatial resolution. Adopted from Otto *et al.* [169].

1.3.2.2 High Intensity Focused Ultrasound (HIFU)

Therapeutic high intensity focused ultrasound (HIFU) or Focused Ultrasound (FUS) is a non-invasive method of depositing heat energy in the body. Medical FUS generally uses frequencies between 0.8 – 3.5 MHz, and the energy delivered in the ultrasound beam is several orders of magnitude greater than standard diagnostic ultrasound devices [168]. The ultrasound transducers for clinical applications are designed to focus the ultrasound waves into a focal area that will experience an ultrasound intensity at least two orders of magnitude higher than the surrounding tissue. It is an advantage to selectively apply heat at the focal point as ultrasound intensity decay exponentially away from it, meaning surrounding tissues within the beam are not damaged [170,171].

HIFU produces thermal heating and cavitation effect in tissue. These effects depend on the acoustic parameters and the type of tissue [170,172]. The thermal effect occurs by absorption of acoustic energy by tissue at the focal point which depends on the magnitude and duration of the energy applied. The temperature of the exposed tissue can rapidly rise to more than 60 ^{o}C and cause irreversible cell death or conversely, a small increase in temperature can be applied for a period of time (minutes or hours) to achieve local hyperthermia [164]. In addition to thermal effect, HIFU can also cause cavitation which damages cellular structures e.g. rupture of microbubbles formed during HIFU. Owing to the influence of altering pressure waves, gas bubbles present in the blood stream begin to oscillate in the US field. This can induce mechanical effects such as improving the permeability of cell membranes or blood vessels [168,170,173–177].

As an illustration, smart nanoparticles respond to changes in temperature (mild hyperthermia) or pressure. Hence, ultrasound waves can be applied in a confined focal area, enabling local release of a therapeutic payload from temperature sensitive smart nanoparticles specifically at the heated focal point. [172,175,178].

Since 1990s there have been several HIFU clinical devices in use, which are classified as extracorporeal, transrectal and interstitial according to the accessibility of the targeted organs [164,170,179]. The most commonly used system is extracorporeal transducers which are used for targeting readily accessible areas. This means that targets are limited to 10 cm in depth from the skin, when the ultrasound waves can

reach without being obstructed by problematic materials such as bone or gas which interfere with US transmission. This target limitation is also known as the acoustic window [170]. Transrectal devices are designed for prostate treatments and the interstitial devices are used for the treatment of biliary duct and oesophageal tumours and inserted into the body through the mouth [164,179].

In oncology, thermal therapy has a long history with currently used techniques including radiofrequency catheters, microwaves, lasers or ultrasound. To this date Thermodox® is the only thermosensitive drug that has reached a phase III clinical trial. This clinical trial was for liver tumours in combination with RF ablation. However, one of the drawbacks of this heating modality is thermal coagulation of the tissue surrounding the RF electrodes which limits the ability to control drug delivery [180]. In light of this, HIFU is a promising approach for attaining controlled hyperthermic exposures and has been advanced in Thermodox® clinical trials for liver tumours [152].

1.3.2.3 MRI Guided Focused Ultrasound (MRgFUS)

HIFU is a promising method that facilitates the deposition of energy inside the tumour whilst avoiding damage to the healthy tissue nearby. The combination of a HIFU system with a high-resolution imaging modality (MRI) provides a guided system able to generate precise anatomical images and non-invasive tissue destruction [181,182]. MRI guided FUS (MRgFUS) benefits from the MR thermometry in order to monitor the temperature change in the targeted area for hyperthermia and ablation purposes [183]. MR thermometry facilitates calculation of thermal dose which can

be used to predict the level of tissue damage as a result of heating. Also, it can be used to avoid damage to surrounding tissues during the application of the ultrasound [170,184]. The proton resonance frequency shift (PRF) method is the current gold standard for the MRI thermometry in clinical use. Reasons include good sensitivity, great linearity with temperature, and it is largely tissue type independent [185]. The mechanism of PRF shift based MR thermometry is that as temperature increases, the hydrogen bonds of water molecules start to stretch, bend and break. This increases their electron screening effect which in turn causes attenuation of the local magnetic field and thus a lower proton resonance frequency with increased temperature [185,186]. Therefore, temperature maps can be created by measuring the phase change in resonance frequency [186]. Moreover, the real time imaging modality of MRgFUS has led to the development of novelties in the field of hyperthermia triggered drug delivery nanoparticles in a theranostic approach [168].

1.3.3 Theranostic Thermosensitive Liposomes

The recent invention of multifunctional nanoparticles enables simultaneous monitoring and treatment of disease by combining the delivery of therapeutic agents with the capacity for *in vivo* imaging. This has led to the term “theranostics” [187–190]. Theranostic nanoparticles can be functionalised to bind selectively to biomarkers on desired cells or lesions for targeting. In addition, they can also trigger release of therapeutic agents in response to internal (pH of tumour) or external stimuli (temperature) [191]. This facilitates the development of bespoke medicines. Besides the active targeting with targeting ligands, theranostic nanoparticles also benefit from the EPR effect which causes an increase in tumour uptake of therapeutic

agents [192,193]. It should be highlighted that the use of imaging agent in the theranostic nanoparticles facilitates a great potential to tag cancer metastases through the ability of enhancing contrast and simultaneously treatment e.g. with HIFU [192].

The previously discussed system, thermosensitive liposomal (TSL) drug delivery can incorporate imaging agents to visualize targets in a non-invasive manner *in vivo* for various imaging modalities such as optical imaging, MRI, and PET [191]. The advantages to patients of being able to monitor the accumulation of TSL in the tumour site during the application of local mild hyperthermia are significant for therapeutic outcomes [194]. The timing of application of heating modality is crucial for the maximum therapeutic effect. Therefore, image guided high intensity focused ultrasound (HIFU) is a great platform for thermosensitive liposomes to deliver their therapeutic agent with the guidance of the imaging modality.

US and MRI are the main imaging modalities that are used for guidance in HIFU therapies [195]. The initial use of US or MRI-guided HIFU therapies were designed to assist in ablation therapies. Even though, US-guided HIFU is a cost-effective therapy relative to MRI guidance, MRI guided HIFU (MRgFUS) provides anatomical and high spatial resolution images that reduce the risk of damaging organs and other structures for precise ablation with HIFU [195,196]. Moreover, another important advantage of MRgFUS over US-guided FUS is its ability to provide quantitative temperature measurements [186]. Nowadays, MRgFUS has become a promising

technology for the hyperthermia triggered drug delivery in order to control the temperature accurately in the mild hyperthermia temperature window [180,197].

In a drug delivery scheme, it is advantageous to be able to observe and control the drug release at the target site with real-time imaging. In this manner, thermosensitve liposomes co-encapsulating gadolinium-based contrast agents were developed to monitor and asses real-time drug release where MRgFUS can be utilised [198]. As previously discussed, de Smet *et al.* have entrapped clinically approved [Gd]HPDO3A, ProHance®, and doxorubicin into various TSL formulations including lysolipid TSLs (LTSLs) and traditional TSLs (TTSLs). *In vitro* studies have shown that LTSL formulations have higher leakage at 37 ^{o}C than the TTSLs, whilst LTSL have faster release of doxorubicin at 42 ^{o}C than TTSL formulation [76]. Following this study, a proof-of-concept study was designed using TTSL formulation composed of DPPC:HSPC:cholesterol:DPPE-PEG^{2000} in molar ratio of 50:25:15:3 due its high stability profile. They have monitored the co-release of the drug and the contrast agent using MRgFUS system at 3 T under local hyperthermia for 30 minutes on tumour bearing rats. The local hyperthermia triggered release of ProHance® was monitored with interleaved T_1 mapping of the tumour and correlated with the co-release of doxorubicin [77].

Expanding on the findings of de Smet *et al*., Hijnen *et al*. have investigated the effects of the MRgFUS heating strategies (hyperthermia, ablation and their combination) on the biodistribution of TSLs (co-encapsulating doxorubicin and ProHance®) and

intravascular release of doxorubicin at tumour site. Hence, determining their therapeutic efficacies *in vivo* using rhabdomyosarcoma bearing rats. They have proposed that the combination of hyperthermia-triggered drug delivery followed by ablation enhances accumulation of TSL at the tumour site and intravascular release of doxorubicin which has contributed to the best therapeutic outcome. This appeared to be due to more homogenous doxorubicin uptake across the tumour instead of accumulating at the tumour rim [199,200].

Kim *et al.* have developed a short-chain elastin-like polypeptide incorporating thermosensitive liposome (STL) encapsulating an MRI contrast agent, gadobenate dimeglumine ([Gd]BOPTA), and doxorubicin. STL formulation was composed of DPPC:DSPC (75:25 mol%) DPPC:DSPC:PEG^{2000}-DSPE:cholesterol in molar ratio of 55:2:10. They encapsulated the MRI contrast agent in order to monitor the drug release from STSL where MRI studies demonstrated the difference in T_1 relaxation times between 37 ^{o}C (body temperature) and 42 ^{o}C (mild hyperthermia) at 4.7 T MRI system. *In vivo* studies with tumour (murine squamous cell carcinoma SCC-7) bearing BALB/c mice have demonstrated high stability (STLs did not release the contrast agent) at 37 ^{o}C. The results showed that the HIFU is able to co-release doxorubicin and [Gd]BOPTA from STL rapidly under mild hyperthermia at tumour site and the efficacy of the drug delivery was confirmed with MRI examination [201].

Previously our group published a study with theranostic thermosensitive liposomes by incorporating an MRI contrast agent and near infrared fluorophore

(XenoLight750) labelled lipids into the bilayer. MRI and NIR labelled thermosensitive liposomes were prepared to encapsulate topotecan (Hycamtin®) for imaging and tracking the biodistribution of the liposomes on dual tumour model *in vivo* on SHO mice bearing ovarian adenocarcinoma tumours (IGROV-1). Hence, the drug was released on the tumour site with application of FUS-induced hyperthermia (3 min at 42 °C). The release was monitored by an increase in intrinsic topotecan fluorescence and the uptake was confirmed with MRI [194].

The ideal chemotherapeutic treatment would be a highly effective therapy that concentrates the drug in tumour and minimizes the damage to normal tissue [201]. In order to increase therapeutically effective drug delivery to the tumour while reducing the damage to healthy tissues, a FUS triggered MRI guided thermosensitive liposome formulation with encapsulating doxorubicin are studied in this thesis. Moreover, novel methodology to assess thermosensitive liposomes' response to increased temperature, focused ultrasound and their integrity under different and challenging conditions were proposed.

The aim of this project is to design and develop a MR-labelled image-guided thermosensitive liposomes (iTSL) loaded with the anticancer agent doxorubicin (iTSL-DOX). An MR contrast agent was covalently linked to the lipid membrane in order to allow real-time imaging. The synthesis of gadolinium chelated lipid has been shown and the efficiency of the contrast agent was evaluated by measuring longitudinal and transverse relaxivities. Further improvement was sought by enhancing the efficiency

of the contrast agent by synthesis of alternative gadolinium chelated lipids with different lengths of spacers between the head group (DOTA) and the lipid tail (DSA). This serves to improve the MRI T_1 relaxivity of iTSLs. In the development of iTSLs it is crucial to determine the gadolinium concentration. However, commonly used analytical techniques (ICP-OES or ICP-MS) require extensive sample preparations for nanoparticles with lipidic content. Therefore, in order to quantify gadolinium content in such nanoparticles in a simple manner, whilst preserving accuracy it was aimed to demonstrate the robustness of TXRF as an analytical technique for our iTSLs studies.

2. Total Reflection X-ray Fluorescence Measurement of Gadolinium in Liposomal Nanoparticles

2.1 Introduction

Magnetic Resonance Imaging (MRI) is a well-established, non-invasive imaging technique that provides high resolution images with valuable anatomical and functional information that can be enhanced by administration of contrast agents (CAs) [202]. CAs have a crucial role in clinical MRI, enabling greater discrimination between normal and pathological tissue [203]. and hence the continued development of CAs with ever greater MRI-activity and safety profiles.

The MRI signal returns to equilibrium following excitation via longitudinal or transverse relaxation mechanisms. CAs increase the relaxation of the MRI signal of surrounding magnetic nuclei (shorten T_1 or T_2), usually water protons. Relaxation can be enhanced by unpaired electrons in paramagnetic metals such as gadolinium. Gadolinium has the highest number of unpaired electrons and is the most effective paramagnetic metal [29]. Often gadolinium CAs are called T_1-CAs as they predominantly enhance T_1-relaxation [22,204]. However, gadolinium ions are toxic, primarily due to their similarity in size to calcium ions, causing transmetallation interference with biological processes, e.g. inhibit cellular activation by substituting for calcium ions and entering cells via voltage-gated calcium channels [22,50] and are therefore, chelated with ligands to avoid toxicity.

Chelation must be achieved while retaining gadolinium paramagnetism but this provides the opportunity to tailor CA pharmacokinetic properties [19]. One

significant approach to increase the effectiveness of T_1-relaxation agents is to associate/concentrate gadolinium chelates into nanoparticles such as dendrimers, polymeric nanoparticles and liposomes [24,205,206]. Thereby, increasing the number of paramagnetic (gadolinium) centres in a unit volume to induce a greater paramagnetic effect. Further, larger sized nanoparticles tumble slower with long rotational correlation times and are thus better relaxation enhancers. Mulder *et al.* has demonstrated that liposomes, biocompatible spherical vesicles that are bound by lipid bilayers, have slowed tumbling rates compared to low molecular weight gadolinium contrast agents [71,106].

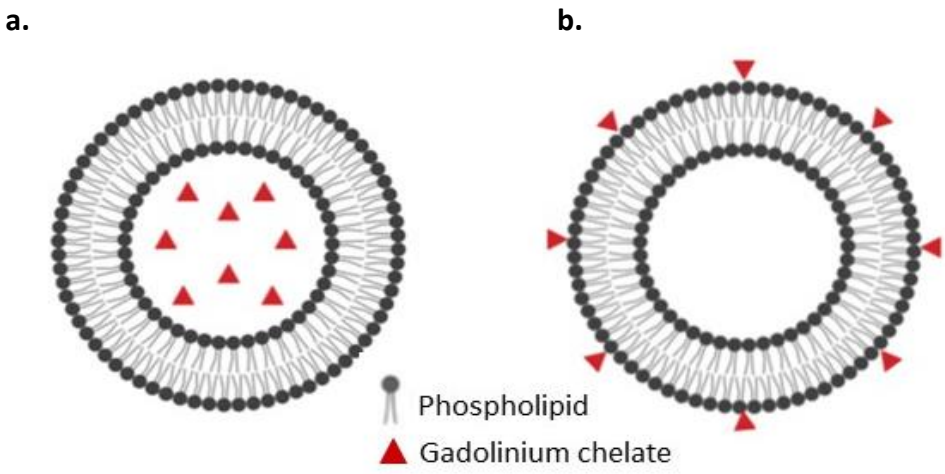

Figure 2.1: There are two types of gadolinium-labelled liposomes for MRI, **(a)** those that encapsulate gadolinium chelate within the liposome core, or **(b)** gadolinium chelates are conjugated to lipids that comprise the liposomal bilayer. Created with BioRender.com

In this study, the key focus was on gadolinium-labelled liposomes (GL) as MRI-CAs which can be formulated in two ways, either gadolinium chelates are encapsulated inside the liposomal core or are conjugated to bilayer components and present on the liposomal surface **(Figure 2.1)** [207,208]. GLs can be modified in a variety of ways to modify their pharmacokinetic profile, e.g., increasing their intravascular half-life by PEGlyation [194,209] and to target specific cellular and molecular targets, e.g., folate receptors of certain ovarian cancer cells, while amplifying the paramagnetic effect by delivering a high payload of gadolinium [209,210]. Accordingly, in this thesis, novel MRI guided thermosensitive liposome formulations were designed where gadolinium chelates were conjugated to lipid that comprise the liposomal bilayer.

CAs are evaluated according to their molar relaxivity (r_1), the higher the r_1, the better the CA at enhancing T_1-relaxation [22,211]. The relaxation rate, R_1, is the reciprocal of T_1 and normalised to the molar CA concentration to give r_1, as CA efficacy is also dependent on the CA (gadolinium) concentration. Thus, determining the concentration of gadolinium is critical for assessing the effectiveness of novel gadolinium-based MRI-CAs. In order to calculate MRI efficiency, the use of Total Reflection X-Ray Fluorescence (TXRF) to measure gadolinium content in nanoparticles for the development of novel MRI-CAs is proposed **(Figure 2.2)**.

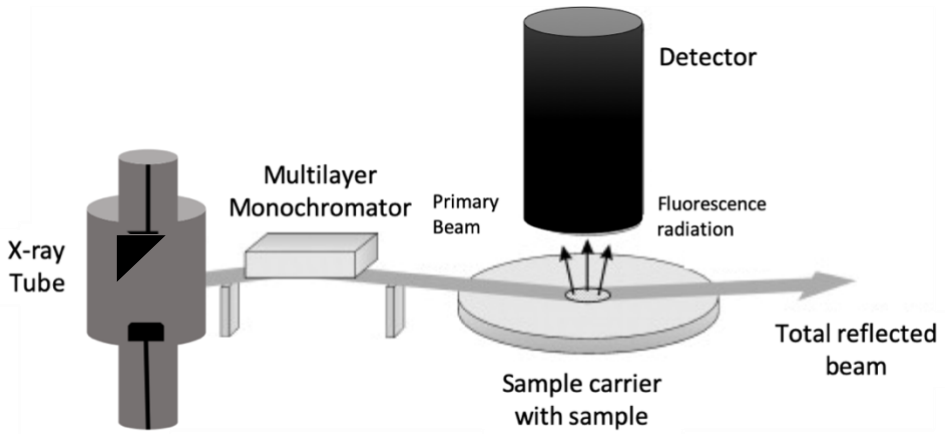

Figure 2.2: Working principle of elemental analysis with TXRF: The X-Ray beam, generated by a molybdenum X-ray tube, which is reflected on multilayer monochromator. This small beam passes the sample carrier with the homogenised sample at a very small angle resulting with total reflected beam. The characteristic fluorescence radiation emitted by the sample is detected by a detector and the intensity is measured.

TXRF works by generating an X-ray beam, called the incident beam. This beam hits an inner shell electron of a sample atom, which removes the electron from the inner shell leaving the atom in an excited state. An electron from the outer shell replaces the removed inner shell electron. The difference in energy levels between inner and outer electron shells is expressed as an emission of a photon quantum (fluorescence radiation) **(Figure 2.3)**. Each element emits its own characteristic wavelength of the

X-ray fluorescence radiation. Since the samples are deposited in a thin layer (0.1-10 µm), the net intensity is linear to concentration of elements **(Equation 2.1)** [97–99].

$$C_i = \frac{C_{IS} \,.\, N_i . S_{IS}}{N_{IS} . S_i}$$

Equation 2.1**:** Quantification equation for TXRF. C_i is concentration of element. C_{IS} is concentration of internal standard. N_i is element net count rate. N_{IS} is internal standard net count rate. S_i is element sensitive factor and S_{IS} is internal standard sensitivity [212].

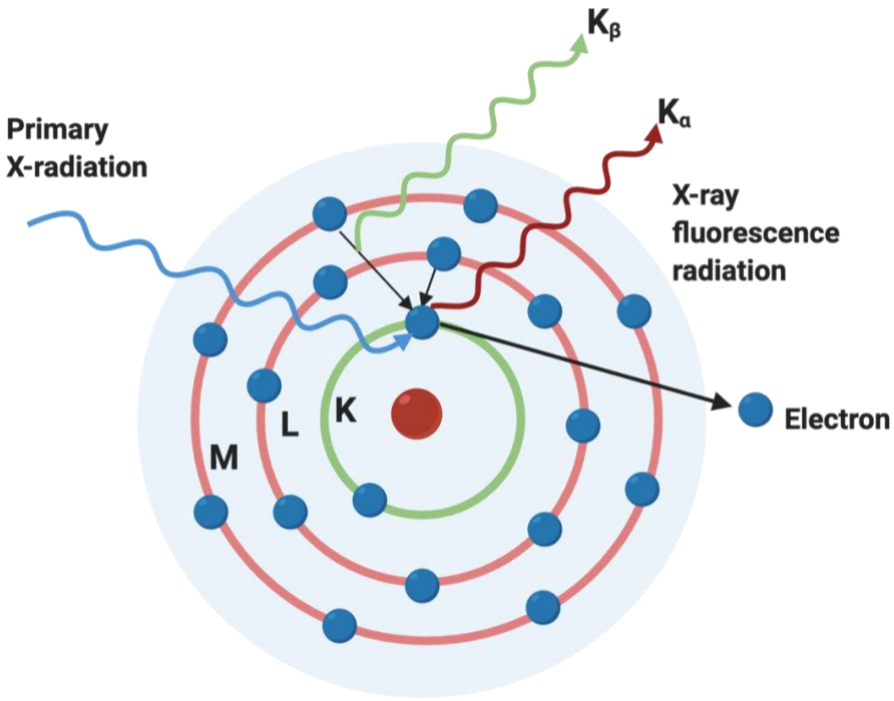

Figure 2.3: Total reflection X-ray Fluorescence. Created with BioRender.com

In the literature, gadolinium is commonly quantified by using Inductively Coupled Plasma-Mass Spectrometry (ICP-MS) or Inductively Coupled Plasma-Optical Emission Spectrometry (ICP-OES) [88,213]. As it was discussed earlier in **Chapter 1.2.6,** quantification of both ICP-hyphenated techniques are similar and based upon use of calibration standards [89]. Both ICP-OES and ICP-MS can detect a wide range of metals, either with optical emission of the characteristic wavelength for individual elements via ICP-OES or the characteristic atomic mass of an element via ICP-MS [91]. Both TXRF and ICP-OES utilise the optical properties of elements and in both techniques detection limits can be as low as a few parts per billion, hence they are suitable for comparison [96,99,214,215].

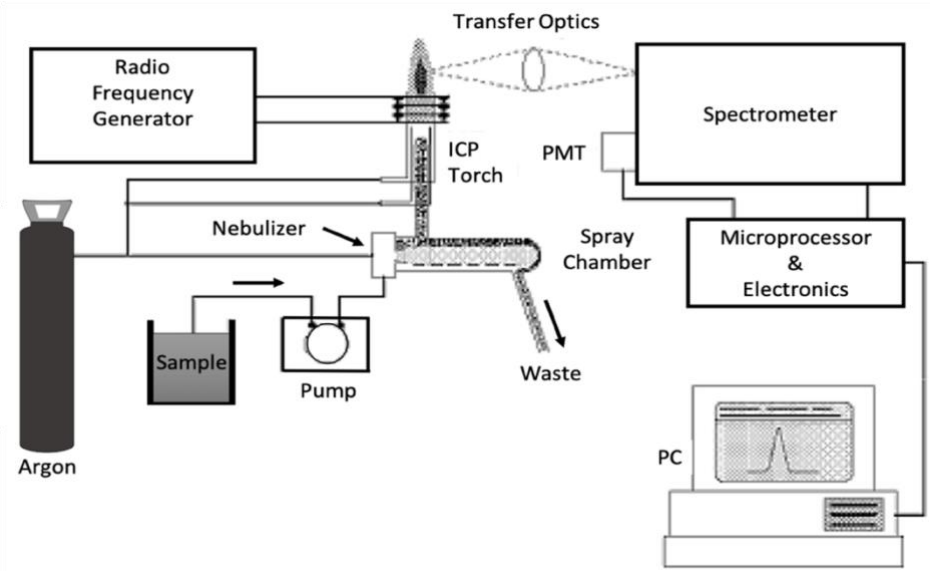

Figure 2.4: Working principle of elemental analysis with ICP-OES: after acidic digestion, diluted samples are nebulized and sprayed into an argon plasma. The resulting atomization and excitation enable quantification of elements by emission wavelengths and intensity.

The working principle of ICP-OES is based on the atoms and ions that can absorb energy to move electrons to an excited state from ground state where the source of the energy is argon plasma **(Figure 2.4 and Figure 2.5)**. Excited electrons relax and emit a photon whose wavelength is characteristic of the element. The concentration of the element in the sample is calculated from the intensity of the emitted light measured by a detector [214,216].

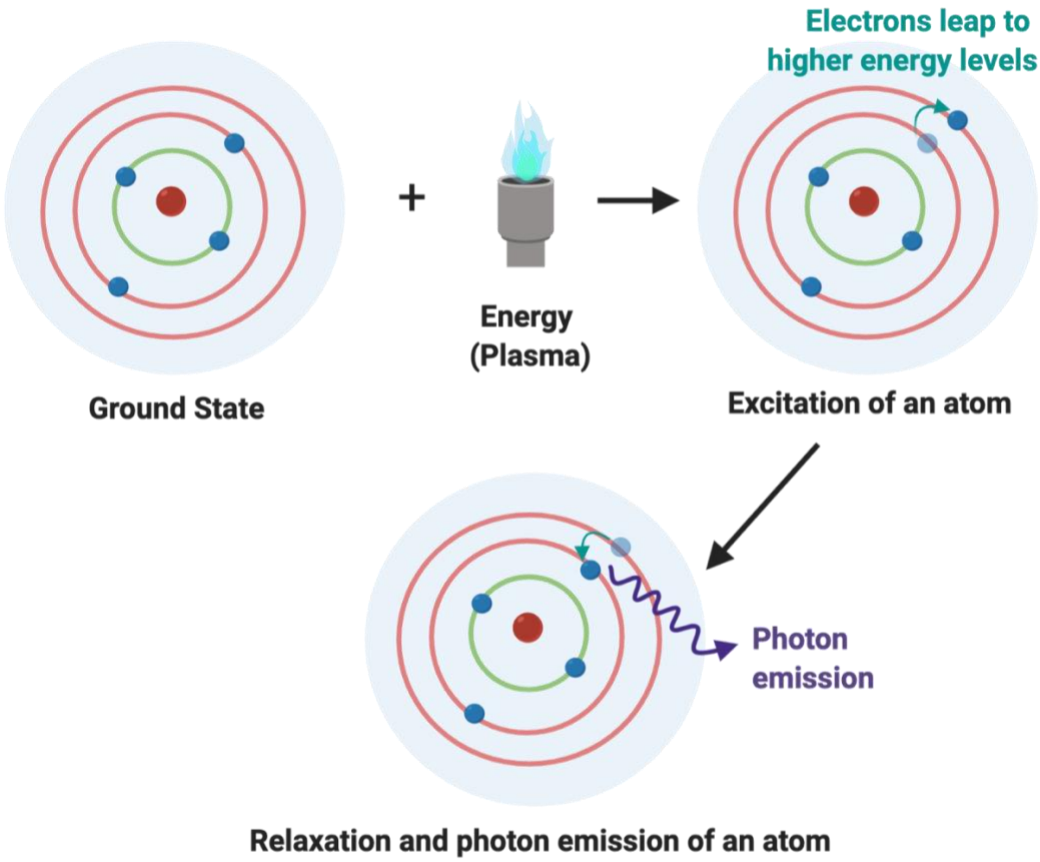

Figure 2.5: Excitation of an atom by a plasma. Created with BioRender.com

One of the important advantages of using TXRF is that it is a relatively matrix-independent technique compared to ICP-OES. As a result of this metal composition of multi-metal samples in liquid, powder or solid form with negligible matrix effect can be quantified as long as an appropriately thin layer of sample is available [97–99,217]. Moreover, for using ICP-OES, samples need to be much more diluted and/or digested; with strong acids/oxidants such as nitric acid (HNO_3); hydrochloric acid (HCl) and/or hydrogen peroxide (H_2O_2). It is important to release metals from nanoparticles like liposomes into aqueous media [89,92,93]. ICP-OES requires a larger sample volume which consequently translates to increased dilution. These requirements may cause issues that can challenge the measurement of trace amounts of elements. For example, sample digestion may be incomplete and/or there can be progressive sample loss with each step, resulting in measurement errors. Contamination at each step is another potential issue, and may originate from reagents, equipment and/or the environment [94,95]. Excessive sample preparation steps that are required for nanoparticles using ICP-OES can be time-consuming, costly, and disadvantageous in quality assurance [96]. Accordingly, quantification of gadolinium in liposomal formulation requires digestion to solubilise the gadolinium into aqueous solution for ICP-OES. However, TXRF can avoid the need for digestion of liposomes and facilitate simpler sample preparation.

In this study, aim is to demonstrate the application of TXRF for simple, robust and accurate quantification of the gadolinium content **(Scheme 2.1)** of gadolinium-labelled liposomes (GL) to vindicate the use of TXRF for the entirety of our project.

The model gadolinium labelled liposome (GL) as a MRI contrast agent encapsulates the commercially available gadolinium chelate contrast agent (CA), Gadovist® **(Figure 2.1),** inside PEGylated liposomes [218]. TXRF and ICP-OES measurements of gadolinium content of Gadovist® and liposome formulations were performed and compared. While digestion of liposomes is required for ICP-OES analysis, both digested and non-digested samples were also directly analysed by TXRF to determine the effects of sample preparation/digestion on gadolinium measurements. ICP-OES and TXRF measurements of gadolinium in both non-digested and digested Gadovist® solutions were recorded too. Although digestion is not required for analysis by either technique since Gadovist® is water-soluble, this provided the proof-of-concept for measuring the amount of gadolinium in non-aqueous solutions of gadolinium chelates conjugated to lipids. Such lipid conjugates may be incorporated into liposomes for MRI tracking **(Figure 2.1a)** but being lipophilic, digestion is needed to solubilise the gadolinium into aqueous solutions for analysis by ICP-hyphenated methods.

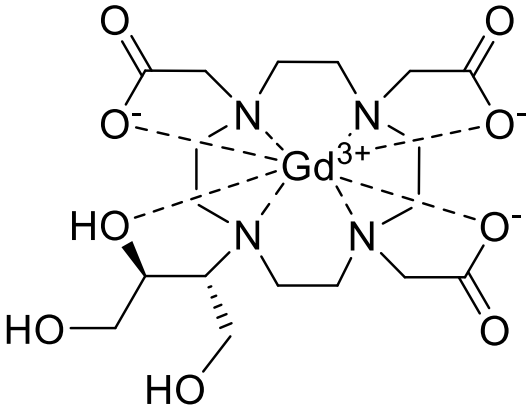

Gadovist®

Gd(BT-DO3A)

$C_{18}H_{31}GdN_4O_9$

MW: 604.72

Scheme 2.1: Structure of gadobutrol, the macrocyclic gadolinium contrast agent, trade name is Gadovist®

2.2 Aim and Objectives:

Aim: To demonstrate the application of TXRF for simple, robust and accurate quantification of the gadolinium content of lipid nanoparticles like liposomes, so that it can be used as an analytical technique for our image-guided thermosensitive liposomes studies.

Objectives 1: To prepare and characterise Gadovist®-encapsulating liposomes (GL).

Objective 2: To compare TXRF and ICP-OES for assaying gadolinium in non-digested and digested Gadovist® and Gadovist®-encapsulating liposomes,

Objective 3: To test accuracy and reproducibility of TXRF measurements.

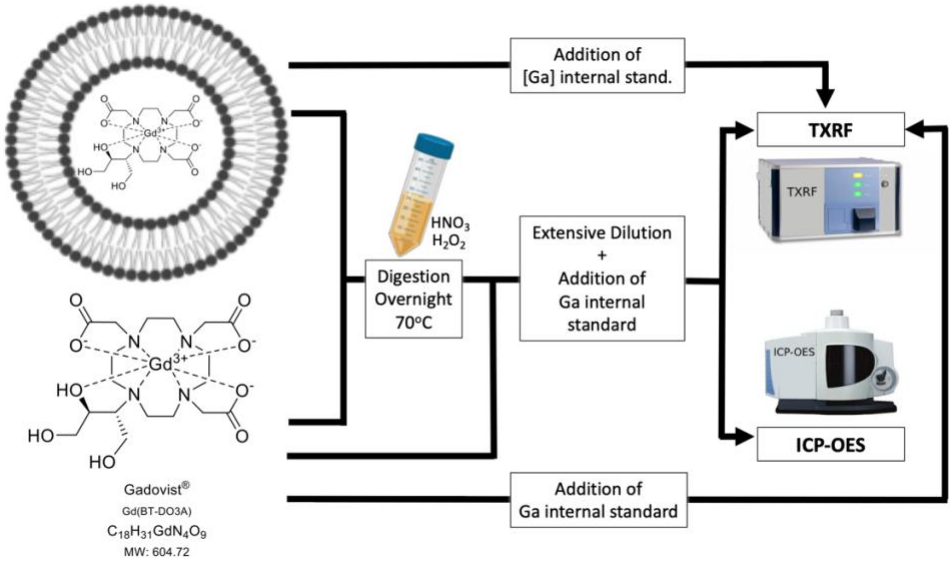

Figure 2.6: Graphical summary of the comparison of TXRF vs. ICP-OES. Gallium (Ga) is internal standard that were used in both analytical techniques.

2.3 Study Design

2.3.1 Formulation of Gadovist®-encapsulated Liposomes (GL)

Gadovist® (1.0 mmol/mL gadobutrol containing 1572.5 mg/L gadolinium; Bayer AG, Germany) was obtained to prepare Gadovist®-encapsulated liposomes **(GL)** and diluted to produce a stock solution containing 78.6 mg/L gadolinium **(Gd1)** with ultrapure water. Liposomes were prepared from DPPC, PEG^{2000}-DSPE and cholesterol were mixed in the following ratios: DPPC:PEG^{2000}-DSPE:cholestrol; 50:5:45 (mol%, 30 mg/mL total) at room temperature. The lipid film was hydrated with 1 mL of Gadovist® stock solution containing 1572.5 mg/L gadolinium. Liposome preparation is explained further in **Chapter 5.**

2.3.2 Preparation of Samples for TXRF and ICP-OES Analysis

All laboratory glassware and plastic bottles were cleaned prior to use to avoid any contamination from other metals. Following soaking in 1.4 M nitric acid for at least 2 hours, equipment was rinsed with acetone and then washed with deionised water (~18.2 MΩcm). The glassware was dried overnight in an oven at 70 ^{o}C.

To compare TXRF and ICP-OES gadolinium measurements of Gadovist®-containing solutions, Gd1 (78.60 mg/L gadolinium) had to be diluted to increase nebuliser efficiency for ICP-OES. Gd1 was diluted further with 5 w% HNO_3 to give a final gadolinium concentration of 0.51 mg/L. A high purity gallium internal standard was added to a final concentration of 1 mg/L.

The gadolinium content of GL was also assessed by both TXRF and ICP-OES. However, while TXRF can directly quantify gadolinium in GL, GL must be digested for ICP-OES analysis. Digestion was also performed on aliquots of Gd1, although digestion was not needed for analysis, to assess the influence of digestion on gadolinium quantification by both ICP-OES and TXRF.

GL and Gd1 were digested with H_2O_2 (30 w% in water) and HNO_3 (68 w% in water) in ratios of GL or Gd1:HNO_3:H_2O_2, 1:3:9 v/v, overnight at 70 ^oC in sealed Falcon tubes. Samples were weighed before and after heating to calculate water loss and the evaporated water was replaced before further dilutions. Following digestion, digested GL and Gd1 samples were diluted further with 5 w% HNO_3 in ultrapure water to provide gadolinium concentrations in the range of 0.5 to 1.0 mg/L (from preliminary TXRF measurements). Gallium internal standard was added to a final gallium concentration of 1.0 mg/L in each sample for absolute quantification.

While Gd1 had to be diluted and GL digested for ICP-OES, TXRF can directly measure gadolinium in Gd1 and GL without the need for dilution or digestion, respectively. Thus, the gallium (Ga) internal standard was added to Gd1 (78.6 mg/L gadolinium) and GL to a final concentration of 10 mg/L for TXRF. Also, to assess the reproducibility of serial TXRF-based gadolinium measurements, a GL sample was kept for 30 days and at approximately weekly intervals, three triplicates were made up as mentioned above and analysed by TXRF.

2.3.3 Statistical Analysis

All statistical analyses were performed with Graphpad Prism v 8.2.1. Values were reported as mean ± standard deviation (SD) and differences were considered significant on statistical testing if $p \leq 0.05$.

A paired Student's t-test was used to compare TXRF against ICP-OES gadolinium measurements. The one sample t-test was used to examine the difference between ICP-OES or TXRF gadolinium measurements and the expected gadolinium concentration. One-way ANOVA was used to test for reproducibility of TXRF gadolinium measurements where GL were recorded at different times.

Bland-Altman analysis was used to assess the agreement between TXRF and ICP-OES gadolinium measurements for Gd1 (both non-digested and digested samples) and digested GL samples. Bland-Altman analysis based on the quantification of the agreement between two quantitative measurements by examining the mean difference and constructing limits of agreement [219].

2.4 Results and Discussion

2.4.1 Physical Characterisation of Gadovist®-encapsulated Liposomes (GL)

The colloidal properties (size stability and polydispersity index, PDI) of GL were assessed immediately and then 30 days after formulation by dynamic light scattering (DLS) at 25 ^{o}C. The mean diameter of GLs was measured to be 141.50 ± 1.44 nm with a PDI of 0.20 ± 0.01 on formulation. The size and PDI of GL were similar on day 30 after formulation, 139.30 ± 1.04 nm ($p > 0.05$) and 0.21 ± 0.01 ($p > 0.05$), respectively, (N=3 per measurement), suggesting GL were stable for at least 30 days after formulation.

2.4.2 Comparison of TXRF and ICP-OES Measurements of Non-digested Gadovist® (Gd1) Solutions

Gadolinium gives rise to resonances at 6.059, 6.027, 6.715, 7.102 and 7.788 keV for Lα1, Lα2, Lβ1, Lβ2 and Lγ1 transitions, respectively, in the TXRF spectra obtained from Gd1 and GL. Peaks from the internal standard, gallium, were also observed at 9.224 and 9.251 keV for Kα1 and Kα2 transitions, respectively.

Gadolinium concentrations were measured to be 81.82 ± 0.80 mg/L and 81.44 ± 0.83 mg/L by TXRF and ICP-OES for Gd1, respectively, and comparable between the two techniques ($p > 0.05$, N=5 per technique). The Bland-Altman plot **(Figure 2.7)** also shows good agreement between TXRF and ICP-OES measurements of gadolinium in

non-digested Gd1 samples, with differences between each TXRF and ICP-MS within the 95% limits of agreement (± 1.96 SD). The mean difference between the pairs of measurements was 0.37 mg/L, suggesting no bias by either measurement technique for assessing gadolinium content in non-digested gadolinium samples. This translates to no significant systematic difference between two techniques.

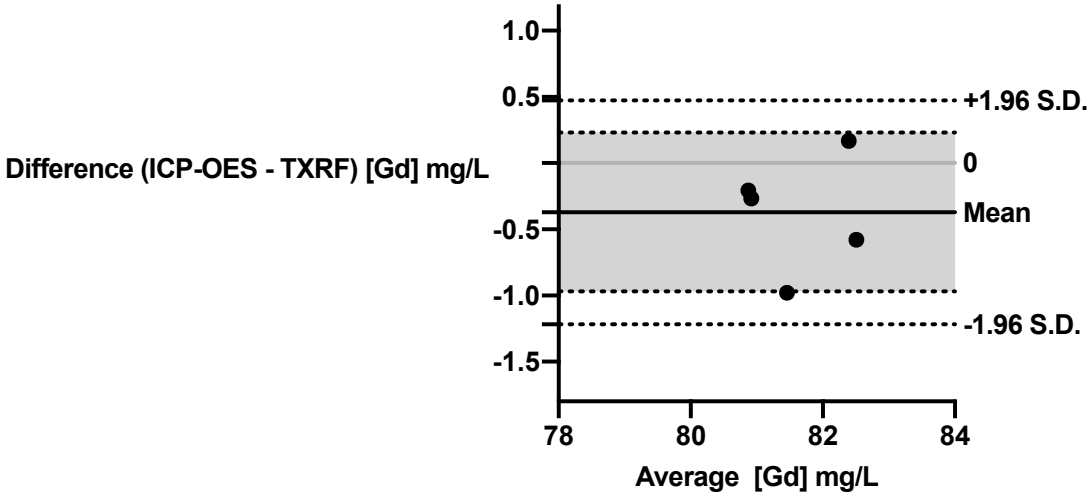

Figure 2.7: Bland-Altman analysis of gadolinium measurements by TXRF and ICP-OES of non-digested Gadovist® solution (Gd1). The average of the difference between pairs (N=5) of TXRF and ICP-OES measurements is indicated by the solid black line and the 95% limits of agreement interval (± 1.96SD), by the dotted lines. The grey line indicates equivalence between the two gadolinium measurement techniques. The shaded area shows confidence interval limits for mean.

However, gadolinium measurements by TXRF and ICP-OES were both significantly different from the known gadolinium concentration (78.60 mg/L) of Gd1 (and p = 0.0008 and p = 0.0016, respectively; N=5 per technique). The calculation of the

gadolinium concentration of Gd1 was based on the concentration obtained for Gadovist® from the manufacturer's information sheet. Thus, the significant difference between measurements and the calculated gadolinium concentration of Gd1 may partly arise from an inaccuracy in the gadolinium content provided by the manufacturer. In study of Veiga *et al.* the presence of rare earth metals in gadolinium based contrast agents (GBCAs) was investigated and results showed that all GBCAs contain impurities of rare earth metals such as terbium (Tb), europium (Eu), thulium (Tm) and lanthanum (La) [213]. However, the difference between gadolinium measurements and the known concentration is more likely to be due to errors arising from significant dilution of Gadovist® from 1572.50 mg/L to 78.60 mg/L for Gd1 and then even further dilution to 0.51 mg/L, although unnecessary for TXRF, this had to be done to be able to perform ICP-OES measurements.

2.4.3 Comparison of TXRF and ICP-OES measurements of digested Gadovist® (Gd1) solutions

Gadolinium concentrations of digested Gd1 were found to be comparable ($p > 0.05$, N=5 per technique) between the two techniques; 80.04 ± 1.61 mg/L and 82.63 ± 2.20 mg/L by TXRF and ICP-OES, respectively, similar to that demonstrated for the non-digested samples. While there was good agreement between ICP-OES and TXRF measurements according to Bland Altman analysis **(Figure 2.8)**. In particular, the 95% confidence interval of the mean difference illustrates the magnitude of the systematic difference. Since the line of equality (0) was in the interval, there was no systematic difference. However, there was a trend towards higher gadolinium

concentrations measured by ICP-OES compared to TXRF with the mean difference of the two techniques being 2.60 mg/L.

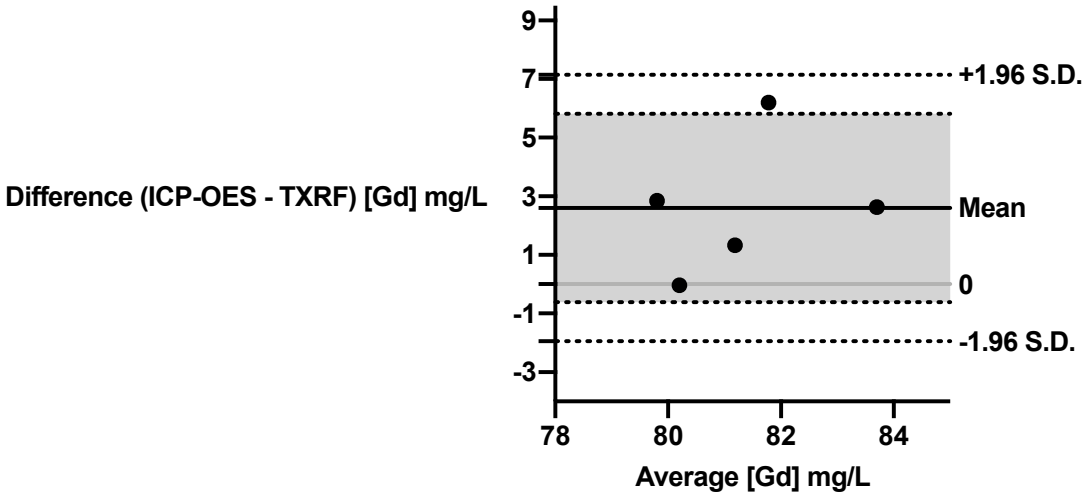

Figure 2.8: Bland-Altman analysis of TXRF and ICP-OES measurements of gadolinium content in a digested solution of Gadovist® (Gd1). The plot shows the difference between paired ICP-OES and TXRF measurements with the mean of the two paired measurements (N=5 pairs) indicated by a solid black line and the 95% limits of agreement interval from ± 1.96 SD represented by the dotted lines. The grey line indicates equivalence between the two gadolinium measurement techniques. The shaded area shows confidence interval limits for mean.

As with non-digested Gd1, gadolinium measurements of digested Gd1 by ICP-OES were significantly different from the known gadolinium concentration (78.60 mg/L; $p = 0.0148$). However, there was not significant difference with TXRF measurements of digested Gd1 ($p > 0.05$), contributing to the tendency for higher ICP-OES values compared to TXRF by Bland Altman analysis. The similarity of the TXRF measurement

of digested Gd1 to the known gadolinium concentration was unexpected, considering TXRF measurements were significantly different for non-digested Gd1. This can be explained if dilution no longer contributes to the difference between TXRF measurements and the known Gadovist® concentration. There may be a lesser effect of dilution for digested Gd1 solutions compared to the non-digested solutions as much dilution was performed at the digestion stage and undertaken by adjusting the mass of the diluent, which is more accurate than adjusting its volume. Further, after digestion (and dilution), the samples were diluted to a lesser degree than for the non-digested samples, by approximately 100-fold, rather than 150-fold. Thus, for digested samples, dilution errors may not contribute to the difference between the ICP-OES measurement and the known concentration.

The bulk composition of a sample is called matrix which can be water, acids, organic compounds, dissolved salts and solids. Matrix effect can impact the ability of an analytical method to identify and quantify target elements from samples by affecting the intensity and resolution of observed signals. All matrix effects need to be considered for results to be reliable [220].The discrepancy in ICP-OES measurements with the known gadolinium content in digested Gd1 samples may arise from matrix effects [94,220]. For digestion, samples were digested with combined HNO_3 and H_2O_2 and while an attempt was made to match matrices of the calibration solutions, acid content is still likely to be variable. Furthermore, Gadovist® itself does not solely contain gadobutrol in water, the solution also contains sodium calcobutrol, trometamol and 1M hydrochloric acid (according to manufacturer's product

information) which can interfere with measurement as again they were not included in the calibration solutions. Thus, we suggest that matrix differences due to digestion procedures may be the major contributor to the discrepancy in the ICP-OES measurement of digested Gd1.

2.4.4 Comparison of TXRF and ICP-OES Measurements of Gadovist®-encapsulated Liposomes (GL)

Gadovist®-encapsulated Liposomes (GL) were digested for gadolinium quantification and gadolinium concentrations were similar ($p > 0.05$) by TXRF (105.14 ± 1.96 mg/L) and ICP-OES (108.11 ± 2.15 mg/L; N=5 per technique). Again, as with the digested Gd1 data, there was a trend of higher gadolinium measurements by ICP-OES compared to TXRF. This was also indicated by the Bland Altman analysis where the average mean difference between the paired measurements was 2.97 mg/L, although agreement between the two assay methods were within 95% limits **(Figure 2.9)**.

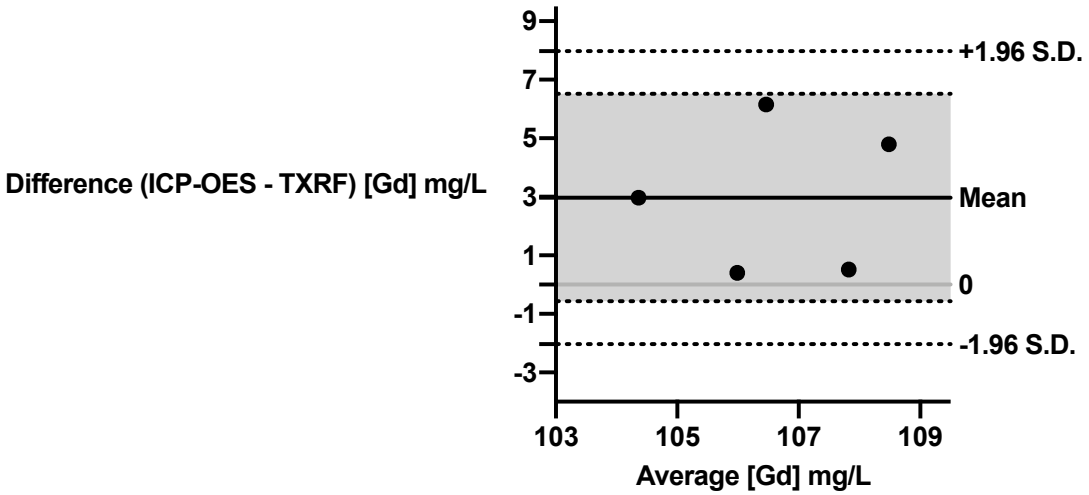

Figure 2.9: Bland-Altman analysis of digested GL showing differences between paired ICP-OES and TXRF gadolinium measurements, with the average of the difference in the paired measurements (N=5 pairs) indicated by the solid black line and the 95% limits of agreement interval (± 1.96 SD) by the dotted lines. The grey line indicates equivalence between the two gadolinium measurement techniques. The shaded area shows confidence interval limits for mean.

2.4.5 Accuracy of TXRF-Gadolinium Measurements of non-digested Gd1

Gd1 had to be greatly diluted (approximately by a factor of 150) for ICP-OES analysis but this was unnecessary for TXRF. Thus, TXRF analysis was performed with minimal dilution of Gd1 to exclude errors due to extensive dilution. Direct TXRF gadolinium measurements of Gd1 were 78.51 mg/L gadolinium, and comparable to the known Gd1 concentration, 78.60 mg/L (one sample t-test; $p > 0.05$, N=5). This suggests differences between our ICP-OES gadolinium measurements from the known Gd1

were largely due to errors in dilution and sample digestion. Indeed, the risk of error in trace elemental analysis increases with decreasing content in the sample, digestion and significant sample dilution, and of course, increased likelihood of contamination with increasing number of sample preparation steps [94].

2.4.6 Reproducibility of TXRF-Gadolinium Measurements of Non-digested GL

TXRF measurements of gadolinium in aliquots of a single sample of GL at three different times during the first 30 days after formulation were found to be similar, 102.70 ± 0.15 mg/L, 102.10 ± 0.58 mg/L and 102.60 ± 0.22 mg/L ($p > 0.05$, N=3 per timepoint, one-way ANOVA test). Thus, TXRF can be used to regularly used to rapidly assess gadolinium in GLs, without the need for large sampling volumes, significant dilution of samples and sample digestion.

2.5 Conclusions

In conclusion, TXRF provide gadolinium measurements of GL comparable to that by ICP-OES and may even be considered superior to the latter as samples do not need to be digested, significantly diluted, or require complex matrix-matching with calibration standards to ensure accurate measurement. The minimum sample preparation required for TXRF as well as minimising measurement errors, reduces the use of hazardous chemicals and renders TXRF to be a relatively rapid and environmentally friendly technique. Alongside its low operating cost, these characteristics of TXRF analysis suggest the technique is well suited to metal determinations, particularly for analysis of samples that would require digestion prior to analysis by ICP-hyphenated methods, the current elemental analysis technique of choice.

Due to the aforementioned desirable properties, the TXRF was widely used for elemental analysis throughout my project including *in vitro* and *in vivo* experiments.

3. Synthesis and Analysis of Gadolinium Lipids for MRI Contrast Enhancement

3.1 Introduction

Magnetic Resonance Imaging (MRI) provides excellent soft tissue contrast and specificity with high spatial resolution as well as good tissue penetration, which can detect abnormalities in anatomy, pathology, and functionality in the body [221]. Contrast in MRI depends on the main three factors: the water proton density (structure of the tissue), longitudinal relaxation time (T_1) and the transverse relaxation time (T_2) of the water protons. The enhancement of the image contrast between normal tissue and diseased tissue has been improved with the use of contrast agents.

MRI contrast agents are biocompatible magnetic materials which can decrease the relaxation times of surrounding water protons in tissue of interest, and as a result enhance the image contrast [35,222]. Therefore, MRI contrast agents have been commonly used to identify tumours at early stages. According to the relaxation mechanism and magnetic characteristics; MRI contrast agents are divided into two parts: T_1 (longitudinal) and T_2 (transverse) contrast agents [12,17,19]. In both cases, contrast agents reduce the relaxation times (T_1 or T_2) of surrounding water protons.

These contrast agents are either paramagnetic such as metal ion complexes synthesized with a lanthanide or transition metal e.g. gadolinium (Gd^{3+})/manganese (Mn^{2+}), or superparamagnetic such as iron oxide nanoparticles (**Table 3.1**) [17]. By changing the concentration of the contrast agent, the proton relaxation rate ($R_{1,2}$:

equivalent to $1/T_{1,2}$) also changes. This rate of change is defined as relaxation efficiency or 'relaxivity'. Thus; relaxivity shows the contrast agents' ability to increase the relaxation rate of the water protons. It has units of $mM^{-1}.s^{-1}$ [16–19]. Relaxivity is dependent on the size and chemical structure of the contrast agent and the water accessibility into the magnetic centre [16].

Contrast Agent Type	Function	Additional Information
Manganese	T_1 signal enhancement (brightening positive signal intensity in image), T_2 signal enhancement also observed	These agents have been used in the detection of liver lesions. They have also been used in animal studies to detect the brain anatomy and activity [17,223]
Iron oxide	T_2 signal enhancement (darkening negative signal intensity in image)	Superparamagnetic iron oxide (SPION) has received great attention as a liver contrast agent. Also, it was the first nanoparticle MRI contrast agent [17,51]
Gadolinium	Predominantly T_1 signal enhancement, T_2 signal enhancement also observed	Most widely used type of contrast agent. Primarily used to enhance vasculature and particularly useful for contrasting lesions/tumors. Nanoparticles and macromolecules that are containing Gd^{3+} have been developed as a new generation of contrast agents [17,19,224]

Table 3.1: The three major types of contrast agents used in MRI, their function, and primary clinical usage [17,19,35].

Since 1988, MRI contrast agents have received clinical validation in imaging and diagnosis. To date; most clinically approved and used contrast agents are gadolinium (Gd) chelates (4,9). Gadolinium-based contrast agents increase both T_1 and T_2 relaxation rates, however the dominant effect is on T_1 relaxation [16]. According to Burtea *et al.,* the contrast agents should demonstrate the following requirements for clinical MRI applications: sufficient relaxivity; safety; low toxicity; kinetic and thermodynamic stability; optimal biodistribution; elimination and metabolism [16].

Gadolinium (Gd) has 7 unpaired electrons, which accounts for the strong paramagnetism. This allows gadolinium cations to contribute in localised water proton relaxation due to the cations' high magnetic moment [19,35]. However, free Gd^{+3} is toxic because it has an ionic radius is similar to Ca^{2+}. This leads to competition between two ions in biological systems that requires Ca^{2+} in order to function (e.g. voltage-gated calcium channels) and since Gd^{3+} may have a higher binding affinity, this can block the systems' activities. The LD_{50} (the lethal dose that kills 50 % of the test animals) of $GdCl_3$ was observed to be 0.2 $mmol.kg^{-1}$ in mice [225,226]. It is therefore crucial to strongly chelate Gd^{3+} to ligands to prepare biocompatible contrast agents with reduced toxicity [29,50,227].

There are multiple parameters governing the relaxation time of the water molecules in the presence of the gadolinium-based contrast agents (GBCAs) **(Figure 3.1).** The key parameters that are influencing the longitudinal relaxivity are; hydration number (q), the water residency time (τ_M) and the rotational correlation time (τ_R) [20,34,71].

Hydration number is the number of the water molecules that are bound to the Gd^{3+} ion directly [61]. Whereas, the τ_M determines the amount of water molecules that can effectively coordinate with Gd^{3+} ions to reduce their T_1 relaxation time, in other words it is the efficiency of the water exchange rate [36] Furthermore, the τ_R is used to describe the characteristic rotational motion of the Gd-complexes, whereas the tumbling of the paramagnetic complex results in a fluctuating magnetic field that induces relaxation of water molecules. Therefore, T_1 relaxation is increasingly effective when the paramagnetic complexes tumble slowly, with the frequency of the fluctuating field closer to the Larmor frequency [34]. These parameters deserve our ongoing attention and can be tuned while designing novel GBCAs.

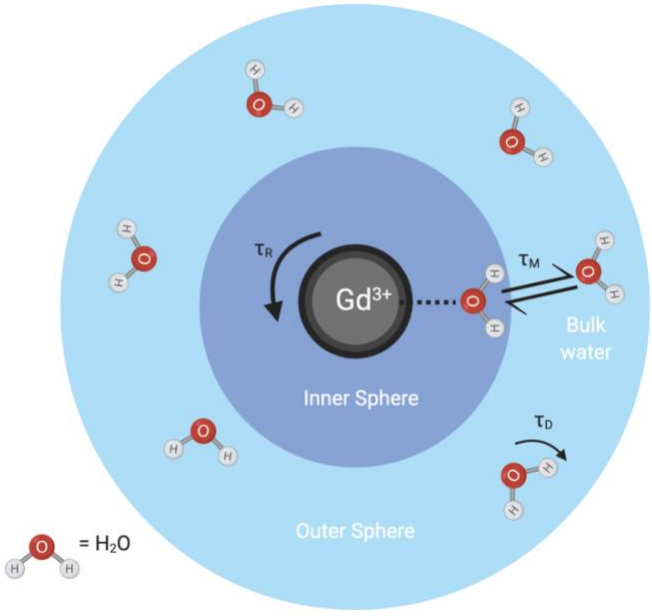

Figure 3.1: Schematic representation of inner and outer sphere water interactions with gadolinium including associated parameters: τ_M: water residency time, τ_R: rotational correlation time and τD: translational diffusion. Created with BioRender.com

Previous generation GBCAs used linear (open ring) DTPA (diethylenetriamine pentaacetic acid) derivatives as a chelator. In particular, [Gd]DTPA (Magnevist®) was the first globally available MRI contrast agent and since then 10 more GBCAs have been developed and become commercially available and the most common GBCAs are shown in **Chapter 1: Figure 1.5** [225]. However, [227] recent concern over the link between nephrogenic systemic fibrosis and released Gd^{3+} ions has meant that stronger chelation with closed ring or cage ligands are now preferred **(see Chapter 1.2.2)** [29]. These are commonly based on the DOTA (tetraaza-cyclododecane tetraacetic acid) macrocycle or similar. The tendency of the linear contrast agents to leach Gd^{3+} under biological conditions and the associated potential toxicity due to transmetallation (i.e. gadolinium deposition in the skin, bone and liver in long-term studies) has resulted in the limitation of their use or withdrawal from the European market due to safety concerns [47,48]. In the USA, the Food and Drug Administration (FDA) has requested new class warnings and patient medication guides to be produced for gadolinium-based contrast agents, informing patients of the potential toxicity of these products [48,49]. Therefore, small macrocyclic gadolinium-containing contrast agents (e.g. Gadovist® or ProHance®, see **Figure 1.5**) are commonly used to enhance blood or tissue visibility and differentiation in clinical MRI. According to the Caravan *et al*., administration of small molecule contrast agents with low molecular weight often results in non-specific biodistribution and fast renal excretion [35]. Equivalent chelated gadolinium complexes may also be attached to larger macromolecular structures. By extension, molecular tumbling decreases therefore the T_1 relaxivity increases [69,228]. For example, among the commercially available contrast agents, MS-325 (gadofosveset trisodium) was

designed to bind to human serum albumin and hence acts as a blood pool agent. The binding of MS-325 to the serum albumin increases the rotational correlation time, due to the larger size and therefore T_1 molar relaxivity increases significantly relative to its unbound form [64]. Moreover, incorporation of multiple Gd-chelates to a nanoparticle demonstrates further increment of r_1 and prolonged blood circulation time compared with low molecular weight GBCAs. Furthermore, nanoparticles benefit from the enhanced permeability and retention (EPR) effect that facilitates passive accumulation of a nanoparticle payload in tumour tissues [68,69,229]. Gadolinium chelates have been attached to various nanoparticles such as dendrimers, micelles, as well as liposomes, which have been studied extensively in the literature, however liposomes are the focus of this report [18,35,68–70,82,85,229].

In this context, liposomal nanoparticles can incorporate many gadolinium chelates, also their functional properties can be tuned to meet specific needs of next generation MRI contrast agents as well as therapeutic applications for drug delivery [82,230]. One approach for the incorporation of the gadolinium chelates into liposomes is to encapsulate hydrophilic small molecule GBCAs into the aqueous core. However, the encapsulation approach limits the accessibility of gadolinium complexes by the surrounding bulk water protons due to the poor water permeability of the membrane, which results in the reduction of the longitudinal relaxivity (r_1) in contrast to unencapsulated agents [70,72]. However, such liposomes can be used in membrane permeability studies. In particular, De Smet *et al*. have

reported a thermosensitive liposomal formulation of doxorubicin and co-encapsulated with a paramagnetic contrast agent (ProHance®). In this system, MRI was used to monitor the phase transition temperature (T_m) whilst also releasing the doxorubicin and the authors confirmed drug release as contrast enhancement increased, post treatment with focused ultrasound (FUS) [76,77].

The incorporation of lipidic MRI contrast agents into the lipid bilayer is another approach which enhances the r_1. This is due to gadolinium chelates on the outer surface having easy access to the bulk water compared to the encapsulated Gd-chelates [19,70]. Moreover, the slow tumbling motion of liposomes also contributes to enhancement of T_1 relaxivity [231]. As mentioned in the introduction of this thesis, Kabalka *et al.* were the pioneers that demonstrated incorporation of [Gd]DTPA derivatives onto the liposome membrane to enhance T_1 relaxivity [80,81]. This thesis continues investigating the paramagnetic liposomes that were suggested by Kamaly *et al.* who have synthesized a macrocyclic Gd-based lipid ([Gd]DOTA.DSA) [83,232].

The relaxation properties of paramagnetic PEGylated liposomes containing Gd-lipids ([Gd]DTPA derivatives) were investigated as a function of composition, temperature and magnetic field strength by Strijkers *et al*. [20]. They have characterized paramagnetic liposomes with DSPC (saturated) and DOPC (unsaturated) phospholipids and with or without cholesterol. All aforementioned liposomes with Gd-lipid have shown higher T_1 molar relaxivity compared to traditional Magnevist® ([Gd]DTPA) at 200 MHz and at variable temperatures (298, 310, and 333 K).

Moreover, they have observed that T_1 relaxivity of Gd-lipid containing liposomes increases as the temperature increases. This is a result of decreased water residency time due to the increased permeability of the membrane (as they reach to phase transition temperature the permeability increases). On the other hand, T_1 relaxivity of Magnevist® decreases with increasing temperature as they tumble faster at increased temperature. The highest molar relaxivity (r_1) of 11.3 $mM^{-1}s^{-1}$ was observed with PEGylated paramagnetic liposomes made of cholesterol and unsaturated DOPC at 25 MHz [20]. Incorporating PEG coat into the liposome's membrane is important to achieve prolonged blood circulation time while reducing the reticuloendothelial system (RES) mediated uptake [206]. Consequently, this can improve the tumour accumulation by the EPR effect [20,71,82].

In another study, Mitchell *et al.* have synthesised various Gd-lipids with spacers (n-ethylene glycol) of different lengths between the head group (DOTA) and the lipid moiety, then incorporated into liposomes. The liposomes with longest spacer showed lower T_1 relaxivity compared to lipids with shorter spacers, due to the greater motility of the spacer as it gets longer [233]. It is important to restrict the local motion of the gadolinium chelate and fix it rigidly to the liposome's outer surface while liposomes are tumbling slowly **(Figure 3.1)** [233]. Thus, in order to enhance the T_1 relaxivity it is important to consider the water accessibility to the Gd^{3+} ion, while restricting the local motion of the Gd-chelate which decreases the effective tumbling rate of liposomes [82,233].

Based upon the studies shown in the literature, the T_1 molar relaxivity of Gd-lipid incorporated liposomes depends on the composition, size and stability of liposomes which reflects on several MRI parameters as shown in **Figure 3.1** [20,71,231]. In addition, the optimal liposome formulation in terms of relaxivity does not necessarily match the desired formulation for optimal biological behaviour (*i.e.* distribution, pharmacokinetics). Thus, lipid composition should be tuned accordingly to find the appropriate liposome design for the intended use.

Previously our group has reported a novel thermosensitive paramagnetic liposome for drug delivery with incorporation of [Gd]DOTA.DSA lipid [194] In this study, it was aimed to improve the MRI contrast of the same formulation by designing and synthesising an alternative novel lipidic contrast agent via the attachment of hydrocarbon chain spacers in different lengths between the DOTA head group and DSA lipid tail. Furthermore, the influence of the length of the spacer on MRI molar relaxivities of liposomes were examined for the image-guided thermosensitive drug delivery system.

3.2 Aim and Objectives:

Aim: To synthesise gadolinium chelated lipidic contrast agents for liposomal formulation with different lengths of spacers between the head group (DOTA) and the lipid tail (DSA) to improve the MRI T_1 relaxivity.

Objective 1: Synthesis of the main Gd-lipid; [Gd]DOTA.DSA.

Objective 2: Synthesis of the alternative Gd-lipids, derived from the main lipid, with differentiating spacers between the DOTA head group and the DSA lipid tail.

Objective 3: To prepare and characterise paramagnetic liposomes that were formulated with the Gd-lipids.

Objective 4: To assess the paramagnetic liposomes for T_1/T_2 relaxivities and compare with the macrocyclic MRI contrast agent; Gadovist®.

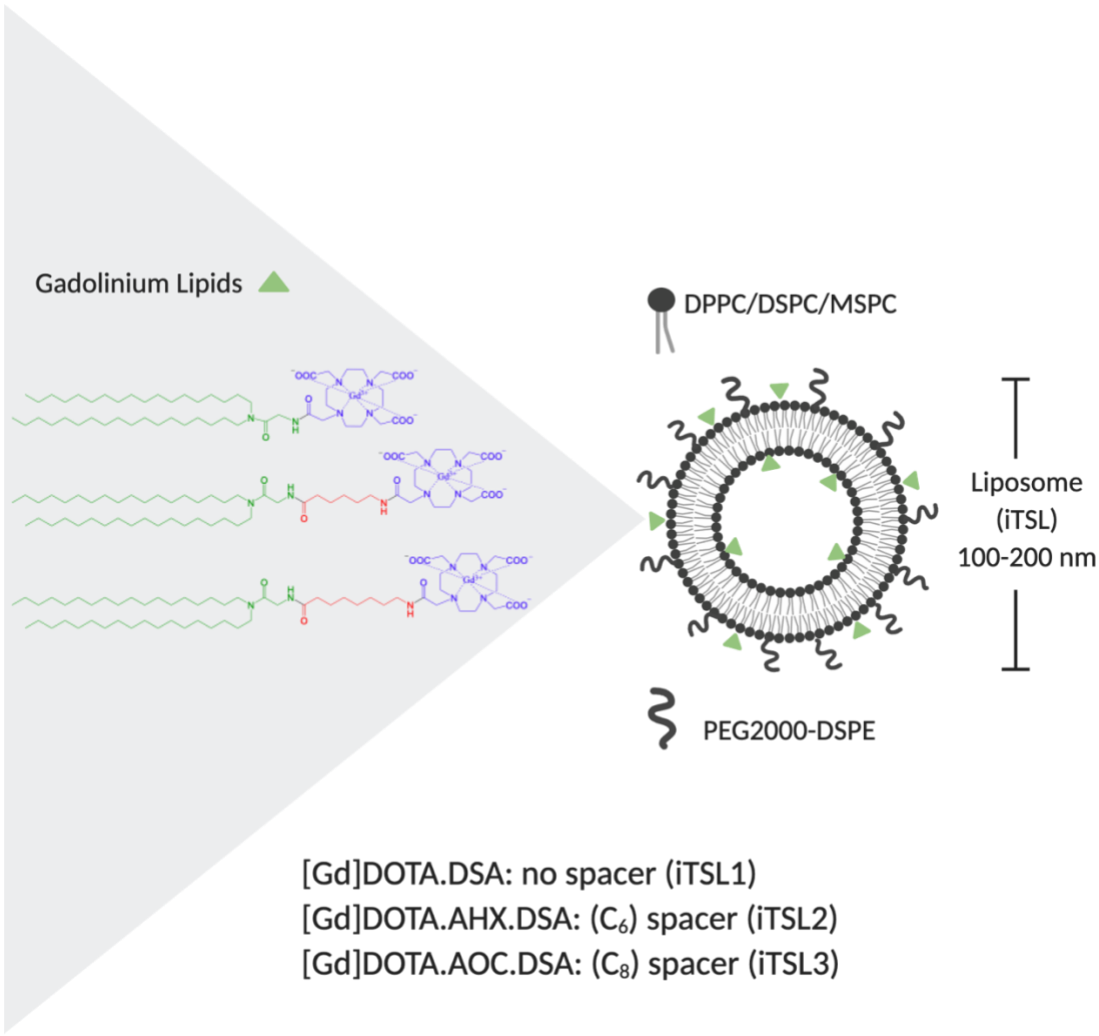

Figure 3.2:Graphical representation of the PEGylated liposomes incorporated with Gd lipids as MRI contrast agents for MRI guided drug delivery system. Created with BioRender.com

3.3 Study Design

Liposomes that are decorated with gadolinium-based lipidic contrast agents have been studied by several research groups over the last 20 years [82]. However, the majority of these studies have been based on the linear chelator head group, e.g. using DTPA. This can be related to the fact that [Gd]DTPA was the first MRI contrast agent clinically approved by the FDA [82]. Due to its recent safety concerns we have selected a stronger chelating ligand; a macrocyclic (DOTA), to encapsulate Gd^{3+} ion in order to attach to our liposomal drug delivery system. Therefore, the [Gd]DOTA head group was conjugated with a saturated 18-carbon long alkyl chain via the amide functional group to form a lipid-like Gd-complex, [Gd]DOTA.DSA, which has been previously designed by Kamaly *et al*. and recently reported by our group Centelles *et al*. [83,194]. Additionally, two novel gadolinium chelated lipids with hydrocarbon chain spacers (hexyl, octyl) were designed and synthesized *in house* as an alternative to the [Gd]DOTA.DSA lipid; [Gd]DOTA.AHX.DSA and [Gd]DOTA.AOC.DSA (AHX: amino-hexanoic- and AOC: amino-octanoic-) **(Scheme 3.1).** Then, the aforementioned lipids were formulated into liposomes with same lipid ratios and named as following (iTSL= image guided thermosensitive liposome): iTSL1 with [Gd]DOTA.DSA lipid, iTSL2 with [Gd]DOTA.AHX.DSA lipid, iTSL3 with [Gd]DOTA.AOC.DSA lipid. In short, the aim of this study is to increase the distance between the [Gd]DOTA and the liposome surface for improved water accessibility in order to identify contrast agents better suited to MRI studies.

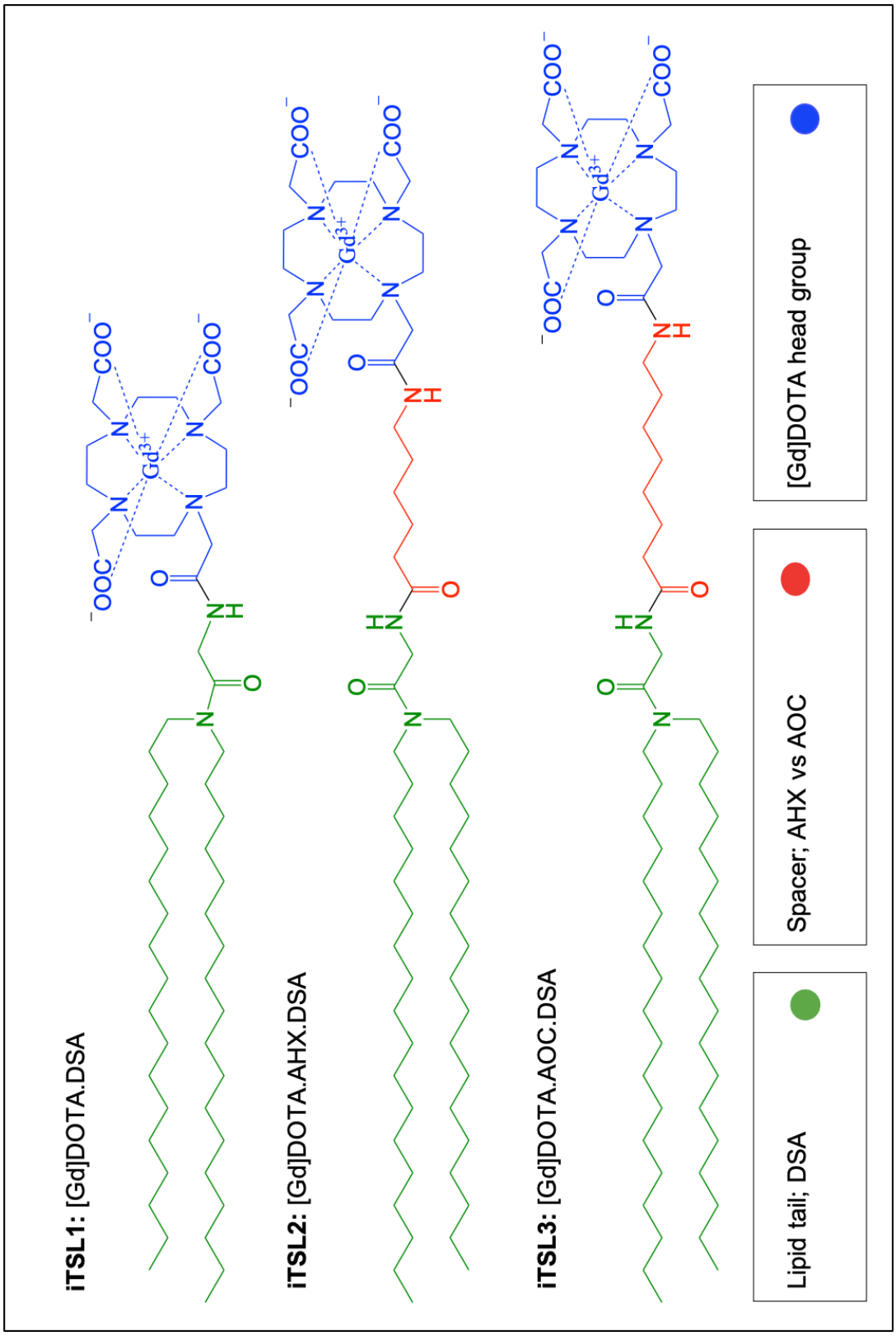

Scheme 3.1: The chemical structures of three distinctive paramagnetic lipids that were formulated into liposomes.

3.4 Results and Discussion

3.4.1 Synthesis of Gadolinium Lipids

The synthetic route for all three lipids starts with DSA (*N,N*-distearylamidomethylamine). The amide coupling of dioctadecylamine **(1)** and BOC-Gly-OH (*tert*-butyloxycarbonyl) was achieved with *N*,*N*,*N*′,*N*′-tetramethyl-*O*-(1*H*-benzotriazol-1-yl)uranium hexafluorophosphate (HBTU) and 4-(dimethylamino)pyridine (DMAP). This was followed by the removal of the BOC protecting group with trifluoroacetic acid (TFA) to yield DSA, **(3), Scheme 3.2** shows the schematic representation of the reaction.

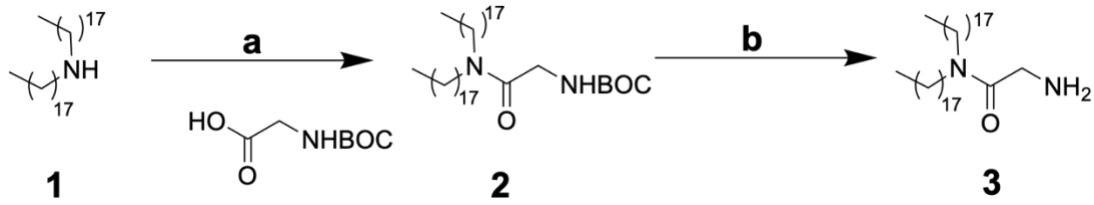

Scheme 3.2: Schematic representation of synthesis of DSA **(3).** Reagents and conditions: **a.** HBTU, DMAP, dry DCM, RT, 24h, **(2)** 95%; **b.** dry DCM, TFA, RT, 12h, **(3)** 97%.

The macrocyclic ligand DOTA-NHS was conjugated to the amine group of the DSA followed by chelation of Gd^{3+} ($GdCl_3.6H_2O$) under reflux at 90°C to form [Gd]DOTA.DSA as shown in **Scheme 3.3.**

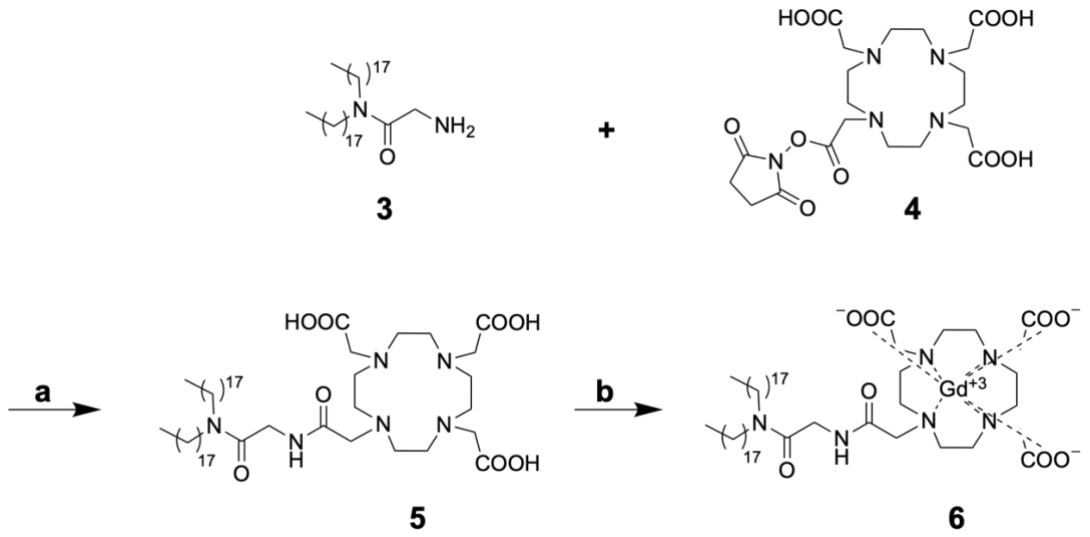

Scheme 3.3: Schematic representation of synthesis of [Gd]DOTA.DSA, **(6)**. Reagents and conditions: **a.** TEA, dry DCM, 35^{o}C, 12h, **(5)** 49%; **b.** $GdCl_3.6H_2O$, H_2O, 90^{o}C, 12h, **(6)** 95%.

The spacer attachment for both lipids attached using standard HBTU/DMAP peptide bond formation from BOC-protected commercial agents; 6-(BOC-amino)hexanoic acid (BOC-AHX-OH) or 8-(BOC-amino)octanoic acid (BOC-AOC-OH) **(Scheme 3.4).** Procedures for the DOTA coupling reaction and the gadolinium metal loading were similar for all, as reported for [Gd]DOTA.DSA **(Scheme 3.3).** Reactions were designed and lipids were prepared by courtesy of Dr. Michael Wright and Mr. Paul Cressey. Reactions were monitored by TLC, mass spectroscopy (see NMR and Mass spectrum **Appendix 5**).

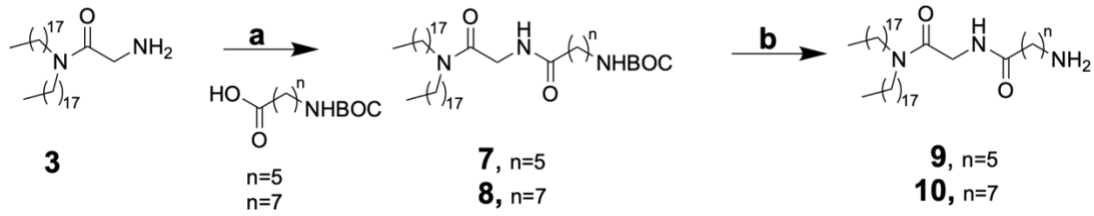

Scheme 3.4: Schematic representation of synthesis of lipid tail with spacer; AHX.DSA **(9)** and AOC.DSA **(10). a.** HBTU/DMAP activated attachment of 6-(BOC-amino)hexanoic acid (BOC-AHX-OH) or 8-(BOC-amino)octanoic acid. (BOC-AOC-OH) **b.** TFA.

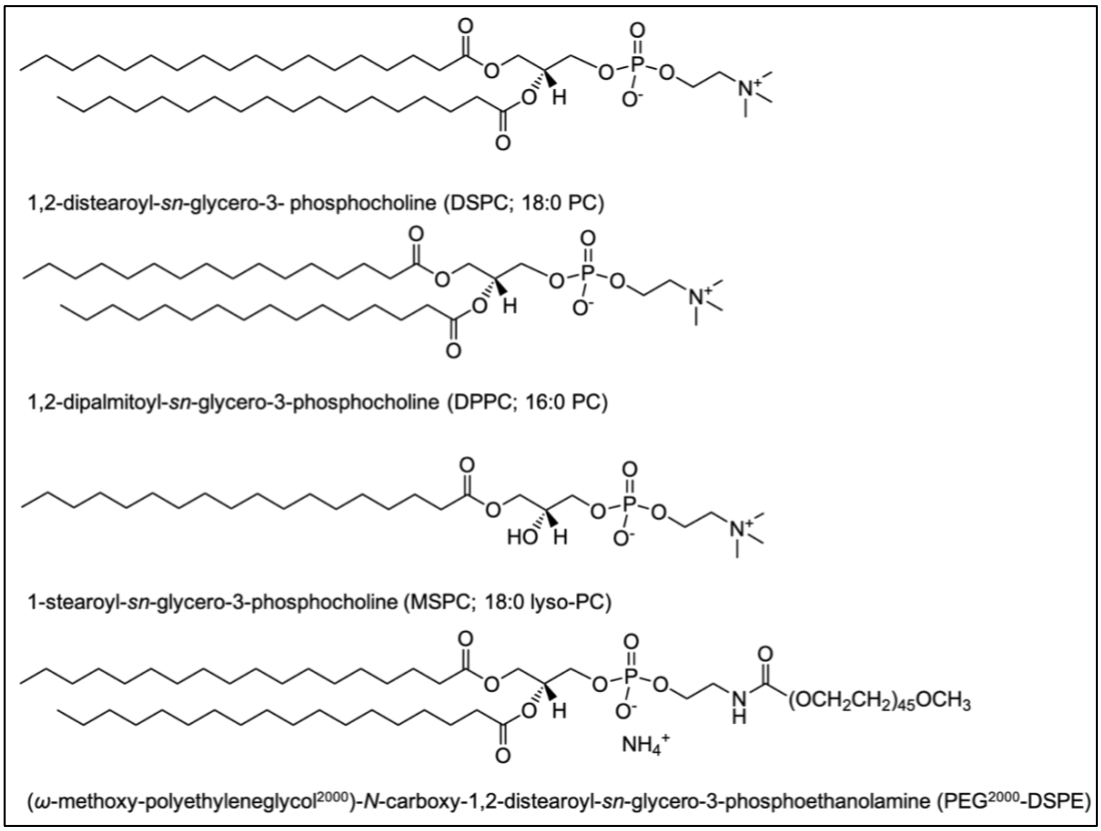

Scheme 3.5: The chemical structures of commercial lipids that were used in the liposome formulations.

3.4.2 Paramagnetic Liposomes (iTSL1, iTSL2, and iTSL3)

iTSL1, iTSL2 and iTSL3 were prepared with the following lipids and ratios; **[Gd]lipids**:DPPC:DSPC:MSPC:PEG^{2000}-DSPE:CF750.DSA (30:53.95:5:5:6:0.05 mol%) **(Scheme 3.5)**

Lipid composition was kept similar for each formulation with variance of the Gd-lipid in order to understand the paramagnetic and the physical characteristics of a particular lipid in a set formulation. Remembering that these lipids have been designed to be of value in image-guided thermosensitive liposomal drug delivery. Also, the lipid content of this selected formulation was previously optimised for the specific [Gd]DOTA.DSA lipid and demonstrated as a thermosensitive drug delivery vesicle by our group [194]. Preparation of the liposomes is demonstrated in the **Figure 3.3.**

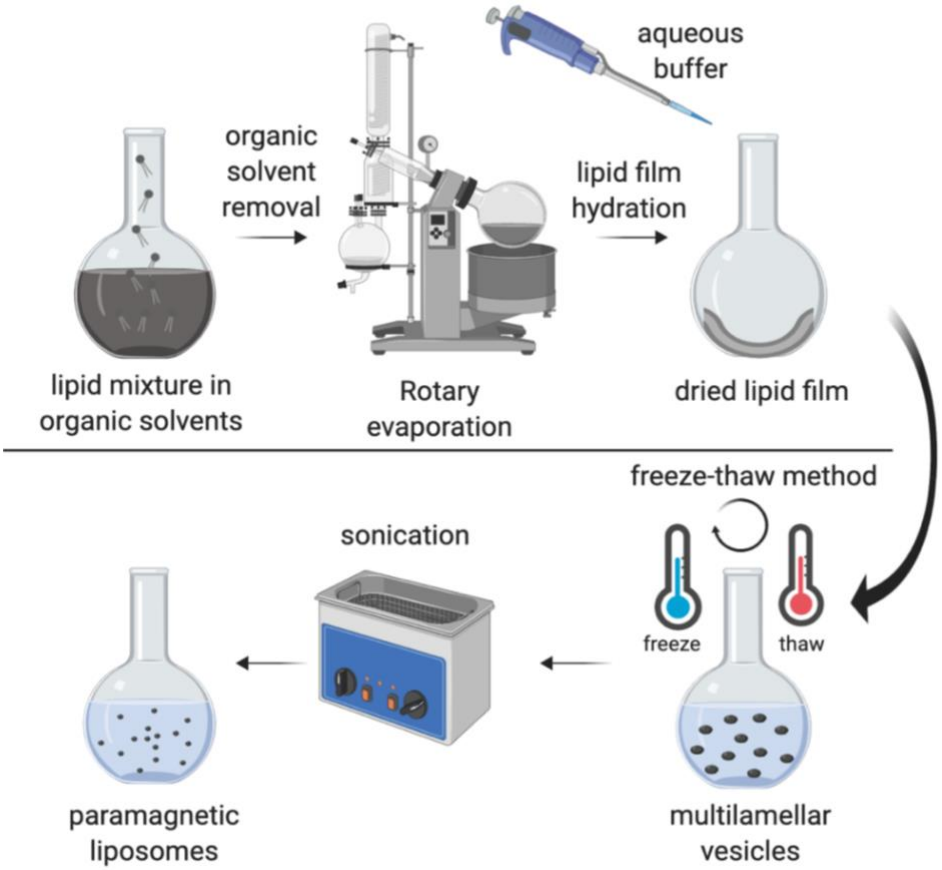

Figure 3.3: Illustration for the preparation of paramagnetic liposome by the freeze-thaw method. The 30 mg lipid film was hydrated in 50 mM HEPES, 5 w% glucose at pH 7.4 (1 mL). After hydration the liposomes were freeze-thawed to breakup of the lipid film and then sonicated further to form paramagnetic liposomes with the desired size and PDI. Created with BioRender.com

Liposomal nanoparticle mean size and polydispersity index (PDI) were measured by Dynamic Light Scattering (DLS). It was aimed to obtain particle sizes less than 200 nm, which was successfully achieved. It was observed that liposomes with spacers, iTSL2

and iTSL3 (both are 110 ± 1 nm), were smaller in size compared to iTSL1 (177 ± 2 nm) **(Table 3.2).** These results from this batch are representative of the trend size of synthesized liposomes. Thus, the short alkyl chain spacers could be affecting the steric bulk of the DOTA head group which promotes the curvature pressure of the lipid and forms smaller liposomes [234,235]. Molecular dynamic studies are required to understand the importance of lipid structure and its effects on size [236]. The PDI values were between 0.14 – 0.34. The variable size and PDI values observed are due to the fact that we avoided using extrusion. Extrusion is a technique that is used by us and others to prepare homogenous size distribution of liposomes. This has the potential of decreasing the lipid content of liposomes extruded through membranes of small pore size as lipids can be removed from the lipid bilayer due to increased temperature and pressure [237]. Hence, avoiding the extrusion step prevents any possible dilution effect and Gd-lipid loss. The zeta (ζ) potential measurements were carried out to determine the charge of the liposomes which was expected to be neutral. The measurements have confirmed that the ζ-potentials of liposomes remained almost constant regardless of the addition of a spacer where all three liposome formulations were found to be neutral, i.e. iTSL1 -2.43 ± 0.18 mV, iTSL2 -1.62 ± 0.12 mV and iTSL3 -1.29 ± 0.46 mV (N=5). The same batch of liposomes were used in all experiments in **Chapter 3** to ensure consistency.

The determination of gadolinium concentration of liposomes is crucial to perform a comparable relaxometry study. Therefore, iTSL1-3 samples were mixed with an internal standard (gallium 10mg/L) and elemental analyses were carried out with

total reflection x-ray fluorescence (TXRF) in triplicates. Results in **Table 3.2** below. Pertinently, Gd concentrations were similar for all formulations.

Liposomes	z-average size (nm)	PDI	Zeta-potential (mV)	Gadolinium concentration (mg/L)	Theoretical [Gd] (mg/L)
iTSL1 ([Gd]DOTA.DSA)	177 ± 2	0.34 ± 0.03	- 2.43 ± 0.18	1360 ± 13	1465 (92.9 ± 0.9 %)
iTSL2 ([Gd]DOTA.AHX.DSA)	110 ± 1	0.22 ± 0.01	- 1.62 ± 0.12	1322 ± 16	1558 (84.9 ± 1.0 %)
iTSL3 ([Gd]DOTA.AOC.DSA)	110 ± 1	0.14 ± 0.01	-1.29 ± 0.46	1340 ± 8	1580 (84.8 ± 0.5 %)

Table 3.2: The data was collected for sizing by dynamic light scattering; for zeta potential by a zeta potential analyser; gadolinium concentrations were obtained by TXRF measurements using gallium (Ga) internal standard (final concentration of Ga was 10 mg/L) (N=5).

The main phase transition temperature (T_m) represents a key node in the occurrence of temperature-triggered drug release in the thermosensitive liposomal drug delivery concept. At the onset of the phase transition, the structure of the lipid bilayer starts to change from a solid gel phase to a liquid-crystalline state which increases its permeability to water and facilitates the drug release [136,238]. In order to understand the impact of the type of the spacers on thermosensitive characteristics of the liposomes, liquid-phase differential scanning calorimetry (DSC) thermograms

were collected with 100-fold diluted samples. Three rounds of sequential heating-cooling cycles were applied and recorded in the temperature range of 25-65 °C at a rate of 1 °C per minute, and normalised heating thermographs of iTSL1-3 formulations were shown in **Figure 3.4.**

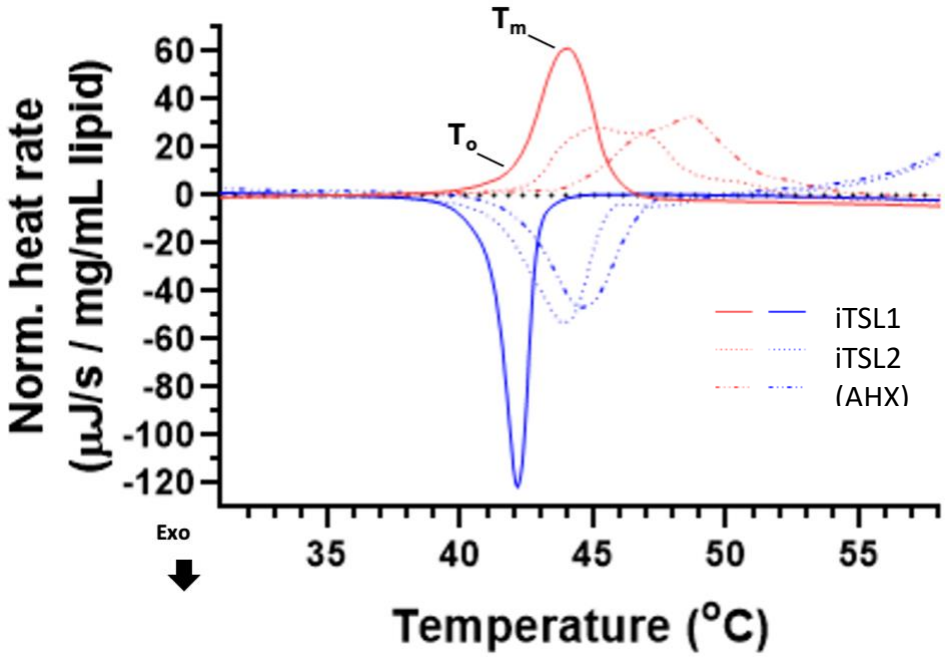

Figure 3.4**:** Thermographs of iTSL liposomes using liquid-phase differential scanning calorimetry. Measurement included 3x heating-cooling cycles; 25-65 °C at 1 °C/min. The range shown is reduced to omit the usual start-up spikes. Key thermosensitivity parameters are the heating curve peak (T_m) and onset (T_o; 5 % of the peak intensity) temperatures. T_o/T_m: iTSL1 41.1/44.1; iTSL2 (AHX) 43.1/48.8; iTSL3 (AOC) 41.5/45.4 all ± 0.3 °C.

The resulting peaks in DSC are mainly due to lipid phase changes in the liposome's membrane. The alkyl chain attachment as a spacer to the Gd-lipid had a significant impact on the T_m of the liposomal formulation. The T_m point of the iTSL1 liposomes without any spacer was 44.1 ^oC. However, with the addition of spacers, T_m point was shifted to 48.8 ^oC with iTSL2 and 45.4 ^oC with iTSL3. The significant effect of the spacer on the T_m of liposomes was unexpected. Besides, the phase transition intervals have also occurred in a wider temperature range than iTSL1 for iTSL2 and iTSL3. DSC findings implicate that iTSL2 and iTSL3 need higher temperatures to release the drug. However, applying a temperature higher than the mild hyperthermia (43 ^oC) brings a risk of heating the tissues to a necrotic level, which indicates that the thermal response of novel Gd-lipid containing liposomes needs to be improved for further studies [135]. It should be noted that the composition and molar ratios of the lipids of the liposome formulation (iTSL1-3) were previously tailored specifically for the [Gd]DOTA.DSA lipid to induce the drug under the mild hyperthermia range of 42-43 ^oC by optimising the appropriate lipids with appropriate ratios.

3.4.3 MRI Studies with Gadolinium Liposomes (iTSL1-3)

In the present study, the MRI contrast sensitivities of liposomes composed of Gd-lipids were investigated (iTSL1-3). NMR relaxometry studies of the iTSL1-3 liposomes in aqueous suspension were performed to detect MRI relaxation times and T_1 relaxivity (r_1) values were calculated accordingly. The molar relaxivities of iTSL1-3 were compared to a clinically relevant contrast agent Gadovist® (gadobutrol) using a

Bruker Advance 400 MHz spectrometer (9.4 T) at 25 ^{o}C. T_1 relaxation times were obtained with standard saturation recovery sequence.

Gadovist® positive control and iTSL1-3 liposomes were serially diluted into 50 mM HEPES, 5 w% glucose, 10 v% D_2O at pH 7.4 at 25^{o}C. The final gadolinium concentrations were in the range of 4.16 to 0.07 mM (minimum 7 dilutions for each iTSL1-3 sample and 5 dilutions for Gadovist® were prepared). The use of deuterium oxide (D_2O) in the sample preparation was crucial to lock the signal in NMR to avoid drift of the magnetic field during the experiment.

The efficacy of a contrast agent has been articulated as the longitudinal relaxivity (r_1) in $mM^{-1}s^{-1}$. The r_1 was calculated from the slope of the linear regression generated from the relaxation rate (R_1= 1/T_1) as a function of gadolinium concentration. The experimentally determined buffer relaxation rate $R_{1(0)}$ (without any contrast agent) was subtracted as a starting value from the relaxation rates (R_1) of the gadolinium samples before the linear regression analysis **(Equation 3.1).**

$$r_i = \frac{\left(R_i - R_{i(0)}\right)}{[CA]} \;\; ; \; (i = 1, 2)$$

Equation 3.1: Equation to calculate relaxivities (r_i, where i= 1, 2); R_i = relaxation rate (1/T_i; i= 1, 2), $R_{i(0)}$ = relaxation rate of the buffer (1/$T_{i(0)}$; i= 1, 2), [CA] = concentration of contrast agent, in this case it is free-gadolinium equivalent [21,22].

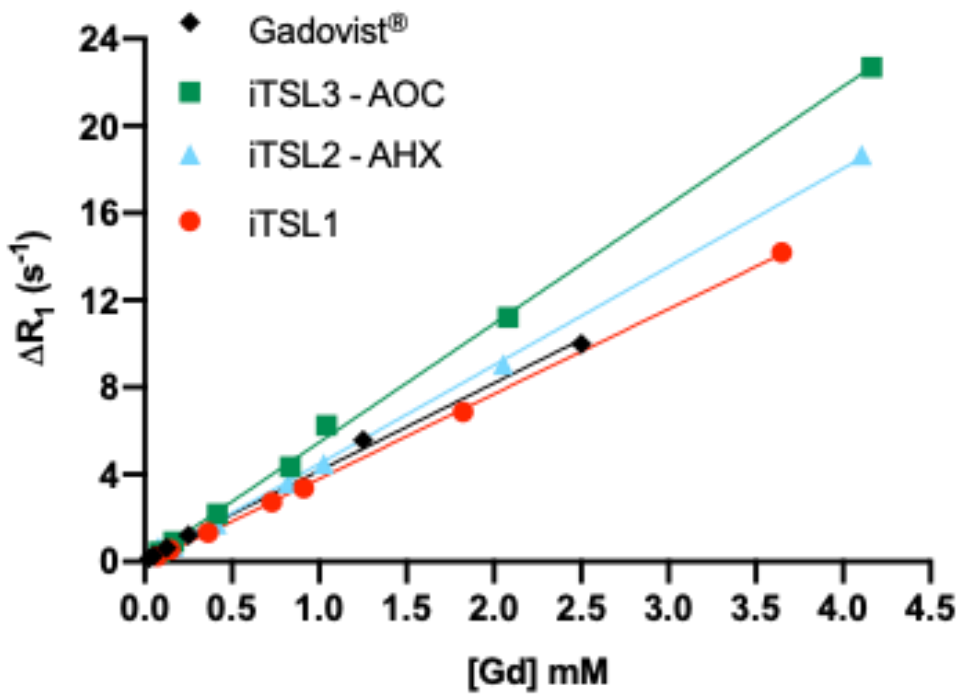

Figure 3.5: Determination of longitudinal relaxivity (r_1) of iTSL1-3 liposome and Gadovist®; in 50 mM HEPES, 10 v% D_2O, 5 w% glucose at pH 7.4, by using a 400 MHz (9.4 T) NMR. The plot of the change in relaxation rates (R_1-$R_{1(0)}$ = ΔR_1) at different gadolinium concentration, measured by TXRF. The slope of linear regression fitting represents the r_1. R^2 = Coefficient of Determination indicating the level of variability in the dependent variable (Relaxation Rate (ΔR_1) in s^{-1}) explained by variability in the independent variable ([Gd] in mM) in the linear regression model. R^2 = 0.9997 iTSL1, R^2 = 0.9992 iTSL2, R^2 =0.9990 iTSL3 and R^2 = 0.9972 Gadovist®.

Contrast Agent	r_1 ($mM^{-1}s^{-1}$) ± SE
Gadovist®	4.01 ± 0.11
iTSL1 ([Gd]DOTA.DSA)	3.89 ± 0.03
iTSL2 ([Gd]DOTA.AHX.DSA)	4.52 ± 0.06
iTSL3 [Gd]DOTA.AOC.DSA	5.45 ± 0.08

Table 3.3: The relaxivity (r_1) values for iTSL1-3 and Gadovist® determined from the slope of the linear regression fitting in **Figure 3.5** (T_1 relaxivities were acquired by 9.4 T NMR). The standard error of slope (SE) represents the average distance that the observed values deviate from the linear regression line. Values were calculated using GraphPad Prism v 8.2.1.

The T_1 relaxivity values of iTSL1-3 formulated from Gd-lipids and Gadovist® were reported in **Table 3.3.** Accordingly, liposomes with the longest spacer ([Gd]DOTA.AOC.DSA), iTSL3, had the dominant result in T_1 relaxivity, compared to other liposome candidates and the macrocyclic contrast agent, Gadovist®, at 9.4 T (NMR). iTSL1 has shown lower T_1 relaxivity in comparison to Gadovist®, both of which have relaxivity values of 3.89 and 4.01 $mM^{-1}s^{-1}$ respectively. However, both liposomes incorporating Gd-lipids with spacers have demonstrated increased T_1 relaxivity compared to Gd-lipid without a spacer and Gadovist® with relaxivity values of 4.52 $mM^{-1}s^{-1}$ (iTSL2) and 5.45 $mM^{-1}s^{-1}$ (iTSL3).

Study	Medium	Field of Strength (Bo)	Temperature (°C)	r_1 ($mM^{-1}s^{-1}$)
Noebauer-Huhmann *et al.* [239]	human plasma	3 T	37 °C	4.9
Shen *et al.* [21]	human blood	3 T	37 °C	4.5
Szomolanyi *et al.* [211]	human plasma	3 T	37 °C	4.9
Szomolanyi *et al.* [211]	human blood	3 T	37 °C	3.5
Noebauer-Huhmann *et al.* [239]	human plasma	7 T	37 °C	4.7
Shen *et al.* [21]	human blood	7 T	37 °C	4.2
Szomolanyi *et al.* [211]	human plasma	7 T	37 °C	3.8
Fries *et al.* [59]	human plasma	9.4 T	37 °C	4.2

Table 3.4: Comparison of T_1 relaxivities, r_1, of the Gadovist® in different biological mediums at 3, 7 and 9.4 T utilized in the literature [21,59,211,239].

In literature, contrast enhancement of the commercial macrocyclic contrast agent Gadovist® has been studied by several groups and T_1 relaxivity was directly compared with ProHance® (gadoteridol) and Dotarem® (gadoterate meglumine) in various medias (e.g. plasma, blood) and magnetic fields (between 1.5 to 9.4 T). It was reported that Gadovist® demonstrates higher relaxivity compared to the other macrocyclic small molecule GBCAs that are clinically available [21,22,211]. Therefore, we used Gadovist® as a control but the absolute values of relaxivity from previous studies as shown in **Table 3.4** were not comparable due to the variations in experimental methods and calculations of relaxivities [21]. Even though small

molecule GBCAs do not interact with plasma proteins, the variability of T_1 relaxivity measurements occur within different medias such as human plasma or whole blood due to differences in the viscosity of the medium. The increased viscosity influences the rotational correlation time of the GBCAs that can increase the r_1 [211].

Furthermore, phantom imaging and relaxometry experiments of the iTSL1-3 liposomes under the 9.4 T preclinical MRI were carried out in order to demonstrate how the contrast enhancement translates into MRI image enhancement and the potential viability in *in vivo* studies. Moreover, the contrast efficacy of the iTSL1-3 formulations was not only determined by their T_1 relaxivities (r_1), but also their T_2 relaxivities (r_2), this is an observation that has been overshadowed in previous studies in medical literature for GBCAs [240]. Consequently, the variation of r_2/r_1 was also estimated to describe the ability of iTSL1-3 liposomes to shorten T_1 or T_2 relaxation times in relation to each other.

As in the previously discussed relaxometry study at 9.4 T NMR, iTSL1-3 and Gadovist® were again serially diluted in 50 mM HEPES with 5 w% glucose for 9.4 T MRI relaxometry study. The final gadolinium concentrations for all samples were diluted into the range of 1-0.8 mM (4 dilutions per sample). Then, T_1 relaxometry studies were performed with a fast spin echo sequence with various repetition times (TR) and T_2 relaxometry studies were performed with spin echo sequence with various echo times (TE). T_1 and T_2 maps were generated from the relaxometry data via pixel-by-pixel fitting to the following **Equation 3.2**:

$$\boldsymbol{a}.\quad M_i = M_0\left(1 - e^{\left(-TR/T_1\right)}\right) \qquad \boldsymbol{b}.\quad M_i = M_0\left(e^{\left(-TE/T_2\right)}\right)$$

Equation 3.2: Equation for determining **(a)** T_1 using standard saturation recovery; **(b)** T_2 using MR sequences with different echo times (TE). M_i: signal intensity, TR: time to repeat, TE: echo time, T_1 = longitudinal relaxation time, T_2: transverse relaxation time; M_0 = equilibrium magnetization (baseline net magnetization) [10].

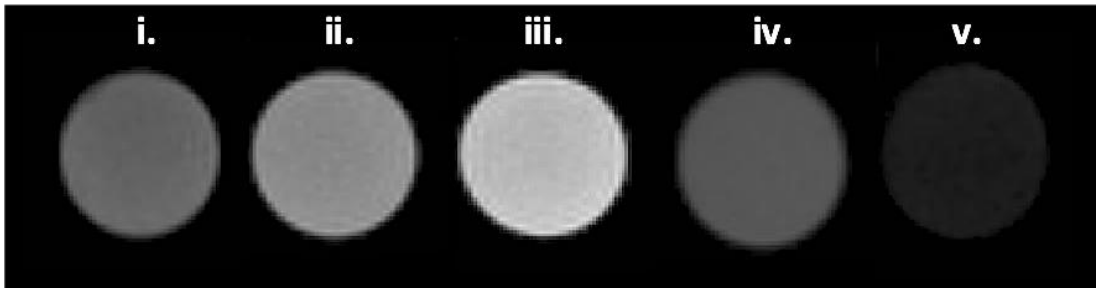

Figure 3.6: T_1-weighted MR images of paramagnetic liposome phantoms and (+/- ve) controls at TR: 35 ms; **(i)** 0.86 mM iTSL1, **(ii)** 0.84 mM iTSL2, **(iii)** 0.85 mM iTSL3, **(iv)** 0.96 mM Gadovist® (+ve control), **(v)** 50 mM HEPES, 5 w% glucose, pH 7.4 buffer (-ve control). All MR phantoms were acquired with a 9.4 T preclinical MRI scanner.

Regions of interest were placed on the T_1 and T_2 maps to determine the T_1 and T_2 relaxation times. The longitudinal T_1 relaxivity (r_1) and transverse T_2 relaxivities (r_2) were calculated from a linear relationship of relaxation rate ($R_{1/2}$: $1/T_{1/2}$) as a function of gadolinium concentration, given by the **Equation 3.1.**

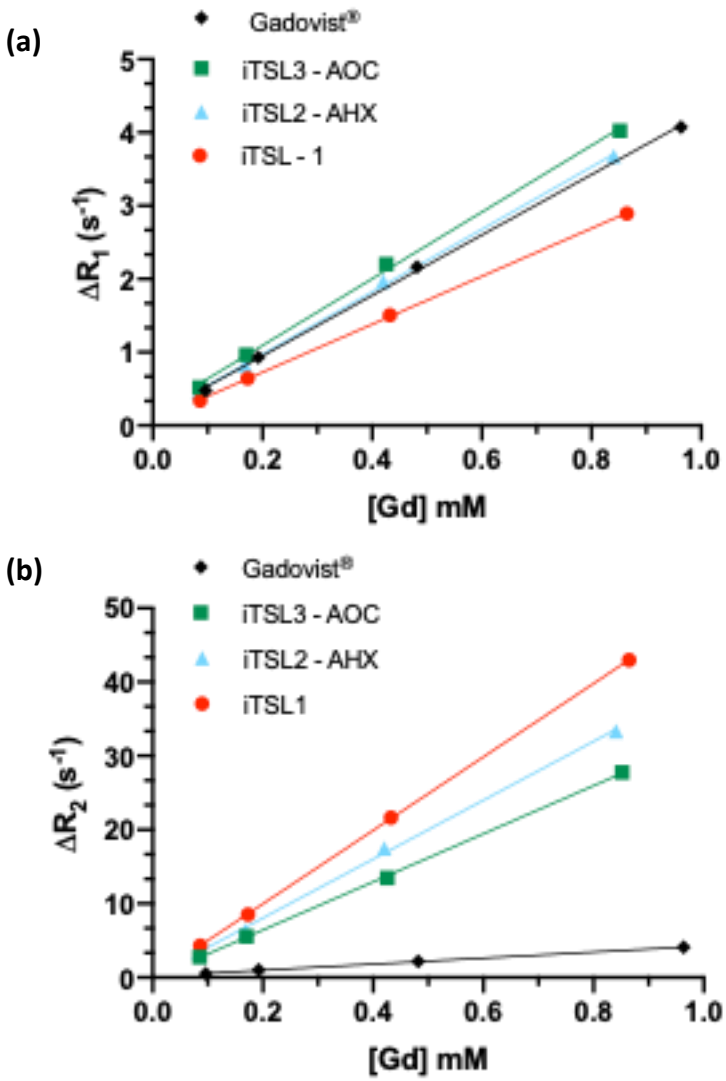

Figure 3.7: Determination of **(a)** longitudinal (r_1) and **(b)** transverse (r_2) relaxivities of iTSL1-3 liposome and Gadovist®; in 50 mM HEPES, 5 w% glucose at pH 7.4, by using a 9.4 T MRI. The plot of the change in relaxation rates ($R_{1,2}$-$R_{1,2(0)}$ = ΔR_1) at different gadolinium concentrations, measured by TXRF. The slope of linear regression fitting represents the $r_{1,2}$. R^2 = Coefficient of Determination indicating the level of variability in the dependent variable (Relaxation Rate (ΔR_1) in s^{-1}) explained by variability in the independent variable ([Gd] in mM) in the linear regression model. For r_1 values: R^2 = 0.9998 iTSL1, R^2 = 0.9992 iTSL2, R^2 =0.9986 iTSL3 and R^2 = 0.9993 Gadovist®. For r_2 values: R^2 = 1 iTSL1, R^2 = 0.9985 iTSL2, R^2 =0.9997 iTSL3 and R^2 = 0.9984 Gadovist®.

Contrast Agent	r_1 ($mM^{-1}s^{-1}$) ± SE	r_2 ($mM^{-1}s^{-1}$) ± SE	r_2/ r_1
Gadovist®	4.13 ± 0.08	4.09 ± 0.05	0.99 ± 0.01
iTSL1 ([Gd]DOTA.DSA)	3.27 ± 0.03	49.71 ± 0.19	15.20 ± 0.08
iTSL2 ([Gd]DOTA.AHX.DSA)	4.27 ± 0.09	39.86 ± 0.95	9.33 ± 0.03
iTSL3 [Gd]DOTA.AOC.DSA	4.55 ± 0.12	32.55 ± 0.41	7.15 ± 0.1

Table 3.5: The relaxivity ($r_{1,2}$) values for iTSL1-3 liposomes and Gadovist® determined from the slope of the linear regression fitting in **Figure 3.7** ($T_{1,2}$ relaxivities were acquired by 9.4 T MRI). The standard error of slope (SE) represents the average distance that the observed values deviate from the linear regression line. Values were calculated using GraphPad Prism v 8.2.1.

The MRI T_1 relaxivity results of iTSL1-3 liposomes are showing a similar trend as the aforementioned NMR T_1 relaxivity study. However, absolute longitudinal relaxivity values between NMR and MRI relaxometry studies have shown variation around 10 % due to the differences between methods, experimental conditions and also data processing. MRI relaxivity values (r_1, r_2) of iTSL1-3 and Gadovist® are shown in the **Table 3.5.** iTSL1 has shown the lowest T_1 relaxivity value of 3.27 $mM^{-1}s^{-1}$ whereas the T_1 relaxivity of Gadovist® was 4.13 $mM^{-1}s^{-1}$. Furthermore, an increase in r_1 was

observed with iTSL2 which is 4.27 $mM^{-1}s^{-1}$ and iTSL3 liposomes have demonstrated the highest r_1 at 4.55 $mM^{-1}s^{-1}$.

In both 9.4 T NMR and MRI relaxometry studies, increasing the length of the spacer between the head group and the lipidic tail has an impact on the T_1 relaxivity. In contrast, iTSL1 liposomes that were formulated without any spacer have demonstrated moderately lower T_1 relaxivity relative to the Gadovsit® (+ve control) in both studies. This could be explained with the limitation of the water accessibility to the gadolinium metal which was encapsulated by the DOTA chelator. Whereas it is possible that the [Gd]DOTA is buried within the shielding layer of the polyethylene glycol (PEG) headgroup since they have a similar length lipid tail. Alternatively, incorporating the Gd-lipid with the longest alkyl spacer could be pushing the macrocyclic Gd-chelate out of the lipid headgroup space and showing enhanced T_1 relaxivity due to the increased potential of water accessibility, thus an improved water exchange rate. Moreover, iTSL1 liposomes were larger in size compared to iTSL2 and iTSL3 where effect of size in relaxivity was not addressed. At moderate magnetic field strengths (e.g. 1.5 T or 3 T) larger contrast agents like nanoparticles demonstrate higher T_1 relaxivity due to slower tumbling compared to small, fast tumbling GBCAs. According to Caravan *et al.* increasing molecular size has no benefit for improving r_1 at ultra-high magnetic fields like 9.4 T. For example at 9.4 T the T_1 relaxivity of MS-325 does not exhibit significant change with (7.16 $mM^{-1}s^{-1}$) or without (5.14 $mM^{-1}s^{-1}$) albumin binding in contrast to lower magnetic fields like 1.4 T (T_1 relaxivity of MS-325 only 7.16 $mM^{-1}s^{-1}$ versus T_1 relaxivity of MS-325+HAS 24.3

$mM^{-1}s^{-1}$) [241]. Therefore, size of iTSL1-3 formulations may not be contributing in the T_1 relaxivity at 9.4 T magnetic field as much as lower magnetic fields. As the potential outcome in this eventuality would be the larger iTSL1 (in size) demonstrating higher T_1 relaxivity (due to slow tumbling). Furthermore, iTSL2 and iTSL3 were similar in size but smaller than iTSL1, however iTSL3 with longer spacer unit has demonstrated higher T_1 relaxivity than iTSL2 irrespective of size. The results have shown the size of liposomes may not be impacting the T_1 relaxivity as much as the spacer, but this requires further investigation.

In our liposomal formulations we have a hydrophilic polymer, PEG, coat which is prone to reducing the tumbling as well as increasing the efficiency of targeting in drug delivery. Liposomes that are coated with a PEG have prolonged survival in the circulation and increase target specific drug delivery [20,70,85,242] Bertini *et al*. have assessed the [Gd]DTPA.DMPE lipid incorporating PEGylated liposomes *in vivo* using mice bearing murine melanoma cells (F10-M3). The T_1 weighted images *in vivo* have shown a pronounced and prolonged contrast enhancement in the tumour with the use of PEGylated paramagnetic liposomes in comparison to small molecule [Gd]DTPA at 1.5 T MRI [243]. Thus, PEGylated liposomes have a potential to improve T_1-weighted contrast relaxivity *in vivo* by providing high target specificity and efficient MRI contrast.

Mitchell *et al*. have studied the effects of the introducing PEG spacers on T1 relaxivity. They have incorporated different length oligoethylene glycol spacer units

between the headgroup and the lipid tail (**Scheme 3.6:** DEG1SL, DEG3SL and DEG6SL) and observed a lower T_1 relaxivity by introducing longer PEG spacers. As an illustration, liposomes with DEG1SL (shortest PEG spacer) have demonstrated T_1 relaxivity of 2.95 $mM^{-1}s^{-1}$, whereas liposomes with DEG6SL(longest spacer) have shown lower T_1 relaxivity of 1.97 $mM^{-1}s^{-1}$ at 9.4 T [233]. The increased length of PEG spacers likely results in the occurrence of a rapid local rotational motion of the Gd-chelates since PEG spacers are highly flexible (non-rigid) **(Scheme 3.6).** The slow tumbling of nanoparticles like liposomes is advantageous for enhancement of T_1 relaxivity. However, rapid local rotational motion of the paramagnetic lipid due to a non-rigid spacer unit between the headgroup and the tail could counteract the advantage of the slow tumbling [7,244].

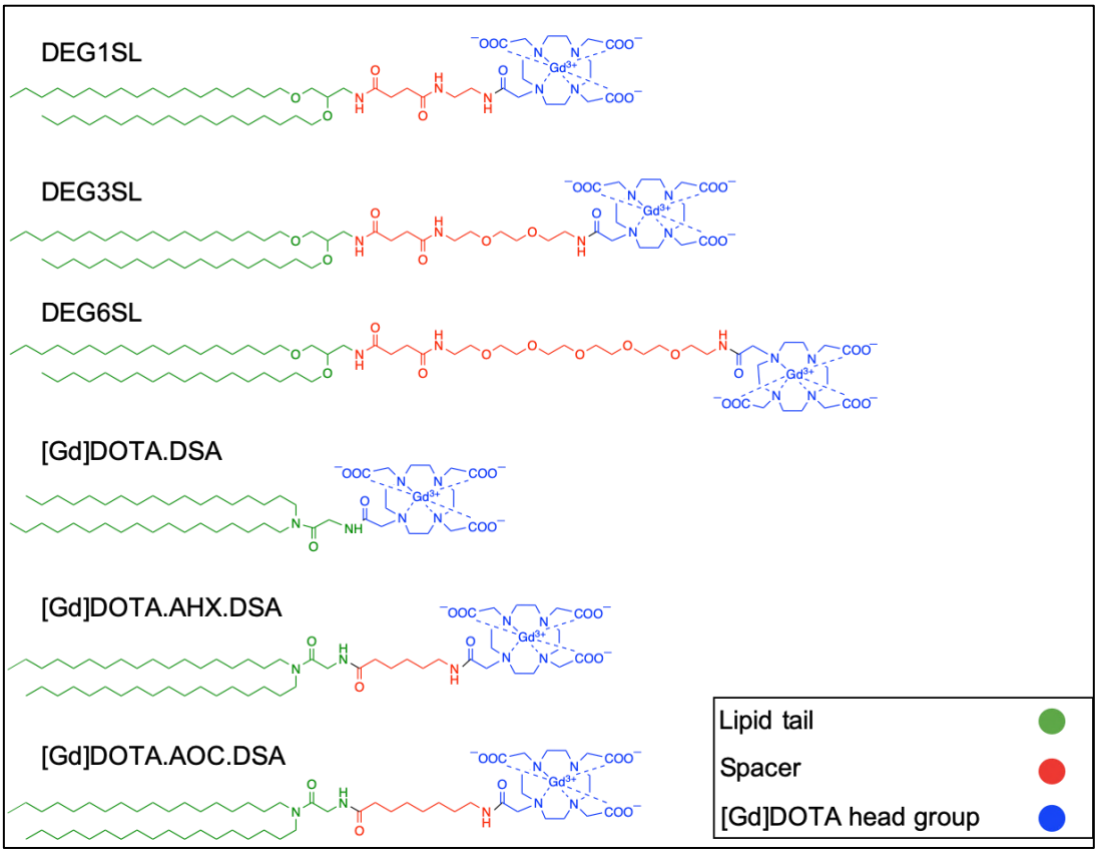

Scheme 3.6: Comparison of the chemical structures of Gd-chelated paramagnetic lipids that were reported by Mitchel *et al.* [233]; DEG1SL, DEG3SL, and DEG6SL synthesised with PEG spacer between headgroup and the tail. Compared with lipids synthesised in house; [Gd]DOTA.DSA, [Gd]DOTA.AHX.DSA and [Gd]DOTA.AOC.DSA incorporated into the liposome formulations (iTSL1-3)

Despite our incorporation of short alkyl spacers ($(CH_2)_6$, $(CH_2)_8$) to the Gd-lipid, longer chain length is potentially increasing the water exchange rate (shorter τ_M), whilst simultaneously increasing the local motion of the Gd-chelate due to the increased flexibility of spacers. Presumably, the net impact of these two opposing forces results in higher relaxivity due to the dominance of water exchange rate over the increased

rotational correlation time of the Gd-chelate. In our approach, [Gd]DOTA complex was extended from the membrane with increasing length of spacer resulting in better access of water and preventing the shielding effect of the PEG coat. Similarly, *Winter et al.* have proposed that water exchange or water accessibility can be facilitated by displacement of the Gd-complex beyond the lipid surface. In this manner, they have demonstrated that T_1 relaxivity of the [Gd]-MeO-DOTA-PE incorporated onto perfluorocarbon nanoparticles improves around 10 % with the addition of the triglycine spacer ([Gd]-MeO-DOTA-triglycine-PE) between the head group and the lipid surface [40]. It is important to understand the optimal length and structure of the spacer to extend the Gd-chelate beyond the membrane surface to improve the water interaction without introducing an undesirable level of local mobility to the Gd-chelate [245].

Pertinently, longitudinal molar relaxivity (r_1) generally decreases with increasing magnetic field, whereas transverse molar relaxivity (r_2) is static or increases with increasing magnetic field strength [241]. Therefore, higher field strength provides a static or an increasing r_2/r_1 ratio. All three liposomes iTSL1-3 have shown significantly higher r_2/r_1 ratio compared to the macrocyclic contrast agent at 9.4 T MRI, which demonstrates pronounced shortening of T_2 relaxation time. Utilizing formulations with shorter spacers between the Gd-chelate and the lipid membrane decreases the transverse relaxivity (r_2). The r_2/r_1 ratio for Gadovist® was calculated as 0.99 ± 0.01, whereas ratio for iTSL1 was found 15.20 ± 0.08 as shown in **Table 3.5.** In the literature, Luc *et al*. have investigated the impact of the size of nanoparticles on r_2/r_1

ratio. They have performed relaxometry studies at various magnetic field strengths to measure both longitudinal and transverse relaxivities (r_1, r_2) of ultra-small gadolinium oxide nanoparticles (US-Gd_2O_3, clusters of 3 nm diameter) and their nanoaggregates (60, 75 and 105 nm diameter). They have reported an increase of transverse relaxivity (r_2) that increases the r_2/r_1 ratio with larger size of nanoparticles at higher external magnetic fields. The r_2/r_1 ratio of US-Gd_2O_3 (105 nm diameter) has shown slight change between 0.47 and 1.41 T, 1.15 ± 0.04 and 1.49 ± 0.04 respectively. However, this ratio has increased significantly at higher magnetic fields such as 13.5 ± 0.8 at 7 T and 21 ± 2 at 11.7 T. Nanoaggregates are large magnetized spheres which are a result of adhesive forces acting on paramagnetic nanocrystals. Therefore, the total magnetic moment is increased when the size of nanoparticles is getting larger which consequently increases the transverse relaxivity (T_2) [246]. Additionally, as similar impact has been observed in the study of Gleen *et al.* They have compared the r_2/r_1 ratios at 1.41 T and 9.4 T of the [Gd]DTPA (small molecule), micelles (15.6 ± 0.2 nm diameter) and liposomes (100.1 ± 3.6 nm diameter) prepared with [Gd]DOTA.DSPE. They have shown that at 9.4 T r_2/r_1 ratios of micelles and liposomes are considerably higher compared with at 1.41 T [247]. In particular, r_2/r_1 ratio of liposomes was 1.58 ± 0.01 at 1.47 T, whereas this ratio significantly increases to 17.9 ± 0.3 at 9.4 T. This indicates that as magnetic field strengths are increasing, gadolinium nanoparticles with high gadolinium concentration display significant shortening in the transverse relaxation time, a noteworthy effect for future MRI applications with gadolinium labelled liposomes [248].

3.4.4 Proton Nuclear Magnetic Resonance Dispersion (NMRD) Study

In earlier studies, Rohrer *et al*. have compared the magnetic properties of commercially available small molecule MRI contrast agents at different magnetic fields (0.47, 1.5, 3, and 4.7 T) in various medias (water, blood plasma, whole blood). It was asserted that the T_1 relaxivities of traditional GBCA are field strength dependent. In particular, T_1 relaxivity of Gadovist® was found to decrease with increasing field strength of MRI [22,211]. T_1 relaxivity of small molecule GBCAs is limited by the rotational correlation time (fast rotation), especially in high magnetic field strengths. i.e. 9.4 T as used in this study. In light of this, proton Nuclear Magnetic Relaxation Dispersion (NMRD) profiles were utilised to demonstrate the impact of magnetic field strength on r_1 of liposomal nanoparticles. A Fast Field Cycling NMR (FFC-NMR) relaxometry was used to obtain the change of T_1 relaxation times over an extended range of Larmor frequencies, corresponding NRMD measurements of Gadovist® and iTSL1 liposomes are shown below **(Figure 3.8)** [249]**.**

The NMRD measurements of Gadovist® and iTSL1 were acquired at three different temperatures (37 ^{o}C, 41 ^{o}C and 42 ^{o}C) from 0.01-40 MHz (up ~1 T) with 25 field points **(Figure 3.8).** For Gadovist® the highest T_1 relaxivity was found at lower field strengths and r_1 continued to decrease as field strength kept increasing, this finding is substantiated in the literature [22]. On the other hand, iTSL1 formulation has demonstrated higher r_1 at higher field strength.

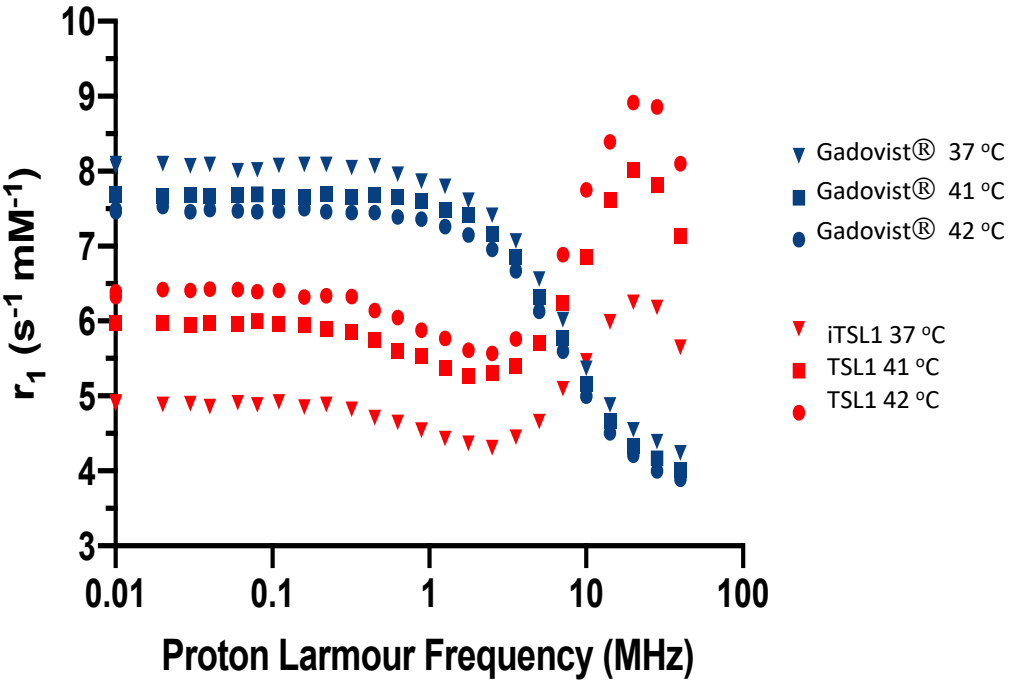

Figure 3.8: NMRD profiles for Gadovist® and iTSL1 formulation in aqueous solution, normalized to 1 mM [Gd] at 37, 41 and 42 °C. Temperature at 41-42 °C is the Tm onset point for the iTSL1 formulation and 37 °C is representative of the body temperature. On the logarithmic axis, the values corresponding to the frequency range of 0.01-40 MHz (40 MHz is around 1 T).

NMRD measurements were performed at 37 °C (body temperature) and at onset phase transition temperature of the iTSL1 (41-42 °C) in order to see the impact on the r_1. T_1 relaxivity of Gadovist® stays almost the same as temperature increases. However, there was a large proportional increase in r_1 of the iTSL1 as the temperature reached close to the phase transition temperature. The permeability of the liposomal membrane at 42 °C increases, facilitating the water transfer to the Gd-

chelates existing within the inner side of the bilayer to drive the increase of the r_1 [230].

A lipid's chain length and structure have an influence on the water permeability of liposomes [78]. Laurent *et al.* have demonstrated that the presence of the unsaturated alkyl chain increases the T_1 relaxivity at 37 ^{o}C because of their looser structure of the membrane facilitating a faster water exchange rate, irrespective of any change in tumbling rate of the liposome [78,231]. However, permeability of the liposomes, particularly at body temperature, is a disadvantage for encapsulating a high payload of the cytotoxic drug in the liposomal core due to potential leakage. Therefore, we emphasise increasing the water accessibility of the Gd-chelates located in the outer layer of the membrane.

In this study, the contribution of the Gd-chelates located in internal layer of the lipid membrane to the overall T_1 relaxivity is lower due to the limited access to water (in particularly at 37 ^{o}C). However, this contribution is increasing with increased temperature (in the range of the phase transition) with the influence of the water permeability [78]. This property is desirable for our image guided thermosensitive drug delivery method, since higher visibility will coincide with drug release at the targeted area. The increase of iTSL1 T_1 relaxivity with temperature increase could be used as a confirmation of hyperthermia and the effect of applied focused ultrasound. This is important for monitoring the effects during MRgFUS therapy.

As a future direction, The NMRD measurements of paramagnetic liposomes can be analysed further with theoretical adjustments by fitting the FFC experimental data into established models [250]. These models assist in determining the MRI parameters of paramagnetic liposomes e.g. rotational correlation times (τ_R) and water exchange correlation times (τ_M) under the different conditions (i.e. magnetic field strengths and/or temperature). This may provide a better understanding of the influence on the relaxivity of liposomes with alternative spacer units accounting for differences in the size of liposomes.

3.5 Conclusion

In conclusion, two novel Gd-chelated lipids with spacer units were prepared to enhance MRI contrast, as an alternative to [Gd]DOTA.DSA which was previously utilised to form an image-guided thermosensitive liposomal formulation [194]. Synthesized Gd-lipids were incorporated into the thermosensitive liposome formulation (iTSL1-3) and characterised to observe the impact of the alkyl spacer unit on longitudinal and transverse magnetic relaxation. Liposomes composed of [Gd]DOTA.AOC.DSA have shown to be an effective T_1 signal enhancer compared to Gd-lipids with shorter chain length and commercially available contrast agent, Gadovist®. Moreover, significant T_2 relaxation shortening has been observed with paramagnetic liposomes relative to Gadovist®, in particular iTSL1 with [Gd]DOTA.DSA (without a spacer unit). Given it is an overlooked property, the effects of Gd liposomes in shortening the T_2 relaxation time warrants further studies to understand its full utility as a contrast agent. The NMRD profile of iTSL1 formulation has demonstrated the water permeability effect on the T_1 relaxivity at phase transition temperature range (41-42 ^{o}C), whereas Gd-lipids located in the inner membrane have likely contributed to the shortening of the T_1 relaxation time. This is important for the translation of these liposomes to the clinic for cancer treatments. As a future endeavour, lipid composition with [Gd]DOTA.AOC.DSA should be re-optimised to attain the desired characteristics for MRI guided thermosensitive drug delivery given it has the highest T_1 relaxivity.

4. MR-labelled Thermosensitive Liposomes and Focused Ultrasound for Precise Drug Release in Triple Negative Breast Cancers

4.1 Introduction

The combination of hyperthermia-induction devices with anticancer drugs was suggested more than 40 years ago [251]. But so far hyperthermia with radiotherapy, chemotherapy and immunotherapy has only been applied to a limited extent for the treatment of cancer. Recent technological advances allow the application of heat to deep seated tissues, with high spatial precision and accurate thermal control. Such approaches are approved for use with microwave and radiofrequency antennae, but emphasis has also been given to the combination of High Intensity Focused Ultrasound (HIFU or FUS) combined with cancer therapies [252]. This is a medical technology developed for interventions that require the deposition of ultrasound energy within small volumes of tissues, that then leads to high intensity localised cavitation and/or an increase in temperature [253]. Magnetic Resonance guided (MRg) FUS allows for highly accurate spatial localisation and is clinically used for precise ablative treatment of solid tumours and neurological disorders [254]. A less clinically investigated application of MR-guided FUS is targeted drug delivery using nanocarriers designed to respond to effects of FUS energy [255,256].

Liposomes have been widely used in the clinic. They are nanocarriers that offer a high level of multifunctionality and versatility [257,258]. Thermosensitive liposomes (TSL) have been introduced during the last two decades as drug delivery systems able to release their cargo almost instantly when warmed to ~42 ^{o}C [259,260]. TSL carrying anticancer drugs have been tested in small and large animals having shown great efficiency when combined with hyperthermia [143,261–264]. A valuable

modification would be the inclusion of MR contrast agents in order to allow for image guidance and monitoring the drug release within a lesion [265–268]

MR-labelled nanocarriers offer significant clinical advantages: **i)** anatomical guidance and feedback; the application of external hyperthermia can be more accurately applied on a "contrast/highlighted" lesion; **ii)** tracking of nanocarrier distribution and tumour uptake allowing the timing of hyperthermia to be coordinated with the nanoparticle kinetics. The application of hyperthermia can be timed for when the liposomes circulate at high plasma concentrations and reach the tumour in a cumulative manner, **iii)** potentially enhanced contrast for smaller lesions (such as metastases and micro-metastases) that were not previously identified. This offers the opportunity of real-time treatment not only of the large tumours but their metastasis as well [269].

Focused ultrasound has been shown that it can be combined with TSL loaded with a paramagnetic MR contrast agent [200]. Contrast agent was released when FUS was applied which was allowing for release confirmation and MR-imaging [270,271]. The technique also confirmed hyperthermia-induced drug release in animals when co-encapsulating both the contrast agent and a drug [267].

The development of liposomal formulations of existing anticancer drugs e.g. Doxil® (which contains doxorubicin) was initially intended to improve the drug's safety. Doxil® received FDA approval in 1995 and became the most widely used nanoparticle

therapy, confirming that localised delivery can improve the therapeutic index [272]. Although safety has been validated [273], efficacy remains at similar levels to aq. doxorubicin. This has been attributed to limited/slow release from the Doxil® formulation [274]. An updated liposomal formulation, ThermoDox® was developed to overcome this issue and was the first responsive nanocarrier that moved to clinical trials. It is doxorubicin encapsulated TSL designed to rapidly release its cargo in response to small increases in temperature (>40 ^{o}C) and was developed at Duke University (NC, U.S.A) with the aim of improving efficacy [260]. A Phase III clinical trial **(NCT00617981)** has recently been completed evaluating the efficacy of ThermoDox® in combination with radiofrequency ablation (RFA) in patients with hepatocellular carcinoma. This study showed the efficacy of the therapy but did not reach the required endpoints (improving patient's progression free and/or overall survival times) in the overall study population. However, a subgroup analysis suggested that efficacy was improved when RFA dwell time for a solitary lesion was ≥ 45 min [275,276]. The OPTIMA follow-on study **(NCT02112656)** aimed to identify the efficacy of ThermoDox® in combination with standardized RFA (sRFA ≥ 45 min) in primary liver cancer, with primary endpoint of overall survival and powered to demonstrate a 33 % improvement. Thermodox® has also been selected to provide additional efficacy in developing radio frequency ablation (RFA) techniques. In a small group of hepatocellular carcinoma patients, RFA alone (N=11) was compared with RFA + Thermodox® (N=11). The study identified that RFA with targeted delivery of chemotherapy facilitated the tumour coagulation necrosis without further toxicity. It was suggested that this combined treatment could improve the clinical efficacy of RFA or doxorubicin and would prolong the survival in patients with

medium to large hepatocellular carcinoma [277]. Thermosome® is another thermal release liposome technology based on a different formula and has been used to develop a variant of TSL-doxorubicin currently in advanced animal trials [278].

TARDOX is a recently published phase I trial that demonstrated the safety of using FUS to produce hyperthermic temperatures (i.e. 39.5-43 ^{o}C) and trigger drug release from Thermodox®. This resulted in very high levels of doxorubicin concentrations in solid tumours compared to the levels seen just before the application of FUS [279]. This study achieved its primary endpoint, e.g. a significant increase in the amount of intratumoral doxorubicin after FUS treatment and during Thermodox® infusion. This was a first-of-kind study that confirmed drug release in tumours with non-invasive FUS heating (RFA requires insertion of an electrode). The study showed that 60 min of FUS treatment significantly increased tumour doxorubicin concentration and provided a strong indication that FUS-enabled non-invasive thermal drug release is both accurate and safe [280].

These initial clinical trial results strongly suggest that there is room for improvement, in particular with respect to the hyperthermia method and parameters. It has been suggested that further development could include e.g. application of FUS to different tumour sizes and incorporation of MR-imaging and -thermometry [281]. Using MR imaging and -thermometry could provide guidance for the application of FUS to improve the localisation while avoiding the tissue damage. With the recent developments in clinical MR-guided FUS it is reasonable to expect to see more

therapeutic applications that use this combination, including image-guided targeted drug delivery [282–285]

Our group have previously presented a study with labelled thermosensitive liposomes for imaging (iTSL, also known as iTSL1 from **Chapter 3**) as a useful tool to provide information on the temporal distribution of drug nanocarriers into tumours. These iTSL facilitate the timing of the application of hyperthermia treatments. This study also showed that imaging provides confirmation of the presence of the drug nanocarrier and this can facilitate the design of treatment protocols or real time treatment decisions (personalised therapy). This information has allowed us to demonstrate that a brief (~3 min) round of mild hyperthermia (~43 ^{o}C) can significantly increase drug delivery efficiency [286]. To allow for the tracking of iTSL *in vivo* a small amount of lipid-conjugated NIRF probe (CF750-DSDA; 0.05 mol%) was also included which does not appear to affect the iTSL colloidal, drug loading/release, or biodistribution behaviours. This label provided valuable information during development, although NIRF is unlikely to be used in the clinic due to limited tissue penetration. In our previously published study, using NIRF imaging in mice have demonstrated both an increase in biodistribution of the iTSLs and coordinated topotecan release into tumours. Surprisingly, short FUS treatments significantly modified liposome tumour distribution and induced rapid drug release [194].

Image tracking both the nanocarrier and drug release during preclinical and clinical development can provide significant information on treatment optimisation. With

this in mind, in this study MR-labelled iTSL was selected and loaded with doxorubicin (iTSL-DOX). Its developability, imageability, stability, and efficacy were investigated. Here, we suggest an iTSL-DOX composition and investigation methodology with the overall target of clinical translation. An MR-labelled lipid ([Gd]DOTA.DSA which was also used in **Chapter 3**) was synthesized and incorporated in the liposome bilayer at almost 1/3 lipid composition. The effects of change on thermo-sensitivity and ability to encapsulate/release doxorubicin were investigated. After optimisation, iTSL-DOX was assessed for stability, leakage of Gd^{3+} from the chelate, then stability and thermal release performance after long term storage. NIRF-imaging was then used to demonstrate the iTSL-DOX accumulation and doxorubicin release into tumours on application of an optimised FUS treatment protocol. This used either a single- or double-tumour model, with the latter only inducing hyperthermia on one side and using the other as a non-FUS control. Treatment efficacy was demonstrated on a triple negative breast cancer murine model. MR-relaxivity parameters were studied *in vivo*, with MR-imaging potential tested in tumour bearing mice at determined time points post intravenous injection.

4.2 Aim and Objectives

Aim: To design and develop MR-labelled image guided thermosensitive liposomes iTSL (also known as iTSL1 from **Chapter 3**) loaded with doxorubicin (iTSL-DOX) for drug delivery.

Objective 1: Synthesis and incorporation of a MR-labelled lipid ([Gd]DOTA.DSA) in the liposome bilayer, as previously discussed in **Chapter 3**.

Objective 2: To prepare and characterise iTSL-DOX along with drug loading, colloidal and storage stability, and thermally induced drug release properties.

Objective 3: To assess iTSL-DOX distribution, uptake enhancement and focused ultrasound (FUS)-induced drug release in *in vivo* experiments.

Objective 5: To assess efficacy of the iTSL-DOX formulation against MDA-MB- 231 (triple negative breast cancer) *in vivo* experiments.

Objective 5: To assess MRI imaging potential of iTSLs

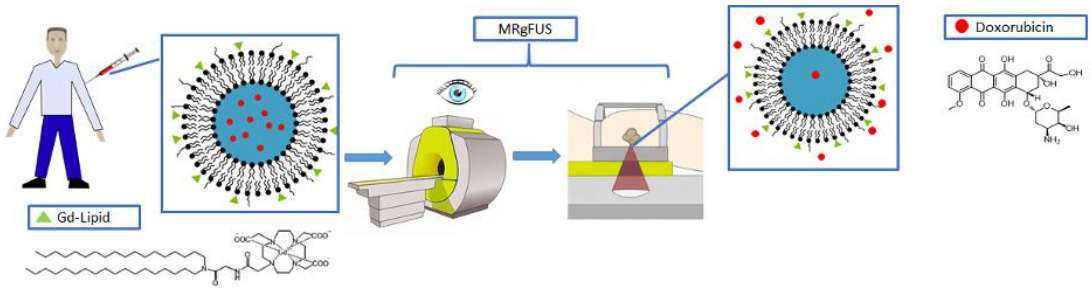

Figure 4.1: Graphical representation of the drug delivery when combined with FUS-induced mild hyperthermia using MRgFUS.

4.3 Results and Discussion

The data in this chapter was put in together with collaboration of Dr. Michael Wright and Dr. Miguel Centelles. I would like to thank them for their input into the data that have been shown in this chapter and for sharing insights.

4.3.1 Synthesis of Imaging Lipids and Preparation of iTSL-DOX:

[Gd]DOTA.DSA **(Scheme 4.1)** was synthesised and characterised as previously described in **Chapter 3**. DOTA-chelation of the gadolinium contrast agent was selected as it is expected to have significantly reduced transmetallation risk compared to classical diethylenetriamine pentaacetate (DTPA) derivatives [287]. iTSL were prepared with a [Gd]DOTA.DSA composition of 30 mol% of the total lipid used. This is quite high and was thought likely to affect iTSL physical, encapsulation and thermal release characteristics. By contrast, CF750.DSA was included at 0.1 mol% and its presence did not appear to modify non-optical characteristics. CF750 is a commercial NIRF dye supplied by Biotium and the structure appears to be proprietary. CF750.DSA incorporation in the iTSL appeared to be consistent between different batches, showing consistent NIRF emission properties.

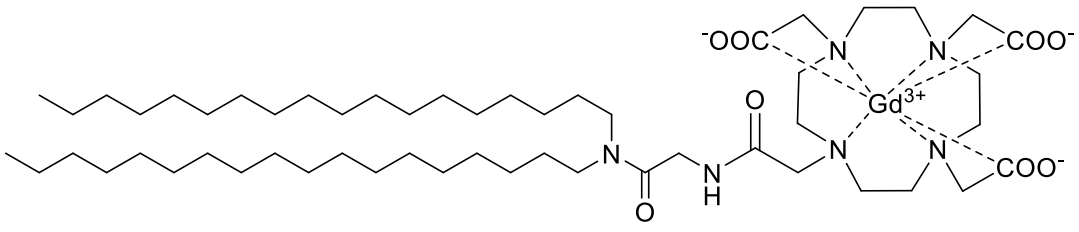

Scheme 4.1: Chemical structure of MR-labelled lipid: [Gd]DOTA.DSA

iTSL-DOX formulation followed a modification of our previously established protocols. Briefly, iTSL were formed in high ionic strength, low pH loading buffer using freeze-thaw, sonication, and then repeated gas-pressure extrusion through 100 nm pore membranes. The external buffer was replaced with lower ionic strength, neutral buffer using gel filtration and then doxorubicin loaded by incubation with careful temperature control **(Figure 4.2)**. Excess doxorubicin was removed by a second round of gel filtration and resulting iTSL-DOX transferred to glass vials for characterisation and storage. Representative characteristics were: Ø Zavg 179 ± 3 nm, PDI 0.2 ± 0.01; ζ -3.2 ± 0.1 mV; [Gd] 560 ± 16 µg/mL; [doxorubicin] 690 ± 15 µg/mL; drug/lipid ratio of 0.03; T_m ~43.5 ^oC.

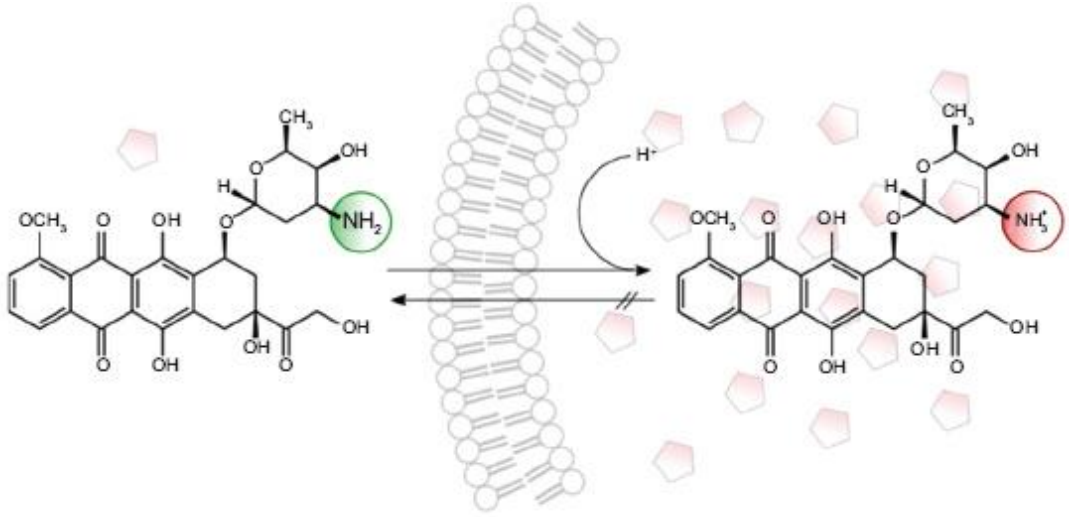

Figure 4.2: Drug loading of doxorubicin into preformed liposomes with a pH gradient and incubation of drug and liposomes at temperature where the membrane is permeable. Inside the liposome, the drug is protonated due to the acidic buffer and trapped. Adopted from Kneidi *et al.* [136]

4.3.2 Thermally Induced Doxorubicin Release

Doxorubicin release studies from iTSL-DOX were carried out by assessing the increase in doxorubicin intrinsic fluorescence on sample incubation over a range of temperatures and times. This took advantage of the strong self-quenching behaviour of encapsulated doxorubicin. **Figure 4.3** indicates little or no drug release at 37 ^{o}C for 30 min in HEPES (4-(2-hydroxyethyl)-1-piperazineethanesulfonic acid) buffer. This was followed by a sudden increase at ≥ 41 ^{o}C with more than 80 % of the encapsulated drug released in less than 2 min at 43 ^{o}C. This sharp release profile is typical of TSL designed for *in vivo* use and can be seen in both buffer and serum-like conditions **(see Figure 4.4).**

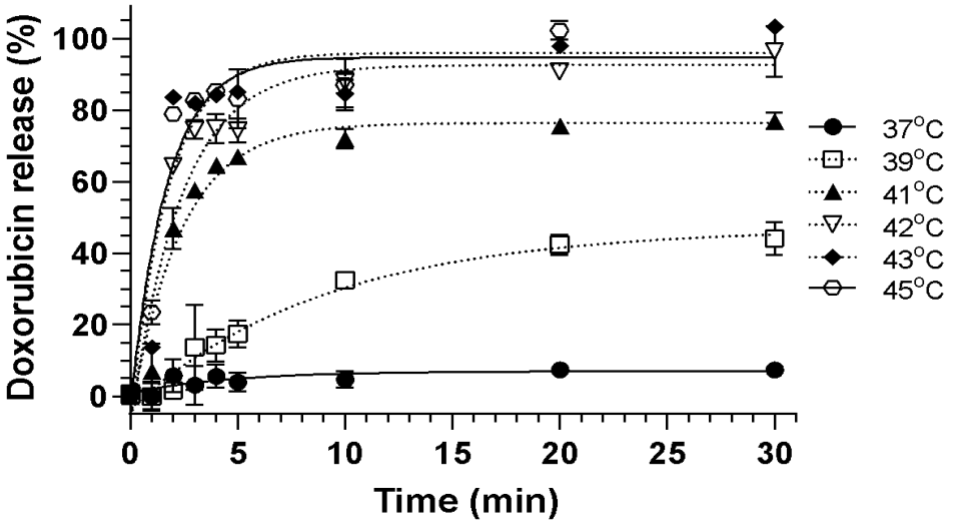

Figure 4.3: iTSL-DOX characterisation. Doxorubicin release from iTSL incubated at various temperatures and times in HEPES (4-(2-hydroxyethyl)-1-piperazineethanesulfonic acid) buffer alone. Release is monitored by the increase of intrinsic doxorubicin fluorescence (Ex_{480}/Em_{600} nm) as it leaves the self-quenched encapsulated state (N=3 ± SD).

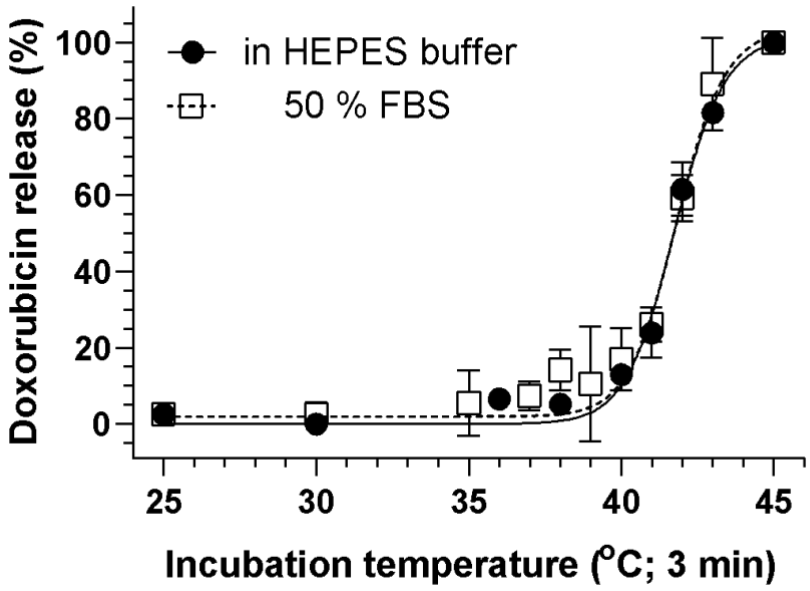

Figure 4.4: iTSL-DOX characterisation. Doxorubicin release from iTSL incubated for 3 min at various temperatures in comparison with HEPES (4-(2-hydroxyethyl)-1-piperazineethanesulfonic acid) buffer alone and buffer containing 50 % v/v fetal bovine serum (FBS) as a blood analogue. Release is monitored by the increase of intrinsic doxorubicin fluorescence (Ex_{480}/Em_{600} nm) as it leaves the self-quenched encapsulated state (N=3 ± SD).

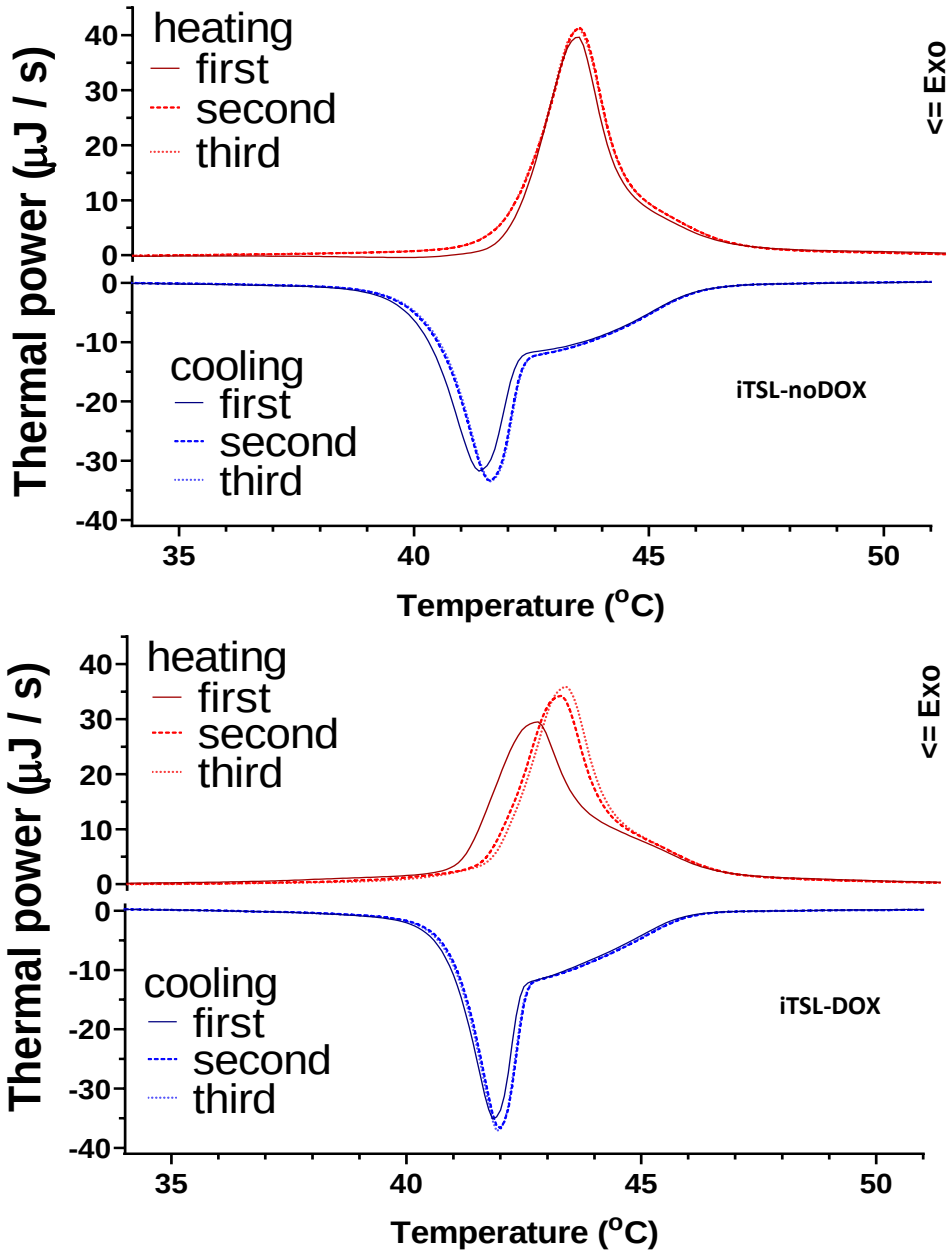

Figure 4.5: Liquid-phase differential scanning calorimetry studies of iTSLs **(a)** without and; **(b)** with encapsulated doxorubicin. Each assay consisted of 3x sequential heating-cooling rounds from 25-70 °C at 1 °C/min. iTSL were in HEPES /glucose buffer and used the same as a thermal reference.

The results in **Figure 4.3 and Figure 4.4** align well with liquid-phase differential scanning calorimetry (DSC) thermograms collected for iTSL (no-DOX) and iTSL-DOX **(see Figure 4.5).** These investigate the change in iTSL heat capacity on heating or cooling from 25-70 ^{o}C (1 ^{o}C/min; 3x sequential heat-cool cycles). The resulting peaks/troughs are mainly due to lipid phase changes in the liposome membrane. Such changes are associated with membrane pore formation, increased porosity, and hence release of encapsulated drug. The leading edge of the peaks in the heating thermograms (~41.5 ^{o}C) is similar to the initiation of doxorubicin release. In addition, iTSL-DOX shows a -1 ^{o}C peak shift for only the first heating thermogram in the cycle **(see Figure 4.5b)**. This matches the doxorubicin release result almost exactly and strongly suggests that the DSC is able to detect the release of encapsulated drug during this first round of heating. Following thermograms then revert to those seen for iTSL (no-DOX) as there is no further doxorubicin to be released. In combination these results indicate successful optimisation of iTSL formulation to adjust for the presence of the MR-contrast agent lipid [142,143,288].

These results show that iTSL-DOX will release the drug at the target elevated temperature. However, the DSC experiments do not provide information on the effect of the blood proteins on T_m and/or drug release characteristics in the blood at 37°C [289]. Thus, the doxorubicin release from iTSL-DOX into 50 % serum at 37 °C was investigated and it was observed that at 60 min incubation there was a substantial release of about 30 % of the encapsulated drug (**see Figure 4.6**) in contrast to 5 % drug release in HEPES buffer. High drug release in plasma conditions

has been observed for lysolipid TSL previously and was attributed to the presence of adhered plasma proteins and the mol% content of the lysolipid [155]. Although this is important for the development of TSL as therapeutics, it is based mainly on *in vitro* conditions. It will be of great importance to quantify the leakage of drugs from TSL during circulation as this will allow an estimate of the relationship of the drug release rate in blood, to the relative rapid DOX clearance from the body.

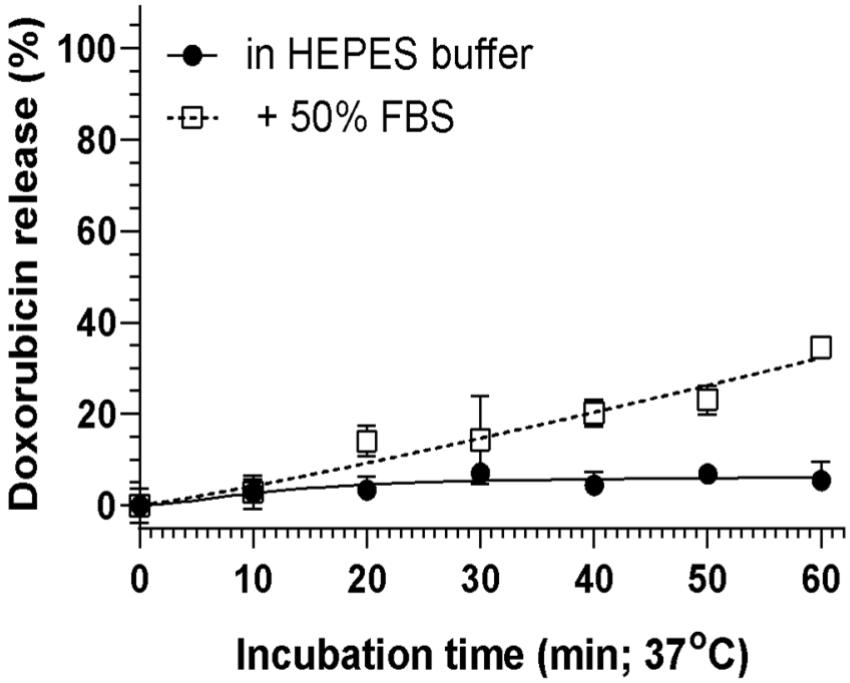

Figure 4.6: Effect of serum proteins on doxorubicin release from iTSL-DOX incubated at 37 ^{o}C for 10 min intervals up to 60 min in HEPES (4-(2-hydroxyethyl)-1-piperazineethanesulfonic acid) buffer (50 mM with 5 w% glucose; pH 7.4) and compared with buffer containing 50 v% fetal bovine serum (FBS) as a blood analogue. Release was monitored by the increase of intrinsic doxorubicin fluorescence (Ex_{480} / Em_{600} nm) as it leaves the self-quenched encapsulated state**.** (N=3 ± SD).

4.3.3 Storage Stability

There are only a few studies that investigate how long-term storage affects or degrades the TSL characteristics [290]. Reported formulations contain lysolipids and may show limited colloidal or drug-retention long-term stability, even at reduced temperature. This can be a particular issue at laboratory scale production where the methods of preparation, sterility assurance, and storage conditions are likely sub-optimal. A three-month stability study was introduced to investigate the effect of fridge storage (~5 °C) on iTSL-DOX formulation integrity.

Figure 4.7 shows the storage stability of a representative batch of aseptic produced iTSL-DOX contained in glass vials with a silicone stopper, with access only via sterile needle and syringe. First an evaluation of the room temperature stability was done to simulate conditions in the clinic as related to a first-in-human trial. Samples were left at room temperature for 3 or 24 h, points selected to mimic the time range that a formulation might be left on a bench during a human trial or large animal study. iTSL-DOX showed only minimum changes to the thermally induced doxorubicin release profile after 24 h. After 3 h there was little or discernible differences indicating a robust formulation that can remain unaltered at least 3 h outside of a fridge. **Figure 4.7b** shows stacked drug-release curves for samples taken at intervals from iTSL-DOX kept in cold-storage for 3 months. There was no apparent change on the release profile as the liposome ages, further confirming the formulation robustness. Dynamic light scattering (DLS) analysis of the same samples also showed

no significant changes to average nanoparticle diameter or the polydispersity index (PDI) over 2 months cold storage.

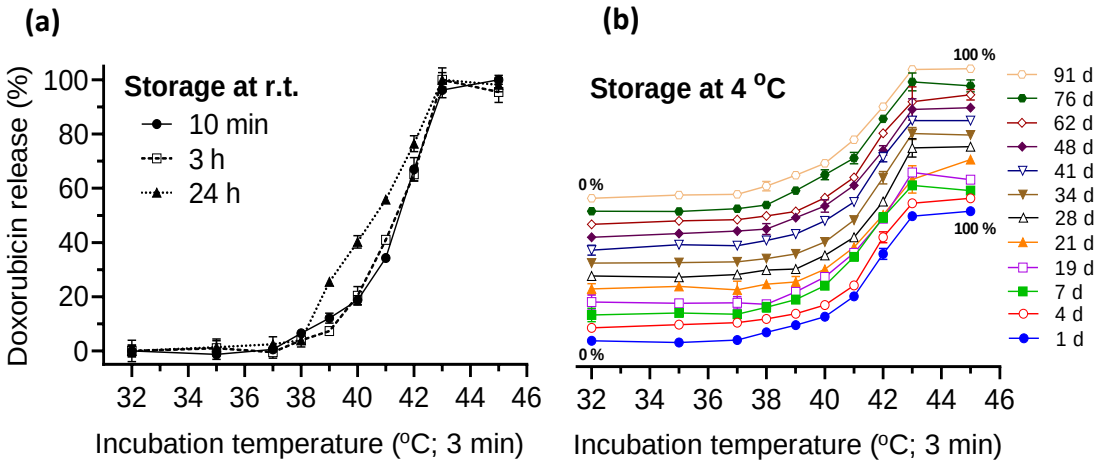

(c)

Day	Size (nm)	PDI	Day	Size (nm)	PDI
1	180.4	0.225	28	180.6	0.211
4	183.1	0.206	34	182.5	0.190
7	173.9	0.225	41	176.9	0.219
19	177.3	0.219	48	177.5	0.236
21	177.4	0.198	62	180.0	0.213

Figure 4.7: Storage stability of iTSL-DOX **(a)** At room temperature; samples taken from stored liposomes, then either assayed immediately after warming up or after being left at room temperature for 3 and/or 24 h; **(b)** In cold storage (~4 °C); stacked drug-release curves for samples assayed after aseptic cold-storage for up to 91 days after liposome preparation. (N=3 ± SD) Little or no change was seen in the release profile as the liposomes ages; **(c)** Dynamic light scattering (DLS) analysis representative average particle diameter and polydispersity index (PDI) data also shows no significant changes on storage for 2 months.

Although published studies generally avoid the investigation of nanomedicine behaviour upon storage, it has been suggested that stability and large-scale production processes require more attention [291,292]. For this iTSL-DOX formulation the incorporation of [Gd]DOTA.DSA at 30 mol% could have had a negative effect on stability. However, it was observed that the formulation maintains the same physicochemical characteristics upon a few months' storage in a fridge or a few hours at room temperature.

4.3.4 Gd^{3+} Retention by the DOTA Chelate

Free Gd^{3+} cations are toxic, due to interference with Ca^{2+}- dependant biochemical processes, amongst other effects [50]. This toxicity is greatly reduced when the metal is chelated. However, links have been demonstrated between the use of certain small-molecule MR contrast agents and rare but serious incidents of nephrogenic systemic fibrosis in patients with poor kidney function [293]. Thus, there is significant concern with respect to the safety of gadolinium contrast agents that may leak Gd^{3+} due to chelation competition from biomolecules in the body. As a result, linear molecule chelates (e.g. DTPA derivatives) are being generally replaced with ring chelates (e.g. DOTA derivatives) which show significantly better Gd^{3+} binding and retention, albeit often at the cost of reduced contrast agent effectiveness [225].

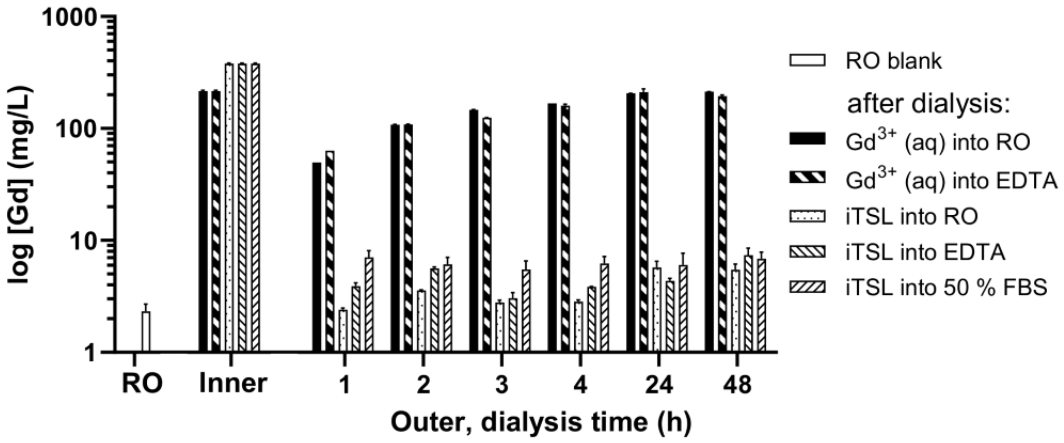

Figure 4.8: Gadolinium leakage analysis using dialysis membranes and TXRF. The potential for loss of the metal from the DOTA-lipid was established by assaying the amount of Gd^{3+} aq. able to escape through a dialysis membrane from an inner chamber containing either iTSL-DOX or 0.2 mg/mL gadolinium standard and into a cuvette containing reverse osmosis (RO) grade water at RT, 2.5 mM aq. ethylenediaminetetraacetic acid (EDTA) aq. at RT, or 50 % fetal bovine serum (FBS) aq. at 4 ^{o}C. The cuvettes were placed on a magnetic stirrer and 10 µL samples were taken at 1-48 h time points. These were analysed by TXRF to determine the concentration of gadolinium (N=3; ± SD). A scaled baseline is also given for N=11 samples of RO water.

In this experiment the integrity of iTSL Gd^{3+} chelation under a variety of challenging conditions was investigated. **Figure 4.8** shows a log plot of the leakage of Gd^{3+} (as assessed by TXRF) through dialysis membranes against water, aq. ethylenediaminetetraacetic acid (EDTA), and serum, over a period of two days. This was compared to the behaviour of similar concentration solutions of free Gd^{3+} from

standards (used in ICP-MS Tracert® standard). The pore size of the dialysis cassette used (10 kDa molecular weight cut-off (MWCO)) was too small for intact iTSL to get through, but large enough for any free Gd^{3+} to cross the membrane. Therefore, any gadolinium assayed from the external chamber was either from the control or was initially part of [Gd]DOTA.DSA and subsequently extracted by competition from the medium. Co-incubation of iTSL with 2.5 mM of EDTA was performed as this is a powerful chelating agent and provides a competitive environment to provoke leaching of Gd^{3+} from the DOTA. However, concentration of EDTA could be increased to an appropriate concentration that it could outcompete the DOTA ligand. Furthermore, competition with FBS was also assessed as serum contains many of the proteins and ions found in blood and provides a fairly realistic approximation of the competition [Gd]DOTA.DSA would encounter once injected *in vivo* **(see Figure 4.8).**

It was observed that while the free Gd^{3+} diffusion equilibrates after ~ 4 h, there was very little leakage from the iTSL samples and no obvious trend of increase of detected Gd^{3+} over the 48 h study. Similar results have been previously reported when gadolinium-based contrast agents were analysed for their metal content at equilibrium. These demonstrated greatly reduced Gd^{3+} leakage from macrocyclic chelators under serum conditions compared to linear chelators [294,295].The finding that Gd^{3+} is well retained within [Gd]DOTA.DSA and the iTSLs indicates that these liposomal contrast agents may be considered sufficiently safe for intravenous administration and further clinical development.

4.3.5 *In Vivo* Pharmacokinetics

In order to develop a better understanding of the pharmacokinetic behaviour of iTSL-DOX, LC-MS/MS and TXRF analysis were used to assess the clearance rates of doxorubicin (N=7) and [Gd]DOTA.DSA (N=6) from blood circulation post-injection of the nanocarrier to healthy CD-1 mice **(see Figure 4.9).** The iTSL-DOX was injected intravenously and blood samples were taken at predetermined time points. Doxorubicin appears to be cleared from the blood stream by 3 h, with a $t_{1/2}$ of ~80 min. In comparison with previously presented data on similar TSL-DOX formulations, data indicates that iTSL-DOX has a slightly shorter half-life [296,297]. Liposome kinetics were also measured based on assessing the level of gadolinium from [Gd]DOTA.DSA. It is evident that while iTSL-DOX circulates in blood up to 3 h post-injection, [Gd]DOTA.DSA is detectable for much longer. Considering the previously identified **(see Figure 4.6)** slow doxorubicin leakage under blood-like conditions it is possible that past 3 h the iTSL are still circulating but are empty of doxorubicin. Alternatively, the iTSL may have decomposed and the lipid [Gd]DOTA.DSA continued to circulate in the blood, potentially disassociated or bound to serum components. Either way it appears that [Gd]DOTA.DSA eliminates from the blood with a $t_{1/2}$ of ~150 min.

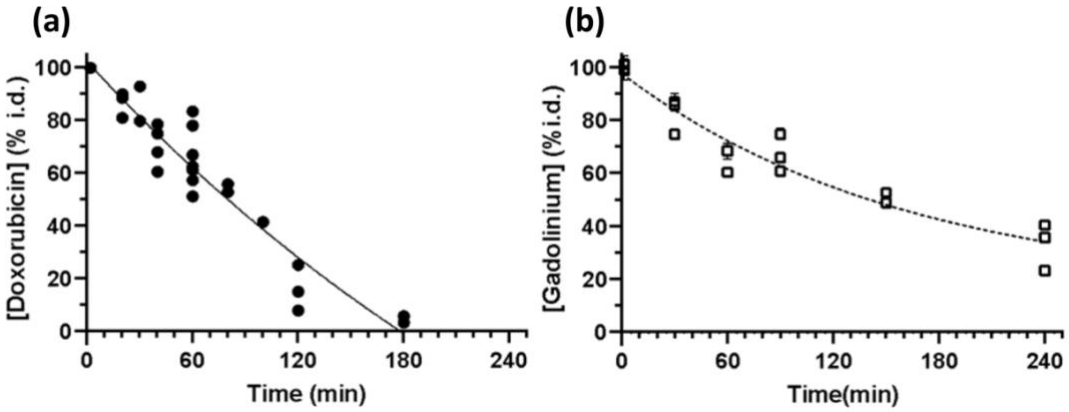

Figure 4.9: Clearance of iTSL-DOX **(a)** doxorubicin, N=7 and **(b)** gadolinium, N=6 from mouse blood circulation, as measured by HPLC-MS and TXRF respectively and shown as % of injected dose (I.D.). Mice were injected (*i.v.* tail) with iTSL-DOX (DOX equivalent 4 mg/kg), then blood samples were collected at time points. Data points shown are the mean average of 2-3 repeat analyses per sample ± SE

In general, TSL formulations are designed to avoid the very long blood circulation times usually observed with liposomes like Doxil®. TSL are intended to be combined with hyperthermia and to deliver a drug into the tumour's interstitial and/or intravascular space. To achieve this regional delivery TSL should be activated while they circulate at high concentrations and while they still retain their drug cargo. This indicates that the triggered drug release should occur before the normal blood clearance $t_{1/2}$ time point of the drug delivered by TSL. This is the suggested time window for when a thermal trigger can be applied for maximum tumour drug concentration [136,262]. Shorter half-lives can have the additional advantage of diminishing long exposure of tissues to doxorubicin as in the case of Doxil® [242].

Such limited exposure may have a significant advantage of limited DOX related cardiotoxicity. However, at this point there is no study to present a comparison of the therapeutic index between Doxil® and TSL-DOX.

4.3.6 *In Vivo* Biodistribution and Efficacy

Collected information on the pharmacokinetics of iTSL-DOX informs the design of the FUS administration protocol. Since the remaining iTSL-DOX encapsulated doxorubicin was significantly reduced after 1 h and effectively eliminated after 3 h. This suggests that FUS-induced hyperthermia should be applied soon after injection to affect release from iTSL that are still loaded with drug. However, this needs to be balanced by allowing sufficient time for the nanocarrier to accumulate in the target and/or by the use of multiple rounds of FUS at intervals to trigger freshly infused iTSL-DOX. Previous imaging results of our group with a similar iTSL-topotecan formulation demonstrated that the drug rapidly releases after brief rounds of FUS-induced hyperthermia treatment and that repetition can maximise the available drug in the tumour [194]. Short rounds of hyperthermia were also found to be equally efficient compared to prolonged continuous hyperthermia in a recent study [180]. It was determined that brief (≤5 min) periods of mild hyperthermia (≤ 43 ^{o}C) are sufficient to induce substantial drug release (intravascular and/or interstitial). In our group's experience brief FUS protocols are also safer than longer ones, being less stressful for the animals, reducing the risk of skin/tumour burns or other over-heating related damage, and avoiding false positive results (i.e. hyperthermic ablation, leading to tumour tissue damage masking the effect of the released chemotherapeutic).

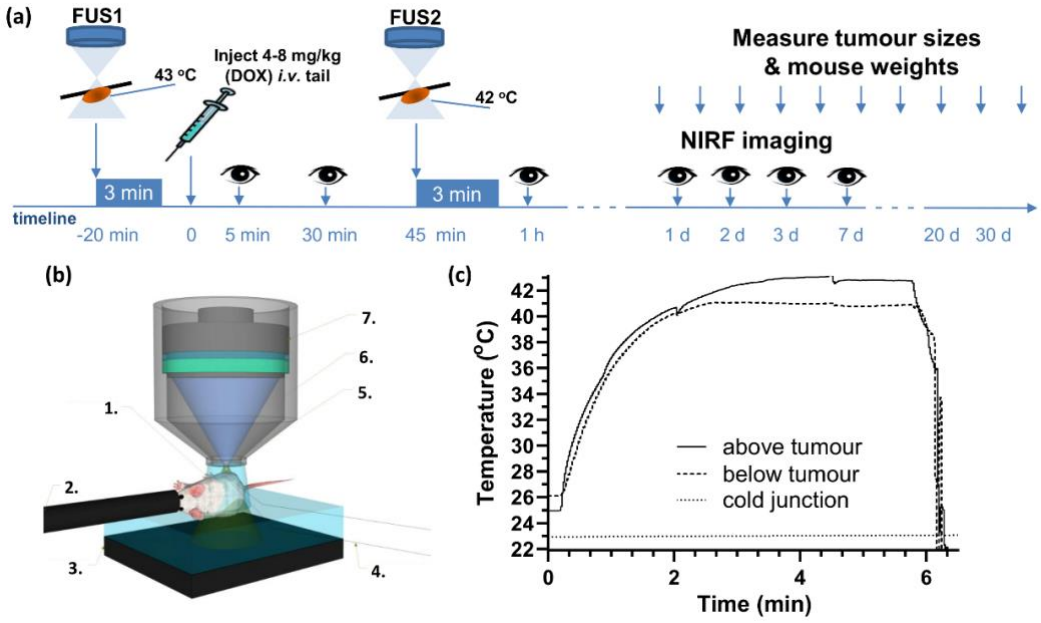

Figure 4.10: Preclinical FUS studies. **(a)** Study outline - once the xenografted tumours were ~5 mm Ø, each animal received: **(i)** leading FUS treatment, warming to 42 - 43 °C for 3 min as monitored by the implanted thermocouples; **(ii)** injection of iTSL-DOX (t=0) **(iii)** FUS treatment (to 42 °C for 3 min) applied once iTSL-DOX would have accumulated in the tumour observed by imaging **(iv)** then monitoring by whole body NIRF imaging, tumour sizing, and body weight until the end of the study; **(b)** TIPS setup with a mouse, showing key components: **1.** degassed gel; **2.** anaesthetic; **3.** acoustic foam; **4.** thermocouples; **5.** focus; **6.** ultrasound biconic; **7.** transducer; **(c)** FUS-induced tumour heating. Temperatures measured using fine-wire thermocouples (0.08 mm) implanted *s.c.* above and below the tumour (with respect to the transducer location). The cold junction is the temperature of the thermocouple electronics and is approximately 2 °C above room temperature. Tumour temperatures were measured at 50 ms resolution and FUS acoustic power settings adjusted manually to converge on the target temperature.

iTSL-DOX was injected at 4 mg/kg dose of doxorubicin (and controls) into mice **(single (right-side) tumour model)** with human triple negative breast cancer cell (TNBC, MDA-MB-231) tumours. Tumours were placed on the haunch to allow easier and safer access of the FUS beam and had a ~5 mm starting diameter. FUS-induced hyperthermia was applied according to the protocol seen at **Figure 4.10**. Just before injection the tumour was treated with FUS for 3 min to elevate its upper surface to a peak temperature of 43 ^{o}C (measured from thermocouples inserted at bottom and top tumour location). Under these conditions the temperature between the tumour and the basal muscle was then 41-42 ^{o}C achieving a mild hyperthermia temperature. This pre-injection FUS treatment has been reported to improve therapeutic efficiency from heating tumours either before the injection of TSL-DOX [259,260], just before and then during infusion [298], or immediately after injection [200,299]. For example, Thermodox® preclinical development information strongly suggests that the heating of the tumour needs to precede the injection of the TSLs [259,275]. Other studies have demonstrated effective treatment with FUS applied just before and then during infusion [298], or immediately after injection [299]. In addition, the phase III HEAT clinical trial computer modelling led to introduction of radiofrequency ablation (RFA) 15 min post infusion [275]. Similarly, the TARDOX study indicated application of FUS shortly after infusion [279]. In the literature there is a high variance of TSL FUS protocols which suggests that better feedback tools are required to allow the identification of optimum timing. Application of FUS can be made easier for clinicians by utilizing feedback through imaging of the TSL during treatment. For instance, FUS could be applied when the tumour's MR contrast is increasing in the tumour. Under clinical conditions FUS-induced hyperthermia would be applied and

controlled using concurrent imaging (e.g MR) which should identify the tumour and margins. This would also be used to monitor the TSL accumulation and provide a confirmation that the appropriate dosage has reached the tumour [300].

According to the optimised protocol shown in **Figure 4.10** one brief sonication before injection was combined with a second brief sonication after injection but with sufficient delay to allow for enhanced iTSL-DOX uptake into the tumour. Selected treatment time points **(see Figure 4.10a)** were based on previous experience and pilot studies that suggested that brief hyperthermia rounds promote tumour nanoparticle accumulation [194] and this is maintained for several hours (data not shown). Near Infrared Fluorescence (NIRF) tracking of iTSL uptake facilitated the selection of a 45 min post-injection time point for the second FUS, leading to significant tumour accumulation [286] which still corresponds to ~70 % availability of injected dose (I.D.) of doxorubicin (and liposomes) in the blood stream **(Figure 4.9).** At this time point, it is also likely that iTSL-DOX still encapsulates the great majority of the doxorubicin in the blood since both doxorubicin and gadolinium are found with same % injected dose (I.D.).

All mice experiments presented here (both single and double tumour models) were performed with preclinical biconic FUS (TIPS; Philips Research, Netherlands) and the FUS focal volume was deliberately placed slightly above and outside the target tumour. This was done to avoid the formation of a hot spot within the tumour body, ensuring the effects seen were due to FUS-induced mild hyperthermia and not

ablative tissue damage. The TIPS window was placed 8.0 mm above the tumour surface where the FUS focal volume was 7 mm above the tumour surface which had radius of 5.2 mm. The gap between TIPS window and mouse tumour was filled with warmed and degassed ultrasound gel. FUS was applied at 1.3 MHz, using a 100 % duty cycle. To control the applied FUS power, tumour temperatures were monitored in real time using fine-wire thermocouples (T150A) that were implanted around the tumour as a part of the setup **(see Figure 4.10b**). Tumour temperatures were measured at 50 ms resolution and TIPS acoustic power settings were adjusted manually 10 to 20 W to converge on the target temperature 42-43 ^{o}C and this could then be maintained with little variation. This was to substitute for the more elaborate MR thermal maps provided by clinical MR-guided FUS equipment [301]. Two fine-wire thermocouples with diameter of 0.08 mm were inserted below and above the tumour. The diameter of thermocouple was selected to be thin with its placement avoiding the FUS focal volume, and temperatures were monitored throughout the treatment. This is important to prevent tissue damage from an overheated thermocouple from FUS. **Figure 4.10c** provides typical thermographs achieved during a FUS treatment. FUS-induced doxorubicin release responsiveness was investigated and optimised prior to animal studies by Dr. Michael Wright as shown in **Appendix 1.**

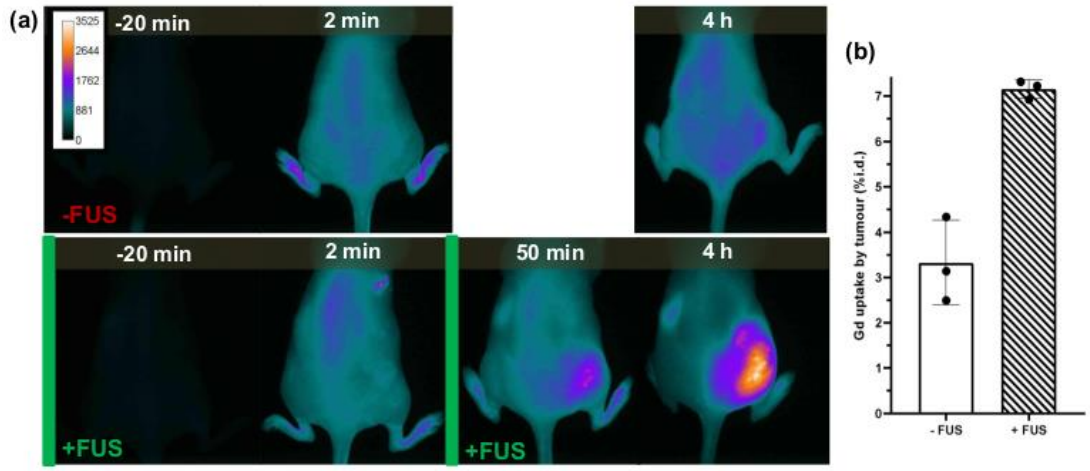

Figure 4.11: Representative images of iTSL-DOX uptake and effects from a single tumour study, tracked by Near Infrared Fluorescence (NIRF) and TXRF gadolinium quantification; **(a)** Comparison of mice injected (*i.v.* tail vein) with iTSL-DOX (4 mg/kg), without (-FUS) and with (+FUS) according to insonation protocol. NIRF imaging are shown pre/post-injection and the FUS treatments are indicated by the green bars. At 4 h the animals were sacrificed, and tumours excised for **(b)** gadolinium tumour concentration analysis by TXRF after acid digestion at 4 h post treatment. Graph shows the mean of N=3 mice; ± SD

NIRF imaging was used to monitor the fluorescence signal from the iTSL within the tumour and the rest of the body (single tumour model). This form of fluorescence imaging has been previously used to monitor tumour accumulation of TSL with hyperthermia [298]. This type of imaging was selected as a robust method that it may significantly facilitate drug development [302]. **Figure 4.11a** shows representative mice from groups that have been administered iTSL either with or without FUS and then undergone real time tracking by NIRF imaging. It is evident that lack of FUS-

induced hyperthermia led to little accumulation of the iTSL in the tumour. However, when the brief treatments of hyperthermia were applied a substantial increase in tumour signal occurred. Based on the kinetic studies **(see Figure 4.9**) mice were monitored up to 4 h. At this time point: (a) remnant circulating iTSL are likely to be empty and; (b) the rate of their partition in the tumour compartment should be decreasing [303]. Gadolinium content of tumour samples were also analysed after the animals were sacrificed at 4 h **(see Figure 4.11b).** Animals were sacrificed, tumours were excised for acid digestion to facilitate TXRF analysis. At this point post treatment and after a single 3 min hyperthermia round it was identified that the amount of iTSL in the FUS-treated tumours was more than double compared to untreated tumours. Such short and mild hyperthermia applied i*n vivo* can lead to a significant enhancement of tumour TSL concentration. With the proper use of imaging it is possible to repeat these rounds focusing mainly in the tumour area.

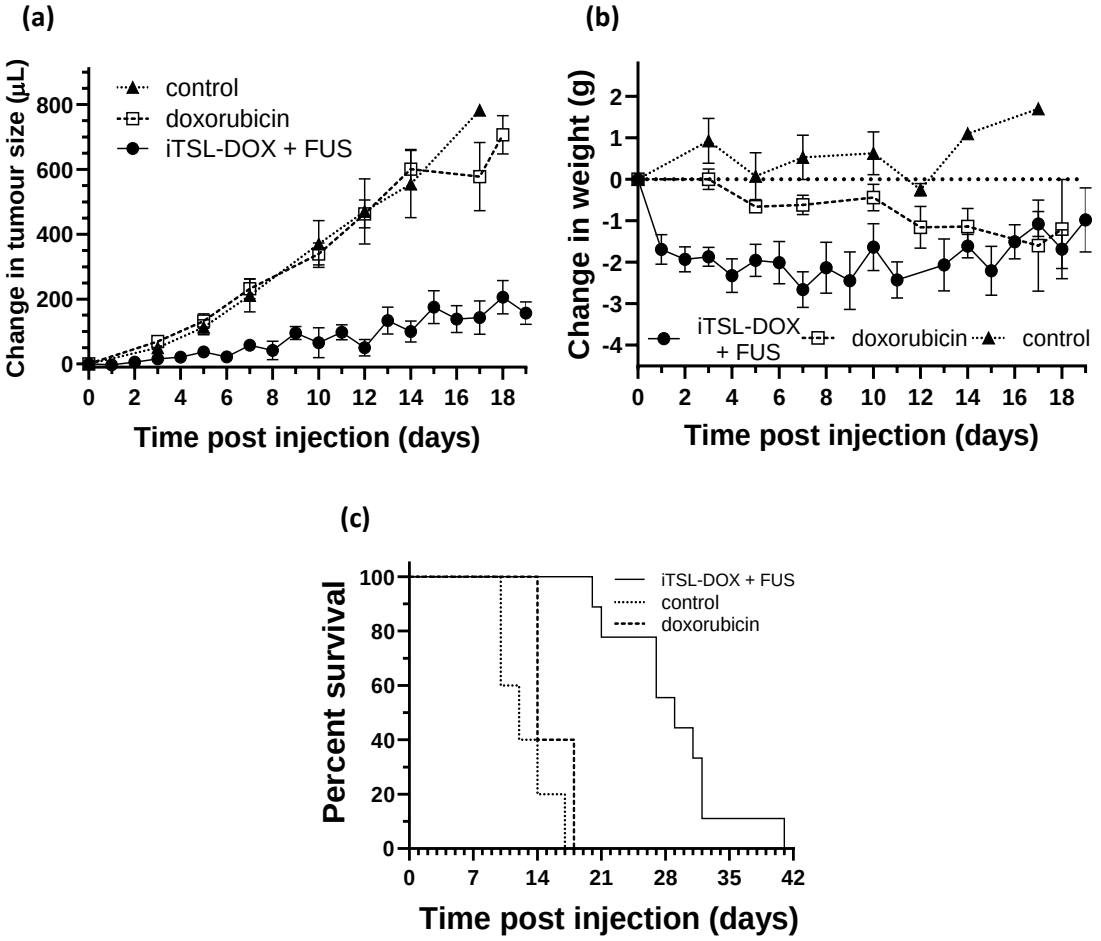

Figure 4.12: Single-tumour mouse studies were performed once tumours were 5-6 mm Ø for each animal. **(a)** Averaged tumour volumes (mean ± 1 SEM) for the control (nil drug; N=5, initial average tumour size 91.01 ± 19.85 μL), doxorubicin (N=5, initial average tumour size 96.04 ± 10.98 μL), and iTSL-DOX + FUS treated (N=9, initial average tumour size 94.52 ± 12.01 μL) mouse groups; **(b)** Body weights and; **(c)** survival graphs for the same. Dosage was 4 mg/kg equivalent of doxorubicin. **Figure 4.10** shows the protocol that was implemented in this study for the iTSL-DOX and FUS treatment group. Initial tumour volumes for all three groups did not exhibit statistically significant differences according to the ANOVA 1-way test (p = 0.846).

For comparative efficacy studies a **single (right-side) tumour model** was used and groups were: (i) iTSL-DOX and FUS (N=9, initial average tumour size 94.52 ± 12.01 μL); (ii) doxorubicin alone (N=5, initial average tumour size 96.04 ± 10.98 μL); and (iii) control treatment (nil drug; N=5, initial average tumour size 91.01 ± 19.85 μL). Dosage was 4 mg/kg equivalent of doxorubicin for both doxorubicin alone and iTSL-DOX and FUS. Single-tumour mouse studies were performed once tumours were 5-6 mm Ø for each animal. The difference in the initial tumour volumes between all three groups was not statistically significant according to the ANOVA 1-way test (p = 0.846). **Figure 4.12a-c** presents the effects of iTSL-DOX in combination with short FUS protocol compared to controls of doxorubicin or control with nil drug (both without FUS). One can observe that brief rounds of hyperthermia induce a powerful retardation in tumour growth in combination with iTSL-DOX. By contrast, little effect is seen in the group treated with dose-matched doxorubicin alone. This breast cancer tumour model was previously used with TSL-DOX and Lokerse *et al*. reported similar levels of tumour growth inhibition at 5 mg/kg doxorubicin [304]. However, in Lokerse's study hyperthermia was applied for 60 min using a hot water bath. Similar effects were achieved with ~$1/10^{th}$ of the hyperthermia application time via the utilized protocol **(see Figure 4.10 and Figure 4.12).** It seems likely that such extended hyperthermia treatments are unnecessary. Clinical MR-imaging could be of significant assistance here, giving location information and informing of the required thermal dose. A related concern is that extended FUS treatments are harder to translate to the clinic, requiring a patient to spend a significant time immobilised in the scanner [180]. Apart from the discomfort, this has important implication on heating precision. Precise hyperthermia for deep seated tumours also requires lack

of motion suggesting that short repeated rounds may be more efficient than 1 hour long thermal treatments. It is likely that even shorter but frequent rounds to have an improved effect. **Figure 4.12b** shows changes of body weight, with the mice initially at ~22 g. Both drug-treated groups showed weight loss, with the doxorubicin-only treated mice showing gradually but continual weight reduction over 2 weeks post-injection. Mice treated with iTSL-DOX+FUS initially lost ~10 % weight (limit being 15 % of initial body weight) but then stabilised and appeared to partially recover. Overall, mice that were treated with iTSL-DOX+FUS responded better and survived longer as seen by the Kaplan-Meir curve at **Figure 4.12c.**

The response to iTSL-DOX plus brief FUS treatment on animals bearing two tumours were also assessed. In this **double tumour model**, the left side received no hyperthermia but iTSL-DOX as normal, while the right side received both. Dosage was 6 mg/kg equivalent of doxorubicin for iTSL-DOX and the study setup was the same as the single tumour model mouse study as shown in **Figure 4.9**. These experiments provide a better understanding of the treatment effects as each animal also served as nil-FUS control. Each animal had two similar sized tumours with each receiving theoretically the same dose of iTSL-DOX per unit time per tumour volume. A paired Student's t-test showed there was not a statistically significant difference between paired left and right initial tumour volumes (p = 0.225). **Figure 4.13** presents real time NIRF imaging of iTSL-DOX kinetics on a mouse bearing two MDA-MB-231 tumours and with the optimised double-FUS protocol **(as shown in Figure 4.9.)** applied on only one side. It is evident that FUS-treated tumour (right) allowed the iTSL-DOX to be

accumulated to a much larger extent compared to the FUS-untreated (left) tumour. It is also evident that intrinsic doxorubicin fluorescence (shown here in red/blue) is distinguishable in the +FUS tumour to larger extent compared to the -FUS and only when the second round of hyperthermia was applied. Since the doxorubicin fluorescence is in the visible region it is strongly absorbed by tissue and extremely difficult to detect in whole animals.

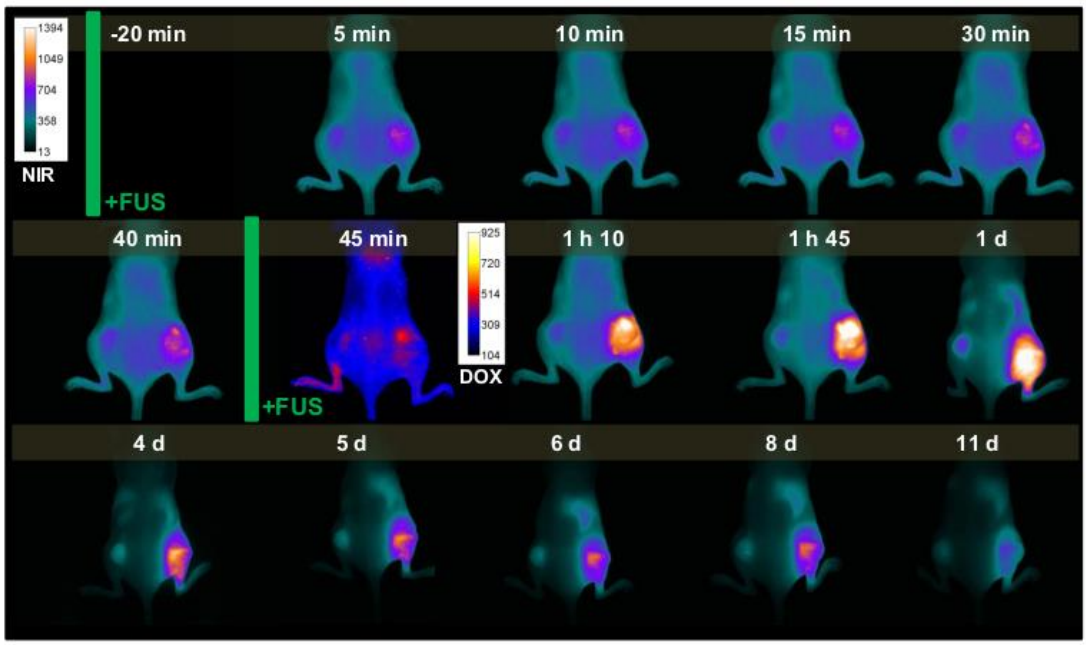

Figure 4.13: Representative examples of NIR and doxorubicin fluorescence imaging of one mouse during the dual-tumour study. Time points are given post-injection and the FUS treatments are indicated by the green bars. Imaging continued for 2 weeks post-treatment. NIR images are coloured cyan-yellow, doxorubicin is indigo-red.

NIR images in **Figure 4.13** demonstrates that the CF750.DSA lipid appears to clear slowly from the treated tumour for up to 2 weeks post administration. The signal from the untreated tumour appears to fade more rapidly, indicating faster clearance. It is possible that FUS-induced hyperthermia enhances the permeation and incorporation of lipophilic CF750.DSA into the tumour tissue itself. The concept of hyperthermic-enhanced delivery of lipophilic drugs transferred with a suitable nanocarrier has not yet been explored.

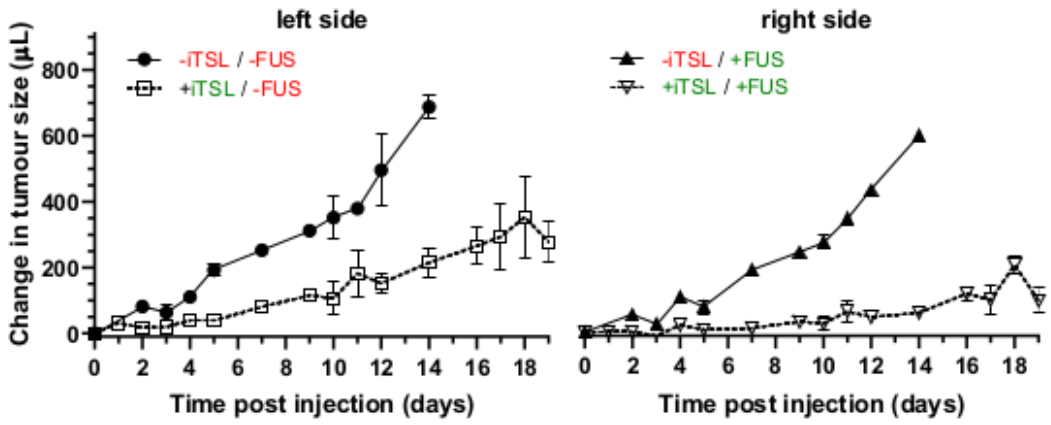

Figure 4.14: Double-tumour mouse studies, in which each mouse carried two haunch tumours, with only the right-side one treated by FUS. Average tumour sizes for the left and right sides (mean ± SE) are shown and each tumour in an individual animal were similar size. A paired Student's t-test showed there was not a significant difference between left and right tumours in the same mouse (p = 0.225). The groups were: nil drug (N=3) received only FUS on the right-side tumour, leaving the left to grow normally as a no-FUS control; and iTSL-DOX (N=10) at equivalent to 6 mg/kg doxorubicin and again FUS only on the right-side.

Doxorubicin is a hydrophilic drug that has a good ability to permeate membranes and distribute between tissue compartments [305,306]. It also rapidly clears from tissues and blood when not encapsulated in liposomes. Although several studies demonstrate the effect of hyperthermia on DOX uptake by tumours, there is no study presenting the DOX clearance from a hot tumour versus a normothermic tumour. Presented NIRF images indicate that released DOX does not remain in tissue. This was also previously observed in a study published by our group with topotecan iTSLs [194].

The effect of FUS-induced iTSL-DOX treatments in this double-tumour model is shown in **Figure 4.14** For this experiment the doxorubicin dose was at 6 mg/kg as animals were bearing two tumours. As with the single tumour experiments iTSL-DOX dosing causes a pronounced reduction in the tumour growth. This occurs even on the nil-FUS tumours, but the most significant tumour growth inhibition occurred when iTSL-DOX was combined with FUS-induced hyperthermia. In this study mice also did not show significant weight loss even if they were bearing two tumours **(Appendix-2)**. The double tumour model helps assessing the effect of FUS in combination with the drug. In a double tumour model, tumours receive the dosing the same way and the effect of FUS can be seen clearly.

4.3.7 *In Vivo* MRI Study:

The synthesised iTSLs were assessed for their abilities to function as MRI contrast agents. MRI contrast agents are used to increase the contrast between tissues, usually by shortening the longitudinal (T_1) relaxation time or the transverse (T_2)

relaxation time. T_1 shortening leads to increased signal intensity in a T_1-weighted MR image, whereas T_2 shortening results in decreased signal intensity in a T_2-weighted MR image. In this study, the effect of iTSLs on MRI contrast was investigated at 9.4 T magnetic field strength. Aim was to identify and quantify iTSL accumulation in tumours by monitoring changes in the T_1 relaxation after administration.

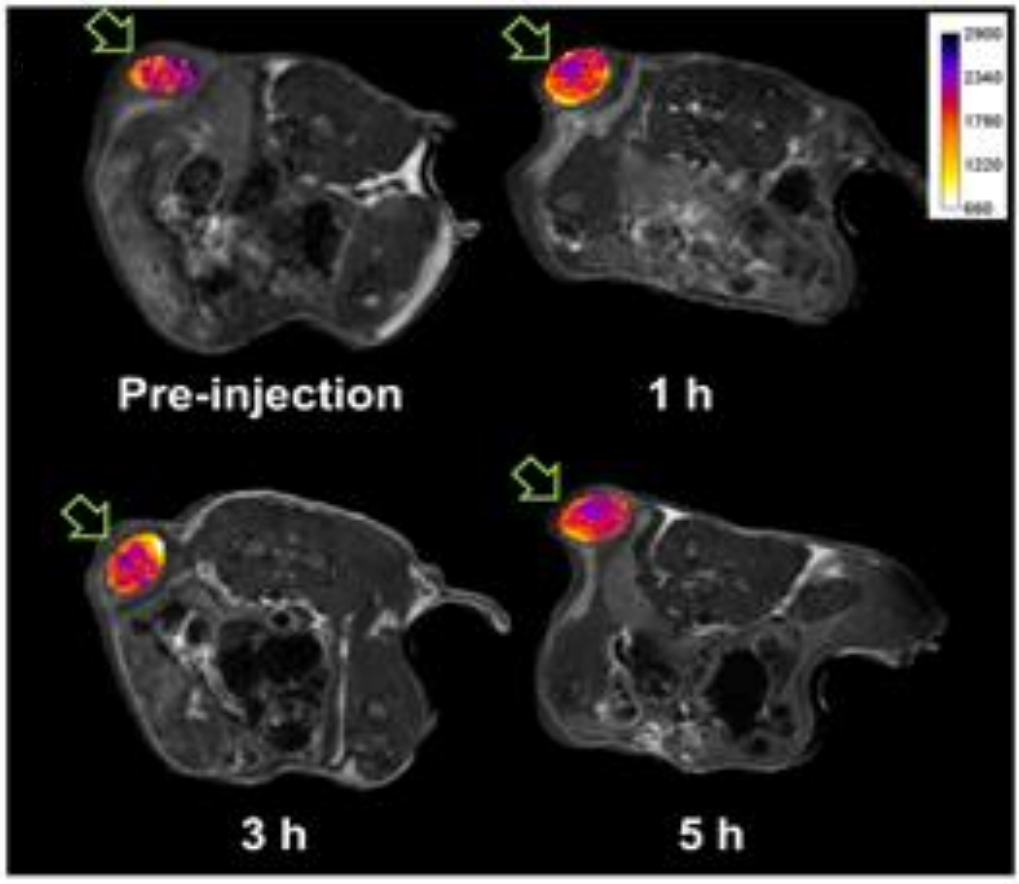

Figure 4.15: Spin-echo transverse T_1 weighted MR imaging, iTSL (1.37 mg/mL gadolinium) was injected (*i.v.* tail vein) to mice. Imaging (9.4 T) of the same representative animal pre-injection, then 1, 3, and 5 h post-injection. Tumours are overlaid with T_1 relaxivity maps for the region-of-interest (ROI), shown in false colour and indicated with arrows.

Six athymic nude mice bearing single tumour (grown to 5-6 mm Ø) were anesthetized and injected (*i.v.* tail vein) with iTSLs (200 µL, 1.37 mg/mL gadolinium concentration), without encapsulation of DOX (to avoid any toxicities while handling). MRI was performed **(see Figure 4.15)** before and immediately after injection, and up to 5 h post injection of iTSLs, without application of FUS-induced hyperthermia. A vial containing Gadovist® ([Gd] 3 ± 0.01 mg/L) was placed adjacent to the animal as a reference standard.

Typical T_1-weighted MR images of the subcutaneously implanted tumour in mice, before and after iTLS injection is shown in **Figure 4.15.** Injection of iTSL resulted in an increased MR signal intensity, highlighting the tumour from the surrounding tissue. Greater perspective could be gained from analysing MR signal intensity in larger animals with larger tumours. Similar studies reported recently by Liu *et al.* used the relative signal intensity from T_1-weighted MR images of kidney and liver to study the kinetics of [Gd]DTPA labelled liposomes [307]. For our study, using MRI to monitor the presence of iTSL in the tumour would greatly facilitate when FUS should be applied. **Figure 4.16** shows changes in mean T_1 of tumours compared to that of two references, a vial of Gadovist® commercial contrast agent and the skeletal muscle. These reference regions were not expected to change over time. Tumours, however, show decreases in T_1 values over time due to the accumulation of iTSLs in the tumour that can be detected within an hour after injection **(see Figure 4.16)**. An increase in the standard deviations of the T_1 values within the tumour were also observed, which could be attributed to heterogeneity of the tumour (necrotic core) and iTSL uptake.

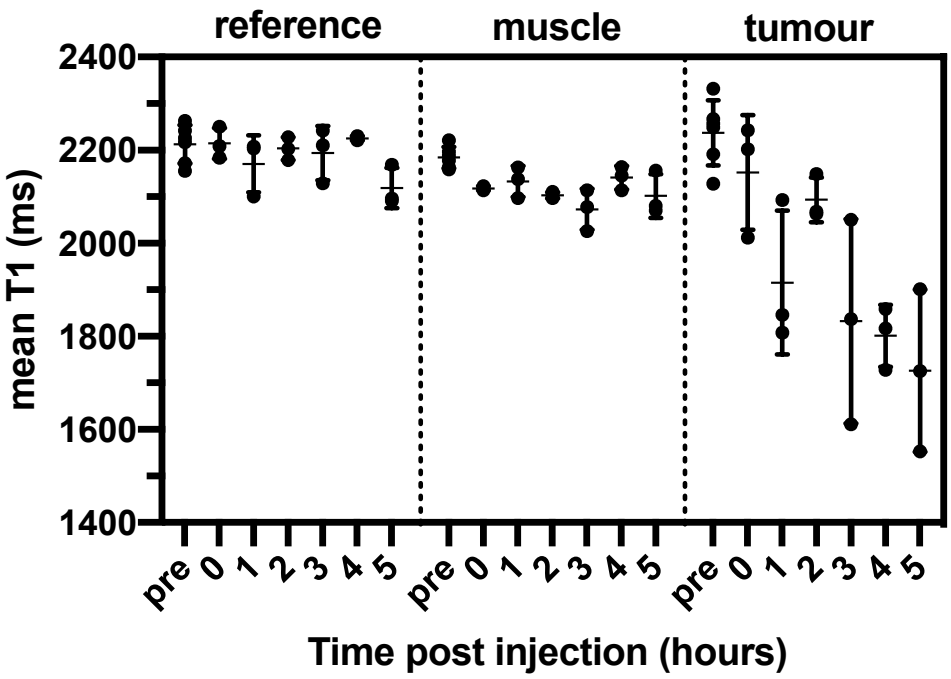

Figure 4.16: Whisker plot showing mean T_1 values (± 1 SD) for the reference (Gadovist®, [Gd] 3 ± 0.01 mg/L), skeletal muscle and tumour before and after iTSL injection into mice (N=6). Tumour T_1 relaxation times (ms) decreased immediately after injection of iTSLs (*i.v.* tail vein) and for up to 5 h post injection. All analysis used Graphpad Prism v 8.2.1. **(Appendix-4)**

This MRI study encourages the clinical translation of iTSL and suggests that true MR-guidance of iTSLs is possible. The observed change of T_1 suggests the accumulation of iTSL-DOX in the tumour soon after injection that persists for at least 5h post-injection. Thus, MRI can serve to guide the appropriate timing of FUS application to induce DOX release from iTSLs.

Overall, iTSL-DOX was prepared that bear the capabilities of a MR contrast agent and triggered release for real image guided drug delivery. A similar approach has been recently suggested that would combine MR imaging and NIR-triggered drug release [308]. The study clearly supports the fact that when a phase change liposome is combined with imaging and a source of energy a substantial antitumor effect can be achieved. Presented study proposes a simpler approach that can be translated to the clinic and be combined with clinical MRgFUS equipment. FUS has no limitation of the depth of the tissue as NIR light has and as a result it can be applied to deep seated tumours.

Also a special attention was taken to introduce to the liposomes a macrocyclic Gd^{3+} chelator that is considered to be substantially safer and it is widely used in clinical imaging [309]. We assessed the gadolinium chelation efficacy under challenging conditions, and we confirm that these iTSL leak minimal Gd^{3+} or doxorubicin under *in vitro* comparable conditions. We also investigate the iTSL-DOX storage stability. To our knowledge this is the first time that such a study considers these important clinical translation steps.

4.4 Conclusion

Theranostic liposomes have repeatedly appeared in the literature for MRI, PET, SPECT. It has been suggested for pH and/or temperature-response or for photodynamic and/or photothermal therapies (PDT, PTT) [310]. As liposome functionalities increase, their development requires more sophisticated design. In this study a novel methodology to assess iTSL-DOX response to increased temperature, focused ultrasound and their integrity under different and challenging conditions was proposed. Single and dual tumour murine models experimentation were utilized to assess the effect of their functionalities (e.g. drug release, imaging). MR detection and assessment of the T_1 relaxation time post *i.v.* injection provide solid evidence that these liposomes can operate as theranostics for image guided focused ultrasound drug delivery. iTSL-DOX in combination with very short rounds of FUS have shown significant tumour growth inhibition suggesting that iTSL are a suitable platform technology for drug FUS combination. Cancer nanomedicine has shown significant advances in the clinic during recent years [311]. Responsive liposomes with imaging potential such as the iTSLs represent a new class of nanomedicine that can be translated to the clinic.

5. Materials and Methods

5.1 Materials

Lipids were purchased from Avanti Polar Lipids, Inc. (Alabaster, AL) or Sigma-Aldrich (St. Louis, MO, USA): 1,2-dipalmitoyl-*sn*-glycero-3-phosphocholine (DPPC; 16:0 PC), 1,2-distearoyl-*sn*-glycero-3- phosphocholine (DSPC; 18:0 PC), 1-stearoyl-*sn*-glycero-3-phosphocholine (MSPC; 18:0 lyso-PC) and (*ω*-methoxy-polyethyleneglycol^{2000})-*N*-carboxy-1,2-distearoyl-*sn*-glycero-3-phosphoethanolamine (PEG^{2000}-DSPE), and cholesterol. DOTA succinimidyl ester (DOTA-NHS-ester) was purchased from CheMatech (France) and CF750 succinimidyl ester (CF750-NHS) from Biotium (Fremont, CA, USA). Gadovist® (1.0 mmol/mL gadobutrol containing 1572.5 mg/L gadolinium) was purchased from Bayer AG (Germany). For digestion process H_2O_2 (30 w% in water; Sigma-Aldrich) and HNO_3 (68 w% aq.; Primar Plus™, Fisher Scientific, Hampton, NH, USA) were used. Metal analysis calibration and controls used TraceCERT® certified reference materials (Sigma Aldrich). Cell media were from Life Technologies (Carlsbad, CA, USA). Other reagents were from Sigma-Aldrich and were of analytical grade unless otherwise stated. All water used reverse osmosis (RO) purified to 18 MOhm or better and stored in sterile plastic. The other lipids were synthesised in-house as described below.

5.2 Methods

^{1}H NMR was carried out on Bruker Advance 400 spectrometer (Bruker, Germany) using residual chloroform or dichloromethane as internal standards. Results were reported as chemical shifts in ppm from TMS, with peaks described as s = singlet, br = broad singlet, d = doublet, t = triplet, q = quartet, m = multiplet, and coupling constants J given in hertz (Hz). Mass spectroscopy was carried out on a Thermo LCQ DECA XP or Agilent HP1100 MSD spectrometers depending on availability. Thin Layer Chromatography (TLC) was carried out on F254 silica gel 60 plates, with spots visualised by UV illumination or iodine staining. Flash column chromatography was performed on 40-63 µm silica gel. Reaction glassware was dried at 100 ^{o}C under vacuum for at least 30 min before use. Differential Scanning Calorimeter (DSC) measurements were carried out with Nano DSC (TA Instruments, New Castle, DE, USA), was used to study the thermal behaviour of liposomes. Dynamic light scattering (DLS) and ζ-potential measurements of liposomes were carried out with Nanoseries Nano ZS Malvern Instruments (Worcestershire, UK). Inductively coupled plasma - optical emission spectrometry (ICP-OES) was performed on a Thermo Scientific ICAP 6300 Duo View (Thermo Scientific Chemical, Hampton, NH). Total reflection X-ray fluorescence (TXRF) was performed on a PICOFOX™-S2 instrument (Bruker Nano GmbH, Karlsruhe, Germany). HPLC using an Agilent 1100 series instrument equipped with a multi-wavelength diode array detector (DAD), a 1260 Infinity fluorescence detector (FLD; all from Agilent, Santa Clara, CA, USA), a Polymer Laboratories PL-ELS-2100 evaporative light scattering (ELS) detector. UV spectroscopy and fluorescence

measurements were performed on an Infinite 200 Pro, Tecan, plate reader (Männedorf, Switzerland).

5.3 Synthesis of Lipids

The protocol for synthesis of Gadolinium (III) 2-(4,7-Bis-carboxymethyl-10-[(*N*,*N*-distearylamidomethyl-*N*'-amidomethyl]-1,4,7,10-tetraazacyclododec-1-yl) acetic acid **([Gd]DOTA.DSA)** was adopted from Kamaly *et al* [83] and reported previously by our group by Centelles *et al* [194]. Experiments were designed by courtesy of Dr. Michael Wright.

N,N-distearylamidomethylamine (DSA); Compound 3

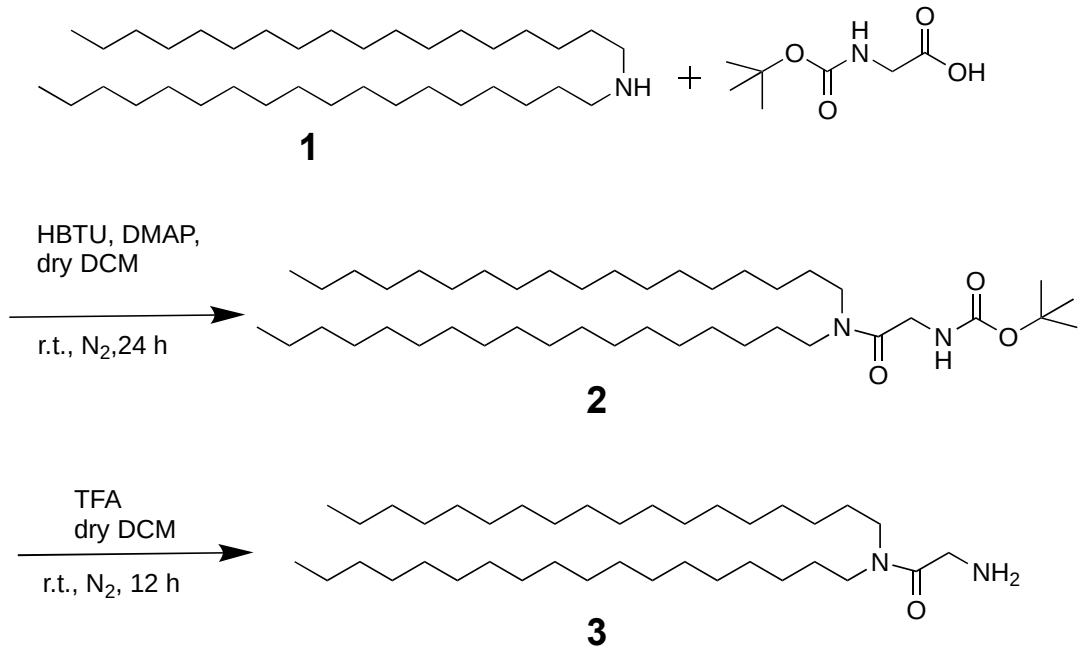

Scheme 5.1: Schematic representation of synthesis of *N,N*-distearylamidomethylamine (DSA).

Dioctadecylamine (**1**; 923.96 g, 1.77 mmol) and BOC-Gly-OH (*tert*-Butyloxycarbonyl) (310 mg, 1.77 mmol) were dissolved in dry dichloromethane (DCM; 30 mL) This was combined with *N*,*N*,*N*′,*N*′-tetramethyl-*O*-(1*H*-benzotriazol-1-yl)uranium hexafluorophosphate (HBTU; 804.12 mg, 2.12 mmol) and 4-(dimethylamino)pyridine (DMAP; 648.72 g, 5.31 mmol) then stirred at rt; under N_2 for 24 h. The volatile solvents were removed in *vacuo*. The resulting residue was resuspended in DCM (50 mL) and washed with water (3 x 50mL). Then it was washed with 7 w% citric acid (3x 100 mL) and brine (3x 100 mL). The organic layers were combined and then dried over $MgSO_4$, frit filtered and organic layer dried *in vacuo* to yield the product BOC-DSA (1.15 g, 1,69 mmol, 95 % yield); ^{1}H NMR (400MHz, $CDCl_3$): δ_H (ppm) 5.50 (s, 1H), 3.87 (d, *J* = 3.9 Hz, 2H), 3.27 – 3.21 (t, *J* = 7.5, 2H), 3.13 – 3.03 (t, *J* = 7.5, 2H), 1.46 (s, 4H), 1.38 (s, 9H), 1.19 (s, 60H), 0.81 (t, *J* = 6.8 Hz, 6H); TLC R_f [DCM:MeOH:NH_3; 17:3:0.1 v/v] 0.75; ESI-MS Calcd. for $[M]^+$: 679.2 a.m.u. Found $[M+H]^+$: 680.0 a.m.u.

The BOC protecting group was removed by dissolving above prepared BOC-DSA (**2**, 1.15 g, 1,69 mmol) in dry DCM (5 mL) with addition of trifluoroacetic acid (TFA; 3 mL) and stirred for 12h at r.t. under N_2. It was dried by rotavap and then re-dissolved in DCM. Then diethyl ether (150 mL) was added. The resulting cloudy suspension was cooled at -20 ^{o}C for 2h. The resulting precipitate was collect by filtration to yield the product as a TFA salt (1.14 g, 1.64 mmol, 97 %); ^{1}H NMR (400MHz, $CDCl_3$): δ_H 8.47 (s, 2H), 3.86 (s, 2H), 3.31 (t, *J* = 7.5, 2H), 3.13 (t, *J* = 7.5, 2H), 1.60 – 1.45 (m, 4H), 1.28 (br, 60H), 0.90 (t, *J* = 6.7 Hz, 6H); ESI-MS Calcd. for $C_{38}H_{78}N_2O$ $[M]^+$: 578.6 a.m.u. Found $[M+H^+]^+$: 579.3 a.m.u.

Gadolinium (III) 2-(4,7-Bis-carboxymethyl-10-[(N,N-distearylamidomethyl-N'-amidomethyl]-1,4,7,10-tetraazacyclododec-1-yl) acetic acid ([Gd]DOTA.DSA) Compound 6

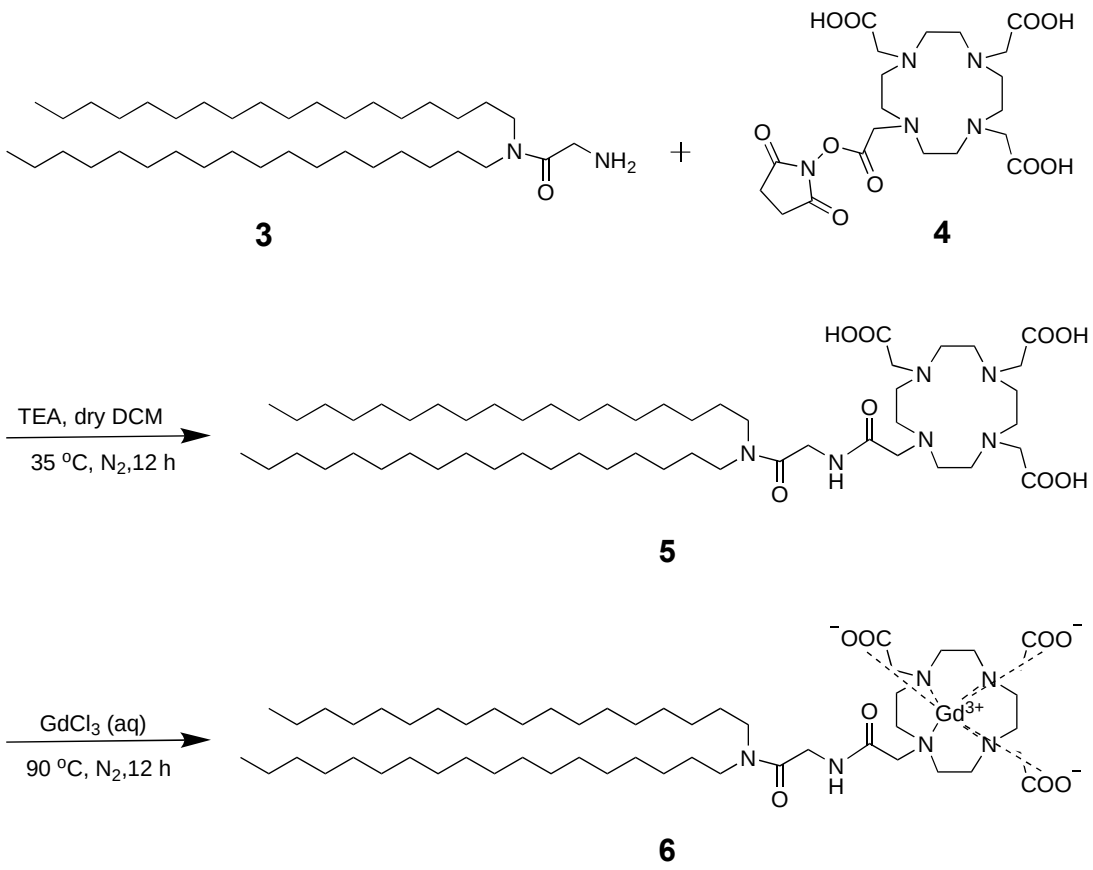

Scheme 5.2: Schematic representation of synthesis of Gadolinium (III) 2-(4,7-Bis-carboxymethyl-10-[(*N*,*N*-distearylamidomethyl-*N*'-amidomethyl]-1,4,7,10-tetraazacyclododec-1-yl) acetic acid ([Gd]DOTA.DSA)

DOTA-NHS-ester; **4;** 100 mg, 0.12 mmol) and DSA (**3;** 80.2 mg, 0.14 mmol) were dissolved in dry DCM (40 mL). Distilled triethylamine (TEA, 67 µL, 0.48 mmol) was added and the mixture stirred under N_2 for 12 h at 35 °C. The solution was dried *in*

vacuo and purified by flash chromatography loaded in 10 % DCM:MeOH:NH_2 (34.5:9:1) mixture in DCM and eluted with increasing concentration to 100 % of the solvent mixture. Fraction were combined and dried to yield a white solid DOTA.DSA (**5**; 57 mg, 0.06 mmol, 49 %). ^{1}H NMR (400MHz, $CDCl_3$): δ_H 7.54 (s, 1H), 4.22 – 2.13 (m, 30H), 1.53 (d, *J* = 28.7 Hz, 4H), 1.28 (s, 60H), 0.90 (t, *J* = 6.7 Hz, 6H); ESI-MS Calcd. for $C_{54}H_{104}N_6O_8$ $[M]^+$: 964.8 a.m.u. Found $[M+Na^+]^+$: 987.7 a.m.u.

Gadolinium complexation was added to the suspension of DOTA-DSA (**6**; 50.4 mg, 0.052 mmol) in a vigorously stirred aqueous solution (5 mL) of g $GdCl_3.6H_2O$ (22.4 mg, 0.06 mmol) heated at 90^{o}C for 12 h under N_2. After settling, the excess water was removed, and minimal DCM was added to dissolve the lipid complex. After vigorous mixing with equal amounts of deionised water, the emulsion was separated by centrifugation and the DCM layer collected and dried *in vacuo* to give a white power (**6**, 54.7 mg; 95 %); ESI-MS Calcd. for $C_{54}H_{101}GdN_6O_8$ $[M]^+$: 1119.7 a.m.u. Found $[M+H^+]^+$: 1120.1 a.m.u.

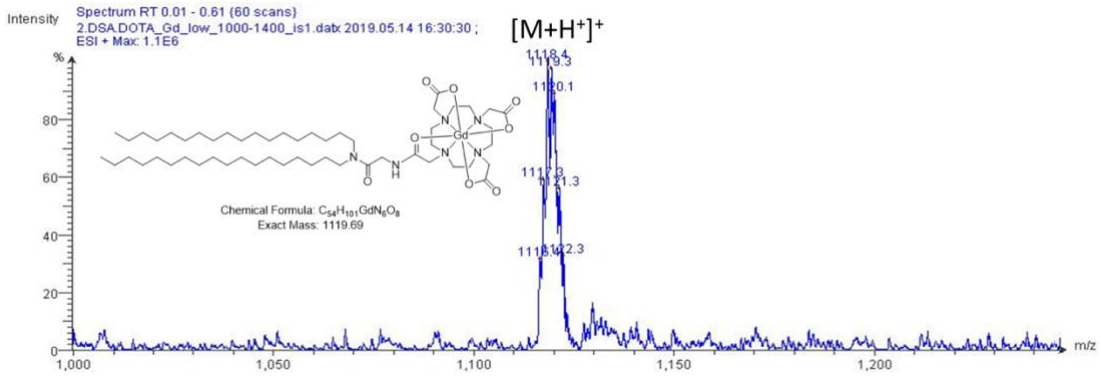

Figure 5.1: Mass spectrum of $C_{54}H_{101}GdN_6O_8$**:** ESI-MS Calcd. for $C_{54}H_{101}GdN_6O_8$ $[M]^+$: 1119.7 a.m.u. Found $[M+H^+]^+$: 1120.1 a.m.u. [Gd]DOTA.DSA **(6)**

Synthesise of [Gd]DOTA.AHX.DSA and [Gd]DOTA.AOC.DSA: Compound 11 and 12

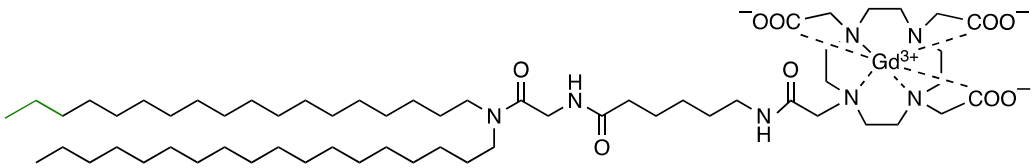

11

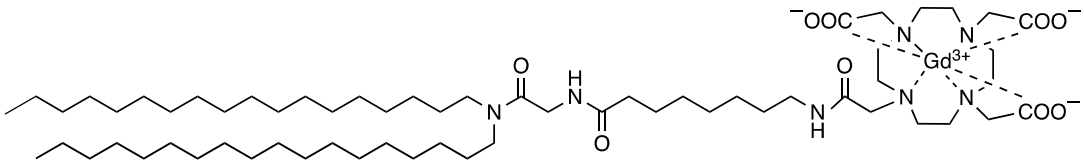

12

Scheme 5.3: Compound **11** [Gd]DOTA.AHX.DSA and Compound **12** [Gd]DOTA.AOC.DSA

[Gd]DOTA.AHX.DSA (8) and [Gd]DOTA.AOC.DSA (9) were synthesised from DSA in 4 step process by Dr. Michael Wright and Mr. Paul Cressey. The spacer attachment for both lipids attached using standard HBTU/DMAP peptide bond formation from BOC-protected commercial agents; 6-(BOC-amino)hexanoic acid (BOC-AHX-OH) or 8-(BOC-amino)octanoic acid (BOC-AOC-OH). Procedures for the DOTA coupling reaction and the gadolinium metal loading were similar for all, as reported for [Gd]DOTA.DSA. This followed by removal of the BOC protecting group with TFA. Moreover, procedures for the DOTA coupling reaction and gadolinium metal loading were similar for both lipids as explained above **(MS and NMR results are provided in Appendix-5)**

N`-CF750-N,N-distearylamidomethylamine (CF750.DSA)

DSA (**3**; 4.2 mg; 7.3 µmol) was dissolved under nitrogen in dry DCM (0.2 mL) with distilled triethylamine (TEA; 20 µL, 0.14 mmol) and CF750-NHS (1 µmol) was dissolved in dry DMSO (100 µL) with vigorous vortexing and added into the flask. The round bottom flask was protected from light and the mixture was gently stirred over 5h. The reaction was monitored with TLC (DCM:MeOH:NH_3; 84.5:15:0.5 v/v). Over 5h, it showed conversion of separate DSA (R_f 0.55) and CF750-NHS (R_f 0.10) spots to a streak (R_f 0.40-0.65). The reaction was then stopped and dried *in vacuo.* The purification was done by flash column chromatography loaded in DCM and eluted with 5 % MeOH in DCM to (DSA; colourless) to 15-20 % MeOH (conjugate; blue; R_f 0.65). The CF750-DSA fractions were combined and dried *in vacuo* which gave a dark-blue solid with an estimate yield of 70 %. This was dissolved with chloroform which gave final lipid concentration of 1 mg/mL, protected from light and stored at -20 ^{o}C.

5.4 Preparation and Characterisation of Liposomes

All lipids were stored at -20 °C as aliquots of 10-20 mg/mL in chloroform, methanol or methanol:chloroform 50:50 (v/v) according to their solubility.

5.4.1 Gadovist®-encapsulated Liposomes (GL)

Appropriate amounts of each lipid solution were combined into dried 5 mL round bottomed flasks to give a mixture of DPPC:PEG^{2000}-DSPE:cholesterol; 50:5:45 (mol%, 30 mg total lipid, per batch) at room temperature. The solvent was then removed using a rotary evaporator and the resulting film dried overnight in *vacuo*, forming an even and thin lipidic film. All buffers were sterilised by filtration through 0.2 µm membranes.

The lipid film was hydrated with 1 mL of Gadovist® solution containing 1572.5 mg/L gadolinium. The flask sealed with a silicone subaseal, and the lipid film fragmented using repeated (~10x) freeze/thaw from liquid nitrogen to a water sonication bath at 60 °C to disrupt the lipid film. After the final freeze-thaw, the preparation underwent a final sonication step for 30 minutes, again at 60 °C. Non-encapsulated Gadovist® was exchanged to sterile storage buffer (20 mM HEPES aq. with 5 w% glucose; pH 7.4) using a PD10 size-exclusion column (Amersham, Buckinghamshire, UK) previously washed and equilibrated in the same buffer (estimated dilution is ~x1.4). The resultant opalescent suspension containing GL was stored at 5 °C prior to gadolinium analysis by **TXRF and ICP-OES.**

5.4.2 MRI Contrast Liposomes (iTSL1-3):

iTSL1-3 liposomes were prepared with the following lipid formation molar ratio; **[Gd]Lipid**:DPPC:DSPC:MSPC:PEG^{2000}-DSPE:CF750.DSA; 30:53.95:5:5:6:0.05 (mol%, 30 mg total lipid, per batch). **[Gd]Lipids** were as following:

- [Gd]DOTA.DSA used to form **iTSL1**
- [Gd]DOTA.AHX.DSA used to form **iTSL2**
- [Gd]DOTA.AOC.DSA used to form **iTSL3**

All lipids were mixed in a round bottom flask at room temperature in an appropriate proportion. The solvent was then removed using a rotary evaporator and the resulting film dried overnight in *vacuo*, forming an even and thin lipidic film. All buffers were sterilised by filtration through 0.2 µm membranes. Dried lipid film was hydrated with 1 mL filtered buffer (50 mM HEPES aq. with 5 w% glucose; pH 7.4). The lipid film was fragmented using repeated cycles of (~10x) freeze/thaw from liquid nitrogen to a water sonication bath at 60 ^{o}C to disrupt the lipid film. The resulting suspension was sonicated further at 60 ^{o}C to form homogenous blue tinged and opalescent solution. Liposomes were stored at 5 ^{o}C.

5.4.3 Doxorubicin Encapsulating Image Guided Thermosensitive Liposomes (iTSL-DOX)

Appropriate amounts of each lipid solution were combined into dried 5 mL round bottomed flasks to give a mixture of [Gd]DOTA.DSA:DPPC:DSPC:MSPC:PEG^{2000}-DSPE:CF750.DSA at 30:53.95:5:5:6:0.05 mol% and 30 mg total lipid, per batch. The solvent was then removed using a rotary evaporator and the resulting film dried

overnight (at least) in *vacuo*. Further preparation stages were then carried out in a cleaned and sterilised fume hood for improved containment and dust control. All equipment and materials were either single use or sterilised by autoclave or ethanol wipe down. All buffers were sterilised by filtration through 0.2 µm membranes.

Each lipid film was hydrated with 1 mL of sterile loading buffer (300 mM ammonium phosphate aq.; pH 4.0), the flask sealed with a silicone subaseal, and the lipid film fragmented using repeated (~10x) freeze/thaw from liquid nitrogen to a water sonication bath at 53 ^{o}C. Further sonication of the lipid fragments continued for several minutes until the flask contained a milky suspension with no eye-visible particulates. This was extruded 3x through a 100 nm pore polycarbonate membrane (Isopore, Merck Milipore, Burlington, MA, USA) using a nitrogen gas powered extruder (LIPEX, Northern Lipids; Burnaby, Canada) heated to 52 ^{o}C and at 15-20 bar pressure. The iTSL was then exchanged to sterile storage buffer (50 mM HEPES aq. with 5 w% glucose; pH 7.4) using a PD10 size-exclusion column (Amersham, Buckinghamshire, UK) previously washed and equilibrated in the same buffer. The resulting opalescent blue suspension was loaded with doxorubicin using a thermocycler (Mastercycler Personal, Eppendorf, Stevenage, UK) in order to provide sufficiently stable and accurate temperature control. Concentrated doxorubicin HCl aq. (stored frozen) was added to 1.2 mg/mL, the combination inverted several times to mix without bubble formation, then incubated at 38.7 ^{o}C for 1h 50m. Excess drug was then immediately removed by repeating the PD10 buffer-exchange. The resulting deep-red coloured iTSL-DOX fraction was collected in a sterile glass vial and

capped with a silicone stopper. Batches were stored at ~5 °C and appeared visually to be stable for months. Sterility was checked by inoculating LB-agar plates with 100-fold diluted iTSL-DOX and incubation overnight at 37 °C. No bacterial colonies were seen, unlike plates inoculated with non-sterile storage buffer.

5.4.4 Colloidal Properties

Nanoparticle size and population parameters for each batch were routinely recorded by dynamic light scattering (DSL) using a Nanoseries Nano ZS (Malvern Panalytical, UK). Samples were diluted 1:100 or 1:20 v/v using storage buffer at 25 °C and contained in disposable micro-cuvettes. Analysis was repeated in triplicate and size modelling carried out using default water and polystyrene bead parameters. Surface charge (ζ potential) measurements were also carried out on representative batches, using default settings and 5 repeats. To assess long-term stability, iTSL-DOX size and polydispersity index (PDI) measurements were repeated at intervals over 3 months using samples taken from sterile vials stored at ~ 5 °C.

5.4.5 Differential Scanning Calorimetry (DSC)

Liquid-phase differential scanning calorimetry (DSC) is a method for assessing a liposome formulation's characteristic thermally-induced phase transitions. This gives valuable information for formulation optimization and quality assurance (batches have the expected properties). Nano DSC (TA Instruments, New Castle, DE, USA) was routinely used to record at least two rounds of heating/cooling cycles (25-70 °C at 1 °C/min; 3 atm) from samples of each liposome batch. Samples were diluted 1:20 or 1:100 (v/v) in degassed storage buffer, sample volume of 600 µL, and plain buffer used as a thermal reference. After baseline correction, the second-cycle heating

thermograph was analysed using a custom spreadsheet to assess the peak phase transition temperature (T_m). Batch-to-batch variance of these values was about ± 0.1 ^oC.

5.4.6 Inductively Coupled Plasma-Optical Emission Spectrometry (ICP-OES)

For quantification by ICP-OES, calibration solutions were prepared with a high purity gadolinium standard (1000 mg/L gadolinium in 2 w% nitric acid, TraceCERT® Sigma-Aldrich, St. Louis, MO). The gadolinium standard was diluted with deionised water (acidified using 5 w% nitric acid) to produce gadolinium solutions ranging from 10.0 µg/L to 5.0 mg/L for measurements in a linear range **(Figure 5.2)**. Gallium was again used as the internal concentration standard and added to each calibration solution so that gallium was present at 1.0 mg/L. ICP-OES was performed on a Thermo Scientific ICAP 6300 Duo View (Thermo Scientific Chemical, Hampton, NH) ICP spectrometer with emission wavelengths for gadolinium and gallium at 335.0 nm and 294.3 nm, respectively. The instrument was calibrated according to manufacturer's recommendations.

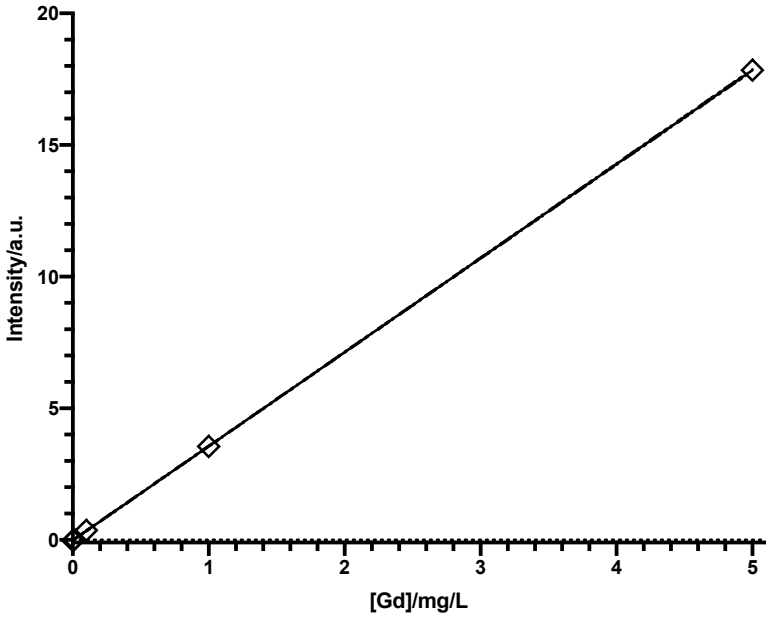

Figure 5.2: A calibration curve of [Gd] showing the linear response of the ICP-OES signal versus the concentration of standards prepared. Gadolinium standard was diluted with 5 w% HNO_3 ranging from 10.0 µg/L to 5.0 mg/L with 1 mg/L gallium internal standard. R^2=1

5.4.7 Total Reflection X-ray Fluorescence (TXRF)

TXRF is an efficient method for the quantification of trace elements in small quantities of complex samples and may be carried out with or without sample digestion. iTSL gadolinium quantification used a PICOFOX™-S2 (Bruker, Billerica, MA, USA) with primary X-ray produced by an air-cooled low power X-ray tube using a molybdenum anode [93]. Liposomes and Gadovist® samples were mixed 1:1 (v/v) with diluted gallium aq. (TraceCERT® certified reference) as an internal standard. Tissues samples were digested with nitric acid and hydrogen peroxide, while heparin-treated blood samples were analysed directly. Sample/standard mixtures were homogenised prior to dispensation of 5-10 µL onto individual siliconised quartz disc

sample carriers (Bruker Nano GMbH, Germany) and oven dried at 70 ^{o}C. Great care was taken to prevent dust contamination and sample carriers were cleaned and prepared according to manufacturer recommendations and checked for contamination prior to use. TXRF results were collected in triplicate over 1000 s using excitation settings of 50 kV and 600 mA. Spectra were inspected and all significant peaks identified, prior to deconvolution using PICOFOX™ V 7.5.3.0 software (Bruker Nano GmbH) against the gallium internal standard.

5.4.8 *In Vitro* Relaxometry Studies

Equations that were used for relaxivity studies are as following:

$$(\boldsymbol{a}) \quad M_i = M_0\left(1 - e^{\left(-TR/T_1\right)}\right) \qquad (\boldsymbol{b}) \quad M_i = M_0\left(e^{\left(-TE/T_2\right)}\right)$$

Equation 5.1: Equation for determining (**a**) T_1 using standard saturation recovery; (**b**) T_2 using MR sequences with different echo times (TE). M_i: signal intensity, TR: time to repeat, TE: echo time, T_1 = longitudinal relaxation time, T_2: transverse relaxation time; M_0 = equilibrium magnetization (baseline net magnetization) [10].

The efficiency of contrast agents was determined by measuring longitudinal (r_1) and transverse molar relaxivities (r_2).

$$r_i = \frac{\left(R_i - R_{i(0)}\right)}{[CA]} \;\; ; \; (i = 1, 2)$$

Equation 5.2: Equation to calculate the efficiency of contrast agents which were determined by measuring longitudinal and transverse molar relaxivities (r_i, where i= 1, 2); R_i = relaxation rate ($1/T_i$; i= 1, 2), $R_{i(0)}$ = relaxation rate of the buffer ($1/T_{i(0)}$; i= 1, 2), [CA] = concentration of contrast agent, in this case it is free-gadolinium equivalent [21,22].

T_1 relaxivity measurements with NMR: Liposomes samples were diluted with 50 mM HEPES, 5 w% glucose, whereas Gadovist® samples were diluted with RO with final concentration of 10 % D_2O. Gadolinium concentrations of liposomes and Gadovist® samples were determined by TXRF as described previously in **Section 5.4.7** (20 mg/L Gallium standard was mixed in 1:1 ratio with liposome or Gadovist® samples). The final free gadolinium concentrations were in the range of 4.16 to 0.07 mM (minimum 7 dilutions for each iTSL1-3 samples and 5 dilutions for Gadovist® sample were prepared). The longitudinal relaxation time (T_1) was determined by 400 MHz Bruker Advance 400 NMR spectrometer at 25 ^oC. T_1 longitudinal relaxation times were measured with a saturation recovery sequence, using a recycle delay at 5ms. The variable delays (vd) used in the relaxation array which were ranging from 2 ms to 3s. The data was fitted to the **Equation 5.1a** to calculate T_1 using TopSpin™ Software 3.6.2 (Bruker, Germany). The measured longitudinal (T_1) relaxation rates (**R_1**: $1/T_1$) are the sum of the intrinsic diamagnetic relaxation rate of the buffer and of the

paramagnetic element contribution. Thus, corrected T_1 rates (ΔR_1) were plotted against the gadolinium concentrations of contrast agents and longitudinal relaxivity (r_1) values were calculated from the slope of the linear regression line according to the **Equitation 5.2.** Graphpad Prism v 8.2.1 (Graphpad Software, San Diego CA, USA), was used.

T_1 and T_2 relaxivity measurements with pre-clinical MRI: iTSL1-3 and Gadovist® were serially diluted in 50 mM HEPES with 5 w% glucose. The final gadolinium concentrations for all samples were in the range of 1-0.8 mM (4 dilutions per sample) which was measured by TXRF as described above. MRI relaxometry studies were performed with a pre-clinical 9.4 T MRI scanner (Bruker Biospin, Ettlingen, Germany) using a 39 mm inner diameter radiofrequency coil (Rapid Biomedical, Rimpar, Germany). T_1 relaxometry was achieved with fast-spin echo (FSE) sequence with various repetition times (TR) of 45, 50, 60, 80, 100, 120, 150, 180, 200, 350, 450, 500, 750, 850, 900, 1000, 1200, 1500,1700, 2000, 3000, 5000 and 10000 ms; echo time (TE), 11 ms; 2 averages for 1 slice. In order to measure T_2, spin-echo sequence was run with various echo times (TE), 6.5, 13,19.5,26, 32.5, 39, 45.5, 52, 58.5, 65, 71.5, 78, 84.5, and 91 ms; TR, 4000 ms; 2 averages for 1 slice. In both studies, coronal slices were set to 2 mm thickness; field of view (FOV) was 26×26 mm and matrix size was 128x128. Image analysis was performed with T_1 and T_2 maps generated by pixel-by-pixel non-linear fitting to **Equation 5.1a** for T_1 and **Equation 5.1b** for T_2) using JIM v8.0 (Xinapse Systems, Alwincle, UK). Regions of interests (ROI) were drawn and placed on the T_1 and T_2 maps to obtain relaxation times. The longitudinal and

transverse relaxivities (r_1, r_2) were calculated from the slope of the linear regression line of the corrected relaxation rates (($\Delta R_{1/2}$) versus concentration of the contrast agent **(Equitation 5.2)** by using Graphpad Prism v 8.2.1 (Graphpad Software, San Diego CA, USA).T_1-weighted images were achieved with spin-echo sequence with TR, 35 ms; TE, 8 ms; 4 averages; field of view (FOV), 26 x 26 mm, matrix size, 128 x 128.

Proton Nuclear Magnetic Resonance Dispersion (NMRD) Study: NMRD profiles were obtained at 37, 41 and 42 ^{o}C on an NMR field cycling relaxometer (Stelar, Mede, Italy) at single concentration for iTSL1 liposomes and Gadovist®. The frequency range was between 0.01 to 40 MHz (40 MHz is around 1 T).

5.4.9 Optical Properties

iTSL-DOX absorbance and fluorescence profiles were collected at 1:200 (v/v) dilution into storage buffer using an Infinite 200 Pro plate reader (Tecan, Switzerland). Expected absorbance peaks were seen at 480 (doxorubicin), 750 nm (CF750) and fluorescence peaks at Ex_{480}/Em_{590} (doxorubicin), Ex_{750}/Em_{800} (CF750). Dilute iTSL-DOX suspensions show a 3-5-fold increase in doxorubicin fluorescence intensity on incubation at temperatures above 40 ^{o}C. This is due to release of encapsulated drug and resulting de-quenching. The NIR fluorescence is not significantly affected by heating.

5.4.10 Doxorubicin Quantification

Total doxorubicin concentration was assessed by reverse-phase HPLC using an Agilent 1100 series instrument equipped with a multi-wavelength diode array

detector (DAD), a 1260 Infinity fluorescence detector (FLD; all from Agilent, Santa Clara, CA, USA), a Polymer Laboratories PL-ELS-2100 evaporative light scattering (ELS) detector, and a 5 cm Hypersil C18 5 µm reverse-phase column (Thermo Fisher, Waltham, MA, USA). Solvents were: water with 0.1 v% trifluoroacetic acid (A) and acetonitrile (B). The DAD was set to 210 and 480 nm, with 8 nm bandwidth c.p. reference at 700 nm, while the FLD used Ex_{480}/Em_{590} nm with PMT-gain 18. Gradient was: 0 min 0 %, 1.5 min 0 %, 5 min 50 %, 6 min 5 %, 7 min 0 %, 8.5 min 0 % and a flow rate of 3.5 mL/min. Samples were accurately diluted at least 50-fold with RO water and injection volume was kept small (~ 1 µL) to ensure all the iTSL-DOX liposome was dissociated on the column. Doxorubicin gave a single peak with retention time ~4.1 min, this area was used to estimate amount after calibration against a doxorubicin HCL European Pharmacopoeia Reference Standard. This approach was seen to be sufficiently accurate (0-200 ng range, R: 0.999) and fast enough for routine triplicate analysis of all batches.

During optimising of the loading conditions, encapsulation efficiency was assessed by gel-filtration HPLC using a Tricorn 5/100 column (GE Life Sciences, Pittsburgh, PA, USA) packed with Sephadex G20 slurry in water. This was washed and run in solvent A at 0.75-1.5 mL/min over 15 min. Detection was as described above and the injection volume was 3 µL. Since this approach does not degrade the iTSL-DOX, two components are seen with an initial liposomal peak (strong DAD, weak FLD due to self-quenching) at ~2 min followed by a broad free-doxorubicin band (weak DAD, strong FLD) over 5-6 min. The iTSL-DOX fluorescence signal is non-linear with

concentration and difficult to calibrate but the free-doxorubicin band gives a valuable estimate for the relative amounts of unencapsulated drug.

5.4.11 Drug/Lipid Ratio Assessment

Drug/lipid ratios were assessed using total lipid concentrations determined using a modified version of the Stewart assay. iTSL-DOX samples (50 µL) were mixed with water (150 µL) and MeOH:$CHCl_3$, 1:1 (v/v; 200 µL) then vortex mixed giving an emulsion. This was centrifuged (4000 g; 2 min) to fully separate the organic and aqueous layers. An aliquot (70 µL) of the organic layer was combined with Stewart reagent (5 µL, $FeCl_3$/NH_4SCN aq.), and the combination vortex mixed, then centrifuged again. Finally, an aliquot (50 µL) was then transferred to a glass 96-well plate (Cayman Chemical, Ann Arbor MI, USA) and 455 nm absorbance measured on a plate reader (Infinite 200 Pro, Tecan, Switzerland) for comparison against known standards.

5.4.12 iTSL-DOX Thermally-Induced Doxorubicin Release *in vitro*

Thermally-induced doxorubicin release from iTSL-DOX was assessed by the increase in Ex_{480}/Em_{590} nm fluorescence seen as it escapes from the highly self-quenched encapsulated state. Measuring changes in fluorescence intensity as a function of time (0-30 min) upon incubation of iTSLs at various temperatures (37-45 ^{o}C) allows the degree of drug release to be observed in near real time. Studies were carried out with separate samples (100 µL; triplicate) diluted 1:100 (v/v) in storage buffer, or the same containing 50 % fetal bovine serum (FBS) (v/v) as a blood analogue. Samples were incubated using a thermocycler to provide sufficiently accurate temperature control and good heat transfer properties. Fluorescence intensity readings were

normalised against unheated iTSL-DOX baseline and samples incubated at 50 °C for 5 min to assess % of release.

Short- and long-term storage effects on the thermally doxorubicin release behaviour were assessed using iTSL-DOX kept in a sterile vial at ~5 °C. The short-term study used samples warmed to room temperature for 10 min, 3 h, or 24 h before incubation at various temperatures (32-36 °C) for 3 min and fluorescence analysis. The long-term study used samples taken directly from the stored vial over a period of 3 months, then analysed in the same way. Little (if any) difference was seen in the thermally-induced release profiles, suggesting storage stability over the time frames of the following studies.

5.4.13 iTSL Gadolinium Retention

The potential for 'loss' of the chelated Gd^{3+} from [Gd]DOTA.DSA was investigated using a dialysis assay. This assayed the amount of metal cation able to escape from within an inner chamber (Slide-A-Lyzer MINI Dialysis Device, 10K MWCO, 0.1 mL; Thermo Scientific) containing either iTSL or 0.2 mg/mL aq. gadolinium standard (TraceCERT®) and into an outer cuvette containing either RO water at RT, 2.5 mM EDTA aq. at RT, or 50 % FBS/RO (v/v) water at 4 °C (to avoid serum protein aggregation). The cuvettes were equipped with a small magnetic bead, placed on stirrer, and 10 µL samples were taken at time points over 48 h. These were then analysed by TXRF (mixed 1:1 of 8 mg/L aq. gallium internal standard) to determine the concentration of gadolinium in comparison to samples from the inner chamber

at the start of the study. Doxorubicin was omitted from this study due to its tendency to block the dialysis membrane pores.

5.5 *In Vivo* Studies

All animal procedures were conducted under the UK Home Office regulations and the Guidance for the Operation of Animals (Scientific Procedures) Act (1986). Female 4-6 week old athymic nude mice and CD-1 mice were purchased from Envigo (Huntingdon, UK) and female 4-6 week old SCID Hairless Outbred (SHO) mice were purchased from Charles River Laboratories (Wilmington, MA, USA). Animals were maintained according to Home Office regulations, with food and water available at *libitum*. Studies started with an average initial body weight of 22 ± 2 g. Unless otherwise stated, injections were given *i.v.* tail vein using a syringe driver (100 µL/min) connected to a cannula. Mice were anaesthetised with isoflurane-oxygen supplied via a facemask throughout treatments and placed on a warmed gel pad.

5.5.1 Breast Cancer Cell Culture

A triple-negative human mammary epithelial cell line MDA-MB-231 was maintained in Dulbecco's modified eagle media (DMEM) supplemented with 10 v% FBS, 1 v% penicillin-streptomycin (5 kU/mL each), at 37 ^{o}C in a humidified atmosphere containing 5 v% CO_2. The cells were passaged every 2-3 d (once they had reached ~90 % confluent) with the media removed by aspiration and cells washed with 5 mL phosphate-buffered saline (PBS). They were then detached from the flask by addition of 3mL of trypsin-EDTA (TrypLETM Express Enzyme (1x), phenol red, (ThermoFisher Scientific, UK) and incubated for 3 min at 37 ^{o}C and 5 % CO_2. After detachment, cells were diluted with 6mL media and centrifuged to removed trypsin-EDTA. Cells were then re-suspended in 15mL media, and then diluted further with the media (1:4 v/v dilution). 15 mL of diluted cells were placed into a new T-75 culture flask. MDA-

MB231 cells were kept until 20 passages, after that they were discarded, and a new batch was prepared.

5.5.2 Gadolinium and Doxorubicin Blood-Clearance of iTSL

Gadolinium blood clearance of iTSLs were studied using CD-1 mice. iTSL (200 µL; [Gd] 1.3 mg/mL) was administered and blood samples (~25 µL) were collected via canula at time intervals (2-240 min post-injection; N=6) and transferred into pre-weighed vials along with heparin (2 µL). The vials were initially stored on ice and then frozen for storage. Analysis was performed by TXRF with each sample initially diluted (1:2 v/v) with ultrapure water. Mixtures were then made of diluted blood (10 µL), gallium internal standard (10 µL; 4 mg/L), and aq. polyvinyl alcohol (PVA; 10 µL; 1.2 g/L) then vigorously vortexed to homogenise them. Mixture samples (10 µL) were then transferred to siliconized quartz glass carriers for analysis as previously described.

In a separate study, CD-1 mice were administered iTSL-DOX (4 mg/kg doxorubicin), blood samples (~55 µL) were collected at intervals (1-180 min post-injection; N=7) with a maximum of 4 from each animal. Samples were transferred to pre-weighed vials with heparin (5 µL) and initially stored on ice. On completion of collection, the samples were centrifuged (4,500 rpm; 5 min; 4 ^{o}C) to isolate plasma which was then stored frozen until analysis. Doxorubicin extraction was carried out by addition of acetonitrile, centrifugation (10,000 rpm; 5 min; 4 ^{o}C) to pelletise the proteins, and collection of the supernatant for analysis by LC-MSMS, using daunorubin as an internal standard. The instrument was an Accela pump and autosampler coupled to a TSQ Quantum Access mass spectrometer. Doxorubicin isolation used a Hypersil Gold aQ 50x2.1 mm 3µ reverse phase column (all Thermo Scientific; Waltham, MA,

U.S.A.) with solvent A: 0.1 v% formic acid in water and solvent B: 0.1 v% formic acid in methanol. The LC gradient was 95-5 v% A over 5 min at 200 µL/min and retention times were 3.3 min for doxorubicin and 3.4 min for daunorubin. The MS used +ve mode ESI with indicative selected reaction monitoring transitions 544.170 → 378.940, 544.170 → 396.950 for doxorubicin and 528.18 → 328.9 for daunorubin. Calibration was against doxorubicin (20-50,000 ng/mL; European Pharmacopoeia Reference Standard).

Final blood concentrations are reported after correction for animal weight and dilution effect from sample preparation. To estimate the % injected dose (%ID) the total blood volume is defined as 58.5 mL/kg (according to the NC3Rs, UK).

5.5.3 Tumour Generation

MDA-MB-231 cells (6×10^6 per tumour) were suspended in phosphate buffered saline (PBS) mixed 1:1 (v/v) with Geltrex Matrix (ThermoFisher). The mixture was then placed *subcutaneously* (*s.c.*) on the dorsal haunch of each mouse, with either single tumour (right side only) or double tumour (both sides) models prepared according to the study needs. Tumour establishment and growth was monitored and considered ready for Focussed Ultrasound (FUS) treatment once they had reached 5-6 mm diameter was measured with a digital calliper. This was normally ~10 d post-inoculation. Normally in the double-tumour studies only one side was treated with FUS, with the second tumour used as an internal control.

5.5.4 Tumoral FUS-induced Hyperthermia

FUS-induced hyperthermia was applied using a Therapy and Imaging Probe System preclinical FUS (TIPS; Philips Research, Netherlands). This is an 8-component annular transducer array (8 separate transducers in the array) mounted on a motorised X-Y platform, with either manual or programmatic control of the z-axis. The transducer is contained within a degassed water tank with a thin-film window at the base to allow transmission of the FUS into the target. Mice were anaesthetised with isoflurane-oxygen supplied via a facemask throughout treatment and placed on a warmed gel pad over an acoustic foam mat to absorb unwanted ultrasound. An electric warming mat and a heat lamp were also used to help maintain body temperature. Two 0.08 mm diameter fine-wire thermocouples (T150A; Linton Instrumentation, U.K.) were carefully implanted around the target tumour. These were placed such that one was just below the skin above the tumour body and the other between the tumour body and muscle below. Both were also aligned to be near but not directly on-axis of the transducer. Thermocouples were connected to a data logger (TC-08; Pico Technology, U.K.) with live monitoring of the temperatures at all times during FUS insonation. Warmed and degassed (by centrifugation) ultrasound gel was used to fill all air gaps between the mouse and the TIPS window, and below it and the gel pad. Any visible bubbles in the gel were then removed with a syringe and needle. Normally the TIPS window was placed 8.0 mm above the tumour surface and FUS was applied at the transducer natural frequency of 1.3 MHz, using a 100 % cycle duty. This setting placed the TIPS focus above the skin surface, minimising the risk of skin burns or unwanted tumour ablation but still allowing for

efficient FUS-induced hyperthermia. The FUS focal volume was 7 mm above the tumour surface which had radius of 5.2 mm. Tumour temperatures were measured at 50 ms resolution and TIPS acoustic power settings were adjusted manually (10-20 W) to converge on the target temperature (42 ^{o}C or 43 ^{o}C). Then this was maintained for a further 3 min with little variation in tumour temperatures. A normal protocol consisted of two rounds of FUS, 20 min pre-injection and 45 min post. FUS-induced doxorubicin release responsiveness were investigated and optimised prior to animal studies by Dr. Michael Wright as shown in **Appendix 1.**

5.5.5 Distribution and Uptake of iTSL

iTSL was tracked in real time by live animal near infrared fluorescence (NIRF) imaging and by gadolinium quantification after sacrifice at time points. Nude mice bearing single tumours anesthetised and administered iTSL (200 µL; [Gd]: 0.56 mg/mL) *i.v.* tail vein by slow infusion. The FUS group (N=3) received two rounds of FUS (20 min pre-inject, 43 ^{o}C, 3 min; 45 min post-inject, 42 ^{o}C, 3 min) while the control (N=3) received no FUS.

The biodistribution of iTSL was monitored by NIRF imaging. This used a Maestro EX (Perkin Elmer, MA, USA) with excitation of the CF750-DSA liposomal label at 704 nm and fluorescence emission collected over 740-950 nm with 20 nm slices. Full body images were collected from dorsal and ventral sides and the resulting image stacks were unmixed against a known spectral profile for CF750-DSA using the supplied software (v 3.0.1), then balanced and false coloured using ImageJ. For the biodistribution study at 4 h the animals were sacrificed, and tumours excised for

gadolinium analysis by TXRF. The tumour was weighed and then digested using concentrated. nitric acid (150 µL) and hydrogen peroxide (50 µL) in tightly sealed plastic tubes at 70 ^{o}C overnight. The digested samples were mixed 1:1 (v/v) with gallium internal standard (4 mg/mL) and gadolinium concentrations were determined by TXRF. Final gadolinium concentrations are given after correction for dilution effects during sample preparation. To estimate the % injected dose (%ID) these concentrations were normalised against animal and tumour weights and against a total blood volume of 58.5 mL/kg.

5.5.6 Real Time Imaging and Efficacy of iTSL-DOX:

iTSL-DOX was studied using both single and double tumour models.

Single tumour model: Three groups were used: -ve control group (N=5) received only a PBS injection; the doxorubicin group (N=5) received aq. doxorubicin (4 mg/kg) intravenous *i.v.* tail vein; and the iTSL-DOX group (N=9) received iTSL-DOX (equivalent to 4 mg/kg doxorubicin) *i.v.* tail vein and the two FUS treatments as previously described (20 min pre-injection, 43 ^{o}C for 3 min; 45 min post-injection, 42 ^{o}C for3 min). NIRF imaging was used to track distribution and tumour uptake of the iTSL-DOX for 24 h post-injection. Tumour size and mouse body weights were then recorded until they reached pre-determined endpoints (>1.2 cm longest axis or >15% loss of initial weight) where the animal was sacrificed. Tumour volume calculations were obtained using **$(d^2 \times D)/2$** where d is the shortest tumour axis and D is the longest.

Double tumour model: Two groups were used: -ve control group (N=3) received only the FUS protocol on the right-side tumour and no drug; the other (N=10) received iTSL-DOX (equivalent to 6 mg/kg doxorubicin) *i.v.* tail vein and the FUS protocol on the right-side tumour. For both groups the left tumour acted as a -ve FUS control. In this case biodistribution of iTSLs were monitored by NIRF imaging for 2 weeks post treatment. Tumour size and mouse body weights were recorded until endpoints, as before.

5.5.7 MR Imaging of iTSLs in Tumour Bearing Mice

In vivo MRI studies were carried out using 9.4 T Bruker BioSpec horizontal bore preclinical scanner and quadrature volume coil as previously described. Athymic nude mice (N=6) bearing single tumours were anesthetised as before and injected *i.v.* tail vein with iTSLs (200 µL; [Gd]: 1.37 mg/mL). Animals were imaged pre-injection, immediately after injection, and at 1, 2, 3, 4 and 5 h after injection of iTSLs (with a limitation that only 3 time points could be collected per animal). In this study, FUS-induced hyperthermia was not applied. A vial containing Gadovist® ([Gd] 3 ± 0.01 mg/L) was placed adjacent to the animal as a reference standard before the animal was inserted into a 39 mm inner diameter radiofrequency coil (Rapid Biomedical, Rimpar, Germany) and into the magnet bore. The mice were maintained at 37 ^{o}C with warm air and a water circulation system feeding a heating blanket. Body temperature was recorded with a rectal temperature probe and respiration monitored throughout scanning using a breathing pillow (Small Animal Instruments, New York, U.S.A.)

T_1-weighted images were achieved with spin-echo sequence with TR, 300 ms; TE, 7.765 ms; 2 averages; field of view (FOV), 35 x 35 mm, matrix size, 175 x 175. Transverse contiguous slices (8, 0.7 mm thick), covering most of the tumour.

T_1-relaxometery was performed with a fast-spin echo (FSE) sequence with various repetition times (TR, 240, 400, 600, 800, 1000, 1200, 1500, and 3000 ms); an effective echo time (TE) of 11 ms; echo train length, 8, and 1 average collected. Contiguous axial slices, 0.7 mm thick, with FOV 35 x 35 mm and matrix size, 128 x 128, were placed to completely cover the tumours.

T_1 maps were generated by pixel-by-pixel non-linear fitting to the **Equation 5.1a,** using JIM 8.0 (Xinapse Systems, Alwincle, UK). Regions of interest (ROIs) were manually drawn for the Gadovist® reference, skeletal muscle, and tumour on each slice. The reference, skeletal muscle and tumour ROIs in all the slices were individually combined to give volumes of interest. and underwent frequency distribution analysis using Graphpad Prism v 8.2.1 (Graphpad Software, San Diego CA, USA) and non-linear regression analysis of the histograms was performed to give a mean T_1 for each volume-of-interest at each time point for each animal **(Appendix-4)**

6. Conclusions and Future Directions

The aim of this PhD was to demonstrate a theranostic approach for the treatment of cancer. Given the advancement in personalised medicine it is important to provide robust and safe solutions for cancer patients which will result in improved outcomes and increased survival. The development of real time imaging to monitor the drug uptake and release is an encouraging advance in personalised medicine. Therefore, MRI guided FUS triggered drug delivery was explored for cancer treatment and novel MR-imageable thermosensitive liposome (iTSL) were developed.

As iTSLs contain gadolinium I considered of high importance to select the proper methodology for detecting the metal during formulation and *in vivo* studies. Accordingly, **Chapter 2** focuses on the potential use of Total Reflection X-Ray Fluorescence (TXRF) as a suitable analytical technique for measuring gadolinium content of liposomal nanoparticles. A comparison was conducted between a conventional analytical technique, Inductively Coupled Plasma-Optical Emission spectrometry (ICP-OES). Here, the comparison of TXRF and ICP-OES for assaying gadolinium in non-digested and digested Gadovist®, and Gadovist®-encapsulated liposomes, the accuracy and reproducibility of TXRF measurements were also tested. It was observed that ICP-OES has more sample preparation requirements including sample digestion to solubilise gadolinium into aqueous solution, significant dilution and handling of relatively large sample volumes. It was concluded that none of these aforementioned requirements are necessary for TXRF without compromising the quality of the results. This result vindicates the use of TXRF for characterisation of

gadolinium incorporated nanoparticles such as iTSLs that contain gadolinium contrast agent for MRI contrast enhancement.

Chapter 3 demonstrates the contrast efficiency of iTSLs. In order to improve the MRI contrast enhancement of iTSLs, two novel gadolinium lipids with varying length of alkyl spacers were proposed as an alternative to [Gd]DOTA.DSA (iTSL(1)). Novel Gd-lipids were synthesized and incorporated into the thermosensitive liposome formulation (iTSL1-3). They were then characterised to study the impact of the alkyl spacer unit on longitudinal and transverse magnetic relaxation. The iTSL3 liposomes with the longest length of alkyl spacer [Gd]DOTA.AOC.DSA have shown a greatest enhancement of T_1 relaxivity in comparison to iTSL2, iTSL1 and commercial contrast agent Gadovist® at 9.4 T. Presumably, as the spacer gets longer it has increased water accessibility of the Gd-complex that increases the T_1 relaxivity. All three paramagnetic liposomes have shown significant impact on T_2 relaxation time relative to Gadovist®. It was observed that shortening of T_2 was consistent with the shortening of the spacer unit between the headgroup and the lipid tail. This effect requires further investigation to understand the efficiency of iTSL1-3 as MRI contrast agents. Furthermore, Nuclear magnetic relaxation dispersion profiles of iTSL1 and Gadovist® were performed at temperatures close to the phase transition temperatures (T_m), 41-42 ^oC, of iTSL1 and body temperature. It was observed that T_1 relaxivity of iTSL1 increases as temperature reaches the T_m. This is the potential result of the contribution of the Gd-lipids in the inner membrane as permeability of iTSL1 increases at higher temperatures. As a future direction, lipid composition of

liposomes incorporating [Gd]DOTA.AOC.DSA need to be re-optimised to achieve the desired characteristics for MRI guided thermosensitive drug delivery, given it has the highest T_1 relaxivity. Also, longer spacers (C_{10} and C_{12}) in between the headgroup and the lipid tail should be attached to investigate the impact on relaxivity of liposomal formulation.

In **Chapter 4**, a novel MR-imageable thermosensitive liposome (iTSL also known as iTSL1) for drug delivery to triple negative breast cancers was presented. In this study, development tests of iTSL-doxorubicin (iTSL-DOX) formulation were reported including assessments of drug loading, colloidal and storage stability, and thermally induced drug release properties. The ability of focused ultrasound (FUS) to significantly influence iTSL uptake in tumours has been previously reported by our group [194]. This study was extended to an iTSL-DOX therapeutic study in mice using MDA-MB-231 triple negative breast cancer cells. Thus, the previously optimised protocol of two brief (3 min) FUS applications to induce mild hyperthermia (~43 ^{o}C) on tumour was utilised. iTSL-DOX distribution and uptake enhancement were assessed along with the effects on tumour growth and animal weights. The results showed that our iTSL-DOX provide accurate control of doxorubicin release in combination with FUS-induced hyperthermia. They also show excellent storage stability (months in a fridge) with reproducible thermal release characteristics. iTSL showed a comparable MR T_1 relaxation time to a clinically approved MR contrast agent (Gadovist®) in phantoms that were explored in **Chapter 2**. *In vivo* T_1 relaxometry studies have shown significantly enhanced contrast of tumours in mice

post intravenous administration. Single doses of iTSL-DOX in combination with FUS significantly retarded tumour growth and prolonged animal survival compared to controls. This demonstrates that MR-imaging can track nanocarrier tumour accumulation and focused ultrasound used to precisely release a drug and halt tumour growth, even with only a single dose.

This is a promising theranostic approach for cancer therapy that can be modified further with inclusion of multiple chemotherapeutic drugs as well as improving the MRI contrast sensitivity by attaching novel lipidic contrast agents.

From a translational point of view, the novel iTSL that was reported in this thesis has a potential future for cancer therapy. Even though the use of MRI sounds expensive, its ability to provide a controlled drug delivery in a non-invasive way in combination with image guided thermosensitive liposomes vindicates the expense. MRI incurs low marginal cost given the machine is always on, so your expense arises from the use of contrast agents, expertise and facilities. In this study with a theranostic approach, imaging and treatment can be carried out simultaneously taking advantage of the frontiers of research, facilitating the combination of PET and MRI in unison to improve the imaging. The ability to optimise the treatment for drug payload, and leveraging its localised nature, has the potential to reduce secondary costs consistent with these treatments via reduced hospitalisation and other secondary expenses incurred through additional care.

7. Appendices

Appendix-1

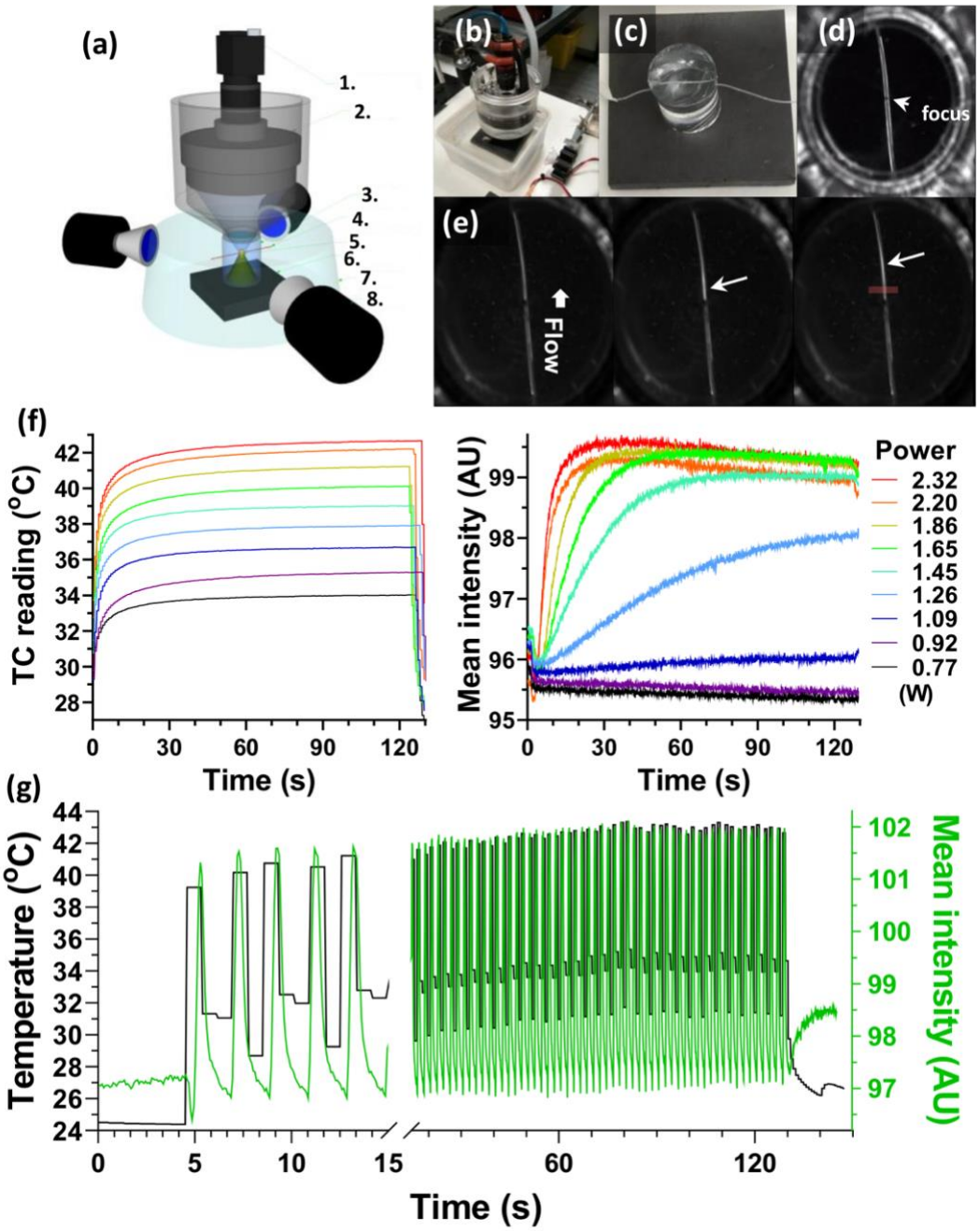

Figure 7.1: Method for assessing doxorubicin release under focused ultrasound (FUS)**,** visualised and measured by intrinsic doxorubicin fluorescence; **(a)** Schematic showing placement of a polyacryamide gel embedded flow-tube, light source and camera, around a TIPS (Philips, Netherlands) small-animal FUS system; 1. camera,

lens, and filter; 2. transducer; 3. gel block; 4. flow tube; 5. focus; 6. acoustic foam; 7. water bath; 8. LED lights; **(b)** shows the equivalent actual setup around the transducer; **(c)** Close up of the gel block and flow tube; **(d)** View from the camera under white-light, showing the flow-tube and an indication of the FUS focus with the fine-wire thermocouple visible in reflection. Pulsed FUS insonation of a flowing iTSL stream then causes synchronised fluorescence intensity increases, indicating boluses of released doxorubicin.; **(e)** Three representative frames showing (left to right) FUS-off, start of FUS and fluorescence increase, and FUS-off again and wash out of the release doxorubicin bolus; **(f)** Graphs of thermocouple reading and fluorescence intensity seen with increasing power levels of constantly applied FUS, using a fresh bolus of iTSL for each 2 min insonation; **(g)** Image fluorescence intensity and temperature plotted against time under pulsed FUS and constant iTSL flow.

FUS-induced doxorubicin release was investigated by Dr. Michael Wright in real time using a custom-made flow-tube setup. Optically transparent polyacrylamide gel with suitable acoustic properties was cast into cylindrical blocks. A fine plastic flow-tube (0.8 mm inner diameter) was placed within the gel block positioned to pass through the focal volume of the transducer. A 0.08 mm diameter fine-wire thermocouple (T150A, 40ga; Linton Instrumentation, U.K.) was threaded through the flow-tube such that the sensing tip was placed next to the focus. The other end of the flow-tube was connected to a syringe of iTSL-DOX (200-fold dilution into storage buffer) pumped by a driver at up to 100 µL/min. A pad of acoustic foam was placed below the gel block to absorb the post-focus FUS and prevent the formation of standing

waves. The gel block was then immersed in a water bath at ~35 ^{o}C and illuminated from the sides, either by white light or 3x blue LEDs (460 nm peak, 10 W; LED Engin LZ4-20B200; Osram, Germany). Imaging was down the barrel of the FUS transducer and used a Blackfly video camera (BFLY-PGE-13E4M-CS; FLIR Systems, OR, USA) equipped with a 550 nm long-pass dichroic glass filter. A pulsed FUS program was used, setting the transducer to 1.4 MHz, acoustic power up to 18 W, duty cycle 25 %, PRF 0.5 Hz (equivalent to 0.5 s on, 1.5 s off). Processing of the resulting videos concentrated on a small rectangular region-of-interest (ROI) placed just downstream of the FUS focus. After conversion of the video to individual frames, the average ROI pixel intensity was calculated using ImageJ v1.4 (National Institutes of Health, USA) and plotted against frame time. The measured temperatures were then collated and aligned.

A solution of iTSL-DOX was pumped through a capillary tube embedded in a block of tissue mimicking gel [312]. FUS was applied using a small-animal transducer array and doxorubicin release was monitored using fluorescence imaging with a video camera, while a thermocouple tracked the temperature near the FUS focus. Acoustic power at 2.32 W with TIPS (Philips, Netherlands) small-animal FUS system, the drug release appears effectively instantaneous. This implies that spatiotemporal control of the application of the acoustic power can lead to precise remote control of the drug released.

Appendix-2

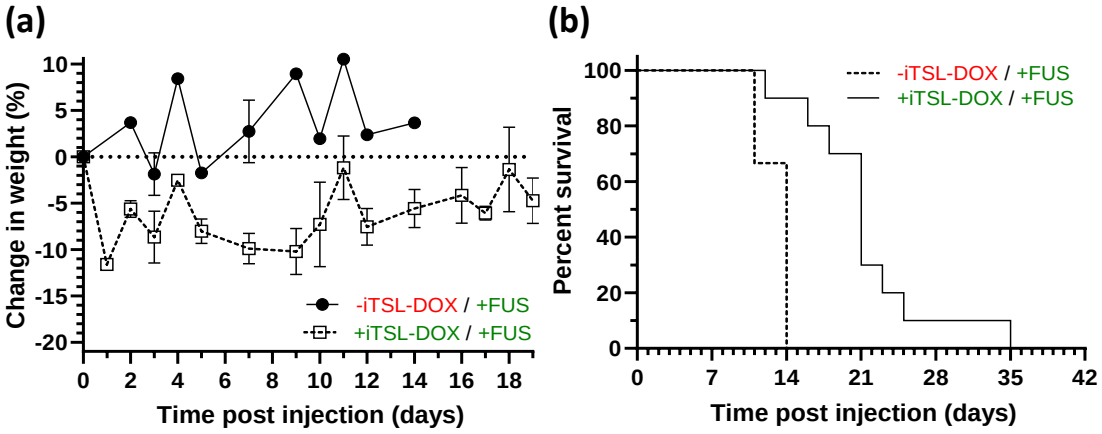

Figure 7.2: Double-tumour mouse studies: **(a)** average body weights and; **(b)** survival curves, ± iTSL-DOX at 6 mg/kg doxorubicin equivalent; FUS at day 0. Weights are given as mean ± 1 SEM. For these double-tumour studies, mouse survival is limited by the growth of the non-FUS tumour, which receives only a reduced dosage of iTSL-DOX. The approach allows for more direct comparison of the effects of FUS across the two tumours of the same animal but reduces overall survival improvements compared to the single-tumour studies.

Appendix-3

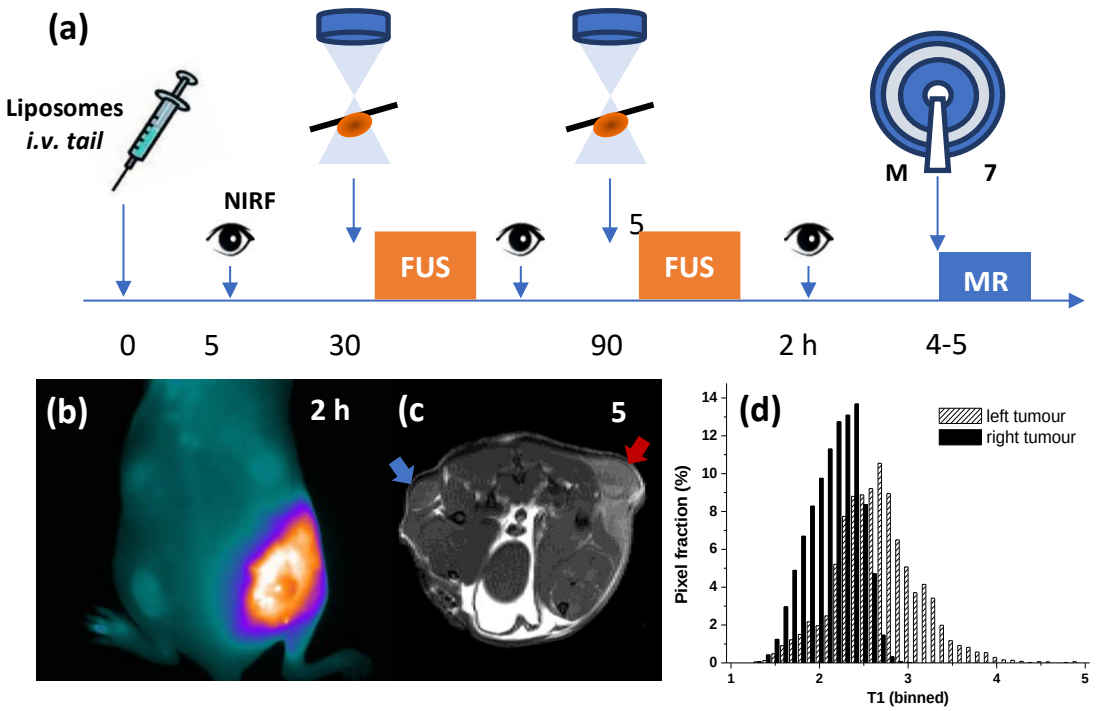

Figure 7.3: MRI imaging after dual FUS application; (**a)** Schematic showing FUS applications to the right-hand tumour followed by fluorescence and MRI imaging; **(b)** TSLs imaging by optical and **(c)** T_1-weighted MRI imaging (field 7 T, TR 320 ms). The same mouse was injected *i.v.* with iTSLs and was treated twice by FUS hypothermia applied to the right-hand tumour at 30 min and 1 h 30 min. NIRF imaging shows the treated mouse in dorsal view at 2 h 45 post injection. Two hours later on the same animal an MRI scan was performed. One axial slice is shown cutting through the region of the flank tumours, these are marked with blue (no FUS) or red (FUS) arrows; **(d)** the left and right tumours T_1 relaxation histograms [194].

Appendix-3

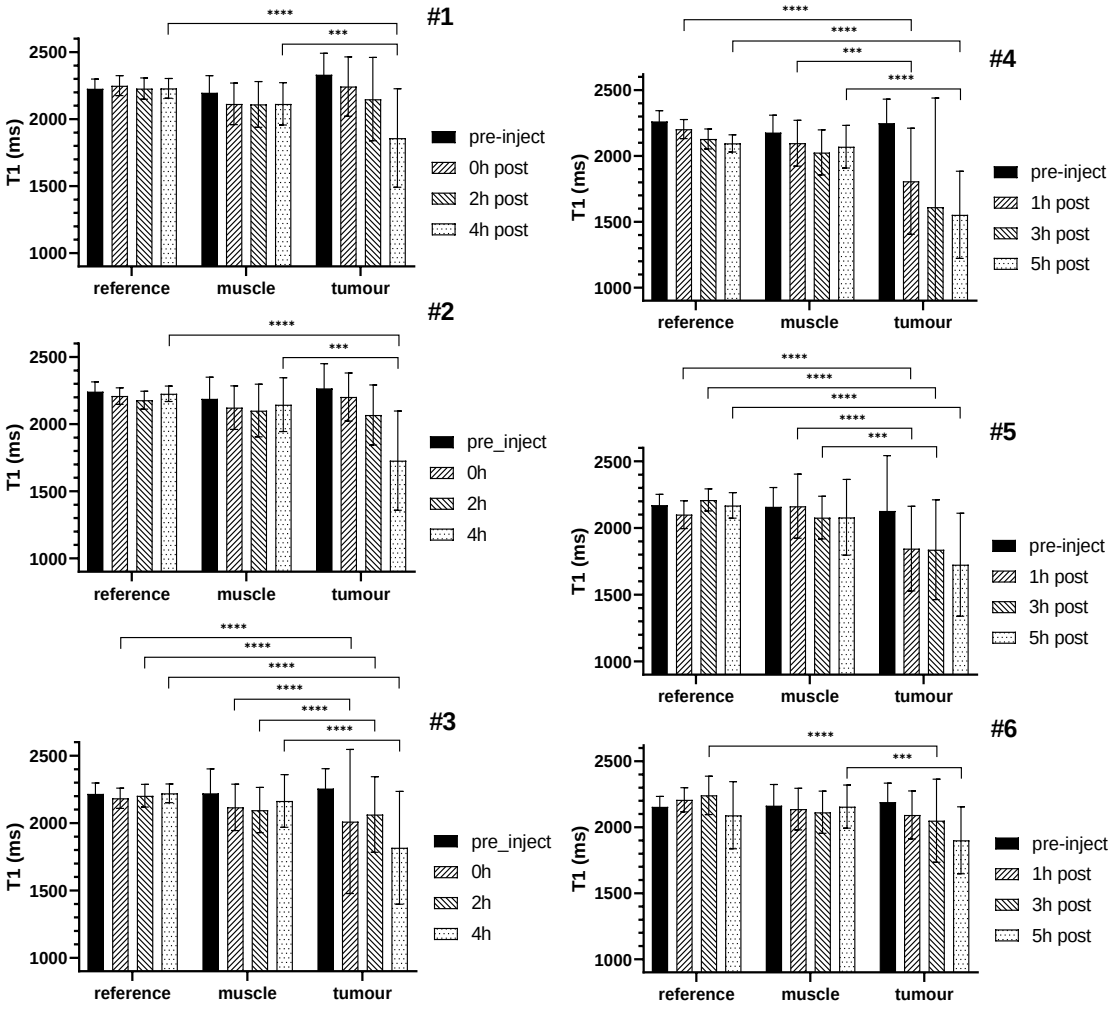

Figure 7.4: Collated pixel intensities from matched ROIs in all T_1 map slices underwent frequency distribution analysis in Prism (Graphpad Software, San Diego CA, USA) with bin-width 50 over 800-3000 units. The resulting histograms were then non-linear regression fit to Gaussian curves and the resulting best-fit value means and SDs (equivalent to the distribution breadth) cross-compared for each animal (N=6), time-point, and ROI. Significance markers refer to ANOVA 1-way analyses on the collated raw data using default settings: *** P < 0.0002, **** P < 0.0001. Little or no difference is seen from either the Gadovist® nor the muscle tissue controls. Significant mean reduction is seen in the majority of tumours immediately post-

injection. There is often an increase in the distribution SD, signifying significant heterogeneity. This likely relates to the increased tumour vascularity and/or the presence of a low-infusion core.

Appendix-5:

^{1}H NMR and Mass spectrum of [Gd]DOTA.AHX.DSA and [Gd]DOTA.AOC.DSA synthesized by Dr. Michael Wright and Mr. Paul Cressey.

BOC-AHX.DSA ^{1}H NMR (400MHz, $CDCl_3$): δ_H 6.54 (s, 1H), 4.47 (s, 1H), 3.96 (d, *J* = 3.8 Hz, 2H), 3.30 – 3.20 (m, 2H), 3.20 – 2.96 (m, 4H), 2.18 (t, *J* = 7.5 Hz, 2H), 1.65 – 1.55 (m, 2H), 1.55 – 1.50 (m, 2H), 1.43 (m, 6H), 1.37 (s, 9H), 1.19 (br, 60H), 0.81 (t, *J* = 6.8 Hz, 6H); ESI-MS Calcd. for $C_{49}H_{97}N_3O_4$ $[M]^+$: 791.7 a.m.u. Found $[M+Na^+]^+$: 814.3 a.m.u. **BOC-AOC.DSA** ^{1}H NMR (400MHz, $CDCl_3$): δ_H 6.55 (s, 1H), 4.44 (s, 1H), 3.96 (d, *J* = 3.8 Hz, 2H), 3.29 – 3.22 (m, 2H), 3.13 – 2.99 (m, 4H), 2.16 (t, *J* = 7.6 Hz, 2H), 1.61 – 1.55 (m, 2H), 1.53 (s, 2H), 1.46 (m, 6H), 1.37 (s, 11H), 1.27 – 1.16 (br, 60H), 0.81 (t, *J* = 6.8 Hz, 6H); ESI-MS Calcd. for $C_{51}H_{101}N_3O_4$ $[M]^+$: 819.8 a.m.u. Found $[M+H^+]^+$: 820.4 a.m.u.

AHX.DSA ^{1}H NMR (400MHz, $CDCl_3$): δ_H 8.18 (s, 2H), 7.23 (s, 1H), 4.02 (d, *J* = 3.4 Hz, 2H), 3.34 – 3.27 (m, 2H), 3.27 – 3.16 (m, 2H), 2.98 (s, 2H), 2.28 (s, 2H), 1.79 – 1.63 (m, 4H), 1.59 (s, 2H), 1.48 (m, 4H), 1.27 (br, 60), 0.90 (t, *J* = 6.7 Hz, 6H); ESI-MS Calcd. for $C_{44}H_{89}N_3O_2$ $[M]^+$: 691.7 a.m.u. Found $[M+H^+]^+$: 692.3 a.m.u. **AOC.DSA** ^{1}H NMR (400MHz, $CDCl_3$): δ_H 8.16 (s, 2H), 6.94 (s, *J* = 112.4 Hz, 1H), 4.01 (s, 2H), 3.30 (s, 2H), 3.17 (s, 2H), 2.94 (s, 2H), 2.22 (s, 2H), 1.55 (s, 10H), 1.25 (br, 64H), 0.86 (d, *J* = 6.5 Hz, 6H); ESI-MS Calcd. for $C_{46}H_{93}N_3O_2$ $[M]^+$: 719.7 a.m.u. Found $[M+H^+]^+$: 720.3 a.m.u.

DOTA.AHX.DSA: ^{1}H NMR (400MHz, $CDCl_3$): δ_H 4.10 – 2.55 (m, 34H), 1.65 (s, 2H), 1.52 (s, 8H), 1.28 (s, 60H), 0.90 (t, *J* = 6.3 Hz, 6H); ESI-MS Calcd. for $C_{60}H_{115}N_7O_9$ $[M]^+$: 1077.9 a.m.u. Found $[M+H]^+$: 1079.0 a.m.u. **DOTA.AHX.DSA:** ^{1}H NMR (400MHz, $CDCl_3$): ^{1}H NMR (400MHz, $CDCl_3$): δ_H 6.94 – 6.74 (m, 2H), 3.96 – 2.55 (m, 34H), 1.46 (s, 10H), 1.19 (s, 64H), 0.81 (t, *J* = 6.6 Hz, 6H); ESI-MS Calcd. for $C_{62}H_{119}N_7O_9$ $[M]^+$: 1105.9 a.m.u. Found $[M+Na]^+$: 1129.0 a.m.u.

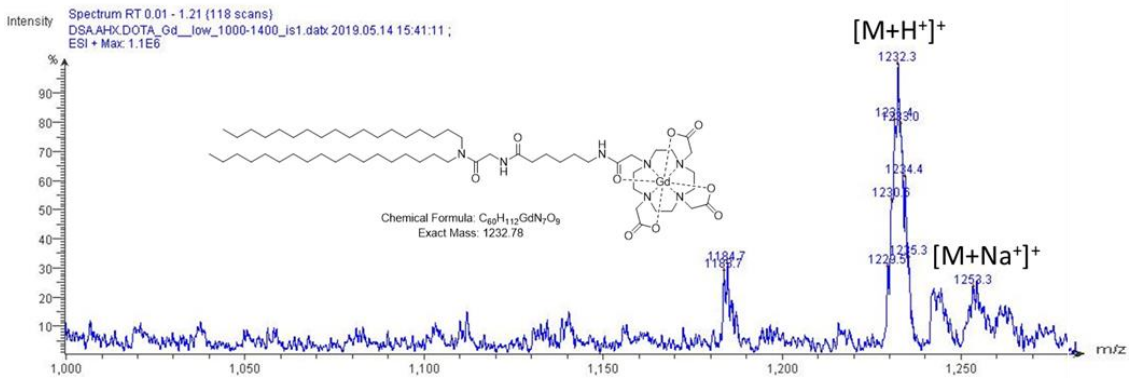

Figure 7.5: Mass spectrum for $C_{60}H_{112}GdN_7O_9$ $[M]^+$: 1232.8 a.m.u. Found $[M]^+$: 1233.0 a.m.u. [Gd]DOTA.AHX.DSA Compound 11

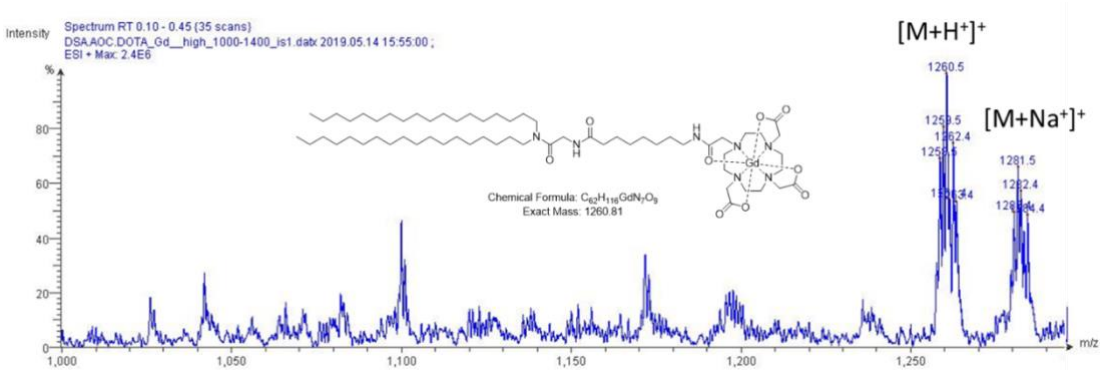

Figure 7.6: Mass spectrum for $C_{62}H_{116}GdN_7O_9$ $[M]^+$: 1260.8 a.m.u. Found $[M]^+$: 1260.5 a.m.u. [Gd]DOTA.AOC.DSA Compund 12

8. References

1. Berger A. Magnetic resonance imaging. BMJ [Internet]. 2002 [cited 30 January 2020]; 324: 35. Available at: https://www.ncbi.nlm.nih.gov/pmc/articles/PMC1121941/
2. Willmann JK, van Bruggen N, Dinkelborg LM, Gambhir SS. Molecular imaging in drug development. Vol. 7, Nature Reviews Drug Discovery. 2008.
3. Huang WY, Davis JJ. Multimodality and nanoparticles in medical imaging. Vol. 40, Dalton Transactions. Europe PMC Funders; 2011.
4. Currie S, Hoggard N, Craven IJ, Hadjivassiliou M, Wilkinson ID. Understanding MRI: Basic MR physics for physicians. Vol. 89, Postgraduate Medical Journal. 2013.
5. Ladd ME, Bachert P, Meyerspeer M, et al. Pros and cons of ultra-high-field MRI/MRS for human application. Prog Nucl Magn Reson Spectrosc. 2018; 109: 1–50.
6. Westbrook C, Talbot J (Writer on magnetic resonance imaging). MRI in practice. 2018.
7. Davies GL, Kramberger I, Davis JJ. Environmentally responsive MRI contrast agents. Chem Commun. 2013; 49: 9704–21.
8. Semmler W (Wolfhard), Schwaiger M. Molecular imaging. I. Springer-Verlag Heidelberg; 2008.
9. Brown MA, Semelka RC. MRI: Basic Principles and Applications [Internet]. 4th ed. NJ: Wiley-Blackwell; 2011 [cited 23 January 2020]. Available at: https://books.google.co.uk/books?hl=en&lr=&id=oYOIHi3YkuMC&oi=fnd&pg=PR9&dq=MRI+principle&ots=ZnLpGvQlBN&sig=1YZfc3Z8GxETAqV7aZ-VEkKM-mw&redir_esc=y#v=onepage&q&f=false
10. Ridgway JP. Cardiovascular magnetic resonance physics for clinicians: Part i. Vol. 12, Journal of Cardiovascular Magnetic Resonance. 2010.
11. Aletras AH. Basic MRI Physics. In: Cardiovascular Magnetic Resonance Imaging. Humana Press; 2008: 1–31.
12. Grover VPB, Tognarelli JM, Crossey MME, Cox IJ, Taylor-Robinson SD, McPhail MJW. Magnetic Resonance Imaging: Principles and Techniques: Lessons for Clinicians. J Clin Exp Hepatol. 2015; 5: 246–55.
13. Bellin MF, Vasile M, Morel-Precetti S. Currently used non-specific extracellular MR contrast media. Vol. 13, European Radiology. 2003.
14. Wahsner J, Gale EM, Rodríguez-Rodríguez A, Caravan P. Chemistry of MRI contrast agents: Current challenges and new frontiers. Chemical Reviews. 2019; 119: 957–1057.
15. Sharma R, Aboagye E. Development of radiotracers for oncology - The

interface with pharmacology. Vol. 163, British Journal of Pharmacology. 2011.

16. Burtea C, Laurent S, Vander Elst L, Muller RN. Contrast Agents: Magnetic Resonance. In 2008: 135–65.

17. Xiao YD, Paudel R, Liu J, Ma C, Zhang ZS, Zhou SK. MRI contrast agents: Classification and application (Review). Int J Mol Med. 2016; 38: 1319–26.

18. Cosottini N·, Baert AL, Reiser · M F, et al. MR Angiography of the Body f the Body: Technique and Clinical Applications. Springer;

19. Zhou Z, Lu Z-RR. Gadolinium-based contrast agents for magnetic resonance cancer imaging [Internet]. Wiley Interdisciplinary Reviews: Nanomedicine and Nanobiotechnology Wiley-Blackwell; Jan, 2013. Available at: http://doi.wiley.com/10.1002/wnan.1198

20. Strijkers GJ, Mulder WJMM, Van Heeswijk RB, et al. Relaxivity of liposomal paramagnetic MRI contrast agents. MAGMA [Internet]. 2005 [cited 27 June 2017]; 18: 186–92. Available at: https://link.springer.com/content/pdf/10.1007%2Fs10334-005-0111-y.pdf

21. Shen Y, Goerner FL, Snyder C, et al. T1 Relaxivities of Gadolinium-Based Magnetic Resonance Contrast Agents in Human Whole Blood at 1.5, 3, and 7 T. Invest Radiol [Internet]. 2015 [cited 31 January 2018]; 50: 330–8. Available at: https://doi.org/10.5167/uzh-109077

22. Rohrer M, Bauer H, Mintorovitch J, Requardt M, Weinmann H-JJ. Comparison of Magnetic Properties of MRI Contrast Media Solutions at Different Magnetic Field Strengths. 2005/10/19. Vol. 40, Investigative Radiology •. 2005 Nov.

23. Strijkers G, M. Mulder W, F. van Tilborg G, Nicolay K. MRI Contrast Agents: Current Status and Future Perspectives. Anticancer Agents Med Chem. 2008; 7: 291–305.

24. Pellico J, Ellis CM, Davis JJ. Nanoparticle-Based Paramagnetic Contrast Agents for Magnetic Resonance Imaging. Contrast Media Mol Imaging. 2019; 2019.

25. Pan D, Caruthers SD, Senpan A, Schmieder AH, Wickline SA, Lanza GM. Revisiting an old friend: Manganese-based MRI contrast agents. Vol. 3, Wiley Interdisciplinary Reviews: Nanomedicine and Nanobiotechnology. 2011.

26. Drahoš B, Lukeš I, Tóth É. Manganese(II) Complexes as Potential Contrast Agents for MRI. Eur J Inorg Chem [Internet]. 2012 [cited 4 February 2020]; 2012: 1975–86. Available at: http://doi.wiley.com/10.1002/ejic.201101336

27. Rashid HU, Martines MAU, Jorge J, et al. Cyclen-based Gd3+complexes as MRI contrast agents: Relaxivity enhancement and ligand design. Vol. 24, Bioorganic and Medicinal Chemistry. Elsevier Ltd; 2016.

28. Sherry AD, Caravan P, Lenkinski RE. Primer on gadolinium chemistry. In: Journal of Magnetic Resonance Imaging. 2009.

29. Idée J-M, Port M, Raynal I, Schaefer M, Le Greneur S, Corot C. Clinical and biological consequences of transmetallation induced by contrast agents for magnetic resonance imaging: a review. Fundam Clin Pharmacol [Internet].

2006 [cited 19 March 2019]; 20: 563–76. Available at: http://doi.wiley.com/10.1111/j.1472-8206.2006.00447.x

30. Lohrke J, Frenzel T, Endrikat J, et al. 25 Years of Contrast-Enhanced MRI: Developments, Current Challenges and Future Perspectives. Adv Ther [Internet]. 2016 [cited 4 February 2020]; 33: 1–28. Available at: http://link.springer.com/10.1007/s12325-015-0275-4

31. Tu C, Louie AY. Strategies for the development of gadolinium-based 'q'-activatable MRI contrast agents. NMR Biomed. 2013; 26: 781–7.

32. Lacerda S, Tóth É. Lanthanide Complexes in Molecular Magnetic Resonance Imaging and Theranostics. ChemMedChem [Internet]. 2017 [cited 23 January 2020]; 12: 883–94. Available at: http://doi.wiley.com/10.1002/cmdc.201700210

33. McDonald RJ, Levine D, Weinreb J, et al. Gadolinium Retention: A Research Roadmap from the 2018 NIH/ACR/RSNA Workshop on Gadolinium Chelates. Radiology [Internet]. 2018 [cited 3 February 2020]; 289: 517–34. Available at: http://pubs.rsna.org/doi/10.1148/radiol.2018181151

34. Jacques V, Dumas S, Sun W-CC, Troughton JS, Greenfield MT, Caravan P. High-relaxivity magnetic resonance imaging contrast agents part 2: Optimization of inner-and second-sphere relaxivity. Invest Radiol [Internet]. 2010 [cited 17 July 2018]; 45: 613–24. Available at: http://www.ncbi.nlm.nih.gov/pubmed/20808234

35. Caravan P, Ellison JJ, McMurry TJ, Lauffer RB. Gadolinium (III) chelates as MRI contrast agents: structure, dynamics, and applications. Chem Rev. 1999; 99: 2293–352.

36. Tóth É, Helm L, Merbach AE. Relaxivity of MRI Contrast Agents. In 2002: 61–101.

37. Micskei K, Helm L, Brücher E, Merbach A. 17O NMR study of water exchange on [Gd(DTPA)(H2O)]2- and [Gd(DOTA)(H2O)]- related to NMR imaging. Inorg Chem. 1993; 32: 3844–50.

38. Caravan P, Cloutier NJ, Greenfield MT, et al. The interaction of MS-325 with human serum albumin and its effect on proton relaxation rates. J Am Chem Soc. 2002; 124: 3152–62.

39. Dumas S, Jacques V, Sun WC, et al. High relaxivity magnetic resonance imaging contrast agents part 1: Impact of single donor atom substitution on relaxivity of serum albumin-bound gadolinium complexes. Invest Radiol. 2010; 45: 600–12.

40. Winter P, Athey P, Kiefer G, et al. Improved paramagnetic chelate for molecular imaging with MRI. In: Journal of Magnetism and Magnetic Materials. 2005.

41. Greenberg SA. Zinc Transmetallation and Gadolinium Retention after MR Imaging: Case Report. Radiology [Internet]. 2010 [cited 10 November 2020]; 257: 670–3. Available at: http://pubs.rsna.org/doi/10.1148/radiol.10100560

42. Laurent S, Elst L V, Copoix F, Muller RN. Stability of MRI paramagnetic contrast media: a proton relaxometric protocol for transmetallation assessment. Invest Radiol [Internet]. 2001 [cited 15 January 2018]; 36: 115–22. Available at: http://www.ncbi.nlm.nih.gov/pubmed/11224760

43. De Leõn-Rodríguez LM, Martins AF, Pinho MC, Rofsky NM, Sherry AD. Basic MR relaxation mechanisms and contrast agent design. J Magn Reson Imaging. 2015; 42: 545–65.

44. Grobner T. Gadolinium–a specific trigger for the development of nephrogenic fibrosing dermopathy and nephrogenic systemic fibrosis? Nephrol Dial Transplant [Internet]. 2006 [cited 3 February 2020]; 21: 1104–8. Available at: http://academic.oup.com/ndt/article/21/4/1104/1932577/Gadolinium-a-specific-trigger-for-the-development

45. Gupta A, Shamseddin MK, Khaira A. Pathomechanisms of nephrogenic systemic fibrosis: new insights. Clin Exp Dermatol [Internet]. 2011 [cited 4 February 2020]; 36: 763–8. Available at: http://doi.wiley.com/10.1111/j.1365-2230.2011.04136.x

46. Kanda T, Ishii K, Kawaguchi H, Kitajima K, Takenaka D. High signal intensity in the dentate nucleus and globus pallidus on unenhanced T1-weighted MR images: Relationship with increasing cumulative dose of a gadoliniumbased contrast material. Radiology. 2014; 270: 834–41.

47. Medicines Agency E. PRAC concludes assessment of gadolinium agents used in body scans and recommends regulatory actions, including suspension for some marketing authorisations [Internet]. 2017 [cited 19 March 2019]. Available at: www.ema.europa.eu/contact

48. Runge VM. Dechelation (Transmetalation): Consequences and Safety Concerns with the Linear Gadolinium-Based Contrast Agents, in View of Recent Health Care Rulings by the EMA (Europe), FDA (United States), and PMDA (Japan). Vol. 53, Investigative Radiology. Lippincott Williams and Wilkins; 2018.

49. FDA warns that gadolinium-based contrast agents (GBCAs) are retained in the body; requires new class warnings.

50. Rogosnitzky M, Branch S. Gadolinium-based contrast agent toxicity: a review of known and proposed mechanisms [Internet]. 2016/04/08. Vol. 29, BioMetals. Springer Netherlands; 2016 [cited 19 March 2019]. Available at: http://www.ncbi.nlm.nih.gov/pubmed/27053146

51. Li L, Jiang W, Luo K, et al. Superparamagnetic iron oxide nanoparticles as MRI contrast agents for non-invasive stem cell labeling and tracking [Internet]. Theranostics 2013. Available at: http://www.thno.org

52. Sharifi S, Seyednejad H, Laurent S, Atyabi F, Saei AA, Mahmoudi M. Superparamagnetic iron oxide nanoparticles for in vivo molecular and cellular imaging. Contrast Media Mol Imaging [Internet]. 2015 [cited 6 February 2020]; 10: 329–55. Available at: http://doi.wiley.com/10.1002/cmmi.1638

53. Wang YXJ, Hussain SM, Krestin GP. Superparamagnetic iron oxide contrast

agents: Physicochemical characteristics and applications in MR imaging. Eur Radiol. 2001; 11: 2319–31.

54. Peng XH, Qian X, Mao H, et al. Targeted magnetic iron oxide nanoparticles for tumor imaging and therapy. Vol. 3, International Journal of Nanomedicine. 2008.

55. Yu F, Zhang L, Huang Y, Sun K, David AE, Yang VC. The magnetophoretic mobility and superparamagnetism of core-shell iron oxide nanoparticles with dual targeting and imaging functionality. Biomaterials. 2010; 31: 5842–8.

56. Corot C, Robert P, Idée JM, Port M. Recent advances in iron oxide nanocrystal technology for medical imaging. Vol. 58, Advanced Drug Delivery Reviews. 2006.

57. Toth GB, Varallyay CG, Horvath A, et al. Current and potential imaging applications of ferumoxytol for magnetic resonance imaging. Vol. 92, Kidney International. Elsevier B.V.; 2017.

58. Semelka RC, Ramalho M, AlObaidy M, Ramalho J. Gadolinium in humans: A family of disorders. Vol. 207, American Journal of Roentgenology. American Roentgen Ray Society; 2016.

59. Fries P, Müller A, Seidel R, et al. P03277-a new approach to achieve: High-contrast enhancement initial results of an experimental extracellular gadolinium-based magnetic resonance contrast agent. Invest Radiol [Internet]. 2015 [cited 9 February 2020]; 50: 835–42. Available at: http://www.ncbi.nlm.nih.gov/pubmed/26186281

60. Robic C, Port M, Rousseaux O, et al. Physicochemical and Pharmacokinetic Profiles of Gadopiclenol. Invest Radiol [Internet]. 2019 [cited 9 February 2020]; 54: 475–84. Available at: http://insights.ovid.com/crossref?an=00004424-201908000-00005

61. Lacerda S. Targeted Contrast Agents for Molecular MRI. Inorganics [Internet]. 2018 [cited 8 February 2020]; 6: 129. Available at: http://www.mdpi.com/2304-6740/6/4/129

62. Li H, Meade TJ. Molecular Magnetic Resonance Imaging with Gd(III)-Based Contrast Agents: Challenges and Key Advances [Internet]. Vol. 141, Journal of the American Chemical Society. American Chemical Society; 2019 [cited 10 February 2020]. Available at: https://pubs.acs.org/doi/10.1021/jacs.9b09149

63. Pesaresi I, Cosottini M. MR Angiography Contrast Agents. In Springer, Berlin, Heidelberg; 2010: 8–16.

64. Caravan P, Parigi G, Chasse JM, et al. Albumin binding, relaxivity, and water exchange kinetics of the diastereoisomers of MS-325, a gadolinium(III)-based magnetic resonance angiography contrast agent. Inorg Chem [Internet]. 2007 [cited 11 February 2020]; 46: 6632–9. Available at: https://pubs.acs.org/doi/10.1021/ic700686k

65. Overoye-Chan K, Koerner S, Looby RJ, et al. EP-2104R: A fibrin-specific gadolinium-based MRI contrast agent for detection of thrombus. J Am Chem

Soc [Internet]. 2008 [cited 10 February 2020]; 130: 6025–39. Available at: https://pubs.acs.org/doi/10.1021/ja800834y

66. Spuentrup E, Botnar RM, Wiethoff AJ, et al. MR imaging of thrombi using EP-2104R, a fibrin-specific contrast agent: Initial results in patients. Eur Radiol. 2008; 18: 1995–2005.

67. Misselwitz B, Schmitt-Willich H, Ebert W, Frenzel T, Weinmann H-J. Pharmacokinetics of Gadomer-17, a new dendritic magnetic resonance contrast agent. Magma Magn Reson Mater Physics, Biol Med. 2001; 12: 128–34.

68. Villaraza AJ, Bumb A, Brechbiel MW. Macromolecules, dendrimers, and nanomaterials in magnetic resonance imaging: The interplay between size, function, and pharmacokinetics. Chem Rev [Internet]. 2010 [cited 9 February 2020]; 110: 2921–59. Available at: https://pubs.acs.org/doi/10.1021/cr900232t

69. Huang C-H, Tsourkas A. Gd-based macromolecules and nanoparticles as magnetic resonance contrast agents for molecular imaging. Curr Top Med Chem [Internet]. 2013 [cited 11 February 2020]; 13: 411–21. Available at: http://www.ncbi.nlm.nih.gov/pubmed/23432004

70. Langereis S, Geelen T, Grüll H, Strijkers GJ, Nicolay K. Paramagnetic liposomes for molecular MRI and MRI-guided drug delivery. NMR Biomed. 2013; 26: 728–44.

71. Mulder WJM, Strijkers GJ, van Tilborg GAF, Griffioen AW, Nicolay K. Lipid-based nanoparticles for contrast-enhanced MRI and molecular imaging. NMR Biomed [Internet]. 2006 [cited 20 March 2019]; 19: 142–64. Available at: http://doi.wiley.com/10.1002/nbm.1011

72. Tilcock C, Unger E, Cullis P, MacDougall P. Liposomal Gd-DTPA: preparation and characterization of relaxivity. Radiology. 1989; 171: 77–80.

73. Hossen S, Hossain MK, Basher MK, Mia MNH, Rahman MT, Uddin MJ. Smart nanocarrier-based drug delivery systems for cancer therapy and toxicity studies: A review. Vol. 15, Journal of Advanced Research. Elsevier B.V.; 2019.

74. Geraldes CFGC, Laurent S. Classification and basic properties of contrast agents for magnetic resonance imaging. Contrast Media Mol Imaging [Internet]. 2009 [cited 13 February 2020]; 4: 1–23. Available at: http://doi.wiley.com/10.1002/cmmi.265

75. Wang T, Hossann M, Reinl HM, et al. In vitro characterization of phosphatidylglyceroglycerol-based thermosensitive liposomes with encapsulated1H MRT1-shortening gadodiamide. Contrast Media Mol Imaging [Internet]. 2008 [cited 14 February 2020]; 3: 19–26. Available at: http://doi.wiley.com/10.1002/cmmi.226

76. de Smet M, Langereis S, den Bosch S van, Grüll H. Temperature-sensitive liposomes for doxorubicin delivery under MRI guidance. J Control Release. 2010; 143: 120–7.

77. de Smet M, Heijman E, Langereis S, Hijnen NM, Grüll H. Magnetic resonance imaging of high intensity focused ultrasound mediated drug delivery from temperature-sensitive liposomes: An in vivo proof-of-concept study. J Control Release [Internet]. 2011 [cited 15 January 2018]; 150: 102–10. Available at: http://www.ncbi.nlm.nih.gov/pubmed/21059375

78. Laurent S, Vander Elst L, Thirifays C, Muller RN. Relaxivities of paramagnetic liposomes: On the importance of the chain type and the length of the amphiphilic complex. Eur Biophys J. 2008; 37: 1007–14.

79. Hak S, Sanders HMHF, Agrawal P, et al. A high relaxivity Gd(III)DOTA-DSPE-based liposomal contrast agent for magnetic resonance imaging. Eur J Pharm Biopharm [Internet]. 2009 [cited 27 June 2017]; 72: 397–404. Available at: http://linkinghub.elsevier.com/retrieve/pii/S0939641108003895

80. Kabalka GW, Davis MA, Holmberg E, Maruyama K, Huang L. Gadolinium-labeled liposomes containing amphiphilic Gd-DTPA derivatives of varying chain length: Targeted MRI contrast enhancement agents for the liver. Magn Reson Imaging. 1991; 9: 373–7.

81. Kabalka GW, Buonocore E, Hubner K, Davis M, Huang L. Gadolinium-labeled liposomes containing paramagnetic amphipathic agents: Targeted MRI contrast agents for the liver. Magn Reson Med [Internet]. 1988 [cited 2 January 2020]; 8: 89–95. Available at: http://doi.wiley.com/10.1002/mrm.1910080111

82. Kamaly N, Miller AD. Paramagnetic liposome nanoparticles for cellular and tumour imaging. Int J Mol Sci. 2010; 11: 1759–76.

83. Kamaly N, Kalber T, Ahmad A, et al. Bimodal paramagnetic and fluorescent liposomes for cellular and tumor magnetic resonance imaging. Bioconjug Chem [Internet]. 2007/11/08. 2008 [cited 15 February 2020]; 19: 118–29. Available at: https://pubs.acs.org/doi/10.1021/bc7001715

84. Mulder WJM, McMahon MT, Nicolay K. The evolution of MRI probes: from the initial development to state-of-the-art applications. NMR Biomed [Internet]. 2013 [cited 12 February 2020]; 26: 725–7. Available at: http://doi.wiley.com/10.1002/nbm.2976

85. Erdogan S, Medarova ZO, Roby A, Moore A, Torchilin VP. Enhanced tumor MR imaging with gadolinium-loaded polychelating polymer-containing tumor-targeted liposomes. J Magn Reson Imaging. 2008; 27: 574–80.

86. Erdogan S, Roby A, Sawant R, Hurley J, Torchilin VP. Gadolinium-loaded polychelating polymer-containing cancer cell-specific immunoliposomes. J Liposome Res [Internet]. 2006 [cited 15 February 2020]; 16: 45–55. Available at: http://www.tandfonline.com/doi/full/10.1080/08982100500528784

87. Silva SR, Duarte EC, Ramos GS, et al. Gadolinium(III) Complexes with N-Alkyl-N-methylglucamine Surfactants Incorporated into Liposomes as Potential MRI Contrast Agents. Bioinorg Chem Appl. 2015; 2015.

88. Skelly Frame EM, Uzgiris EE. Gadolinium determination in tissue samples by inductively coupled plasma mass spectrometry and inductively coupled

plasma atomic emission spectrometry in evaluation of the action of magnetic resonance imaging contrast agents. Analyst. 1998; 123: 675–9.

89. Olesik JW. Elemental Analysis Using ICP-OES and ICP/MS. Anal Chem [Internet]. 1991 [cited 21 December 2019]; 63: 12A-21A. Available at: https://pubs.acs.org/doi/abs/10.1021/ac00001a711

90. Braun M, Baranyai Z, Carniato F, Botta M. Contrast Agents for MRI: Experimental methods. Pierre VC, Allen MJ, Eds. London : Royal Society of Chemistry; 2017.

91. Scheffer A, Engelhard C, Sperling M, Buscher W. ICP-MS as a new tool for the determination of gold nanoparticles in bioanalytical applications. Anal Bioanal Chem. 2008; 390: 249–52.

92. Bolann BJ, Rahil-Khazen R, Henriksen H, Isrenn R, Ulvik RJ. Evaluation of methods for trace-element determination with emphasis on their usability in the clinical routine laboratory. Vol. 67, Scandinavian Journal of Clinical and Laboratory Investigation. 2007.

93. Telgmann L, Holtkamp M, Künnemeyer J, et al. Simple and rapid quantification of gadolinium in urine and blood plasma samples by means of total reflection X-ray fluorescence (TXRF). Metallomics. 2011; 3: 1035–40.

94. Tölg G, Griepink B, Tolg G. Sample Digestion for the Determination of Elemental Traces in Matrices of Environmental Concern [Internet]. Vol. 61, Pure and Applied Chemistry. Belguim; 1989 Jan [cited 19 March 2019]. Available at: http://citeseerx.ist.psu.edu/viewdoc/download?doi=10.1.1.576.3921&rep=rep1&type=pdf

95. Bedson P, Prichard E, Points J, Mackay GM, Thomas JDR. Trace analysis: A structured approach to obtaining reliable results. Chromatographia [Internet]. 2007 [cited 12 November 2019]; 46: 95. Available at: https://doi.org/10.1007/BF02490937

96. Marguí E, de Fátima Marques A, de Lurdes Prisal M, Hidalgo M, Queralt I, Carvalho ML. Total reflection X-ray spectrometry (TXRF) for trace elements assessment in edible clams. 2014 [cited 20 March 2019]; 68. Available at: http://www.ncbi.nlm.nih.gov/pubmed/25286343

97. Kregsamer P, Streli C, Wobrauschek P. Total Reflection XRF (TXRF). In 2001: 559–602.

98. Wobrauschek P. Total reflection x-ray fluorescence analysis—a review. X-Ray Spectrom [Internet]. 2007 [cited 20 March 2019]; 36: 289–300. Available at: http://doi.wiley.com/10.1002/xrs.985

99. Riaño S, Regadío M, Binnemans K, Vander Hoogerstraete T. Practical guidelines for best practice on Total Reflection X-ray Fluorescence spectroscopy: Analysis of aqueous solutions. Spectrochim Acta - Part B At Spectrosc [Internet]. 2016 [cited 19 March 2019]; 124: 109–15. Available at: https://core.ac.uk/download/pdf/80794206.pdf

100. Principles of Total Reflection XRF. In: Total-Reflection X-Ray Fluorescence Analysis and Related Methods [Internet]. Hoboken, New Jersey: John Wiley & Sons, Inc.; 2014 [cited 25 February 2020]: 79–125. Available at: http://doi.wiley.com/10.1002/9781118985953.ch02

101. Ashraf A, Stosnach H, Parkes HG, et al. Pattern of Altered Plasma Elemental Phosphorus, Calcium, Selenium, Iron and Copper in Alzheimer's Disease. Sci Rep. 2019; 9.

102. Van Tilborg GAF, Strijkers GJ, Pouget EM, et al. Kinetics of avidin-induced clearance of biotinylated bimodal liposomes for improved MR molecular imaging. Magn Reson Med [Internet]. 2008 [cited 25 February 2020]; 60: 1444–56. Available at: http://doi.wiley.com/10.1002/mrm.21780

103. Ray S, Cheng CA, Chen W, Li Z, Zink JI, Lin YY. Magnetic heating stimulated cargo release with dose control using multifunctional MR and thermosensitive liposome. Nanotheranostics. 2019; 3: 166–78.

104. Bangham AD, Horne RW. Negative staining of phospholipids and their structural modification by surface-active agents as observed in the electron microscope. J Mol Biol. 1964; 8: 660IN2-668IN10.

105. Pattni BS, Chupin V V., Torchilin VP. New developments in liposomal drug delivery. Chem Rev. 2015; 115: 10938–66.

106. Akbarzadeh A, Rezaei-Sadabady R, Davaran S, et al. Liposome: Classification, preparation, and applications. Nanoscale Res Lett. 2013; 8.

107. Sercombe L, Veerati T, Moheimani F, Wu SY, Sood AK, Hua S. Advances and challenges of liposome assisted drug delivery. Vol. 6, Frontiers in Pharmacology. Frontiers Media S.A.; 2015.

108. Barenholz YC. Doxil®—the first FDA-approved nano-drug: lessons learned. J Control Release. 2012; 160: 117–34.

109. Shi Y, Moon M, Dawood S, McManus B, Liu PP. Mechanisms and management of doxorubicin cardiotoxicity. Herz. 2011; 36: 296–305.

110. Gabizon A, Catane R, Uziely B, et al. Prolonged Circulation Time and Enhanced Accumulation in Malignant Exudates of Doxorubicin Encapsulated in Polyethylene-glycol Coated Liposomes 1. Vol. 154, CANCER. 1994.

111. Kobayashi H, Watanabe R, Choyke PL. Improving conventional enhanced permeability and retention (EPR) effects; What is the appropriate target? Theranostics 2014.

112. Matsumura Y, Maeda H. A new concept for macromolecular therapeutics in cancer chemotherapy: mechanism of tumoritropic accumulation of proteins and the antitumor agent smancs. Cancer Res. 1986; 46: 6387–92.

113. Stone NRH, Bicanic T, Salim R, Hope W. Liposomal Amphotericin B (AmBisome®): A Review of the Pharmacokinetics, Pharmacodynamics, Clinical Experience and Future Directions. Vol. 76, Drugs. Springer International Publishing; 2016.

114. Forssen EA, Ross ME. Daunoxome® treatment of solid tumors: Preclinical and clinical investigations. J Liposome Res. 1994; 4: 481–512.

115. Petre CE, Dittmer DP. Liposomal daunorubicin as treatment for Kaposi's sarcoma. Int J Nanomedicine. 2007; 2: 277–88.

116. Glantz MJ, LaFollette S, Jaeckle KA, et al. Randomized trial of a slow-release versus a standard formulation of cytarabine for the intrathecal treatment of lymphomatous meningitis. J Clin Oncol [Internet]. 1999 [cited 19 February 2020]; 17: 3110–6. Available at: http://www.ncbi.nlm.nih.gov/pubmed/10506606

117. Pillai G. Nanomedicines for Cancer Therapy: An Update of FDA Approved and Those under Various Stages of Development. 2014; 1: 1–13.

118. Carvalho B, Roland LM, Chu LF, Campitelli VA, Riley ET. Single-dose, extended-release epidural morphine (DepoDur™) compared to conventional epidural morphine for post-Cesarean pain. Anesth Analg. 2007; 105: 176–83.

119. Bovier PA. Epaxal®: A virosomal vaccine to prevent hepatitis A infection. Vol. 7, Expert Review of Vaccines. Expert Rev Vaccines; 2008.

120. Burade V, Bhowmick S, Maiti K, Zalawadia R, Ruan H, Thennati R. Lipodox® (generic doxorubicin hydrochloride liposome injection): In vivo efficacy and bioequivalence versus Caelyx® (doxorubicin hydrochloride liposome injection) in human mammary carcinoma (MX-1) xenograft and syngeneic fibrosarcoma (WEHI 164) mouse models. BMC Cancer. 2017; 17.

121. Boulikas T. Clinical overview on Lipoplatin ™: a successful liposomal formulation of cisplatin. Expert Opin Investig Drugs. 2009; 18: 1197–218.

122. Bao P, Zheng Y, Wang C, Gu K, Jin F, Lu W. Vincristine Sulfate Liposomes Injection (VSLI, Marqibo): Results From a Phase I Study in Children, Adolescents, and Young AdultsWith Refractory Solid Tumors or Leukemias. Pediatr Blood Cancer. 2016; 63: 997–1005.

123. Sarris AH, Hagemeister F, Romaguera J, et al. Liposomal vincristine in relapsed non-Hodgkin ' s lymphomas : Early results of an ongoing phase II trial. Ann Oncol. 2000; 11: 69–72.

124. Zhang H. Onivyde for the therapy of multiple solid tumors. Onco Targets Ther. 2016; 9: 3001–7.

125. Lyon PC, Griffiths LF, Lee J, et al. Clinical trial protocol for TARDOX: A phase I study to investigate the feasibility of targeted release of lyso-thermosensitive liposomal doxorubicin (ThermoDox®) using focused ultrasound in patients with liver tumours. J Ther Ultrasound. 2017; 5: 1–8.

126. Hong CW, Libutti SK, Wood BJ. Liposomal doxorubicin plus radiofrequency ablation for complete necrosis of a hepatocellular carcinoma. Curr Oncol. 2013; 20: 274–7.

127. Hua S, Wu SY. The use of lipid-based nanocarriers for targeted pain therapies. Vol. 4 NOV, Frontiers in Pharmacology. Front Pharmacol; 2013.

128. Li M, Du C, Guo N, et al. Composition design and medical application of liposomes. Vol. 164, European Journal of Medicinal Chemistry. Elsevier Masson SAS; 2019.

129. Moghimi SM, Szebeni J. Stealth liposomes and long circulating nanoparticles: Critical issues in pharmacokinetics, opsonization and protein-binding properties. Vol. 42, Progress in Lipid Research. Elsevier Ltd; 2003.

130. Veronese FM, Pasut G. PEGylation, successful approach to drug delivery. Drug Discov Today. 2005; 10: 1451–8.

131. Riaz MK, Riaz MA, Zhang X, et al. Surface functionalization and targeting strategies of liposomes in solid tumor therapy: A review. Vol. 19, International Journal of Molecular Sciences. MDPI AG; 2018.

132. Moghimipour E, Rezaei M, Ramezani Z, et al. Folic acid-modified liposomal drug delivery strategy for tumor targeting of 5-fluorouracil. Eur J Pharm Sci. 2018; 114: 166–74.

133. Li S, Goins B, Zhang L, Bao A. Novel multifunctional theranostic liposome drug delivery system: Construction, characterization, and multimodality MR, near-infrared fluorescent, and nuclear imaging. Bioconjug Chem [Internet]. 2012 [cited 18 February 2020]; 23: 1322–32. Available at: https://pubs.acs.org/doi/10.1021/bc300175d

134. Sawant RR, Torchilin VP. Multifunctional nanocarriers and intracellular drug delivery. Vol. 16, Current Opinion in Solid State and Materials Science. Elsevier Ltd; 2012.

135. Bi H, Xue J, Jiang H, et al. Current developments in drug delivery with thermosensitive liposomes. Vol. 14, Asian Journal of Pharmaceutical Sciences. Shenyang Pharmaceutical University; 2019.

136. Kneidl B, Peller M, Winter G, Lindner LH, Hossann M. Thermosensitive liposomal drug delivery systems: state of the art review. Int J Nanomedicine. 2014; 9: 4387.

137. Yatvin MB, Weinstein JN, Dennis WH, Blumenthal R. Design of Liposomes for Enhanced Local Release of Drugs by Hyperthermia. Science [Internet]. 1978 [cited 30 March 2017]; 202: 1290–3. Available at: http://www.ncbi.nlm.nih.gov/pubmed/364652

138. Tejera-Garcia R, Parkkila P, Zamotin V, Kinnunen PKJ. Principles of rational design of thermally targeted liposomes for local drug delivery. Nanomedicine Nanotechnology, Biol Med [Internet]. 2014 [cited 15 January 2018]; 10: 1243–52. Available at: https://www.sciencedirect.com/science/article/pii/S1549963414001312

139. Mazzotta E, Tavano L, Muzzalupo R. Thermo-sensitive vesicles in controlled drug delivery for chemotherapy. Vol. 10, Pharmaceutics. MDPI AG; 2018.

140. Lindner LH, Eichhorn ME, Eibl H, et al. Novel Temperature-Sensitive Liposomes with Prolonged Circulation Time. Clin Cancer Res. 2004; 10: 2168–78.

141. McElhaney RN. The use of differential scanning calorimetry and differential

thermal analysis in studies of model and biological membranes. Chem Phys Lipids. 1982;

142. Demetzos C. Differential Scanning Calorimetry (DSC): A Tool to Study the Thermal Behavior of Lipid Bilayers and Liposomal Stability. J Liposome Res [Internet]. 2008 [cited 29 March 2017]; 18: 159–73. Available at: http://www.tandfonline.com/doi/full/10.1080/08982100802310261

143. Ta T, Porter TM. Thermosensitive liposomes for localized delivery and triggered release of chemotherapy. J Control Release [Internet]. 2013 [cited 15 January 2018]; 169: 112–25. Available at: http://www.ncbi.nlm.nih.gov/pubmed/23583706

144. Chen W, Duša F, Witos J, Ruokonen SK, Wiedmer SK. Determination of the Main Phase Transition Temperature of Phospholipids by Nanoplasmonic Sensing. Sci Rep. 2018; 8: 1–11.

145. Li J, Wang X, Zhang T, et al. A review on phospholipids and their main applications in drug delivery systems. Asian Journal of Pharmaceutical Sciences Elsevier Ltd;

146. Gaber MH, Hong K, Huang SK, Papahadjopoulos D. Thermosensitive Sterically Stabilized Liposomes: Formulation and in Vitro Studies on Mechanism of Doxorubicin Release by Bovine Serum and Human Plasma. Pharm Res An Off J Am Assoc Pharm Sci. 1995; 12: 1407–16.

147. Anyarambhatla GR, Needham D. Enhancement of the phase transition permeability of DPPC liposomes by incorporation of MPPC: A new temperature-sensitive liposome for use with mild hyperthermia. J Liposome Res. 1999; 9: 491–506.

148. Needham D, Anyarambhatla G, Kong G, Dewhirst MW. A New Temperature-sensitive Liposome for Use with Mild Hyperthermia : Characterization and Testing in a Human Tumor Xenograft Model Advances in Brief A New Temperature-sensitive Liposome for Use with Mild Hyperthermia : Characterization and Testing in a H. Cancer Res. 2000; 1197–201.

149. Mills JK, Needham D. Lysolipid incorporation in dipalmitoylphosphatidylcholine bilayer membranes enhances the ion permeability and drug release rates at the membrane phase transition [Internet]. Biochimica et Biophysica Acta - Biomembranes Elsevier; Oct 15, 2005. Available at: http://linkinghub.elsevier.com/retrieve/pii/S0005273605002683

150. Needham D, Park JY, Wright AM, Tong J. Materials characterization of the low temperature sensitive liposome (LTSL): Effects of the lipid composition (lysolipid and DSPE-PEG2000) on the thermal transition and release of doxorubicin. Faraday Discuss. 2012; 161: 515–34.

151. Kong G, Anyarambhatla G, Petros WP, et al. Efficacy of Liposomes and Hyperthermia in a Human Tumor Xenograft Model : Importance of Triggered Drug Release Efficacy of Liposomes and Hyperthermia in a Human Tumor Xenograft Model : Importance of Triggered Drug Release 1. Cancer Res. 2000;

60: 6950–7.

152. Dou Y, Hynynen K, Allen C. To heat or not to heat: Challenges with clinical translation of thermosensitive liposomes. J Control Release [Internet]. 2017 [cited 19 April 2017]; 249: 63–73. Available at: http://ac.els-cdn.com/S0168365917300238/1-s2.0-S0168365917300238-main.pdf?_tid=2dd0378c-2517-11e7-b521-00000aacb360&acdnat=1492616894_622b451239bc6d3186c148be26ea3d40

153. Zagar TM, Vujaskovic Z, Formenti S, et al. Two phase I dose-escalation/pharmacokinetics studies of low temperature liposomal doxorubicin (LTLD) and mild local hyperthermia in heavily pretreated patients with local regionally recurrent breast cancer. Int J Hyperth. 2014; 30: 285–94.

154. Needham D. Drug Delivery Fundamentals and Applications. Hillery AM, Park K, Eds. CRC Press; 2016.

155. Banno B, Ickenstein LM, Chiu GNC, et al. The functional roles of poly(ethylene glycol)-lipid and lysolipid in the drug retention and release from lysolipid-containing thermosensitive liposomes in vitro and in vivo. J Pharm Sci. 2009/11/11. 2010; 99: 2295–308.

156. Hossann M, Wiggenhorn M, Schwerdt A, et al. In vitro stability and content release properties of phosphatidylglyceroglycerol containing thermosensitive liposomes. Biochim Biophys Acta - Biomembr. 2007; 1768: 2491–9.

157. Tagami T, Ernsting MJ, Li SD. Efficient tumor regression by a single and low dose treatment with a novel and enhanced formulation of thermosensitive liposomal doxorubicin. J Control Release. 2011; 152: 303–9.

158. Tagami T, Foltz WD, Ernsting MJ, et al. MRI monitoring of intratumoral drug delivery and prediction of the therapeutic effect with a multifunctional thermosensitive liposome. Biomaterials [Internet]. 2011 [cited 30 March 2017]; 32: 6570–8. Available at: http://www.ncbi.nlm.nih.gov/pubmed/21641639

159. Boissenot T, Bordat A, Fattal E, Tsapis N. Ultrasound-triggered drug delivery for cancer treatment using drug delivery systems: From theoretical considerations to practical applications [Internet]. Journal of Controlled Release Nov 10, 2016. Available at: http://www.sciencedirect.com/science/article/pii/S0168365916308070

160. Kim YS, Rhim H, Min JC, Hyo KL, Choi D. High-intensity focused ultrasound therapy: An overview for radiologists. Vol. 9, Korean Journal of Radiology. 2008.

161. Mitragotri S. Healing sound: The use of ultrasound in drug delivery and other therapeutic applications. Nat Rev Drug Discov. 2005; 4: 255–60.

162. Edler I, Lindström K. The history of echocardiography. Ultrasound Med Biol. 2004; 30: 1565–644.

163. Toosonix.

164. Izadifar, Izadifar, Chapman, Babyn. An Introduction to High Intensity Focused Ultrasound: Systematic Review on Principles, Devices, and Clinical Applications. J Clin Med [Internet]. 2020 [cited 17 February 2020]; 9: 460. Available at: https://www.mdpi.com/2077-0383/9/2/460

165. Tu J, Ha Hwang J, Chen T, et al. Controllable in vivo hyperthermia effect induced by pulsed high intensity focused ultrasound with low duty cycles. Appl Phys Lett. 2012; 101.

166. Nelson TR, Fowlkes JB. Ultrasound biosafety considerations for thepracticing sonographer and sonologist. J Ultrasound Med. 2009; 139–50.

167. O'Brien WD. Ultrasound-biophysics mechanisms. Prog Biophys Mol Biol. 2007; 93: 212–55.

168. Thanou M, Gedroyc W. MRI-guided focused ultrasound as a new method of drug delivery. J Drug Deliv. 2013; 2013.

169. Otto C. Principles of echocardiographic image acquisition and Doppler analysis. Textbook of clinical echocardiography. 2000.

170. Zhou Y-FY-F. High intensity focused ultrasound in clinical tumor ablation. 2011; 2.

171. Canney MS, Bailey MR, Crum LA, Khokhlova VA, Sapozhnikov OA. Acoustic characterization of high intensity focused ultrasound fields: A combined measurement and modeling approach. J Acoust Soc Am. 2008; 124: 2406–20.

172. Christian E, Yu C, Apuzzo MLJ. Focused ultrasound: Relevant history and prospects for the addition of mechanical energy to the neurosurgical armamentarium. World Neurosurgery. 2014.

173. Chaplin V, Caskey CF. Multi-focal HIFU reduces cavitation in mild-hyperthermia. J Ther Ultrasound. 2017; 5.

174. Sun T, Samiotaki G, Wang S, Acosta C, Chen CC, Konofagou EE. Acoustic cavitation-based monitoring of the reversibility and permeability of ultrasound-induced blood-brain barrier opening. Phys Med Biol. 2015; 60: 9079–94.

175. Tharkar P, Varanasi R, Wong WSF, Jin CT, Chrzanowski W. Nano-Enhanced Drug Delivery and Therapeutic Ultrasound for Cancer Treatment and Beyond. Vol. 7, Frontiers in Bioengineering and Biotechnology. Frontiers Media S.A.; 2019.

176. Izadifar Z, Babyn P, Chapman D. Ultrasound Cavitation/Microbubble Detection and Medical Applications. Vol. 39, Journal of Medical and Biological Engineering. Springer Berlin Heidelberg; 2019.

177. Kok HP, Cressman ENK, Ceelen W, et al. Heating technology for malignant tumors: a review. Int J Hyperth [Internet]. 2020 [cited 11 November 2020]; 37: 711–41. Available at: https://www.tandfonline.com/doi/full/10.1080/02656736.2020.1779357

178. Wang M, Zhang Y, Cai C, Tu J, Guo X, Zhang D. Sonoporation-induced cell

membrane permeabilization and cytoskeleton disassembly at varied acoustic and microbubble-cell parameters. Sci Rep. 2018; 8: 1–12.

179. Hsiao YH, Kuo SJ, Tsai H Der, Chou MC, Yeh GP. Clinical application of high-intensity focused ultrasound in cancer therapy. Vol. 7, Journal of Cancer. Ivyspring International Publisher; 2016.

180. Santos MA, Goertz DE, Hynynen K. Focused Ultrasound Hyperthermia Mediated Drug Delivery Using Thermosensitive Liposomes and Visualized With in vivo Two-Photon Microscopy. Theranostics [Internet]. 2017/08/19. 2017 [cited 24 February 2020]; 7: 2718–31. Available at: https://www.ncbi.nlm.nih.gov/pubmed/28819458

181. Roberts A. Magnetic Resonance-Guided Focused Ultrasound for Uterine Fibroids. Semin Intervent Radiol. 2008; 25: 394–405.

182. Lindner U, Ghai S, Spensieri P, et al. Focal magnetic resonance guided focused ultrasound for prostate cancer: Initial North American experience. Can Urol Assoc J. 2012; 6: E283-6.

183. Lewis MA, Staruch RM, Chopra R. Thermometry and ablation monitoring with ultrasound. Int J Hyperth. 2015; 31: 163–81.

184. Rivens I, Shaw A, Civale J, Morris H. Treatment monitoring and thermometry for therapeutic focused ultrasound. Int J Hyperth. 2007; 23: 121–39.

185. Odéen H, Parker DL. Magnetic resonance thermometry and its biological applications – Physical principles and practical considerations. Vol. 110, Progress in Nuclear Magnetic Resonance Spectroscopy. Elsevier B.V.; 2019.

186. Kim YS. Advances in MR image-guided high-intensity focused ultrasound therapy. Int J Hyperth [Internet]. 2015 [cited 24 February 2020]; 31: 225–32. Available at: http://www.tandfonline.com/doi/full/10.3109/02656736.2014.976773

187. Roy Chowdhury M, Schumann C, Bhakta-Guha D, Guha G. Cancer nanotheranostics: Strategies, promises and impediments. Biomed Pharmacother. 2016; 84: 291–304.

188. Jo SD, Ku SH, Won YY, Kim SH, Kwon IC. Targeted nanotheranostics for future personalized medicine: Recent progress in cancer therapy. Theranostics. 2016; 6: 1362–77.

189. Wright M, Centelles M, Gedroyc W, Thanou M. Image guided focused ultrasound as a new method of targeted drug delivery. In: Theranostics and Image Guided Drug Delivery. 2018: 1–39.

190. Ferreira Soares DC. Theranostic Nanoparticles: Imaging and Therapy Combined. J Mol Pharm Org Process Res. 2014; 02: 1–2.

191. Ryu JH, Lee S, Son S, et al. Theranostic nanoparticles for future personalized medicine. J Control Release [Internet]. 2014; 190: 477–84. Available at: http://dx.doi.org/10.1016/j.jconrel.2014.04.027

192. Kalyane D, Raval N, Maheshwari R, Tambe V, Kalia K, Tekade RK. Employment

of enhanced permeability and retention effect (EPR): Nanoparticle-based precision tools for targeting of therapeutic and diagnostic agent in cancer. Vol. 98, Materials Science and Engineering C. Elsevier Ltd; 2019.

193. Duan L, Yang L, Jin J, et al. Micro/nano-bubble-assisted ultrasound to enhance the EPR effect and potential theranostic applications. Vol. 10, Theranostics. Ivyspring International Publisher; 2020.

194. Centelles MNMN, Wright M, So P-W, et al. Image guided thermosensitive liposomes for focused ultrasound drug delivery: Using NIRF labelled lipids and topotecan to visualise the effects of hyperthermia in tumours. J Control Release. 2018; 280: 87–98.

195. Li S, Wu P-HH. Magnetic resonance image-guided versus ultrasound-guided high-intensity focused ultrasound in the treatment of breast cancer. Chinese Journal of Cancer BioMed Central; 2013.

196. Garello F, Terreno E. Sonosensitive MRI Nanosystems as Cancer Theranostics: A Recent Update. Front Chem [Internet]. 2018 [cited 2 August 2018]; 6: 157. Available at: http://www.ncbi.nlm.nih.gov/pubmed/29868560

197. Grüll H, Langereis S. Hyperthermia-triggered drug delivery from temperature-sensitive liposomes using MRI-guided high intensity focused ultrasound. J Control Release [Internet]. 2012; 161: 317–27. Available at: http://dx.doi.org/10.1016/j.jconrel.2012.04.041

198. Hossann M, Wang T, Syunyaeva Z, et al. Non-ionic Gd-based MRI contrast agents are optimal for encapsulation into phosphatidyldiglycerol-based thermosensitive liposomes. J Control Release. 2013; 166: 22–9.

199. de Smet M, Hijnen NM, Langereis S, et al. Magnetic resonance guided high-intensity focused ultrasound mediated hyperthermia improves the intratumoral distribution of temperature-sensitive liposomal doxorubicin. Invest Radiol [Internet]. 2013 [cited 20 March 2017]; 48: 395–405. Available at: http://content.wkhealth.com/linkback/openurl?sid=WKPTLP:landingpage&an=00004424-201306000-00006

200. Hijnen N, Kneepkens E, de Smet M, et al. Thermal combination therapies for local drug delivery by magnetic resonance-guided high-intensity focused ultrasound. Proc Natl Acad Sci U S A [Internet]. 2017/06/02. 2017 [cited 28 February 2020]; 114: E4802–11. Available at: https://www.ncbi.nlm.nih.gov/pubmed/28566498

201. Kim HR, You DG, Park S-J, et al. MRI monitoring of tumor-selective anticancer drug delivery with stable thermosensitive liposomes triggered by high-intensity focused ultrasound. Mol Pharm [Internet]. 2016 [cited 18 February 2020]; 13: 1528–39. Available at: https://pubs.acs.org/doi/10.1021/acs.molpharmaceut.6b00013

202. Crich SG, Terreno E, Aime S. Nano-sized and other improved reporters for magnetic resonance imaging of angiogenesis. Adv Drug Deliv Rev [Internet]. 2017 [cited 19 March 2019]; 119: 61–72. Available at:

http://www.ncbi.nlm.nih.gov/pubmed/28802567

203. Jeong Y, Hwang HS, Na K. Theranostics and contrast agents for magnetic resonance imaging [Internet]. Biomaterials Research 2018. Available at: https://biomaterialsres.biomedcentral.com/articles/10.1186/s40824-018-0130-1

204. Na H Bin, Song IC, Hyeon T. Inorganic Nanoparticles for MRI Contrast Agents. Adv Mater [Internet]. 2009 [cited 27 December 2019]; 21: 2133–48. Available at: http://doi.wiley.com/10.1002/adma.200802366

205. André JP, Tóth É, Fischer H, Seelig A, Mäcke HR, Merbach AE. High Relaxivity for Monomeric Gd(DOTA)-Based MRI Contrast Agents, Thanks to Micellar Self-Organization. Chem - A Eur J [Internet]. 1999 [cited 20 March 2019]; 5: 2977–83. Available at: http://doi.wiley.com/10.1002/%28SICI%291521-3765%2819991001%295%3A10%3C2977%3A%3AAID-CHEM2977%3E3.0.CO%3B2-T

206. Ayyagari AL, Zhang X, Ghaghada KB, Annapragada A, Hu X, Bellamkonda R V. Long-circulating liposomal contrast agents for magnetic resonance imaging. Magn Reson Med [Internet]. 2006 [cited 20 March 2019]; 55: 1023–9. Available at: http://doi.wiley.com/10.1002/mrm.20846

207. Ghaghada K, Hawley C, Kawaji K, Annapragada A, Mukundan S. T1 Relaxivity of Core-encapsulated Gadolinium Liposomal Contrast Agents-Effect of Liposome Size and Internal Gadolinium Concentration. Acad Radiol. 2008; 15: 1259–63.

208. Ghaghada KB, Ravoori M, Sabapathy D, Bankson J, Kundra V, Annapragada A. New Dual Mode Gadolinium Nanoparticle Contrast Agent for Magnetic Resonance Imaging. Yang S, Ed. PLoS One [Internet]. 2009 [cited 19 March 2019]; 4: e7628. Available at: http://www.ncbi.nlm.nih.gov/pubmed/19893616

209. So P-W, Kalber T, Hunt D, et al. Efficient and rapid labeling of transplanted cell populations with superparamagnetic iron oxide nanoparticles using cell surface chemical biotinylation for in vivo monitoring by MRI. Cell Transplant [Internet]. 2010 [cited 22 December 2019]; 19: 419–29. Available at: http://www.ncbi.nlm.nih.gov/pubmed/20579412

210. Kalber TL, Kamaly N, So PW, et al. A low molecular weight folate receptor targeted contrast agent for magnetic resonance tumor imaging. Mol Imaging Biol. 2011; 13: 653–62.

211. Szomolanyi P, Rohrer M, Frenzel T, et al. Comparison of the Relaxivities of Macrocyclic Gadolinium-Based Contrast Agents in Human Plasma at 1.5, 3, and 7 T, and Blood at 3 T. Invest Radiol [Internet]. 2019 [cited 12 January 2020]; 54: 559–64. Available at: http://www.ncbi.nlm.nih.gov/pubmed/31124800

212. Corporation B. S2 PICOFOX - OVERVIEW, TXRF SPECTROMETER FOR TRACE ANALYSIS [Internet]. Corporation B, Ed. Vol. 2016. Bruker Corporation; 2016. Available at: https://www.bruker.com/products/x-ray-diffraction-and-elemental-analysis/micro-xrf-and-txrf/s2-picofox/overview.html

213. Veiga M, Mattiazzi P, de Gois JS, Nascimento PC, Borges DLG, Bohrer D. Presence of other rare earth metals in gadolinium-based contrast agents. Talanta. 2020; 216: 120940.

214. Wilschefski S, Baxter M. Inductively Coupled Plasma Mass Spectrometry: Introduction to Analytical Aspects. Clin Biochem Rev [Internet]. 2019 [cited 22 November 2020]; 40: 115–33. Available at: /pmc/articles/PMC6719745/?report=abstract

215. Mistra NL, Mudher KDS. Total reflection x-ray fluorescence: A technique for trace element analysis in materials. Prog Cryst Growth Charact Mater. 2002; 45: 65–74.

216. Nelms SM. Inductively coupled plasma mass spectrometry handbook. CRC press; 2005.

217. Pahlke S, Fabry L, Kotz L, Mantler C, Ehmann T. Determination of ultra trace contaminants on silicon wafer surfaces using total-reflection X-ray fluorescence TXRF 'state-of-the-art'. Spectrochim Acta - Part B At Spectrosc. 2001; 56: 2261–74.

218. So PW, Ekonomou A, Galley K, et al. Intraperitoneal delivery of acetate-encapsulated liposomal nanoparticles for neuroprotection of the penumbra in a rat model of ischemic stroke. Int J Nanomedicine. 2019; 14: 1979–91.

219. Giavarina D. Understanding Bland Altman analysis. Biochem Medica [Internet]. 2015 [cited 23 November 2020]; 25: 141–51. Available at: /pmc/articles/PMC4470095/?report=abstract

220. Todolí JL, Gras L, Hernandis V, Mora J. Elemental matrix effects in ICP-AES [Internet]. Vol. 17, Journal of Analytical Atomic Spectrometry. Royal Society of Chemistry; 2002 [cited 23 November 2020]. Available at: https://pubs.rsc.org/en/content/articlehtml/2002/ja/b009570m

221. Lauffer RB. Paramagnetic metal complexes as water proton relaxation agents for NMR imaging: theory and design. Chem Rev [Internet]. 1987 [cited 27 December 2019]; 87: 901–27. Available at: https://pubs.acs.org/doi/abs/10.1021/cr00081a003

222. Tóth É, Helm L, Merbach AE. Metal Complexes as MRI Contrast Enhancement Agents.

223. Massaad CA, Pautler RG. Manganese-Enhanced Magnetic Resonance Imaging (MEMRI).

224. Yokoyama M, Shiraishi K. Stability evaluation of Gd chelates for macromolecular MRI contrast agents. Magn Reson Mater Physics, Biol Med. 2019;

225. Clough TJ, Jiang L, Wong KL, Long NJ. Ligand design strategies to increase stability of gadolinium-based magnetic resonance imaging contrast agents. Nat Commun [Internet]. 2019/03/31. 2019 [cited 29 February 2020]; 10: 1420. Available at: https://www.ncbi.nlm.nih.gov/pubmed/30926784

226. Spencer A, Wilson S, Harpur E. Gadolinium chloride toxicity in the mouse. Hum

Exp Toxicol [Internet]. 1998 [cited 29 February 2020]; 17: 633–7. Available at: http://www.ncbi.nlm.nih.gov/pubmed/9865421

227. Port M, Idée JM, Medina C, Robic C, Sabatou M, Corot C. Efficiency, thermodynamic and kinetic stability of marketed gadolinium chelates and their possible clinical consequences: A critical review. Vol. 21, BioMetals. 2008.

228. Tang J, Sheng Y, Hu H, Shen Y. Macromolecular MRI contrast agents: Structures, properties and applications. Vol. 38, Progress in Polymer Science. Elsevier Ltd; 2013.

229. Lux J, Sherry AD. Advances in gadolinium-based MRI contrast agent designs for monitoring biological processes in vivo. Vol. 45, Current Opinion in Chemical Biology. Elsevier Ltd; 2018.

230. Mulder WJM, Strijkers GJ, Griffioen AW, et al. A Liposomal System for Contrast-Enhanced Magnetic Resonance Imaging of Molecular Targets. Bioconjug Chem [Internet]. 2004 [cited 20 March 2019]; 15: 799–806. Available at: https://pubs.acs.org/sharingguidelines

231. Laurent S, Vander Elst L, Thirifays C, Muller RN. Paramagnetic Liposomes: Inner versus Outer Membrane Relaxivity of DPPC Liposomes Incorporating Lipophilic Gadolinium Complexes. Langmuir [Internet]. 2008 [cited 21 January 2020]; 24: 4347–51. Available at: https://pubs.acs.org/doi/10.1021/la800148a

232. Kamaly N, Kalber T, Kenny G, Bell J, Jorgensen M, Miller A. A novel bimodal lipidic contrast agent for cellular labelling and tumour MRI. Org Biomol Chem. 2009; 8: 201–11.

233. Mitchell N, Kalber TL, Cooper MS, et al. Incorporation of paramagnetic, fluorescent and PET/SPECT contrast agents into liposomes for multimodal imaging. Biomaterials [Internet]. 2013 [cited 25 July 2018]; 34: 1179–92. Available at: https://www.sciencedirect.com/science/article/pii/S0142961212010939?via%3Dihub

234. Risselada HJ, Marrink SJ. Curvature effects on lipid packing and dynamics in liposomes revealed by coarse grained molecular dynamics simulations. Phys Chem Chem Phys. 2009; 11: 2056–67.

235. Koller D, Lohner K. The role of spontaneous lipid curvature in the interaction of interfacially active peptides with membranes. Vol. 1838, Biochimica et Biophysica Acta - Biomembranes. Elsevier; 2014.

236. Curtis EM, Hall CK. Molecular dynamics simulations of DPPC bilayers using 'lIME', a new coarse-grained model. J Phys Chem B. 2013; 117: 5019–30.

237. Ong SGM, Chitneni M, Lee KS, Ming LC, Yuen KH. Evaluation of extrusion technique for nanosizing liposomes. Pharmaceutics. 2016; 8.

238. Pignatello R, Musumeci T, Basile L, Carbone C, Puglisi G. Biomembrane models and drug-biomembrane interaction studies: Involvement in drug design and development. J Pharm Bioallied Sci [Internet]. 2011 [cited 19 January 2020]; 3:

4. Available at: http://www.jpbsonline.org/text.asp?2011/3/1/4/76461

239. Noebauer-Huhmann IM, Szomolanyi P, Juras V, Kraff O, Ladd ME, Trattnig S. Gadolinium-Based Magnetic Resonance Contrast Agents at 7 Tesla. Invest Radiol [Internet]. 2010 [cited 12 January 2020]; 45: 554–8. Available at: https://insights.ovid.com/crossref?an=00004424-201009000-00008

240. Shen Y, Goerner FL, Heverhagen JT, et al. In vitro T2 relaxivities of the Gd-based contrast agents (GBCAs) in human blood at 1.5 and 3 T. Acta Radiol [Internet]. 2019 [cited 2 March 2020]; 60: 694–701. Available at: http://www.ncbi.nlm.nih.gov/pubmed/30205704

241. Caravan P, Farrar CT, Frullano L, Uppal R. Influence of molecular parameters and increasing magnetic field strength on relaxivity of gadolinium- and manganese-based T1 contrast agents. Contrast Media Mol Imaging. 2009; 4: 89–100.

242. Gabizon A, Shmeeda H, Barenholz Y. Pharmacokinetics of pegylated liposomal Doxorubicin: review of animal and human studies. Clin Pharmacokinet [Internet]. 2003/05/13. 2003; 42: 419–36. Available at: https://www.ncbi.nlm.nih.gov/pubmed/12739982

243. Bertini I, Bianchini F, Calorini L, et al. Persistent contrast enhancement by sterically stabilized paramagnetic liposomes in murine melanoma. Magn Reson Med [Internet]. 2004 [cited 1 January 2020]; 52: 669–72. Available at: http://doi.wiley.com/10.1002/mrm.20189

244. Cittadino E, Botta M, Tei L, et al. In Vivo Magnetic Resonance Imaging Detection of Paramagnetic Liposomes Loaded with Amphiphilic Gadolinium(III) Complexes: Impact of Molecular Structure on Relaxivity and Excretion Efficiency. Chempluschem [Internet]. 2013 [cited 15 January 2020]; 78: 712–22. Available at: http://doi.wiley.com/10.1002/cplu.201300096

245. Winter PM, Caruthers SD, Yu X, et al. Improved molecular imaging contrast agent for detection of human thrombus. Magn Reson Med [Internet]. 2003; 50: 411–6. Available at: http://www.ncbi.nlm.nih.gov/pubmed/12876719

246. Luc F, Fortin M-A, Petoral RM, Söderlind F. Impact of agglomeration on the relaxometric properties of paramagnetic ultra-small gadolinium oxide nanoparticles. Nanotechnology. 2011; 22: 295103.

247. Geelen T, Paulis LE, Coolen BF, Nicolay K, Strijkers GJ. Passive targeting of lipid-based nanoparticles to mouse cardiac ischemia-reperfusion injury. Contrast Media Mol Imaging [Internet]. 2013 [cited 15 January 2020]; 8: 117–26. Available at: http://doi.wiley.com/10.1002/cmmi.1501

248. Fossheim SL, Fahlvik AK, Klaveness J, Muller RN. Paramagnetic liposomes as MRI contrast agents: influence of liposomal physicochemical properties on the in vitro relaxivity. Magn Reson Imaging. 1999; 17: 83–9.

249. Bödenler M, de Rochefort L, Ross PJ, et al. Comparison of fast field-cycling magnetic resonance imaging methods and future perspectives. Mol Phys [Internet]. 2019 [cited 4 March 2020]; 117: 832–48. Available at: https://www.tandfonline.com/doi/full/10.1080/00268976.2018.1557349

250. Bertini I, Luchinat C, Parigi G, Ravera E. Chapter 10 - Relaxometry and contrast agents for MRI. In: Bertini I, Luchinat C, Parigi G, Ravera E, Eds. NMR of Paramagnetic Molecules (Second Edition) [Internet]. Second Edition. Boston: Elsevier; 2017: 313–45. Available at: http://www.sciencedirect.com/science/article/pii/B9780444634368000107

251. Hahn GM. Potential for therapy of drugs and hyperthermia. Cancer Res [Internet]. 1979/06/01. 1979; 39: 2264–8. Available at: https://www.ncbi.nlm.nih.gov/pubmed/87263

252. Zhu L, Altman MB, Laszlo A, et al. Ultrasound Hyperthermia Technology for Radiosensitization. Ultrasound Med Biol [Internet]. 2019/02/19. 2019; 45: 1025–43. Available at: https://www.ncbi.nlm.nih.gov/pubmed/30773377

253. Kennedy JE. High-intensity focused ultrasound in the treatment of solid tumours. Nat Rev Cancer [Internet]. 2005/03/19. 2005; 5: 321–7. Available at: https://www.ncbi.nlm.nih.gov/pubmed/15776004

254. Elhelf IAS, Albahar H, Shah U, Oto A, Cressman E, Almekkawy M. High intensity focused ultrasound: The fundamentals, clinical applications and research trends. Diagn Interv Imaging [Internet]. 2018/05/21. 2018; 99: 349–59. Available at: https://www.ncbi.nlm.nih.gov/pubmed/29778401

255. Fisher DG, Price RJ. Recent Advances in the Use of Focused Ultrasound for Magnetic Resonance Image-Guided Therapeutic Nanoparticle Delivery to the Central Nervous System. Front Pharmacol [Internet]. 2019/12/05. 2019; 10: 1348. Available at: https://www.ncbi.nlm.nih.gov/pubmed/31798453

256. Basha SA, Salkho N, Dalibalta S, Husseini GA. Liposomes in Active, Passive and Acoustically-Triggered Drug Delivery. Mini Rev Med Chem [Internet]. 2019/04/10. 2019; 19: 961–9. Available at: https://www.ncbi.nlm.nih.gov/pubmed/30961495

257. Karimi M, Ghasemi A, Sahandi Zangabad P, et al. Smart micro/nanoparticles in stimulus-responsive drug/gene delivery systems. Chem Soc Rev [Internet]. 2016/01/19. 2016; 45: 1457–501. Available at: https://www.ncbi.nlm.nih.gov/pubmed/26776487

258. Karimi M, Sahandi Zangabad P, Ghasemi A, et al. Temperature-Responsive Smart Nanocarriers for Delivery Of Therapeutic Agents: Applications and Recent Advances. ACS Appl Mater Interfaces [Internet]. 2016/06/29. 2016; 8: 21107–33. Available at: https://www.ncbi.nlm.nih.gov/pubmed/27349465

259. Needham D, Dewhirst MW. The development and testing of a new temperature-sensitive drug delivery system for the treatment of solid tumors. Adv Drug Deliv Rev [Internet]. 2001/12/18. 2001; 53: 285–305. Available at: https://www.ncbi.nlm.nih.gov/pubmed/11744173

260. Needham D, Anyarambhatla G, Kong G, Dewhirst MW. A new temperature-sensitive liposome for use with mild hyperthermia: characterization and testing in a human tumor xenograft model. Cancer Res [Internet]. 2000/03/23. 2000 [cited 22 February 2020]; 60: 1197–201. Available at: https://www.ncbi.nlm.nih.gov/pubmed/10728674

261. Haemmerich D, Motamarry A. Thermosensitive Liposomes for Image-Guided Drug Delivery. Adv Cancer Res [Internet]. 2018/06/27. 2018; 139: 121–46. Available at: https://www.ncbi.nlm.nih.gov/pubmed/29941102

262. Dicheva BM, Koning GA. Targeted thermosensitive liposomes: an attractive novel approach for increased drug delivery to solid tumors. Expert Opin Drug Deliv [Internet]. 2013/12/11. 2014; 11: 83–100. Available at: https://www.ncbi.nlm.nih.gov/pubmed/24320104

263. Dewhirst MW, Landon CD, Hofmann CL, Stauffer PR. Novel approaches to treatment of hepatocellular carcinoma and hepatic metastases using thermal ablation and thermosensitive liposomes. Surg Oncol Clin N Am [Internet]. 2013/04/30. 2013; 22: 545–61. Available at: https://www.ncbi.nlm.nih.gov/pubmed/23622079

264. Lindner LH, Reinl HM, Schlemmer M, Stahl R, Peller M. Paramagnetic thermosensitive liposomes for MR-thermometry. Int J Hyperth [Internet]. 2005/09/09. 2005; 21: 575–88. Available at: https://www.ncbi.nlm.nih.gov/pubmed/16147441

265. Kono K, Nakashima S, Kokuryo D, et al. Multi-functional liposomes having temperature-triggered release and magnetic resonance imaging for tumor-specific chemotherapy. Biomaterials [Internet]. 2010/11/26. 2011; 32: 1387–95. Available at: https://www.ncbi.nlm.nih.gov/pubmed/21093041

266. Aoki I, Yoneyama M, Hirose J, et al. Thermoactivatable polymer-grafted liposomes for low-invasive image-guided chemotherapy. Transl Res [Internet]. 2015/08/26. 2015; 166: 660-673 e1. Available at: https://www.ncbi.nlm.nih.gov/pubmed/26303887

267. Peller M, Willerding L, Limmer S, et al. Surrogate MRI markers for hyperthermia-induced release of doxorubicin from thermosensitive liposomes in tumors. J Control Release [Internet]. 2016/07/02. 2016; 237: 138–46. Available at: https://www.ncbi.nlm.nih.gov/pubmed/27364227

268. Viglianti BL, Abraham SA, Michelich CR, et al. In vivo monitoring of tissue pharmacokinetics of liposome/drug using MRI: illustration of targeted delivery. Magn Reson Med [Internet]. 2004/06/02. 2004; 51: 1153–62. Available at: https://www.ncbi.nlm.nih.gov/pubmed/15170835

269. Tang WL, Tang WH, Li SD. Cancer theranostic applications of lipid-based nanoparticles. Drug Discov Today. 2018/04/17. 2018; 23: 1159–66.

270. Negussie AH, Yarmolenko PS, Partanen A, et al. Formulation and characterisation of magnetic resonance imageable thermally sensitive liposomes for use with magnetic resonance-guided high intensity focused ultrasound. Int J Hyperth [Internet]. 2011 [cited 15 January 2018]; 27: 140–55. Available at: http://www.tandfonline.com/doi/full/10.3109/02656736.2010.528140

271. Rizzitelli S, Giustetto P, Faletto D, Delli Castelli D, Aime S, Terreno E. The release of Doxorubicin from liposomes monitored by MRI and triggered by a combination of US stimuli led to a complete tumor regression in a breast

cancer mouse model. J Control Release. 2016; 230: 57–63.

272. Barenholz Y. Doxil® - The first FDA-approved nano-drug: Lessons learned. J Control Release [Internet]. 2012; 160: 117–34. Available at: http://dx.doi.org/10.1016/j.jconrel.2012.03.020

273. Rafiyath SM, Rasul M, Lee B, Wei G, Lamba G, Liu D. Comparison of safety and toxicity of liposomal doxorubicin vs. conventional anthracyclines: a meta-analysis. Exp Hematol Oncol [Internet]. 2012/12/06. 2012; 1: 10. Available at: https://www.ncbi.nlm.nih.gov/pubmed/23210520

274. Laginha KM, Verwoert S, Charrois GJ, Allen TM. Determination of doxorubicin levels in whole tumor and tumor nuclei in murine breast cancer tumors. Clin Cancer Res [Internet]. 2005/10/06. 2005; 11: 6944–9. Available at: https://www.ncbi.nlm.nih.gov/pubmed/16203786

275. Tak WY, Lin SM, Wang Y, et al. Phase III HEAT study adding lyso-thermosensitive liposomal doxorubicin to radiofrequency ablation in patients with unresectable hepatocellular carcinoma lesions. Clin Cancer Res. 2018; 24: 73–83.

276. Celik H, Wakim P, Pritchard WF, et al. Radiofrequency Ablation Duration per Tumor Volume May Correlate with Overall Survival in Solitary Hepatocellular Carcinoma Patients Treated with Radiofrequency Ablation Plus Lyso-Thermosensitive Liposomal Doxorubicin. J Vasc Interv Radiol [Internet]. 2019/08/15. 2019; 30: 1908–14. Available at: https://www.ncbi.nlm.nih.gov/pubmed/31409568

277. Yang W, Lee JC, Chen MH, et al. Thermosensitive liposomal doxorubicin plus radiofrequency ablation increased tumor destruction and improved survival in patients with medium and large hepatocellular carcinoma: A randomized, double-blinded, dummy-controlled clinical trial in a single cent. J Cancer Res Ther [Internet]. 2019/08/23. 2019; 15: 773–83. Available at: https://www.ncbi.nlm.nih.gov/pubmed/31436231

278. Zimmermann K, Hossann M, Hirschberger J, et al. A pilot trial of doxorubicin containing phosphatidyldiglycerol based thermosensitive liposomes in spontaneous feline soft tissue sarcoma. Int J Hyperth [Internet]. 2016/09/07. 2017 [cited 23 February 2020]; 33: 178–90. Available at: https://www.tandfonline.com/doi/full/10.1080/02656736.2016.1230233

279. Lyon PC, Gray MD, Mannaris C, et al. Safety and feasibility of ultrasound-triggered targeted drug delivery of doxorubicin from thermosensitive liposomes in liver tumours (TARDOX): a single-centre, open-label, phase 1 trial. Lancet Oncol [Internet]. 2018/07/14. 2018; 19: 1027–39. Available at: https://www.ncbi.nlm.nih.gov/pubmed/30001990

280. Gray MD, Lyon PC, Mannaris C, et al. Focused Ultrasound Hyperthermia for Targeted Drug Release from Thermosensitive Liposomes: Results from a Phase I Trial. Radiology [Internet]. 2019/01/16. 2019 [cited 19 February 2020]; 291: 232–8. Available at: http://pubs.rsna.org/doi/10.1148/radiol.2018181445

281. Haemmerich D. Non-invasive image-guided targeted drug delivery. Lancet

Oncol [Internet]. 2018/07/14. 2018; 19: 1000–1. Available at: https://www.ncbi.nlm.nih.gov/pubmed/30001989

282. Yiannakou M, Menikou G, Yiallouras C, Ioannides C, Damianou C. MRI guided focused ultrasound robotic system for animal experiments. Int J Med Robot [Internet]. 2017/02/18. 2017; 13. Available at: https://www.ncbi.nlm.nih.gov/pubmed/28211622

283. Menikou G, Yiallouras C, Yiannakou M, Damianou C. MRI-guided focused ultrasound robotic system for the treatment of bone cancer. Int J Med Robot [Internet]. 2016/07/17. 2017; 13. Available at: https://www.ncbi.nlm.nih.gov/pubmed/27422861

284. Meng Y, MacIntosh BJ, Shirzadi Z, et al. Resting state functional connectivity changes after MR-guided focused ultrasound mediated blood-brain barrier opening in patients with Alzheimer's disease. Neuroimage [Internet]. 2019/06/30. 2019; 200: 275–80. Available at: https://www.ncbi.nlm.nih.gov/pubmed/31254646

285. Lipsman N, Meng Y, Bethune A, et al. Blood-brain barrier opening in Alzheimer's disease using MR-guided focused ultrasound. Nat Commun. 2018; 9: 1–8.

286. Rosca E V., Wright M, Gonitel R, Gedroyc W, Miller AD, Thanou M. Thermosensitive, Near-Infrared-Labeled Nanoparticles for Topotecan Delivery to Tumors. Mol Pharm. 2015; 12: 1335–46.

287. Marasini R, Thanh Nguyen TD, Aryal S. Integration of gadolinium in nanostructure for contrast enhanced-magnetic resonance imaging. Wiley Interdiscip Rev Nanomed Nanobiotechnol [Internet]. 2019/09/06. 2020; 12: e1580. Available at: https://www.ncbi.nlm.nih.gov/pubmed/31486295

288. Sandström MC, Ickenstein LM, Mayer LD, et al. Effects of lipid segregation and lysolipid dissociation on drug release from thermosensitive liposomes. J Control Release [Internet]. 2005/07/19. 2005; 107: 131–42. Available at: https://www.ncbi.nlm.nih.gov/pubmed/16023753

289. Al-Ahmady ZS, Hadjidemetriou M, Gubbins J, Kostarelos K. Formation of protein corona in vivo affects drug release from temperature-sensitive liposomes. J Control Release [Internet]. 2018/03/10. 2018; 276: 157–67. Available at: https://www.ncbi.nlm.nih.gov/pubmed/29522832

290. Li S, Yin G, Pu X, Huang Z, Liao X, Chen X. A novel tumor-targeted thermosensitive liposomal cerasome used for thermally controlled drug release. Int J Pharm [Internet]. 2019/09/07. 2019; 570: 118660. Available at: https://www.ncbi.nlm.nih.gov/pubmed/31491484

291. Chang EH, Harford JB, Eaton MA, et al. Nanomedicine: Past, present and future - A global perspective. Biochem Biophys Res Commun [Internet]. 2015/11/01. 2015; 468: 511–7. Available at: https://www.ncbi.nlm.nih.gov/pubmed/26518648

292. Bozzuto G, Molinari A. Liposomes as nanomedical devices. Int J Nanomedicine [Internet]. 2015/02/14. 2015; 10: 975–99. Available at:

https://www.ncbi.nlm.nih.gov/pubmed/25678787

293. Huynh K, Baghdanian AH, Baghdanian AA, Sun DS, Kolli KP, Zagoria RJ. Updated guidelines for intravenous contrast use for CT and MRI. Emerg Radiol [Internet]. 2020/01/12. 2020; Available at: https://www.ncbi.nlm.nih.gov/pubmed/31925592

294. Frenzel T, Lengsfeld P, Schirmer H, et al. Stability of gadolinium-based magnetic resonance imaging contrast agents in human serum at 37 degrees C. Invest Radiol [Internet]. 2008/11/13. 2008 [cited 16 February 2020]; 43: 817–28. Available at: https://www.ncbi.nlm.nih.gov/pubmed/19002053

295. Prybylski JP, Semelka RC, Jay M. The stability of gadolinium-based contrast agents in human serum: A reanalysis of literature data and association with clinical outcomes. 2017/01/17. 2017; 38: 145–51.

296. Dicheva BM, Seynhaeve AL, Soulie T, Eggermont AM, Ten Hagen TL, Koning GA. Pharmacokinetics, Tissue Distribution and Therapeutic Effect of Cationic Thermosensitive Liposomal Doxorubicin Upon Mild Hyperthermia. Pharm Res [Internet]. 2015/11/01. 2016; 33: 627–38. Available at: https://www.ncbi.nlm.nih.gov/pubmed/26518763

297. Lokerse WJ, Kneepkens EC, ten Hagen TL, Eggermont AM, Grull H, Koning GA. In depth study on thermosensitive liposomes: Optimizing formulations for tumor specific therapy and in vitro to in vivo relations. Biomaterials [Internet]. 2016/01/14. 2016; 82: 138–50. Available at: https://www.ncbi.nlm.nih.gov/pubmed/26761778

298. Motamarry A, Negussie AH, Rossmann C, et al. Real-time fluorescence imaging for visualization and drug uptake prediction during drug delivery by thermosensitive liposomes. Int J Hyperth [Internet]. 2019/08/28. 2019; 36: 817–26. Available at: https://www.ncbi.nlm.nih.gov/pubmed/31451077

299. de Smet M, Langereis S, van den Bosch S, et al. SPECT/CT imaging of temperature-sensitive liposomes for MR-image guided drug delivery with high intensity focused ultrasound. J Control Release [Internet]. 2013/04/20. 2013; 169: 82–90. Available at: https://www.ncbi.nlm.nih.gov/pubmed/23598044

300. Sanches PG, Grull H, Steinbach OC. See, reach, treat: ultrasound-triggered image-guided drug delivery. Ther Deliv [Internet]. 2012/07/27. 2011; 2: 919–34. Available at: https://www.ncbi.nlm.nih.gov/pubmed/22833903

301. Kuroda K. MR techniques for guiding high-intensity focused ultrasound (HIFU) treatments. J Magn Reson Imaging [Internet]. 2017/06/06. 2018; 47: 316–31. Available at: https://www.ncbi.nlm.nih.gov/pubmed/28580706

302. Yi XM, Wang FL, Qin WJ, Yang XJ, Yuan JL. Near-infrared fluorescent probes in cancer imaging and therapy: an emerging field. Int J Nanomedicine [Internet]. 2014/03/22. 2014; 9: 1347–65. Available at: https://www.ncbi.nlm.nih.gov/pubmed/24648733

303. Huang Y, Gu B, Liu C, et al. Thermosensitive Liposome-Mediated Drug Delivery in Chemotherapy: Mathematical Modelling for Spatio-temporal Drug Distribution and Model-Based Optimisation. Pharmaceutics [Internet].

2019/12/05. 2019; 11. Available at: https://www.ncbi.nlm.nih.gov/pubmed/31795486

304. Lokerse WJMM, Bolkestein M, Dalm SU, et al. Comparing the therapeutic potential of thermosensitive liposomes and hyperthermia in two distinct subtypes of breast cancer. J Control Release [Internet]. 2017/05/10. 2017; 258: 34–42. Available at: https://www.ncbi.nlm.nih.gov/pubmed/28479096

305. Zhan W, Gedroyc W, Xu XY. The effect of tumour size on drug transport and uptake in 3-D tumour models reconstructed from magnetic resonance images. PLoS One [Internet]. 2017/02/18. 2017; 12: e0172276. Available at: https://www.ncbi.nlm.nih.gov/pubmed/28212385

306. Regev R, Eytan GD. Flip-flop of doxorubicin across erythrocyte and lipid membranes. Biochem Pharmacol. 1997; 54: 1151–8.

307. Liu C, Ewert KK, Wang N, Li Y, Safinya CR, Qiao W. A multifunctional lipid that forms contrast-agent liposomes with dual-control release capabilities for precise MRI-guided drug delivery. Biomaterials. 2019; 221: 119412.

308. Dai Y, Su J, Wu K, et al. Multifunctional Thermosensitive Liposomes Based on Natural Phase-Change Material: Near-Infrared Light-Triggered Drug Release and Multimodal Imaging-Guided Cancer Combination Therapy. ACS Appl Mater Interfaces. 2019; 11: 10540–53.

309. Layne KA, Wood DM, Dargan PI. Gadolinium-based contrast agents–what is the evidence for 'gadolinium deposition disease' and the use of chelation therapy? Vol. 58, Clinical Toxicology. Taylor and Francis Ltd; 2020.

310. Lee W, Im HJ. Theranostics Based on Liposome: Looking Back and Forward. Nucl Med Mol Imaging (2010). 2019; 53: 242–6.

311. Tran S, DeGiovanni P-J, Piel B, Rai P. Cancer nanomedicine: a review of recent success in drug delivery. Clin Transl Med. 2017; 6.

312. Guntur SR, Choi MJ. An improved tissue-mimicking polyacrylamide hydrogel phantom for visualizing thermal lesions with high-intensity focused ultrasound. Ultrasound Med Biol [Internet]. 2014/09/16. 2014; 40: 2680–91. Available at: https://www.ncbi.nlm.nih.gov/pubmed/25220272